# Assessment and Prediction of Carbon Dioxide Fluxes with Eddy Covariance and Machine Learning Techniques

Von der Fakultät für Georessourcen und Materialtechnik der Rheinisch -Westfälischen Technischen Hochschule Aachen

zur Erlangung des akademischen Grades eines

Doktors der Naturwissenschaften

genehmigte Dissertation

vorgelegt von

Oliver Reitz, M. Sc.

Berichter: Univ.-Prof. Dr. rer. nat. Michael Leuchner

Univ.-Prof. Dr. Jörg Bendix

Tag der mündlichen Prüfung: 03.08.2023

Diese Dissertation ist auf den Internetseiten der Universitätsbibliothek online verfügbar

#### **Abstract**

Land use and land cover changes and the terrestrial carbon sink are two important components of the global carbon budget. Several methodological approaches exist to measure fluxes of  $CO_2$  and other greenhouse gases between ecosystems and the atmosphere. With an accurate quantification of these fluxes, it is possible to compare carbon source and sink strengths between different land covers and to evaluate environmental influences on these terms. Out of those methods, the eddy covariance technique has the advantage of providing direct and quasi-continuous turbulent flux observations at the ecosystem scale. However, to compare eddy covariance data to, e.g., top-down methods and to achieve spatially gapless data sets, these point measurements with a relatively small footprint require a spatial upscaling with statistical methods such as machine learning and ancillary remote sensing data.

Another issue with eddy covariance data sets is the underrepresentation of certain ecosystem types and climatic regions. Recently disturbed ecosystems belong to this group, but usually also exhibit non-ideal characteristics for eddy covariance measurements such as abrupt surface changes and heterogeneous regrowth. Therefore, it is important to assess the uncertainty of eddy covariance measurements for disturbed ecosystems in regard to different choices of measurement design and processing and thus to improve the interpretability of such measurements.

On the other hand, a changing climate can also enforce a reduced sink strength on ecosystems through, e.g., heat and drought. In this way, eddy covariance derived data on CO<sub>2</sub> uptake in combination with other environmental measurements and advanced statistical analyses can reveal limiting conditions for photosynthesis and thus a reduced efficiency to use light for CO<sub>2</sub> assimilation. In this dissertation, these three issues, i) spatial upscaling of eddy covariance data, ii) methodological uncertainties of obtaining flux data at disturbed sites, and iii) environmental impacts on ecosystem-scale photosynthesis, are addressed within the TERENO Eifel/Lower Rhine Valley Observatory, which comprises the Rur catchment, mostly located in western Germany.

In a first study, eddy covariance CO<sub>2</sub> flux data from different land covers within the Rur catchment were upscaled to the whole catchment area using a random forest machine learning model incorporating MODIS remote sensing and COSMO-REA6 reanalysis data. For this task, state-of-the-art predictor variable selection methods for machine learning models were evaluated. Results of this study show that combining eddy covariance flux data with remote sensing products and reanalysis data is a feasible way to upscale CO<sub>2</sub> flux information to the regional scale at a relatively high spatial resolution (250 m) and across various land covers. The study further indicates that averaging multiple model runs in the feature selection process can improve these results. Although an R<sup>2</sup> of 0.41 is in the range of other studies using a spatial cross validation scheme, this value reveals that there is still room for improvement. Main limitations of the analysis include a low prediction performance on high magnitude fluxes as a narrower range was predicted than observed, and the fact that differences between land cover classes were also narrower in the upscaled product than between eddy covariance stations.

The further analyses were confined to a subregion within the Rur catchment, the Wüstebach site in the northern Eifel low mountain range. The site encompasses the Wüstebach headwater region and is mostly composed of a planted spruce forest but also contains a deforested area of 8.6 ha with unmanaged regrowth. This fast-growing vegetation requires a regular adjustment of the eddy covariance measurement height in order to ensure a stable flux source area in the long run and to prevent high spectral losses. In a second study, CO<sub>2</sub> and H<sub>2</sub>O fluxes were hence measured over the deforested area with eddy covariance systems in two different heights and were processed with five

different spectral corrections. In this way, the uncertainty from measurement height and choice of spectral correction was assessed, and insights were gained in the trade-offs that must be considered at a site with non-ideal characteristics. For the deforested site, results show that at the lower height spectral corrections were higher and had a higher standard deviation among methods compared to the upper height for both CO<sub>2</sub> and H<sub>2</sub>O fluxes. The average standard deviation between heights was even higher than between spectral corrections at the same height (24.8% of CO<sub>2</sub> flux; 9.7% of H<sub>2</sub>O flux). Furthermore, the energy balance closure was on average about 9% better for the upper system than for the lower system. On the other hand, the modelled footprints of both heights did not match the average footprint of the previous years at the lower height. Hence, the study indicates a difficulty of achieving a stable flux source area over longer time periods for fast growing vegetation but also emphasizes the importance of a carefully adjusted measurement height. Although the study improved the interpretability of flux measurements for a disturbed site, its main limitation comprises the difficulty to apply one of the common footprint models to estimate the flux source area for this site with complex flow, especially over the forest edges.

A third study concerned the Wüstebach spruce forest. For this site gross primary productivity derived from eddy covariance CO<sub>2</sub> flux data was combined with measurements of green canopy absorbed photosynthetically active radiation (APAR<sub>g</sub>), sap flow, and other meteorological and plant physiological data. In this way, water-limiting conditions for photosynthesis and the light use efficiency of a spruce forest were evaluated. In addition, the importance of environmental variables for the prediction of gross primary productivity was assessed with state-of-the-art machine learning variable importance measures. In this study, data from the 2021 growing season was analyzed, for which the light use efficiency of green parts of the forest was on average 4.0 ± 2.3% and showed a unimodal relation to air temperature with a maximum around 15 °C. For modelling gross primary productivity with treebased machine learning models, canopy chlorophyll content likely as a seasonal variable for photosynthetic capacity and APAR<sub>g</sub> likely as a diurnal variable for energy supply were the most important variables. On days with high vapor pressure deficit, tree-scale sap flow and ecosystem-scale gross primary productivity both shifted to a clockwise hysteretic response to APAR<sub>g</sub>. It is demonstrated that the onset of such a clockwise hysteretic pattern of sap flow to APAR<sub>g</sub> can be a useful indicator of afternoon stomatal closure related to water-limiting conditions. However, the main limitation of this case study is its limited extent, as just one comparatively cool and wet growing season at a single site with a single dominant tree species, Picea abies, was investigated.

Overall, this dissertation highlights the use of direct flux measurements and machine learning methods for both the evaluation of land cover changes and the impact of changing environmental conditions on the  $CO_2$  source and sink strengths of terrestrial ecosystems.

#### Zusammenfassung

Landbedeckungs- und Landnutzungsänderungen sowie die terrestrische Kohlenstoffsenke sind zwei wichtige Komponenten im globalen Kohlenstoffhaushalt. Es existieren mehrere methodische Ansätze zur Messung von CO<sub>2</sub>- und anderen Treibhausgasflüssen zwischen Ökosystemen und der Atmosphäre. Mit einer genauen Quantifizierung dieser Flüsse ist es möglich, Kohlenstoffquellen und -senken zwischen verschiedenen Landbedeckungen zu vergleichen und Umwelteinflüsse auf diese Terme zu bewerten. Von diesen Methoden hat der Eddy Kovarianz Ansatz den Vorteil, direkte und quasikontinuierliche turbulente Flussmessungen auf der Ökosystemebene zu ermöglichen. Um jedoch Eddy Kovarianz Daten mit z.B. top-down Methoden zu vergleichen und lückenlose Daten zu generieren, erfordern diese Punkt-Messungen mit einem relativ kleinen Quellgebiet eine räumliche Hochskalierung mit statistischen Methoden wie z.B. maschinellem Lernen und begleitenden Fernerkundungsdaten.

Ein weiteres Problem von Eddy Kovarianz Datensätzen ist die Unterrepräsentation bestimmter Ökosystemtypen und Klimaregionen. Ökosysteme, die kürzlich Störungen erfahren haben, gehören zu dieser Gruppe, weisen aber in der Regel auch nicht ideale Eigenschaften für Eddy Kovarianz Messungen auf, wie z.B. abrupte Rauigkeitsänderungen und heterogene nachwachsende Vegetation. Daher ist es wichtig, die Unsicherheit von Eddy Kovarianz Messungen für gestörte Ökosysteme in Bezug auf verschiedene Messdesigns und Prozessierungsmethoden bewerten und interpretieren zu können. Auf der anderen Seite kann der Klimawandel auch durch z.B. Hitze und Dürre auf Ökosysteme rückwirken und eine verringerte CO<sub>2</sub> Senkenstärke verursachen. Auf diese Weise können von Eddy Kovarianz Messungen abgeleitete Daten zur CO<sub>2</sub>-Aufnahme in Kombination mit anderen Umweltmessungen und fortgeschrittenen statistischen Analysen limitierende Bedingungen für die Photosynthese aufdecken und somit eine reduzierte Effizienz bei der Verwendung von Licht zur CO<sub>2</sub>-Assimilation identifizieren. In dieser Dissertation werden diese drei Themen, i) räumliches Hochskalieren von Eddy Kovarianz Daten, ii) methodische Unsicherheiten von Flussmessungen in gestörten Ökosystemen, und iii) Umwelteinflüsse auf die Photosyntheseleistung, im Rahmen der TERENO Eifel/Lower Rhine Valley Observatory behandelt, welche das Rur-Einzugsgebiet im Westen Deutschlands umfasst.

In einer ersten Studie wurden CO<sub>2</sub>-Flussdaten mittels Eddy Kovarianz Messungen von verschiedenen Landbedeckungen im Rur-Einzugsgebiet mit Hilfe eines Random Forest Machine Learning Modells unter Verwendung von MODIS-Fernerkundungsdaten und COSMO-REA6-Reanalysedaten auf das gesamte Einzugsgebiet hochskaliert. Für diese Aufgabe wurden zudem neuste Methoden zur Auswahl von Vorhersagevariablen für Machine Learning Modelle evaluiert. Die Ergebnisse dieser Studie zeigen, dass die Kombination von Eddy Kovarianz Flussdaten mit Fernerkundungsprodukten und Reanalysedaten eine praktikable Möglichkeit ist, um CO<sub>2</sub>-Flussinformationen auf die regionale Ebene mit relativ hoher räumlicher Auflösung (250 m) und über verschiedene Landbedeckungen hochzuskalieren. Die Studie zeigt weiterhin, dass das Mitteln mehrerer Modellläufe im Feature-Auswahlprozess die Ergebnisse verbessern kann. Obwohl ein R² von 0,41 im Bereich anderer Studien mit einem räumlichen Kreuzvalidierungsschema liegt, zeigt dieser Wert, dass noch viele Möglichkeiten zur Verbesserung bestehen. Die Hauptbeschränkungen der Analyse umfassen eine niedrige Vorhersageleistung bei hohen Flussmagnituden, da eine engere Bandbreite vorhergesagt als beobachtet wurde, sowie die Tatsache, dass die Unterschiede zwischen Landbedeckungsklassen im hochskalierten Produkt kleiner waren als zwischen Eddy Kovarianz Stationen.

Die weiteren Analysen beschränken sich auf eine Teilregion des Rur-Einzugsgebiets, den Standort Wüstebach in der nördlichen Eifel. Dieser Standort umfasst die Quellregion des Wüstebachs und besteht hauptsächlich aus einem gepflanzten Fichtenforsts, enthält aber auch eine entwaldete Fläche

von 8,6 ha mit unkontrolliertem Nachwuchs. Diese schnell wachsende Vegetation erfordert eine regelmäßige Anpassung der Messhöhe der Eddy Kovarianz Messungen, um eine stabile Quellregion der turbulenten Flüsse auf lange Sicht sicherzustellen und hohe spektrale Verluste zu vermeiden. In einer zweiten Studie wurden daher CO2- und H2O-Flüsse über der entwaldeten Fläche mit der Eddy Kovarianz Methode in zwei verschiedenen Höhen gemessen und mit fünf verschiedenen spektralen Korrekturen prozessiert. Auf diese Weise wurde die Unsicherheit der Messhöhe und der Wahl der spektralen Korrektur bewertet und die Abwägungen beleuchtet, die an einem Standort mit nicht idealen Eigenschaften berücksichtigt werden müssen. Für den entwaldeten Standort zeigen die Ergebnisse, dass für die untere Messhöhe die spektralen Korrekturen höher waren und diese eine höhere Standardabweichung zwischen den Methoden aufwiesen als bei der oberen Höhe, sowohl für CO<sub>2</sub>- als auch für H<sub>2</sub>O-Flüsse. Die durchschnittliche Standardabweichung zwischen den Höhen war sogar höher als zwischen den spektralen Korrekturen in derselben Höhe (24,8% des CO<sub>2</sub>-Flusses; 9,7% des H<sub>2</sub>O-Flusses). Darüber hinaus war die Schließung der Energiebilanz für das obere System im Durchschnitt um etwa 9% besser als für das untere. Andererseits stimmten die modellierten Footprints beider Höhen nicht mit dem durchschnittlichen Footprint der Vorjahre auf der niedrigeren Höhe überein. Daher bestätigt die Studie die Schwierigkeit, über längere Zeiträume einen stabile Footprint für schnell wachsende Vegetation zu erreichen, unterstreicht aber auch die Wichtigkeit einer sorgfältig angepassten Messhöhe. Obwohl durch diese Studie Interpretierbarkeit von Flussmessungen für ein gestörtes Ökosystem verbessert wurde, besteht ihre Hauptbeschränkung aus der Schwierigkeit eines der gängigen Footprint-Modelle anzuwenden, um den Quellbereich der turbulenten Flüsse für diesen Standort mit komplexem Strömungseigenschaften abzuschätzen, was insbesondere für die Waldränder zutrifft.

Eine dritte Studie betrifft den Fichtenforst am Wüstebach. Dort wurden Informationen zur Bruttoprimärproduktion (BPP), abgeleitet aus Eddy Kovarianz basierten CO₂-Flussdaten, mit Messungen der von grünen Blättern absorbierten photosynthetisch aktiven Strahlung (APARg), dem Saftfluss und anderen meteorologischen und pflanzenphysiologischen Daten kombiniert. Auf diese Weise wurden wasserlimitierende Bedingungen für die Photosynthese sowie die Lichtnutzungseffizienz eines Fichtenwaldes untersucht. Darüber hinaus wurde die Bedeutung einzelner Umweltvariablen für die Vorhersage der BPP mit neusten Machine Learning Methoden bewertet. Für diese Studie wurden Daten der Vegetationsperiode 2021 analysiert. Die Lichtnutzungseffizienz der grünen Bestandteile des Fichtenwaldes betrug hierfür im Durchschnitt 4,0 ± 2,3% und zeigte eine unimodale Beziehung zur Lufttemperatur mit einem Maximum bei etwa 15 °C. Für die Modellierung der BPP mit Machine Learning Modellen waren Canopy Chlorophyll Content vermutlich als saisonale Variable für die photosynthetische Kapazität und APAR<sub>g</sub> vermutlich als tageszyklische Variable für das Energiedargebot die wichtigsten Variablen. An Tagen mit hohem Sättigungsdefizit von Wasserdampf in der Luft wiesen sowohl der Saftfluss auf Baumebene als auch die BPP auf Ökosystemebene eine in Bezug auf APARg im Uhrzeigersinn verschobene hysteretische Reaktion auf. Es wurde somit gezeigt, dass das Einsetzen einer solchen im Uhrzeigersinn verschobenen Hystereseschleife des Saftflusses in Bezug auf APARg ein guter Indikator für das nachmittägliche Schließen der Stomata aufgrund von wasserlimitierenden Bedingungen sein kann. Die Hauptlimitierung dieser Fallstudie besteht jedoch in ihrem begrenzten Umfang, da nur eine vergleichsweise kühle und feuchte Vegetationsperiode an einem einzigen Standort mit einer einzigen dominanten Baumart, Picea abies, untersucht wurde.

Zusammenfassend wurde durch diese Dissertation der Nutzen direkter Flussmessungen und Methoden des maschinellen Lernens sowohl für die Quantifizierung von Landnutzungsänderungen als auch für den Einfluss sich ändernder Umweltbedingungen auf die CO<sub>2</sub> Quellen- und Senkenstärken terrestrischer Ökosysteme herausgestellt.

## Table of contents

A	bstrac	t		İ
Zı	usamn	nen	fassung	iii
Ta	able of	f co	ntents	V
Li	st of fi	igur	es	viii
Li	st of ta	able	s	xi
1	Int	rod	uction	1
	1.1	R	ationale and Objectives	1
	1.2	Т	ne Ecosystem Scale Carbon Exchange – Definitions and Limitations	4
	1.3	Ε	nergy Pathways of Absorbed Radiation at the Leaf Scale	5
2	Stu	ıdy	Area: The Wüstebach Research Site within the Eifel/Lower Rhine Valley Obs	ervatory 6
	2.1	Т	ne Eifel/Lower Rhine Valley Observatory	6
	2.2	Т	ne Wüstebach Research Site	8
3	Me	etho	ods	11
	3.1	Е	ddy Covariance	11
	3.2	Т	ree-based Machine Learning	14
4	Up	sca	ing Net Ecosystem Exchange over Heterogeneous Landscapes with Machine	Learning 17
	4.1	Ir	stroduction	18
	4.2	D	ata and Methods	19
	4.2	2.1	Study Area	19
	4.2	2.2	Eddy Covariance Data	20
	4.2	2.3	Raster Data	21
	4.2	2.4	Random Forest Model	23
	4.2	2.5	Cross Validation	24
	4.3	R	esults	25
	4.3	3.1	Cross Validation Results	25
	4.3	3.2	Upscaling Results	28
	4.4	D	iscussion	31
	4.5	С	onclusion	33
	4.6	D	ata Availability Statement	34
	4.7	Α	cknowledgements	34
5			of Measurement Height and Low-Pass-Filtering Corrections on Eddy-Covari	
IV			ents Over a Forest Clearing with Complex Vegetation	
	5.1		itroduction	36
	5.2	N	laterials and Methods	37

	5.2.	.1	Site Description	37
	5.2.	.2	Eddy-Covariance Set-Up and Processing	39
	5.2.	.3	Low-Pass-Filtering Correction	40
	5.2.	.4	Energy Balance	41
	5.2.	.5	Footprint Estimation	41
	5.3	Res	ults	42
	5.3.	.1	Spectral Analysis	42
	5.3.	.2	Correction Factors	43
	5.3.	.3	Flux Results	45
	5.3.	.4	Energy Balance Closure	48
	5.3.	.5	Footprint	49
	5.4	Disc	cussion	50
	5.4.	.1	Assessment of Measurement Height	50
	5.4.	.2	Spectral Corrections	52
	5.5	Con	clusion	54
	5.6	Ack	nowledgements	54
6			nental Drivers of Gross Primary Productivity and Light Use Efficiency of a Temp	
Sp			· · · · · · · · · · · · · · · · · · ·	
	6.1		oduction	56
	6.2		cerials and Methods	58
	6.2.		Study Area Description	58
	6.2.		Eddy Covariance, Meteorological, and Sap Flow Measurements	58
	6.2.		Sentinel-2 Derived Vegetation Indices	59
	6.2.		PAR and R/FR Measurements	59
	6.2.		Evaluation of Environmental Drivers	61
	6.3	Res		63
	6.3.		Interpretation of Environmental Drivers	63
	6.3.		Importance of Environmental Drivers for Machine Learning Models	65
	6.3.		Sap Flow – GPP Relationship and their Response to Environmental Drivers	67
	6.4	Disc	cussion	68
	6.4.		Identification of Photosynthesis Limiting Conditions	68
	6.4.	.2	Environmental Drivers	69
	6.4.		Variability and Uncertainties of LUE <sub>g</sub> Estimates	70
	6.5		clusions	71
	6.6		a Availability Statement	71
	6.7	Ack	nowledgments	72

	6.8	Supporting Information	72
	6.8.	1 Text S1. Calculation of GPP <sub>dev</sub>	72
	6.8.2	2 Figures	73
7	Synt	thesis and Outlook	83
8	Dan	ksagung/Acknowledgments	88
9	Refe	erences	90
	9.1	Publication List	90
	9.2	External References	90

## List of figures

<b>Figure 2.1</b> Elevation of the Rur catchment area from SRTM data (Jarvis et al., 2008) and Walter and Lieth climate diagrams for the TERENO Wüstebach site and three weather stations from the German Weather Service (DWD, 2022), all for the years 2011-2021 to match the Wüstebach time series.	7
<b>Figure 2.2</b> The Wüstebach intensive research site with instrumentation and aerial images demonstrating the deforested area. Figure adapted without changes from Bogena et al. (2018), under CC BY-NC-ND 4.0.	8
<b>Figure 2.3</b> Photography of the 38 m Wüstebach tower, mounted with, an eddy covariance system and sensors for photosynthetically active radiation, among others. Published with the kind permission of the authors Carsten Montzka and Jordan Bates, Forschungszentrum Jülich.	9
<b>Figure 3.1</b> Schematic depiction of a single decision tree with arbitrary variables and values in each node (blue rectangles) and leaf (green circles). The values in the leaves are the average target values of all training samples that fall within the respective leaf. For random forest, the predictions of all trees are averaged. For gradient boosting, predictions from the last tree are taken.	16
<b>Figure 4.1</b> Elevation from SRTM data (Jarvis et al., 2008) and eddy covariance stations used for training within the Rur catchment area (left), the location of the study area and the FLUXNET stations within Germany (middle) and simplified land cover classes after Lussem and Herbrecht for the Rur catchment (2019) (right).	19
<b>Figure 4.2</b> Schematic depiction of the spatial and temporal cross validation (CV) strategies that have been applied for this analysis. t1, t2 and t3 refer to three different time steps (years in our case), while ta refers to the FLUXNET data which are outside the timespan of TERENO data (prior to 2010) and tb refers to the years included in the TERENO data (2010–2014). The figure was recreated and modified after Meyer et al. (2018).	24
<b>Figure 4.3</b> Assessment of prediction quality in comparison to observations from TERENO test data. (a) scatter plot with regression line (blue) and identity line (black); (b) boxplots with mean values displayed as crosses; (c) density plot of predicted (blue) and observed (red) NEE values; (d) absolute error by observed NEE. The vertical line at zero marks the border between CO <sub>2</sub> sinks (left) and CO <sub>2</sub> sources (right).	28
<b>Figure 4.4</b> Yearly courses of predicted net ecosystem exchange (NEE) aggregated by each land cover class for the period 2010-2018 (points), and smoothed by a loess function (lines; above). Standard deviation (±) for each of those lines separately (gray bands; below).	30
<b>Figure 4.5</b> Predicted net ecosystem exchange (NEE) of the Rur catchment aggregated for the whole investigation period 2010-2018 and for each season. Mean values for each map are 0.86 g C $\text{m}^{-2}\text{d}^{-1}$ (winter), -2.14 (spring), -2.02 (summer), 0.75 (fall) and -0.65 (year).	31
<b>Figure 5.1</b> Location of the study area in EPSG:32632 (a), vegetation heights of woody plants from a 2017 vegetation mapping in inside the fence (b), and view of the eddy-covariance (EC) tower looking north (c).	38
<b>Figure 5.2</b> Binned means of flow tilt angles by wind direction during near-neutral conditions calculated from yaw-rotated wind components (a) and after application of a sector-wise planar fit rotation (b), as well as the $u *$ ratio between the upper and lower system after planar fit	

rotation, with binned mean values displayed in red and the distorted sector shaded in grey (c). Vertical dotted lines indicate the direction of the tower.	39
<b>Figure 5.3</b> Ensemble cospectra (Co) during unstable conditions of fluxes measured at the upper system (a), and at the lower system (c), as well as the ratio between $w'C'$ and $w'Ts'$ cospectra (b), and $w'q'$ flux and $w'Ts'$ cospectra (d). The normalized frequency is the natural frequency in Hz multiplied with $z$ and divided by $U$ . Vertical dotted lines indicate the range used for calculating integrals.	43
<b>Figure 5.4</b> Boxplots of CO <sub>2</sub> flux correction factors at the upper system (a) and lower system (b) for each spectral correction method.	44
<b>Figure 5.5</b> CO <sub>2</sub> flux correction factors (CF) of the low-pass filtering correction methods against wind speed (U) for the upper system (black dots) and the lower system (red dots).	45
<b>Figure 5.6</b> CO <sub>2</sub> fluxes and $\lambda E$ aggregated by wind direction for the upper system (a, c) and the lower system (b, d). The shaded area indicates excluded data from northern wind directions.	47
<b>Figure 5.7</b> Cumulative non gap-filled evapotranspiration (a) and $CO_2$ fluxes (b) including both daytime and night-time situations that passed quality control. Up and Lo stand for the upper and lower system, respectively.	48
<b>Figure 5.8</b> Cumulative flux footprint estimates for daytime situations and all wind directions of the upper system (a) and the lower system (b) in 10% steps from 10 to 90%. The shaded area indicates excluded wind directions for data filtering.	49
<b>Figure 5.9</b> Relative importance of pixels more important for the upper system (a) and pixels more important for the lower system (b), without observations from north. Please note the different colour scales for the subplots, which were expedient to visualize the relatively smaller importance of individual pixels in (a) compared to (b). The coordinate origin is at the eddy-covariance station and the white line delineates the fence for orientation.	50
<b>Figure 6.1</b> Light Detection And Ranging (LiDAR) derived canopy heights from the Wüstebach forest site, western Germany. LiDAR data collected on a March 2022 measurement campaign and were used for visualization only.	57
<b>Figure 6.2</b> Gross primary productivity (GPP) against green canopy absorbed photosynthetically active radiation (APAR $_{\rm g}$ ) during the 2021 growing season, colored by canopy chlorophyll content (CCC) and dot sizes by vapor pressure deficit (VPD).	62
<b>Figure 6.3</b> Time series of daily averaged daytime values of (a) green canopy light use efficiency (LUE <sub>g</sub> ), (b) gross primary productivity (GPP), (c) green canopy absorbed photosynthetically active radiation (APAR <sub>g</sub> ), (d) canopy chlorophyll content (CCC), (e) air temperate ( $T_{air}$ ), (f) vapor pressure deficit (VPD), (g) soil water content (SWC <sub>AVG</sub> ), and (h) sap flow density (J <sub>S</sub> ) from April 20 to September 30. For LUE <sub>g</sub> and GPP, only those days with at least 25% non-gap-filled GPP	
data were considered.	63
<b>Figure 6.4</b> Green canopy light use efficiency (LUE <sub>g</sub> ) at a half-hourly scale with log10-transformed y-axes (left) and at a daytime scale (right) against air temperature (a,b), vapor pressure deficit (c,d), diffuse fraction (e,f), red to far-red ratio difference between above and below canopy (g,h), and soil water content (i, j), each with a LOESS (locally estimated scatterplot smoothing) function in blue and a 0.95 confidence interval in grey. For daily LUE <sub>g</sub> ,	
only those days with at least 25% non-gap-filled GPP data were considered.	64

Figure 6.5 Average conditional permutation importance (unitless) of environmental variables for a random forest gross primary productivity (GPP) model with error bars displaying one standard deviation between 10 iterations (a), and SHAP values of those variables for a gradient boosting GPP-model (b). The more values deviate from 0, the more important was the respective variable for the prediction, with negative values related to low GPP outcomes. Numbers on the left show the average absolute SHAP value (unitless) of each variable. R<sup>2</sup> of a random 5-fold cross-validation of the models was 0.83 for random forest and 0.84 for gradient boosting. 65 Figure 6.6 Sap flow density (J<sub>S</sub>) against gross primary productivity (GPP) colored by daily maximum vapor pressure deficit (VPD<sub>mx</sub>) (a) and J<sub>s</sub> against VPD colored by canopy chlorophyll content (CCC) (b). The star symbols in panel (b) represent observations with solar zenith angle > 70° and VPD > 5 hPa. 66 Figure 6.7 Hysteresis plots between sap flow density (J<sub>S</sub>) and vapor pressure deficit (VPD) (ad), gross primary productivity (GPP) and VPD (e-h), J<sub>s</sub> and green canopy absorbed photosynthetically active radiation (APAR<sub>g</sub>) (i-l), and GPP and APAR<sub>g</sub> (m-p), averaged for four different daily maximum VPD classes (columns). A clockwise (anti-clockwise) pattern occurs if afternoon and evening values of J<sub>S</sub> or GPP are higher (lower) than in the morning at the same 67 VPD or APARg. Figure 6.8 Light use efficiency of green parts of the canopy (LUEg) by absorbed photosynthetically active radiation of green parts of the canopy (APAR<sub>g</sub>) for half-hourly values (a) and daytime averaged values (b). 73 Figure 6.9 Gross primary productivity (GPP) plotted against green canopy absorbed photosynthetically active radiation by green parts of the canopy (APAR<sub>g</sub>), colored by canopy chlorophyll content (CCC) and dot sizes by vapor pressure deficit (VPD). The black line denotes an upper limit of GPP in relation to APARg bins (GPPopt) as modelled by a generalized additive 74 model. Figure 6.10 Deviations from optimal gross primary productivity (GPP<sub>dev</sub>) (left columns) and green canopy light use efficiency (LUEg) with a log10-transformed y-axis (right column) at a half-hourly scale against time (a, b), air temperature (Tair) (c, d), vapor pressure deficit (VPD) (e, f), diffuse fraction (d/I) (g, h), the difference of the red to far-red ratios between above and 75 below canopy (R/FR<sub>diff</sub>) (i, j) and soil water content (SWC<sub>AVG</sub>) (k, l). Figure 6.11 Scatterplots of daily gross primary productivity (GPP) and Canopy Chlorophyll Content (CCC) (a) and diffuse fraction (d/I) against the difference of the R/FR ratio above and below the canopy (R/FRdiff) (b), with a LOESS (locally estimated scatterplot smoothing) function 76 in blue and a 0.95 confidence interval in grey. Figure 6.12 Scatterplot of observed against predicted gross primary productivity (GPP) by a 77 random forest model (a) and a gradient boosting model (b) with a linear fit displayed in blue. Figure 6.13 Variable importance results for predictors but in contrast to Fig. 6.4 with solar zenith angle (SZA) and day pf year (DOY) instead of absorbed photosynthetically active radiation and canopy chlorophyll content. Average conditional permutation importance (unitless) for a random forest gross primary productivity model with error bars displaying one standard deviation between 10 iterations (a), and SHAP values of those variables for a gradient

boosting GPP model (b). Numbers on the left show the average absolute SHAP value (unitless)

of each variable.

78

<b>Figure 6.14</b> SHAP values of each predictor of Fig. 6.4b against the predictor values, with a locally estimated scatterplot smoothing (LOESS) function in red.	79
<b>Figure 6.15</b> Hysteresis plot for vapor pressure deficit (VPD) in relation to green canopy absorbed photosynthetically active radiation (APAR <sub>g</sub> ), averaged over all days of the 2021 growing season.	80
<b>Figure 6.16</b> Time series of half-hourly green canopy absorbed photosynthetically active radiation (APAR <sub>g</sub> ) (a), vapor pressure deficit (VPD) (b), sap flow density (J <sub>S</sub> ) (c), gross primary productivity (GPP) (d) and soil water content (SWC <sub>AVG</sub> ) (e) between June 12 and June 29, 2021.	01
Figure 6.17 Maximum coefficient of variation (CV) of fraction of absorbed photosynthetically active radiation (fAPAR) by the number of canopy-transmitted PAR sensors and for different dataset filtered by diffuse fraction (d/I), solar zenith angle (SZA) and wind speed (WS).	81
Calculation of CV was conducted analogous to Putzenlechner et al. 2019b.	82
List of tables	
<b>Table 4.1</b> Description of the Eddy Covariance Stations Providing CO <sub>2</sub> Flux Data Used for Model Training	20
Table 4.2 Predictor Variables Used for Model Training	22
<b>Table 4.3</b> General Algorithm of the Backward Feature Elimination (BFE), the Indications in Square Brackets Refer to the R-Packages Used for the Respective Step	24
<b>Table 4.4</b> Cross Validation Results for Different NEE Data Sets and Different Feature Selection Methods	26
Table 4.5 Importance of Each Variable Selected by BFE for the 48 Data Set	27
<b>Table 4.6</b> NEE in g C m <sup>-2</sup> d <sup>-1</sup> Aggregated by Land Cover and Season of Upscaled Data Over Vegetated Parts of the Rur Catchment (above) and of eddy covariance (EC) Measurements Within the Catchment Described in Table 1 (below)	29
<b>Table 5.1</b> Mean daytime values of 30 min $H$ , $\lambda E$ , and $CO_2$ fluxes that passed the quality tests for both systems and each LPF correction method with cumulative fluxes in parentheses. For $CO_2$ , $u$ *-filtered night-time values are also given	46
<b>Table 5.2</b> Energy balance coefficients from reduced major axis regression, as well as its coefficient of determination $(R2)$ , and energy balance ratio (EBR)	49

#### 1 Introduction

#### 1.1 Rationale and Objectives

Carbon dioxide ( $CO_2$ ) that is emitted by fossil combustion and net land use and land cover change accumulates either (i) in the atmosphere, (ii) on the land surface mainly as organic carbon via photosynthesis, or (iii) in oceans as dissolved  $CO_2$  or organic carbon (Canadell et al., 2021). Out of these two source and three sink terms, land use/cover change emissions as well as the terrestrial carbon sink are driven by various anthropogenic and natural processes on the Earth's surface and thus are of special interest from a geographic point of view.

Cumulative net carbon emissions from land use changes for 1850–2020 were ca.  $200\pm65$  Gt C, about 30% of total emissions (Friedlingstein et al., 2022). However, different carbon bookkeeping models still vary a lot in their estimates with 140 Gt C (Houghton & Nassikas, 2017), 270 Gt C (BLUE; Hansis et al., 2015), and 195 Gt C (OSCAR; Gasser et al., 2020). In contrast to increasing fossil emissions, net land use change emissions were relatively constant or slightly decreasing in the last decades (from  $1.3\pm0.7$  Gt C yr<sup>-1</sup> 1970–1999 to  $1.1\pm0.7$  Gt C yr<sup>-1</sup> 2011–2020; Friedlingstein et al., 2022). In absolute terms, net land use change emissions peaked at a value of  $1.61\pm0.55$  Gt C yr<sup>-1</sup> in 1959 (Gasser et al., 2020). Nevertheless, with  $80\pm45$  Gt C during the period 1960–2020, net land use change emissions still accounted for 18% of total emissions (Friedlingstein et al., 2022). Gross emissions are about 2-4 times larger than net emissions, with a slight increase from  $3.4\pm0.9$  Gt C yr<sup>-1</sup> in the 1960s to  $3.8\pm0.6$  Gt C yr<sup>-1</sup> in the 2010s. Gross removals due to land use change, however, increased even more from  $1.9\pm0.4$  Gt C yr<sup>-1</sup> in the 1960s to  $2.7\pm0.4$  Gt C yr<sup>-1</sup> in the 2010s (Friedlingstein et al., 2022).

Main components of these gross emissions include deforestation, e.g., for wood harvest or conversion to cropland or pasture, as well as peatland draining and burning. Gross removals, on the other hand, are slower processes and are mainly related to afforestation and regrowth and concomitant soil regeneration following wood harvest or on abandoned agricultural land (Hansis et al., 2015; Pongratz et al., 2021; Friedlingstein et al., 2022). The global forest area has declined by 81.7 million ha from 1960 to 2019, with a forest loss of 437.3 million ha outweighing a forest gain of 355.6 million ha (Estoque et al., 2022). Deforestation is mostly confined to tropical areas resulting from an expansion of agricultural land (Houghton & Nassikas, 2017), with 25% of global land use change emissions being related to beef and other red meat production (Hong et al., 2021). Afforestation was highest in Europe during the last centuries with an increase of forested area by 484,000 km<sup>2</sup> since 1600, mainly from coniferous trees (McGrath et al., 2015). Globally, afforestation at suitable land has an estimated further mitigation potential of about 4.9 Gt CO<sub>2</sub> yr<sup>-1</sup> (Doelman et al., 2019). However, afforestation oftentimes causes a reduction of surface albedo, depending on the afforested land cover (Kirschbaum et al., 2011; Mykleby et al., 2017). In this way, the increased absorbed radiation can counteract the increased CO<sub>2</sub> fixation in terms of a cooling effect (Luyssaert et al., 2018). Because of this, accurate light use efficiency estimates are required for forest ecosystems in order to quantify and potentially minimize the absorbed radiation not used for photosynthesis in afforestation projects (Genesio et al., 2021).

Out of total anthropogenic carbon emissions of  $10.6 \pm 0.8$  Gt C yr<sup>-1</sup> from 2011-2020 (including fossil combustion and net land use change emissions),  $3.1 \pm 0.6$  Gt C yr<sup>-1</sup> (ca. 29%) were assimilated by terrestrial vegetation. The global land sink increased to this value from just  $1.2 \pm 0.5$  Gt C yr<sup>-1</sup> during the 1960s (Friedlingstein et al., 2022), which can mainly be attributed to  $CO_2$  fertilization effects (Dusenge et al., 2018). Peatlands are considered one of the few persistent terrestrial carbon sinks, having accumulated about 600 Gt of carbon since the last glacial period despite covering only about 3% of the land surface (Yu et al., 2011; Gorham et al., 2012). With ongoing climate change and related

water table depth changes, it is uncertain whether these ecosystems will continue to sequester carbon, or their huge carbon pool will be respired (Malhotra et al., 2016; Alexandrov et al., 2020). Global forests, on the other hand, store about  $861 \pm 66$  Gt of carbon, with 44% of it in soil, 42% in live biomass and 13% in litter and deadwood (Pan et al., 2011). Regrowing forest stands sequester about 1.3 Gt C yr<sup>-1</sup> and even old growth forest stands do not eventually reach a carbon neutral state but remain a carbon sink by sequestering about 0.85 Gt C yr<sup>-1</sup> globally (Pugh et al., 2019), likely due to carbon accumulation in soils, coarse woody debris and charcoal (Luyssaert et al., 2008). However, with increasing warming and moisture stress, forest ecosystems such as the Amazon rainforest could turn into a carbon source (Baccini et al., 2017; Gatti et al., 2021). In the Amazon, forest degradation even exceeds deforestation, with 337,427 km<sup>2</sup> of degraded forest compared to 308,311 km<sup>2</sup> of deforested area between 1992 and 2014 (Matricardi et al., 2020), and degradation contributing to 73% of aboveground biomass loss compared to 27% from deforestation (Qin et al., 2021). Other regions such as the southwest USA, southeast Europe and South Africa are already modelled a carbon source linked to reduced rainfall, and globally climate change is estimated to have reduced the terrestrial sink by 0.45  $\pm$  0.39 Gt C yr<sup>-1</sup> for 2011-2020 (Friedlingstein et al., 2022). With an expected shift from energy-limited to water-limited conditions for most terrestrial ecosystems due to climate change (Denissen et al., 2022), the combination of heat and drought is a major concern for the decrease of gross primary productivity (GPP) and the efficiency of which light is used for photosynthesis (Zhang et al., 2015; Stocker et al., 2018; von Buttlar et al., 2018). In Europe, the 2018 drought caused a modelled reduction of GPP of 130-340 Mt C (Smith et al., 2020) and resulted in unprecedented levels of forest disturbances (Senf & Seidl, 2021). As a consequence thereof, the drought decreased net CO<sub>2</sub> uptake by 17.8% among micrometeorological flux stations (Graf et al., 2020), and turned temperate regions of Europe to a carbon neutral state or even a small carbon source in summer 2018 (Thompson et al., 2020). These observations confirm the concern of an eventual positive feedback between increased atmospheric CO<sub>2</sub> and a reduced global carbon uptake (Friedlingstein et al., 2001).

Therefore, accurate estimates of the atmosphere – biosphere CO<sub>2</sub> exchange of different and especially transitioning land covers and under different climatic extremes are necessary to provide insights into regional carbon budgets and to counsel promising mitigation efforts against climate change (Ciais et al., 2022). Methods to estimate the carbon exchange can generally be divided into top-down and bottom-up approaches. Atmospheric inversion approaches are top-down methods, which estimate the surface exchange from atmospheric transport models and CO2 concentration measurements, either from surface stations or total column data from satellites such as GOSAT and OCO-2 (Wang et al., 2019a). Bottom-up methods to estimate carbon stock changes include repeated biomass estimates such as from forest inventories and remote sensing data. However, these methods usually include only above-ground biomass stock changes and inventories have a low (e.g., annual) temporal resolution (Pongratz et al., 2021; Ciais et al., 2022). Remotely sensed vegetation properties such as leaf area and chlorophyll content are nevertheless important for empirical modelling of carbon uptake (Croft et al., 2015). Process-based models like the global TRENDY application (Sitch et al., 2015), on the other hand, are not tightly driven by observational data, but these are in few cases only used to calibrate model parameters. Such dynamic global vegetation models conserve mass and provide a gridded carbon exchange output, but also can differ substantially from observations (Ciais et al., 2022). Networks of eddy covariance stations are an approach of direct and quasi-continuous CO<sub>2</sub> flux measurements at the ecosystem scale (Baldocchi, 2014). Besides CO<sub>2</sub>, the water vapor flux (evapotranspiration) is commonly measured with the eddy covariance method, which can also be used to assess fluxes of other greenhouse gases such as  $CH_4$  and  $N_2O$ . Hence eddy covariance measurements are recommended to be used within elaborated carbon cycle projects such as RECCAP-2 (Ciais et al., 2022), but the small spatial footprint of such point measurements is required to be upscaled to gridded products with data driven models incorporating remote sensing and meteorological data in order to

be comparable to e.g., inversion products (Kondo et al., 2015). However, eddy covariance sites are not randomly distributed over the globe but exhibit a sampling bias of overrepresented and underrepresented regions and ecosystems. The incorporation of relatively few recently disturbed ecosystems in global flux data bases likely is one reason for the mismatch between upscaled eddy covariance products such as FLUXCOM and other global carbon budgets (Zscheischler et al., 2017; Ciais et al., 2022).

Based on those considerations, the general goal of this dissertation is to contribute to the knowledge of ecosystem—atmosphere exchange processes of CO<sub>2</sub> and H<sub>2</sub>O for an exemplary study area by applying eddy covariance and machine learning methods. Experiments were conducted in a nested approach, mainly concerning a partly deforested spruce forest at the upper Wüstebach stream in the Eifel mountains in western Germany, but also spanning over the higher-order Rur catchment area. In order to tackle this goal, three general research questions are formulated, which are approached in three studies within this dissertation, each with more specific research questions, hypotheses or objectives:

- 1) How accurate can CO<sub>2</sub> fluxes from eddy covariance stations be upscaled to the Rur catchment across different land covers using machine learning with state-of-the-art feature selection methods?
- 2) How are eddy covariance measurements over a deforested, fetch-limited site with unmanaged regrowth affected by choices of measurement height and spectral correction?
- 3) How are different environmental conditions related to the light use efficiency and gross primary productivity of a temperate spruce forest?

The first research question is addressed for the whole Rur catchment area, while the second research question is addressed for an 8.6 ha deforested area at the upper Wüstebach, and the third research question for a spruce forest next to it. All of these sites are part of a long-term TERENO (TERrestrial ENvironmental Observatories) research program to observe Global Change consequences at representative terrestrial ecosystems (Zacharias et al., 2011).

In order to approach these research questions, the presented dissertation is structured in seven main chapters. Besides a general introduction giving reasons for the outlined research questions, Chapter 1 also comprises background information about the total carbon exchange at the ecosystem scale, definitions of its compartments and their measurability with the eddy covariance method. In addition, the chapter describes energy pathways of absorbed radiation at the leaf scale as the processual basis of the terrestrial carbon sink. Chapter 2 summarizes the nested research area in terms of land use, climate, vegetation, geology and soils, as well as instrumentation and the embedment in the general TERENO long-term project. Chapter 3 elucidates the general concepts, constraints and advantages of the two main methods applied for this dissertation, first the eddy covariance method for experimentally assessing greenhouse gas fluxes, and second tree-based machine learning techniques for prediction and inference.

The following three Chapters 4, 5 and 6 are the core part of this dissertation and approach the three research questions respectively. Chapter 4, published in *Journal of Geophysical Research: Biogeosciences* (Reitz et al., 2021a), concerns the spatial upscaling of eddy covariance derived CO<sub>2</sub> flux measurements to the regional scale across different land covers. Therefore, state-of-the-art training approaches were evaluated for a random forest machine learning model, which was trained with several predictor variables including remotely sensing vegetation indices and reanalysis data. Chapter 5, published in *Boundary-Layer Meteorology* (Reitz et al., 2022), concerns the uncertainty of eddy covariance measurements over a fetch-limited, deforested area with near-natural regrowth in regard to experimental design and data processing. For this site with non-ideal characteristics for eddy

covariance measurements, two measurement heights and five different spectral corrections were compared. In this way, the uncertainty of measurements at recently disturbed ecosystems can be better evaluated and the flux data better interpreted for further potential applications such as the comparison to other land covers. And in Chapter 6, published in *Journal of Geophysical Research: Biogeosciences* (Reitz et al., 2023), the light use efficiency and GPP of a temperate spruce forest were assessed with in-situ measurements. These were related to meteorological and forest canopy conditions, by applying, among others, state-of-the-art variable importance measures for machine learning models. Furthermore, water-limiting conditions for photosynthesis were identified by analyzing hysteretic responses of tree-scale sap flow measurements and ecosystem-scale photosynthesis estimates to meteorological variables. And finally, Chapter 7 includes a synthesis of the conducted research and gives an outlook for future research possibilities in the field of atmosphere-biosphere interactions.

#### 1.2 The Ecosystem Scale Carbon Exchange – Definitions and Limitations

The exchange between a surface and the atmosphere is measured as a flux and is defined as the integral of an entity that passes through a Gaussian surface per unit of time (Burba, 2022). A surface is considered a source if the net flux leaves it (goes upwards), and a sink if the net flux goes toward the surface (downwards). In the context of eddy covariance measurements, the net ecosystem exchange (NEE) is the total CO2 exchange of turbulent fluxes adjusted by a storage term but does not include other carbon transport processes. In this way, a negative NEE corresponds to a CO2 sink, and a positive NEE to a CO<sub>2</sub> source. NEE is commonly expressed in μmol CO<sub>2</sub> m<sup>-2</sup> s<sup>-1</sup> at the half-hourly scale and in g C m<sup>-2</sup> d<sup>-1</sup> at the daily scale. Net ecosystem production (NEP) describes the same quantity as NEE but rather from an annual ecosystem stock change point of view and thus with opposite signs (NEP = -NEE; Kirschbaum et al., 2001). The two components of NEE are GPP and ecosystem respiration (Reco). GPP refers to the fixated carbon by photosynthesis minus the CO<sub>2</sub> lost by photorespiration, and R<sub>eco</sub> refers to the respired CO<sub>2</sub> by autotrophic (R<sub>A</sub> or R<sub>PLANT</sub>) and heterotrophic organisms (R<sub>H</sub>) (Kirschbaum et al., 2001). Soil respiration (R<sub>SOIL</sub>) instead combines R<sub>A</sub> of plant roots and R<sub>H</sub> of decomposing soil organisms (Bond-Lamberty et al., 2004). Hence, NEE equals Reco - GPP (Tramontana et al., 2020). Net primary productivity (NPP), on the other hand, refers to the net growth of plant organic carbon, which is GPP minus the carbon respired by plants themselves (NPP =  $GPP - R_A$ ; Kirschbaum et al., 2001). Hence,  $R_{eco}$ , GPP and NPP all range from zero to positive values only.

However, several carbon fluxes are not included in this definition of NEE as a full assessment of all components is not achievable with a single method. Fluxes of reduced C compounds such as CH<sub>4</sub>, CO and other volatile organic compounds (VOCs) can make up a substantial part of the total carbon exchange, depending on the ecosystem. Out of those, CH<sub>4</sub> is a potent greenhouse gas itself, and all reduced C compounds eventually oxidize to CO<sub>2</sub> in the atmosphere (Ciais et al., 2022). Although less widespread than CO<sub>2</sub> due to being more cost-intensive, a CH<sub>4</sub> flux network of eddy covariance stations exists (Delwiche et al., 2021), and first attempts to measure VOC fluxes with the eddy covariance method have also been made (Fischer et al., 2021). Neither included in NEE are lateral carbon fluxes which are fundamentally not measurable with the eddy covariance method due to not being transported by turbulent motions. Such lateral fluxes include transport and consumption of trade items such as wood, crops or hay, which are especially important for carbon budgets of managed lands, runoff of eroded soils and dissolved carbon, or animal grazing (Chapin et al., 2009; Ciais et al., 2022). The combustion of organic carbon by wildfires theoretically is included in measured NEE by eddy covariance systems but experiments have shown an underestimation of released CO<sub>2</sub> (Clark et al.,

2009), and the transport of soot is neither measured. Advective fluxes of  $CO_2$  such as large-scale circulations and nocturnal drainage flows, on the other hand, are strived to be minimized due to an optimal eddy covariance site and setup, which are described in more detail in Chapter 3.1.

#### 1.3 Energy Pathways of Absorbed Radiation at the Leaf Scale

The light use efficiency is on the one hand an important concept for modelling GPP (Pei et al., 2022), and on the other hand an important measure for quantifying and potentially reducing the absorbed energy not used for  $CO_2$  assimilation (Genesio et al., 2021). Therefore, it is relevant to point out the energy pathways of absorbed radiation within and around a leaf and the environmental controls on these pathways, which determine the light use efficiency and in this way are the processual basis for the terrestrial carbon sink.

Only one of these pathways, which energy from photosynthetically active radiation that is absorbed by a green leaf (APAR<sub>g</sub>) can take, ultimately results in the fixation of CO<sub>2</sub>. At first, radiation can be absorbed by non-photosynthetic molecules such as cuticular wax, water, or other pigments such as anthocyanins as a protection against ultraviolet light (Ustin & Jacquemoud, 2020). This energy can either be re-emitted as long wave radiation, transported as sensible heat by turbulent motions or is used for the vaporization of liquid water and the transpiration of water vapor through open stomata or the evaporation of intercepted water on the leaf surface.

APAR<sub>g</sub> that actually is absorbed by chlorophyll a & b induces the light reaction and also fluorescence, which is typically only 1-2% of total absorbed light (Maxwell & Johnson, 2000). Within the light reaction, adenine triphosphate (ATP) as an energy storage molecule and the reduced form of nicotinamide adenine dinucleotide phosphate (NADPH) as a hydrogen carrier are synthetized through an electron transport chain (Schopfer & Brennicke, 2010). However, during periods of high light intensity, water stress or cold temperatures, more light energy is harvested than can be used for the fixation of CO<sub>2</sub>. To prevent harm from the leaf structures, excess energy is dissipated as heat via non-photochemical quenching (NPQ) in the xanthophyll cycle (Jahns & Holzwarth, 2012), which at full light makes up about 50-70% of all absorbed energy by the photosystems (Heldt & Piechulla, 2015).

ATP and NADPH as products from the light reaction are finally utilized for the assimilation and reduction of  $CO_2$  to glucose through the Calvin cycle, also called dark reaction as it is not directly dependent on light (Verma et al., 2017). However, photorespiration is also a possible result of the Calvin cycle in  $C_3$  plants and much less in  $C_4$  and CAM plants. In this way, photosynthetic energy is wasted as the enzyme RuBisCO assimilates  $O_2$  instead of  $CO_2$ , which in turn is released as a by-product. The probability of photorespiration increases with an increased ratio of the  $O_2$  to  $CO_2$  content in solution, which in turn increases with higher temperatures (Foyer et al., 2009). Then again, the probability of photorespiration also depends on the  $CO_2$  to  $O_2$  ratio in the atmosphere, and in this way increased atmospheric  $CO_2$  also has the potential to suppress photorespiration (Serk et al., 2021).

In summary, different environmental conditions influence the energy pathways of absorbed radiation, the most important being air temperature, water content in soil and air, the amount of (excess) absorbed radiation, atmospheric CO<sub>2</sub>, and the availability of nutrients such as nitrogen and phosphorus.

### 2 Study Area: The Wüstebach Research Site within the Eifel/Lower Rhine Valley Observatory

#### 2.1 The Eifel/Lower Rhine Valley Observatory

The Eifel/Lower Rhine Valley Observatory, coordinated by Forschungszentrum Jülich, is one of four terrestrial environmental observatories of the TERENO project in Germany and covers the Rur catchment in western Germany with small portions in Belgium and the Netherlands (Bogena et al., 2018). TERENO is a long-term research program of four Helmholtz Research Centers and provides long time-series of system variables to observe Global Change consequences for terrestrial ecosystems. More specifically, the complex implications and feedbacks from climate and land use changes on, e.g., water balance, CO<sub>2</sub> exchange, soil fertility, regional climate and biodiversity of terrestrial systems are investigated for four German regions being representative for Central Europe (Zacharias et al., 2011). The Eifel/Lower Rhine Valley Observatory hereby represents the north-western part of the Central European low mountain area and also the transitional area towards the northern Central European lowlands. All data collected within the TERENO program are distributed with free access via the open GIS-platform TEODOOR (Kunkel et al., 2013).

The Rur catchment covers an area of 2354 km<sup>2</sup> and exhibits significant north-south gradients in elevation, temperature, precipitation, land use, soil properties and geology (Bogena et al., 2018). The southern half of the Rur catchment is part of the Eifel low mountain range with elevations up to 680 m above sea level (asl), while the northern half is a flat lowland area with an average elevation of about 100 m asl down to about 20 m asl at the mouth of the Rur river (excluding the open pit mines of the Rhenish lignite coal area). The northern lowland area is a fertile loess plain and is dominated by arable land of which in 2011 41% was winter wheat (Triticum aestivum), 28% sugar beet (Beta vulgaris) and 10% maize (Zea mays) as the most common crops (Reichenau et al., 2016). Settlements are mainly located in the northern and central parts of the catchment. The upland areas instead are dominated by coniferous and deciduous forests, pastures and fenlands (Lussem & Herbrecht, 2019; see also Fig. 4.1 in Sect. 4.2). The Eifel mountains of the upper Rur catchment are part of the Rhenish Massif and are mostly composed of Paleozoic consolidated rocks with some Mesozoic sandstone and limestone outcroppings near the south-eastern border of the catchment. The northern half is dominated by unconsolidated Tertiary sediments covered by Pleistocene terrace deposits of the Meuse and Rur rivers and by aeolian loess deposits with significant portions of anthropogenic spoil tips (Bogena et al., 2018). Fluvisols, Gleysols and Eutric Cambisols are major soils of the southern upland area, while the fertile arable land is dominated by Haplic Luvisols and Cumulic Anthrosols with a silt loam texture and high field capacities above 200 mm (Korres et al., 2015; Bogena et al., 2018).

For the most recent climatological normal 1991–2020, the highest mean annual temperatures (MAT) in the Rur catchment were recorded in the northern lowlands, for example 10.9 °C at the station Elsdorf and 10.7 °C at Heinsberg-Schleiden (DWD, 2022). The lowest MAT is expected in the highest parts of the Eifel mountains. Schneifelforsthaus, located about 13 km south of the Rur catchment and at 649 asl, which is similar to the highest parts of the catchment, had a MAT of 7.3 °C, and the highest official station within the Rur catchment, Kall-Sistig at 505 m asl, had a MAT of 8.3 °C (DWD, 2022). Mean annual precipitation (MAP) exhibits not only a north–south gradient, but also a decreasing gradient from west to east, especially in the southern half (Bogena et al., 2005). In the northern lowlands, MAP was 681 mm at Heinsberg-Schleiden, while in the southern uplands MAP ranges from 1253 mm at Hellenthal-Udenbreth in the windward southwestern corner to 783 mm at Kall-Sistig in a leeward area just 13 km away (DWD, 2022). This steep precipitation gradient is also evident in Fig. 2.1, showing a precipitation difference over 400 mm between Wüstebach and Kall-Sistig for the period 2011–2021.

Resulting from the dominating south-western wind directions, the lowest MAP of the Rur catchment was recorded in the leeward areas along the Rur river with 616 mm at Düren (DWD, 2022). The relation between winter and summer precipitation also is not equally distributed over the catchment, with approximately 15% higher winter precipitation in the southern upland regions and about 10% higher summer precipitation in the northern lowland regions (Bogena et al., 2005).

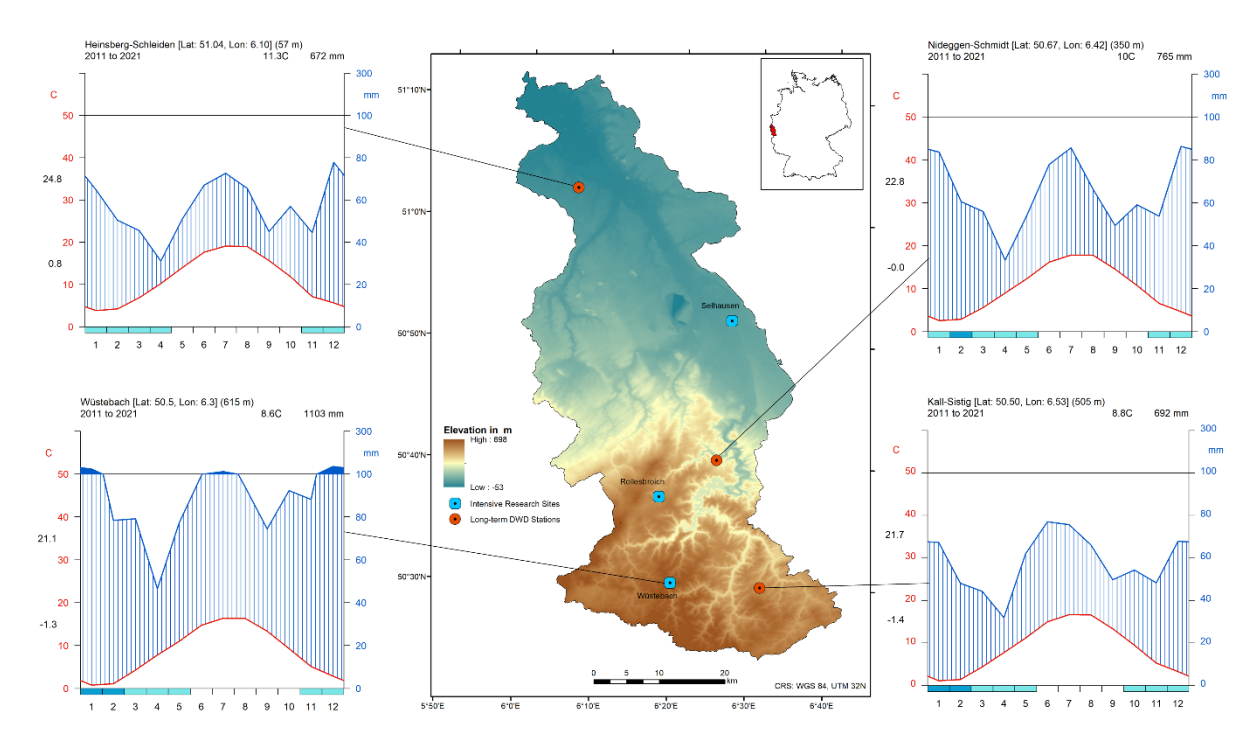


**Figure 2.1** Elevation of the Rur catchment area from SRTM data (Jarvis et al., 2008) and Walter and Lieth climate diagrams for the TERENO Wüstebach site and three weather stations from the German Weather Service (DWD, 2022), all for the years 2011-2021 to match the Wüstebach time series.

Instrumentation is distributed over the observatory in a nested multiscale approach, with (i) sparse measurements of runoff gauging stations scattered over the whole Rur catchment, (ii) moderate instrumentation within three subcatchments (Ellenbach, Kall, Erkensruhr), and (iii) intensive instrumentation at three research sites (Selhausen, Rollesbroich, Wüstebach) within these subcatchments (Bogena et al., 2018). The Selhausen site (50.865°N, 6.447°E) at about 100 to 110 m asl in the northeastern part of the catchment represents the agricultural landscape with spatiotemporally varying crops (Schmidt et al., 2012). The Rollesbroich site (50.622°N, 6.303°E) from 474 to 518 m asl covers a 20 ha managed grassland area in the Eifel mountains with different fields that are individually fertilized and cut (Borchard et al., 2015). The Wüstebach site (50.504°N, 6.333°E) partly covers a spruce monoculture and a deforested area with undisturbed regrowth around the Wüstebach headwater region in the Eifel mountains and is described in more detail in the next section.

At each research site, energy and CO<sub>2</sub> fluxes are measured by an eddy covariance tower, which are part of the Integrated Carbon Observation System (ICOS; Heiskanen et al., 2022). Besides continuous eddy covariance data, additional trace gas measurements include tunnel flux chambers (Graf et al., 2013) and elevator-based profile measurements (Ney & Graf, 2018). Further measurements at each site include meteorological parameters such as air temperature and humidity, precipitation, short- and long-wave radiation, wind speed and direction, as well as soil temperature and water content sensors connected to the wireless sensor network SoilNet (Bogena et al., 2010). Soil moisture is additionally estimated at the field scale by 10 cosmic-ray neutron stations (Baatz et al., 2014; Andreasen et al.,

2017). This method was also applied for mobile surveys (Jakobi et al., 2020) and soil moisture data were assimilated within land surface models to predict evapotranspiration at the regional scale (Baatz et al., 2017). At each research site one to three lysimeter stations were installed to observe actual evapotranspiration across the catchment and are part of the SOILCan network (Pütz et al., 2016). Recent remote sensing activities for the Rur catchment include Sentinel-2 based monitoring of spruce stands using cloud computing infrastructures (Montzka et al., 2021) and biomass estimations from Light Detection And Ranging (LiDAR) sensors on unmanned aircraft vehicles (Bates et al., 2022).

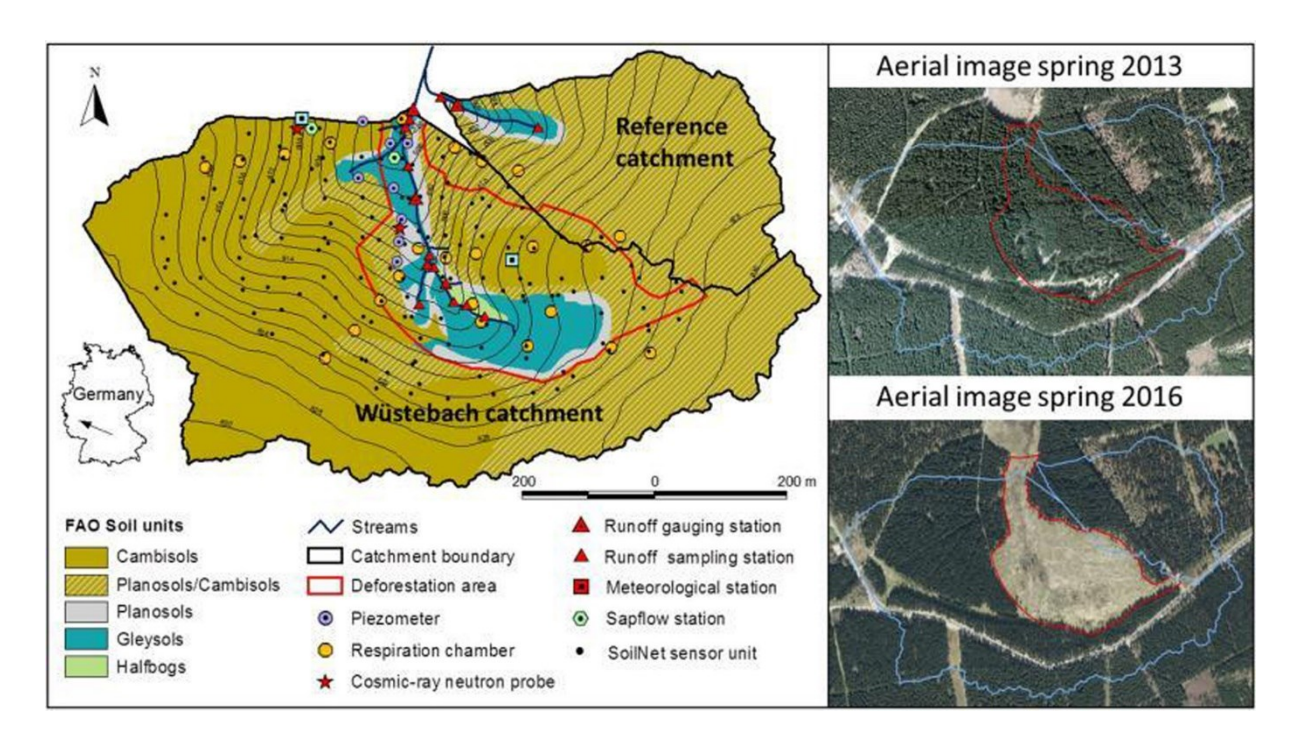


**Figure 2.2** The Wüstebach intensive research site with instrumentation and aerial images demonstrating the deforested area. Figure adapted without changes from Bogena et al. (2018), under <u>CC BY-NC-ND 4.0</u>.

#### 2.2 The Wüstebach Research Site

The research site is situated within the Eifel National Park and encompasses the upper Wüstebach catchment including an unnamed tributary catchment to the north serving as an unaffected reference (see Figure 2.2). The upper Wüstebach research site covers an area of 38.5 ha and ranges between elevations of 596 m asl at the northern outflow of the stream to 629 m asl at the eastern corner with an average slope of 3.6 % and a maximum slope of 10.4% (Bogena et al., 2015). The bedrock consists of Devonian shales which are superimposed by periglacial solifluction layers. Cambisols and Planosols with a silty-clay loam texture are the dominant soil types on hillslopes while Gleysols and Histosols (half-bogs) have formed along the stream under groundwater influence (Bogena et al., 2018).

The site has a long history of human impact. During medieval and early modern times, beech forests in the northern Eifel were cut for pastureland and charcoal production used in iron melting industries. This resulted in a largely deforested landscape until reforestation with spruce trees was initiated in the 19<sup>th</sup> century under Prussian rule (Suck, 1999). Following area-wide devastation during the Battle of the Bulge in 1944-1945, which included heavy fighting at the Wüstebach site with remaining trenches and explosion craters, the area was planted again mostly (ca. 90%) with *Picea abies* in the 1950s (Lehmkuhl et al., 2010; Borchardt, 2012). In 2009, the catchment had an average canopy height of 25 m, a tree

density of 370 trees ha<sup>-1</sup> and a dry biomass of 310.5 t ha<sup>-1</sup> corresponding to about 3670 t of carbon (Etmann, 2009). The potential natural vegetation of the Wüstebach site is classified as a montane base-poor wood rush/beech forest (Suck et al., 2014). Following the National Park's approach to convert the spruce monoculture to a near-natural beech forest, a deforestation experiment was conducted in September 2013, for which an area of 8.6 ha around the stream was clear-cut with the exception of few alder stocks. Only about 3% of the original biomass remained on site, mostly stumps, litter and individual trunks (Baatz et al., 2015). After deforestation the area was left without plantings for undisturbed regrowth, and a fence was erected around a core area against animal browsing. In the remaining parts of the Wüstebach site, however, the spruce monoculture was not cut and beech saplings were planted in the understory to impede natural regeneration of spruce trees with process conservation as the long-term goal (Nationalparkverwaltung Eifel, 2014).



**Figure 2.3** Photography of the 38 m Wüstebach tower, mounted with an eddy covariance system and sensors for photosynthetically active radiation, among others. Published with the kind permission of the authors Carsten Montzka and Jordan Bates, Forschungszentrum Jülich.

The research site contains two eddy covariance systems, one installed on a 38 m high tower in 2010 to observe fluxes of the spruce forest to the west of the stream (Fig. 2.3), and one for the deforested area installed in 2013 (Fig. 5.1c). The spruce monoculture was a significant carbon sink from 2010 to 2017 with a NEE of -660 g C m<sup>-2</sup> y<sup>-1</sup> (Ney et al., 2019). In comparison, the clear-cut area changed from a strong carbon source (NEE of 521 g C m<sup>-2</sup> y<sup>-1</sup>) in the initial year after deforestation towards an almost neutral NEE of 83 g C m<sup>-2</sup> y<sup>-1</sup> in the fourth year after deforestation, mostly due to an increase of GPP by regrowing vegetation (Ney et al., 2019). In 2020, the vegetation of the clear-cut area was dominated

by various grasses (e.g., *Deschampsia spec.*, *Molinia spec.*), shrubs and bushes of different size (e.g., *Cytisus scoparius*, *Calluna vulgaris*, *Epilobium angustifolium*), and young trees (*Sorbus aucuparia*, *Betula pubescens*, *Picea abies*). Regarding hydrological effects, the deforestation caused a decrease of evapotranspiration, which in turn caused an increase of soil water storage and discharge, especially in summer (Wiekenkamp et al., 2016). Furthermore, the concentration of most ions (Na<sup>+</sup>, Ca<sup>2+</sup>, Mg<sup>2+</sup>, Cl<sup>-</sup>, and SO<sub>4</sub><sup>-</sup>) in the stream water showed a decreasing trend after deforestation (Płaczkowska et al., 2022). In the forested part of the research site, physiological processes of three spruce trees are intensively monitored by dendrometers and sap flow sensors. The major drought of 2018 caused the spruce trees to halt their hydraulic systems and photosynthesis, resulting in a narrower tree-ring width (Neuwirth et al., 2021). For future research, the Wüstebach site will be one of four German pilot areas to establish a standardized monitoring system for assessing growth reactions of important Central European tree species under climatic extremes.

#### 3 Methods

#### 3.1 Eddy Covariance

For this dissertation, turbulent fluxes were experimentally assessed with the eddy covariance (EC) technique. This method is a micrometeorological approach to measure the turbulent flux of momentum, energy and scalars such as the greenhouse gases  $H_2O$ ,  $CO_2$ ,  $CH_4$ , and  $N_2O$  between a surface and the atmosphere within the atmospheric boundary layer. These scalars are transported in all three directions in the atmosphere by turbulent whirls of varying size, also called eddies (Eugster & Merbold, 2015). In order to describe turbulent motions, a modification of the Navier-Stokes equations is required. An approximate solution of these equations is realized by applying Reynolds decomposition, i.e., by decomposing a time series of a variable into its average and fluctuating components to enable a statistical representation of turbulent motions (Reynolds, 1895). Hence, a vertical flux F of a constituent in the atmosphere can be represented as

$$F = \overline{P_d w s} = (\overline{P_d} + P'_d)(\overline{w} + w')(\overline{s} + s'), \tag{Eq. 3.1}$$

where  $P_d$  is air density, w is vertical wind speed, and s the dry mole fraction of a gas of interest, for which the overbars represent averages and the primes instantaneous deviations (Burba, 2022). After opening the parentheses, the equation can be simplified by deleting terms considering averaged deviations from an average are zero, and assuming that (i) air density fluctuations are negligible, and (ii) mean vertical flow is negligible over flat, horizontally homogeneous surfaces (Burba, 2022). The resulting eddy flux can then be described as

$$F \approx \overline{P_d} \, \overline{w's'},$$
 (Eq. 3.2)

where  $\overline{w's'}$  is the statistical covariance between vertical wind speed and a scalar of interest. However, this application is only valid under certain conditions, otherwise the surface flux is not properly represented by the formula in Eq. 3.2. Following the ergodic hypothesis, which states that time averages are equivalent to ensemble averages and in this way time averages of a sampling volume can be related to a surface area, fluxes have to be stationary over the averaging period and homogeneous over the surface area to remain representative (Katul et al., 2004; Foken et al., 2012). A test for stationarity for example examines whether the averages of shorter averaging intervals do not differ by more than 30% from the whole averaging interval (Foken & Wichura, 1996). In practice, fluctuations are oftentimes assessed every 0.1 or 0.05 seconds (10 or 20 Hz) and values are averaged over 30 minutes or one hour because this domain falls into a spectral gap between turbulent fluctuations and mesoscale diurnal cycles and thus facilitates stationarity. Stationarity and homogeneity can be violated by intermittency in the very stable boundary layer (Mahrt, 2014). In such conditions, turbulence is usually not sustained due to buoyant damping, but for example Kelvin-Helmholtz instabilities can temporarily and locally increase the flow shear and thus create limited patches of active turbulence in time and space (Aubinet, 2008; Finnigan, 2008).

Air density fluctuations are assumed to be negligible, which is usually valid near sea level, but those can be significant at high altitudes and high wind speeds (Massman & Lee, 2002). The method further assumes a negligible mean vertical flow. This basically requires an adequately flat and homogeneous surface to exclude flow divergence and convergence and thus advective processes. In this way, it has always to be ensured that turbulence is the dominant transport mechanism and other processes such as advection and molecular diffusion are negligible. Advective mechanisms that result in a non-zero mean vertical wind can be summarized to i) convection as stationary cells during periods of low mechanical turbulence, ii) synoptic scale subsidence due to high pressure systems and iii) local

circulations driven by surface heterogeneity including drainage flows, which are especially important for  $CO_2$  budgets (Lee, 1998). Well-developed turbulence is usually assessed by friction velocity thresholds (Goulden et al., 1996), though more sophisticated approaches to detect vertical decoupling also exist (e.g., Peltola et al., 2021a). Turbulent exchange is impeded especially during calm nights with stable stratification, which in terms of  $CO_2$  budgets carry the risk of underestimating nighttime respiration. In such cases, respired  $CO_2$  either accumulates below the observation height and is transported upwards after turbulence develops again, is transported downslope by gravitational force without being measured by the EC system, or a combination of both (Aubinet, 2008). Hence, the total  $CO_2$  exchange between an ecosystem and the atmosphere consists of a turbulent flux, an advective flux and a storage term. Ideally, the advective flux has to be assessed separately through the measurement of vertical and horizontal gradients, though this is not feasible as a routine procedure (Finnigan, 2008).

Another constraint of the method concerns the measurement height, as an inadequate height results in fluxes not being representative of the ecosystem of interest. Instruments have to be placed high enough in the well-mixed layer not to be influenced by individual roughness elements, to cover a representative source area, and to be not subject to high spectral losses (Schmid & Lloyd, 1999; Munger et al., 2012). On the other hand, flux measurements have to be low enough within the atmospheric boundary layer to not become significantly affected by the linear flux decrease with height until the flux vanishes at the inversion layer. The decrease at a given measurement height also depends on the boundary layer height, which is why in stable nights with a low boundary layer height the missed flux at tall towers can be significant (Eugster & Merbold, 2015). In addition, in real world cases the ecosystem of interest extends only to a certain distance in the upwind direction and is not perfectly homogeneous in all directions. Hence, it has also to be ensured that the footprint of the instruments is to a large extent congruent with the ecosystem of interest, which also depends on atmospheric stability and surface roughness. This is further limiting the measurement height and requires an assessment of the flux source area in order to interpret the signals (Rannik et al., 2012).

For daytime conditions, the energy balance closure is a common way to estimate the validity of EC flux measurements. With an ideal set-up the sum of sensible and latent heat fluxes measured by an EC system should equal the net radiation minus soil heat flux, energy used for photosynthesis, and energy stored in the air below measurement height (Wilson, 2002). The fact that EC measurements consistently underestimate energy fluxes is attributed to low frequency eddies associated with convection not detectable by EC sensors (Foken, 2008).

Despite these constraints and general limitations concerning the total carbon exchange stated in Sect. 1.2, the EC method holds marked advantages, making it a widely applied technique to estimate net ecosystem exchange. It is a direct method to measure flux densities, it causes only minor disturbances to the vegetation or soil (such as shading and maintenance-related soil compaction), yields a quasicontinuous time series, and represents an area at the ecosystem scale (Baldocchi, 2014). With a large network of stations and some time series now exceeding 20 years of data, the breathing of the biosphere in respect to changing environmental conditions can be better understood (Baldocchi, 2019). Alternative methods include leaf, soil and canopy chambers for smaller scale measurements, gradient-based models such as the Bowen Ratio method for similar ecosystem scale applications, or remote sensing products of the total column gas concentration dynamics at the global scale (Burba, 2022).

In order to calculate the covariance between fluctuations of vertical wind velocity and, e.g., CO<sub>2</sub>, two sensors recording at a high enough frequency of at least 10-20 Hz are required. Sonic anemometers are used for measurements of wind speed and sonic temperature. The underlying principle is to

measure the transit time of an ultrasound wave burst between three pairs of transducers being a known distance apart. The transit time between them depends on the speed of sound and the assumed uniform velocity of the air in their path. As the speed of sound does not depend on the direction, the wind speed in three directions can be deduced by calculating differences of the measured transit times between both directions for all three opposing pairs (Kaimal & Businger, 1963; Munger et al., 2012). On the other hand, the speed of sound can be calculated from the sum of transit times. And since the speed of sound is temperature dependent – besides humidity and atmospheric pressure, which are usually also measured –, the sonic temperature and thus the sensible heat flux can also be deduced from sonic anemometers (Schotanus et al., 1983). As sonic anemometers in the field cannot be perfectly aligned perpendicular to the mean flow, w is usually contaminated by the two horizontal wind vectors (Rebmann et al., 2012). Two common corrections for this error exist, the first being coordinate rotation to set  $\overline{w}=0$ . Over more complex surfaces, however, half-hourly  $\overline{w}$  cannot always be considered zero. For such cases, the planar fit method establishes a hypothetical plane fitted to the streamlines in different wind directions from measurements over several weeks to months and only assumes  $\overline{w}=0$  for these time periods (Wilczak et al., 2001).

Infrared gas analyzers measure the molar densities of e.g., H<sub>2</sub>O and CO<sub>2</sub> by detecting the intensity reduction of an infrared beam caused by the absorption of H<sub>2</sub>O and CO<sub>2</sub> in a sampling volume (Munger et al., 2012). With an open-path design, such as used for this dissertation, sensors are exposed to ambient conditions and the air is moved through the sensor path by the wind. In this way, gas density measurements are affected by temperature, humidity and air pressure fluctuations. In order to exclude the influence from such air expansions or contractions and to relate the measured changes only to the gas flux, the Webb-Pearman-Leuning terms have to be added (Webb et al., 1980). With these terms accounted for, measured molar densities, i.e., the amount of material per unit volume in mol m<sup>-3</sup>, can be converted to the required dry mole fractions, i.e., the ratio of the constituent to the dry air with this constituent in mol mol<sup>-1</sup> (Burba, 2022). Moreover, the anemometer and gas analyzer exhibit a time delay resulting from their physical separation and thus asynchronous signal acquisition. Their time series are usually aligned by maximizing the covariance between them within a certain time window (Mauder & Foken, 2011). Spectral corrections to account for high frequency losses mainly due to (for open path designs) a limited frequency response, sensor separation and path averaging of the sensors are an important step in the processing chain. These corrections are described in detail in Chapter 5.2.3 and are usually applied by comparing actual spectra or cospectra to those of a hypothetical ideal system under given ambient conditions or to, for example, measured sensible heat flux cospectra as an approximation of unattenuated cospectra. In addition, spectral corrections also account for low frequency losses mainly due to block averaging (Moncrieff et al., 2004).

In recent years, efforts have been made to unify processing schemes and create huge datasets of comparable flux data such as the worldwide FLUXNET database (Pastorello et al., 2020), the ICOS network in Europe (Rebmann et al., 2018), or the TERENO network in Germany (Mauder et al., 2013). However, remote and tropical regions in particular are still underrepresented in such networks and upscaling techniques combining remote sensing and machine learning methods are required to achieve spatiotemporal gapless flux information. In addition, these EC networks also need to be expanded in regard to other greenhouse gases such as CH<sub>4</sub> and N<sub>2</sub>O (Baldocchi, 2019).

#### 3.2 Tree-based Machine Learning

Machine learning, or statistical learning, is a set of algorithms to learn from relationships between data. By fitting a model on a training data set, general knowledge can be extracted inductively even for complex cases when a thorough understanding of relationships is not achievable beforehand (Mailund, 2017; Dramsch; 2020). Machine learning algorithms can be classified into two general approaches, each with different aims, supervised and unsupervised learning. For supervised learning, there is a target variable that is predicted using a set of predictor variables. Hence for each observation of a predictor variable there is an associated observation of the target variable. If the target variable is numerical, the modelling is called *regression*, and *classification* if the target variable is categorical (James et al., 2021). In the machine learning context, *predicting* should be distinguished from *forecasting*, as models do not necessarily aim to predict into the future (Meyer et al., 2018). For unsupervised learning, there are no associated target observations and the model instead learns patterns such as clusters in the data without predefined goals (Mailund, 2017). For this dissertation, only supervised approaches for regression were applied.

The aims for modelling can be further distinguished between prediction and inference. For prediction, the goal is accurately predicting the target variable for new cases, while for inference the goal is a better understanding of the relation between target and predictor variables (James et al, 2021). Unfortunately, for almost all complex cases there is a trade-off between model accuracy and interpretability. Restrictive models such as linear regression have a low prediction performance in complex, non-linear cases but are relatively easy to interpret. In this way, a linear model can be used to infer model parameters, i.e., to falsify whether there was a significant linear relationship between target and predictor (Mailund, 2017). Flexible models such as neural networks, on the other hand, usually have a better accuracy but are also difficult to interpret, i.e., how their outcome is related to individual predictors (James et al, 2021). However, variable importance metrics can improve the interpretability of flexible models such as random forest (Grömping, 2009; Williamson et al., 2021). Machine learning models were applied with the focus on prediction in Chapter 4 and with the focus on inference in Chapter 6.

Another important issue for machine learning approaches is the trade-off between bias and variance as it is difficult for a model to exhibit both, a low bias and a low variance. A bias error results from an underfitted model with erroneous approximations about the relationship of predictor and target variables. A variance error refers to the high sensitivity of a model to variations of the training data. Ideally, a model should not vary much by different samples of training data in order to avoid modelling random noise. Otherwise, the model is overfitted to a specific training sample. Flexible models are prone to overfitting and thus require certain hyperparameters that can be fitted in an internal cross validation with independent test data within the model building process. In order to assess the overall model performance, an additional external cross validation with validation data fully excluded from the whole model building process is also required (James et al., 2021). However, for spatiotemporal prediction tasks, a random partition of data into training and validation sets is not sufficient, but validation should be conducted with spatial and temporal blocking to prevent an overoptimistic model assessment (Roberts et al., 2017). This is because common predictor variables that vary in space but not in time such as elevation, land cover or soil properties together act as a unique ID for each location with training data and the model is thus prone to overfitting (Meyer et al., 2018). In order to solve this issue, a feature selection with an internal spatial cross validation strategy can be conducted to exclude such spatially autocorrelated predictor variables (Meyer et al., 2019).

Decision trees form the basis of different tree-based machine learning methods such as random forest, gradient boosting or AdaBoost. The general principle of regression trees is to split the predictor space into several smaller, more homogeneous subgroups. The if-then rules constituting the model can be represented by a binary tree structure (Bergen et al., 2019; see Fig. 3.1). Hence at each *node* the data is split into two groups and each *leaf* is a terminal of the decision tree, at which observations are not further split. At each node the training data is split into two groups as homogeneous as possible by a threshold of a predictor variable. The predictor variable and its threshold are determined by the smallest sum of squared residuals of the observed target values to the averages of each group. The final prediction then is the average target value of all observations in the respective leaf. For typical decision trees, overfitting is reduced by a minimum number of observations required to be within a node to allow a further split. Pruning large trees, i.e., replacing a split by a leaf containing the average of both former groups, is another method to reduce overfitting (Kubat, 2017). To find the optimal size of the pruned tree, a penalty parameter for each additional leaf is introduced that can be tuned within the model building process.

Single decision trees usually are weak learners, but the prediction accuracy can be highly improved by ensemble methods such as random forest. This method consists of many decision trees (usually at least 500) and was introduced by Breiman (2001). The general concept is based on bootstrap aggregating or bagging. Here, each tree is grown with a random bootstrap sample of the training set with replacement (Efron, 1979). These trees are not pruned, and hence each individual tree has a low bias but a high variance. Results from all trees are averaged for the final prediction, in this way reducing the variance of the whole random forest model. A side-effect of this procedure is the possibility to calculate the out-of-bag error of the model as a quick substitute for cross validation. For this, the target value of each observation can be predicted only by the bagged trees that did not include the observation for fitting (James et al., 2021). Another method to decorrelate individual trees is to allow only a random subset of predictors as split candidates for each node in a decision tree. Although appearing limiting, without that restriction most or all trees would use the strongest variable in the first split, yielding similar trees with correlated predictions. Averaging uncorrelated predictions, however, reduces variance far more efficiently than averaging correlated ones (James et al., 2021). The number of variables allowed as split candidates is the most important hyperparameter that can be tuned in the model building process. Advantages of random forest are the few hyperparameters that have to be tuned and the higher interpretability due to variable importance measures compared to more opaque methods like neural networks. The latter is especially important if physical insights into the analyzed system should be gained (Bergen et al., 2021). Comparison studies of different machine learning methods for environmental science applications have shown that the performance of random forest was consistent or even better than neural networks or kernel methods (Appelhans et al., 2015; Tramontana et al., 2016).

Gradient boosting is also a tree-based method but unlike random forest the decision trees are not grown independently but additively with information from previous trees. The method was developed by Friedman (2002) and is not based on bagging. Instead, it starts with a single leaf containing the target variable average of the whole training data. Then a size restricted tree is built to predict the residuals of the previous tree instead of the raw target variable. That means, the second tree predicts the deviations of the predictions of the first tree from the target variable observations and a third tree would predict the residuals from the second tree and so on. This procedure is repeated until a given maximum number of trees is reached or the loss function is not improved anymore. In addition, a learning rate between 0 and 1 is introduced as a tuning parameter and is multiplied with the residual prediction of each tree. In this way only gradual improvements to a better prediction are forced upon the algorithm in order to reduce overfitting (James et al., 2021).

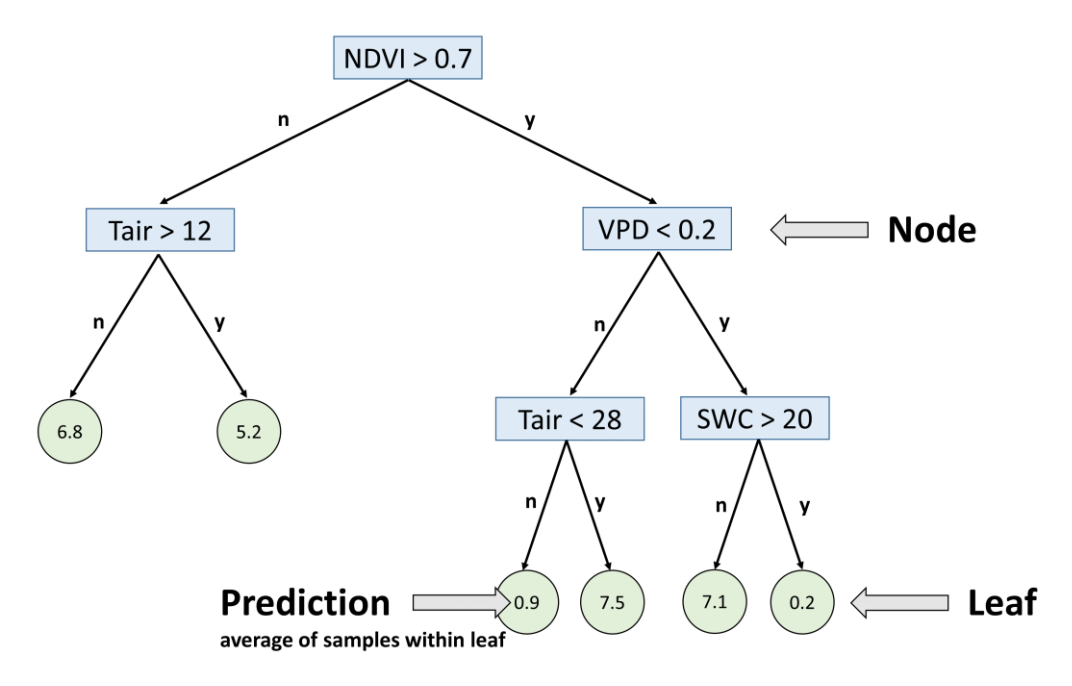


**Figure 3.1** Schematic depiction of a single decision tree with arbitrary variables and values in each node (blue rectangles) and leaf (green circles). The values in the leaves are the average target values of all training samples that fall within the respective leaf. For random forest, the predictions of all trees are averaged. For gradient boosting, predictions from the last tree are taken.

In environmental science the quantity and complexity of gathered data is increasing nearly exponentially which requires advanced data analysis techniques (Zhong et al., 2021). The combination of increasing computing power including cloud computing and the rapid progress in the field of machine learning with open-source frameworks is a promising precondition to apply machine learning for analyzing large environmental and spatiotemporal datasets (Bergen et al., 2019). The applications for machine learning within environmental science can be summarized to three inter-related goals: (i) automation of complex prediction tasks such as spatiotemporal interpolation, (ii) improving the understanding of complex relationships between environmental variables as conducted with variable important measures, and (iii) the discovery of unanticipated or counter-intuitive patterns and structures, e.g., finding new materials for CO<sub>2</sub> adsorption (Bergen et al., 2021; Zhong et al., 2021). In this way machine learning can be applied as a faster surrogate of numerical simulations that require even higher computation resources (Chen et al., 2020). It is also possible to incorporate physical knowledge or constraints within machine learning models e.g., by partial differential equations (Tramontana et al., 2020). Recent outstanding applications of machine learning in the field of biosphere-atmosphere interactions exemplary include scaling of carbon and energy fluxes to the global scale (Jung et al., 2019, 2020), continental scale (Ichii et al., 2017), predicting circumpolar methane emissions (Peltola et al., 2019), and gap filling of eddy covariance methane flux measurements (Kim et al., 2019). However, machine learning models always require a careful investigation whether their predictions are consistent with fundamental principles and experimental knowledge of environmental science (Zhong et al., 2020). In this way, inference results from machine learning in general are prone to spurious correlations, and by no means they should be taken as causal relations but rather can initiate more in-depth research. Other challenges include scarcity and quality of training data such as non-uniform data sampling strategies and small sample sizes (Zhong et al., 2020). Hence recent developments focus on the integration of machine learning with mechanistic models to improve model interpretability and the creation of large and open science benchmark datasets with uniform sampling strategies such as the FLUXNET database for eddy covariance data.

## 4 Upscaling Net Ecosystem Exchange over Heterogeneous Landscapes with Machine Learning

O. Reitz<sup>1</sup>, A. Graf<sup>2</sup>, M. Schmidt<sup>2</sup>, G. Ketzler<sup>1</sup>, M. Leuchner<sup>1</sup>

This chapter was originally published as the following article: Reitz, O., Graf, A., Schmidt, M., Ketzler, G., & Leuchner, M. (2021), Upscaling Net Ecosystem Exchange over Heterogeneous Landscapes with Machine Learning. *Journal of Geophysical Research: Biogeosciences*, 126, e2020JG005814. https://doi.org/10.1029/2020JG005814

As the first and corresponding author, OR designed the research framework, conducted the data preprocessing and implementation of the machine learning algorithms, and analyzed the results. OR further designed the structure and content of the article and wrote the manuscript with input from all co-authors.

#### **Abstract**

This paper discusses different feature selection methods and CO<sub>2</sub> flux data sets with a varying qualityquantity balance for the application of a Random Forest model to predict daily CO2 fluxes at 250 m spatial resolution for the Rur catchment area in western Germany between 2010 and 2018. Measurements from eddy covariance stations of different ecosystem types, remotely sensed vegetation data from MODIS, and COSMO-REA6 reanalysis data were used to train the model and predictions were validated by a spatial and temporal validation scheme. Results show the capabilities of a backwards feature elimination to remove irrelevant variables and an importance of high-qualitylow-quantity flux data set to improve predictions. However, results also show that spatial prediction is more difficult than temporal prediction by reflecting the mean value accurately though underestimating the variance of CO<sub>2</sub> fluxes. Vegetated parts of the catchment acted as a CO<sub>2</sub> sink during the investigation period, net capturing about 237 g C m<sup>-2</sup>y<sup>-1</sup>. Croplands, coniferous forests, deciduous forests and grasslands were all sinks on average. The highest uptake was predicted to occur in late spring and early summer, while the catchment was a CO<sub>2</sub> source in fall and winter. In conclusion, the Random Forest model predicted a narrower distribution of CO<sub>2</sub> fluxes, though our methodological improvements look promising in order to achieve high resolution net ecosystem exchange data sets at the regional scale.

#### **Plain Language Summary**

Whether ecosystems absorb or emit  $CO_2$  plays a major role in the global carbon cycle and impacts climate change. This exchange is already measured at scattered stations, but creating spatially resolved data sets remains a challenge. In this paper, we used satellite images of vegetation and meteorological data to predict the  $CO_2$  exchange of the Rur catchment area near the German-Dutch-Belgian border for every day from 2010 to 2018. In order to assess the prediction quality, we compared actual measurements from several stations within the catchment with the predictions at the locations of these stations. Results show that our method could increase prediction quality compared to previous process-based models, though the error remains rather high. Vegetated parts of the catchment including coniferous forests, deciduous forests, grasslands and croplands were all  $CO_2$  sinks on average. In late spring and early summer, they were the strongest sink, but in fall and winter a  $CO_2$  source.

<sup>&</sup>lt;sup>1</sup> Physical Geography and Climatology, RWTH Aachen University, Aachen, Germany

<sup>&</sup>lt;sup>2</sup> Agrosphere Institute, IBG-3, Forschungszentrum Jülich GmbH, Jülich, Germany

#### 4.1 Introduction

Land use changes are important drivers of anthropogenic climate change. For example, deforestation or afforestation can highly affect the carbon uptake and storage capacities of an ecosystem (Schimel et al., 2001). Net ecosystem exchange (NEE), the difference between carbon dioxide ( $CO_2$ ) uptake through photosynthesis and respiration within an ecosystem (Luyssaert et al., 2007), represents a major feature of the global carbon cycle and, thus, helps to assess ecosystem services and the impact of land use changes on them (negative NEE =  $CO_2$  uptake, positive NEE =  $CO_2$  emission) (Abdalla et al., 2013; Schmitt et al., 2010; Xu et al., 2017).

The eddy covariance (EC) technique is the most direct way of measuring CO<sub>2</sub> fluxes, however, it provides point measurements from a sparse network of stations each representing a footprint with an along-wind extent typically less than 800 m (Chen et al., 2009). Top-down approaches for spatial NEE assessment include global atmospheric inversion models from satellites such as GOSAT and OCO-2 (Wang et al., 2019a), which are especially useful for areas with limited or no EC coverage (Kondo et al., 2015) but are restricted to a coarse spatial resolution. Thus, bottom-up approaches scaling up EC measurements are expedient to quantify CO<sub>2</sub> fluxes for larger areas (Denman et al., 2007; J. Xiao et al., 2012), though they are also challenging due to the high spatiotemporal variability of those fluxes (Borchard et al., 2015; Kondo et al., 2017).

Process-based biogeochemical models have been widely applied for this purpose (e.g., Post et al., 2018; J. Xiao et al., 2011), but subject to assumptions and model parametrizations. Data driven machine learning techniques such as Random Forest (RF) are another promising approach to predict NEE as they can grasp even highly nonlinear relationships to explanatory variables as is usual in environmental data (Cutler et al., 2007). Previous attempts using statistical modeling include nonspatial predictions of NEE at the EC tower scale (Dou et al., 2018; Safa et al., 2019; Zhou et al., 2019). Other attempts aimed at upscaling of carbon fluxes to the continental or national scale (Papale et al., 2015; Sun et al., 2011; J. Xiao et al., 2008) or the globe, most notably the FLUXCOM approach (Bodesheim et al., 2018; Jung et al., 2011, 2020). Upscaling to the regional scale at high spatial resolution has rarely been done although NEE estimates of heterogeneous regional and local ecosystems are of high value for assessing ecosystem services in spatial planning (Tammi et al., 2017). Furthermore, products at a finer spatial resolution are less prone to contain mixed pixels with contamination of the main land use class by e.g. roads, settlements or tree rows (Zhang et al., 2011) developed a regression model for the U.S. Great Plains based on EC towers representing grassland only. Post et al. (2018) already upscaled NEE to the study area of this analysis, though with a processbased model.

Spatial cross validation, that is, excluding whole locations from model training and testing the model on them, is crucial for a realistic assessment of the reliability of spatial predictions beyond the locations of training data. A substantial performance decrease is to be expected in comparison to a random split of data points into training and test sets, which hence overrates model performance due to spatial autocorrelation (Meyer et al., 2018; Roberts et al., 2017). Tramontana et al. (2016) conducted a profound cross validation analysis for spatial predictions of various carbon and energy fluxes with the conclusion that NEE is especially difficult to predict. Feature selection of explanatory variables, on the other hand, can considerably improve data driven model performance as it reduces overfitting and removes irrelevant or redundant variables (Hall & Smith, 1999). Meyer (2018) proposed a sequential feature selection algorithm based on spatial cross validation to remove spatially autocorrelated predictors. In contrast to this, conventional feature selection as implemented in the caret package (Classification And REgression Training, Kuhn, 2020) is based on internal cross validations within the training data, and hence fails to improve model performance when testing on locations not used for

model training (Meyer et al., 2019). Genetic algorithms like the Guided Hybrid Genetic Algorithm (GHGH, Jung & Zscheischler, 2013) are useful for very large numbers of features (>100), though generally they do not rely on spatial cross validation. Quality of EC data is another issue for upscaling attempts, especially when aggregating half-hourly to daily fluxes. While data quality improves when excluding low-confidence values based on quality control, too small data sets also limit the learning capacities of machine learning algorithms (Ließ et al., 2012). A common practice is to indicate daily data as missing if more than 20% of half-hourly values are missing or of low quality (Tramontana et al., 2016; Yuan et al., 2010). However, to our knowledge a sensitivity analysis to different percentages has not been done before.

In conclusion, NEE upscaling with data driven methods at high spatiotemporal resolutions and incorporating different land uses remains a major task to be handled in order to approach the goal of flux information "everywhere, all of the time" (Baldocchi, 2014). Thus, the objectives of this paper are i) to perform upscaling of daily NEE over heterogeneous landscapes of the Rur catchment in western Germany for the years 2010 –2018 with a RF model incorporating EC measurements, remote sensing and reanalysis data and ii) to assess the impact of EC data quality and feature selection on the model performance.

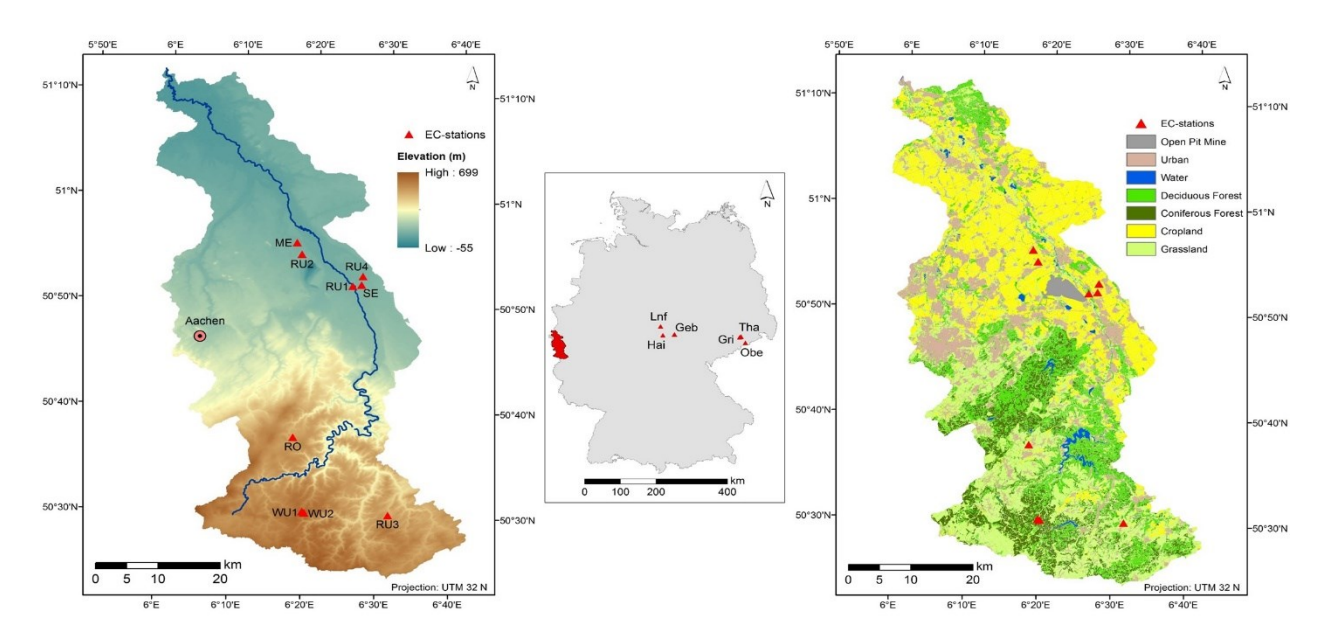


**Figure 4.1** Elevation from SRTM data (Jarvis et al., 2008) and eddy covariance stations used for training within the Rur catchment area (left), the location of the study area and the FLUXNET stations within Germany (middle) and simplified land cover classes after Lussem and Herbrecht for the Rur catchment (2019) (right).

#### 4.2 Data and Methods

#### 4.2.1 Study Area

The Eifel/Lower Rhine Valley Observatory covers the Rur catchment located near the German-Belgian-Dutch border and is one of four TERrestrial ENvironmental Observatories (TERENO) in Germany (Zacharias et al., 2011). These areas were selected for the TERENO network because they are representative of typical landscapes found in Central Europe (Bogena et al., 2016). The catchment covers an area of 2,354 km² and can be divided into a northern lowland part with intensive agriculture and a relatively high proportion of built-up areas and a southern low mountain part where pastures

and forests prevail, as shown in Figure 4.1. Based on a simplified land cover classification by Lussem and Herbrecht (2019), the catchment consists of 27.6% grassland, 25.7% cropland, 17.7% deciduous forest, 8.5% coniferous forest, and 20.4% other land cover types including urban areas, open cast mines and water bodies. Mean annual temperatures range from about 7.5 –10.2 °C, increasing from south to north. Mean annual precipitation decreases from 1,200 mm in the southern low mountain parts to 700 mm in the north (Baatz et al., 2014).

Table 4.1 Description of the Eddy Covariance Stations Providing CO<sub>2</sub> Flux Data Used for Model Training.

		Sensing	Ecosystem	Elevation			
Name	ID	Period	Туре	(m)	Latitude	Longitude	Documentation
TERENO							
		05/2011 -					
Merzenhausen	ME	12/2018	Cropland	92	50.9297879	6.2969924	Eder et al. (2015)
		05/2011 -					
Rollesbroich	RO	12/2018	Grassland	514	50.6219142	6.3041256	Gebler et al. (2015)
		10/2011 -					Schmidt & Schween
Ruraue	RU1	08/2017	Grassland	101	50.8636289	6.4274571	(2018)
		08/2012 -					
Engelsdorf	RU2	10/2012	Cropland	108	50.9115426	6.3088546	Schmidt (2019)
		08/2012 -					
Kall-Sistig	RU3	07/2013	Grassland	499	50.5026827	6.525401	Post et al. (2015)
		04/2013 -					
Niederzier	RU4	07/2013	Cropland	101	50.8795149	6.4498871	Schmidt (2014)
		04/2011 -					
Selhausen	SE	12/2018	Cropland	101	50.8658521	6.4473198	Schmidt et al. (2012)
Wüstebach		06/2010 -	Coniferous				
forest	WU1	12/2018	forest	624	50.5049269	6.33096248	Graf et al. (2014)
Wüstebach		09/2013 -					
deforested	WU2	12/2018	Deforested	628	50.50305	6.33596	Wiekenkamp et al. (2016)
FLUXNET							
		01/2002-					
Gebesee	DE-Geb	12/2014	Cropland	162	51.09973	10.91463	10.18140/FLX/1440146
		01/2004-					
Grillenburg	DE-Gri	12/2014	Grassland	385	50.95004	13.51259	10.18140/FLX/1440147
		01/2002-	Deciduous		E4 07024	40 45247	
Hainich	DE-Hai	12/2012	Forest	430	51.07921	10.45217	10.18140/FLX/1440148
		01/2002-	Deciduous				
Leinefelde	DE-Lnf	12/2012	Forest	451	51.32822	10.3678	10.18140/FLX/1440150
		01/2008-	Coniferous				
Oberbärenburg	DE-Obe	12/2014	Forest	734	50.78666	13.72129	10.18140/FLX/1440151
J		01/2002-	Coniferous				
Tharandt	DE-Tha	12/2014	Forest	385	50.96256	13.56515	10.18140/FLX/1440152

#### 4.2.2 Eddy Covariance Data

CO<sub>2</sub> flux measurements from nine EC stations covering different land cover types and elevations within the study area have been used for model training and prediction (see Table 1 for details and abbreviations). The nine stations are all part of the TERENO network (Zacharias et al., 2011). Measurements from these stations were processed with the TK3 software (Mauder & Foken, 2011); 20 Hz frequency data were hereby processed to 30 min fluxes and corrected for storage terms to obtain NEE values. All processing and quality-control schemes were carried out according to the standardized strategy presented by Mauder et al. (2013), which also includes a test on developed turbulence after Foken and Wichura (1996). Detailed measurement and processing descriptions can be found in the references listed in Table 1, a short description of each site is given here.

RO is an extensively managed grassland site, which is cut several times per year and mostly consists of ryegrass and smooth meadow grass (*Lolium perenne*, *Poa pratensis*). The EC tower was placed in the middle of two neighboring pastures with slightly different management regimes (Borchard et al., 2015; Korres et al., 2010). RU3 is a grassland site with similar characteristics (Post et al., 2015), while RU1 is a grassland site at significantly lower elevation (Lussem & Herbrecht, 2019). SE, ME, RU2 and RU4 are cropland sites with rotating crops, mostly sugar beet, winter wheat and winter barley (Eder et al., 2015; Lussem & Herbrecht, 2019; Post et al., 2015; Schmidt et al., 2012). WU1 is located above a planted spruce forest (*Picea abies*) of uniform height (Graf et al., 2014), while nearby WU2 is placed in an 8.6 ha area which was deforested in 2013 to allow a natural succession toward a European beech forest (Ney et al., 2019; Wiekenkamp et al., 2016). Currently (2020), spontaneous vegetation of the deforested area consists mostly of grass, shrubs (e.g., *Cytisus scoparius*) and young trees (*Sorbus aucuparius, Betula pubescens*).

EC data were aggregated from half-hourly fluxes to daily data. As only high to moderate quality EC data were used (quality flags 0 and 1), frequent gaps were created. The number (n) of days containing all 48 half-hourly intervals (100%) was only 386 for all TERENO stations combined, which is about 3.2% of all possible days and constitutes the first data set. Additional data sets were created with a varying number of missing 30 min intervals allowed: minimum 45/48 (93.75%) intervals of high to moderate quality (n = 1,035; 8.5% of possible days), 42/48 (87.5%) (n = 2,032; 16.6% of possible days), and 36/48 (75%) (n = 3,996; 32.7% of possible days). For the calculation of these daily NEE values, gap-filled data inferred with the REddyProc package (Wutzler et al., 2018) were used. In case gap-filled data were not available, the mean was calculated of all nonfilled values of each respective day. Based on the minimum of reliable half-hourly values included, these data sets are referred to in this paper as 48, 45, 42 and 36, respectively.

Forest sites were underrepresented in the TERENO data, as only one coniferous forest site and no deciduous forest site were included. To achieve a better representation of each ecosystem type and to broaden the environmental envelope, we added daily NEE data with variable ustar-thresholds of six further stations (two coniferous forest, two deciduous forest, one grassland, one cropland site) from the FLUXNET2015 database (Pastorello et al., 2020), as shown in Table 1. Because quality-flag schemes may have differed among these sites, we filtered the FLUXNET data according to the relative uncertainty instead. In order to create data sets of equal proportions as the 48, 45, 42 and 36 data sets, we took the X days with the lowest relative uncertainty, with X being 3.2%, 8.5%, 16.6% and 32.7%, respectively. Finally, these FLUXNET data sets, were added to the 48, 45, 42 and 36 data sets. The sensitivity of each of these data sets with a varying quality-quantity balance to the RF performance was then further evaluated with the feature selection and cross validation strategies described below.

#### 4.2.3 Raster Data

Explanatory variables were compiled from various sources and were of different spatial and temporal resolutions, as shown in Table 2. These variables were chosen because they are regarded to potentially affect NEE, and were selected by availability for the whole time period 2010-2018. Vitale et al. (2016) showed that variations of vegetation indices such as Leaf Area Index (LAI) can highly influence carbon fluxes. Ishtiaq and Abdul-Aziz (2015) concluded that meteorological parameters have a strong linkage with CO<sub>2</sub> fluxes, especially "radiation-energy" components. Datetime variables such as Day of Year can also be a useful proxy for estimating CO<sub>2</sub> fluxes (Acosta et al. 2018). We used the following remotely sensed MODIS Version 6 products: MCD18A1 for downward shortwave radiation (2018 only) (Wang, 2017), MOD44B for percent tree cover, percent nontree vegetation and percent nonvegetated land cover (Dimiceli et al., 2015), MCD15A2H for LAI and Fraction of Absorbed Photosynthetically Active

Radiation (fAPAR) (Myneni et al., 2015), and MYD13Q1 and MOD13Q1 for Normalized Difference Vegetation Index (NDVI) and Enhanced Vegetation Index (EVI) (Didan, 2015). All of these data sets were quality controlled to exclude contaminated pixels with the quality assurance raster included in the MODIS products. Subsequently, for NDVI, EVI, LAI and fAPAR a Whittaker smoother (Atzberger & Eilers, 2011) was applied to fill gaps and smooth out noise in the data occurring from undetected clouds. Finally, these vegetation data sets were linearly interpolated in time from 8-day to daily data.

Daily gridded data for the meteorological variables air temperature and relative humidity in 2 m, soil temperature, precipitation, zonal and meridional wind speed in 10 m, long wave upward and downward radiation at the surface and net shortwave and longwave radiation at the surface were obtained from the COSMO REA6 regional reanalysis data set (Bollmeyer et al., 2015) and were regridded with Climate Data Operators (Schulzweida, 2019). Furthermore, daily downward shortwave radiation from 2010 to 2017 was acquired from the Heliosat (SARAH-2) Surface Solar Radiation Data Set (Pfeifroth et al., 2019), other variables include a digital elevation model from the Shuttle Radar Topography Mission (Jarvis et al., 2008), and soil moisture and potential evapotranspiration from the German Weather Service (DWD, 2019) based on Löpmeier (1994).

Raster data were used and further processed at two different steps in the analysis, to i) extract values at the coordinates of each site for model training and validation, and ii) predict NEE for the entire catchment area. For the latter, all raster sets were homogenized to the same extent and same spatial resolution of 250 m with bilinear interpolation of the raster package in R (Hijmans, 2020).

Table 4.2 Predictor Variables Used for Model Training.

Nr.	ID	Name	Source	Temporal	Spatial	Unit
				Resolution	Resolution	
1	NDVI	Normalized Difference Vegetation Index	MODIS	8 days	250 m	
2	EVI	Enhanced Vegetation Index	MODIS	8 days	250 m	
3	LAI	Leaf Area Index	MODIS	8 days	500 m	m²/m²
4	fAPAR	Fraction of absorbed Photosynthetic Active Radiation	MODIS	8 days	500 m	%
5	Tree	Percent_Tree_Cover	MODIS	yearly	250 m	%
6	NonTree	Percent_NonTree_Vegetation	MODIS	yearly	250 m	%
7	NonVeget	Percent_NonVegetated	MODIS	yearly	250 m	%
			Heliosat (2010 -		0.05°	
8	SWI	Downward Shortwave Radiation	2017)	daily	(Heliosat) 5	W/m²
			MODIS (2018)		km (MODIS)	
9	SWB	Net Shortwave Radiation	COSMO-REA6	daily	6 km	W/m²
10	LWI	Downward Longwave Radiation	COSMO-REA6	daily	6 km	W/m²
11	LWU	Upward Longwave Radiation	COSMO-REA6	daily	6 km	W/m²
12	LWB	Net Longwave Radiation	COSMO-REA6	daily	6 km	W/m²
13	Precip	Precipitation	COSMO-REA6	daily	6 km	mm
14	Tair	Air Temperature (2 m)	COSMO-REA6	daily	6 km	K
15	Tsoil	Soil Temperature	COSMO-REA6	daily	6 km	K
16	rH	Relative Humidity (2 m)	COSMO-REA6	daily	6 km	%
17	u	Zonal Wind Speed (10 m)	COSMO-REA6	daily	6 km	m/s
18	v	Meridional Wind Speed (10 m)	COSMO-REA6	daily	6 km	m/s
19	ETpot	Potential Evapotranspiration	DWD	daily	1 km	mm
20	Soilm	Soil Moisture	DWD	daily	1 km	%
21	Month	Month		monthly	static	
22	Season	Season		3 months	static	
23	DoY	Day of Year		daily	static	
24	DEM	Elevation	SRTM	static	30 m	m

#### 4.2.4 Random Forest Model

RF is a machine learning method based on an ensemble of many binary decision trees. The algorithm was introduced by Breiman (2001) and is widely used for classification and regression in ecology (e.g., Aide et al., 2012; Prasad et al., 2006; Tramontana et al., 2016). Each decision tree is grown with a random subsample with replacement of the input data, called bootstrapping (Efron, 1979). At each node in the decision tree, a threshold of a randomly selected explanatory variable is ascertained to split the data into the two most homogeneous subgroups, i.e. with the lowest variance. The leaf nodes at the end of the tree do not further split the data but contain predictions of the target variable. This value is the mean of the target variable of all elements in the corresponding subgroup. For the final prediction, results of all trees (in this case 500) are averaged to overcome weaknesses of single trees. One consequence of this algorithm, however, is that predictions cannot be out of bounds of the training range. In this study, we used the implementation of the RF code in the randomForest package in R by Liaw and Wiener (2002) to predict NEE in a regression approach. In order to identify an ideal number of predictor variables used at each split node ("mtry"), model tuning was conducted with the caret package, which is a wrapper to perform model tuning for various predictive models.

In order to perform feature selection, we first split the data into spatial and temporal folds (described in the next section in detail) with the CAST package (Meyer, 2018). In a next step, we applied the forward feature selection (FFS) procedure of this package with Root Mean Squared Error (RMSE) as performance metric to punish high errors in particular. The advantage of CAST FFS is that feature selection results are based on spatiotemporal cross validation rather than on training data only. However, as FFS sometimes selected very few variables with unsatisfactory performance (see Section 3.1), a slightly modified version of this procedure has been devised and compared to FFS. We applied a backward feature elimination (BFE), which starts with all features and iteratively removes the worst feature based on a spatial or temporal cross-validation. Conversely, FFS iteratively adds features to the best combination of two features. Since RF relies on randomization, results can significantly differ between model runs. Hence, each iteration within BFE was repeated five times to average out such randomization effects. This leads, however, to a significant increase in computation time. The general algorithm of the BFE procedure is described in Table 3. To illustrate the impact of these two feature selection procedures on model performance, model runs without any feature selection were evaluated too.

**Table 4.3** General Algorithm of the Backward Feature Elimination (BFE), the Indications in Square Brackets Refer to the R-Packages Used for the Respective Step.

#### Algorithm 1 Split data into spatial or temporal folds [CAST] 01: 02: Do 5 times with all predictor variables: 03: Train and test model with a leave-one fold-out cross validation [caret] 04: Calculate RMSE over all folds 05: Get *previous* ← Averaged RMSE over 5 repetitions 06: For each remaining predictor variable do: 07: Exclude variable 08: Do 5 times: Train and test model with a leave-one fold-out cross validation [caret] 09: 10: Calculate RMSE over all folds 11: Average RMSE over 5 repetitions 12: Get bestSubset ← variable subset with lowest average RMSE Get bestRMSE ← RMSE of bestSubset 13: 14: If bestRMSE < previous: stop 15: Else: *previous* ← *bestRMSE* 16: repeat from step 06 onwards with bestSubset



CV	Fold	Training data			Test data
<u></u>	1				
spatial	2				
S	3				
ra	1			$\bigcirc \triangle$	
tempora	2				
ter	3				

Figure 4.2 Schematic depiction of the spatial and temporal cross validation (CV) strategies that have been applied for this analysis. t1, t2 and t3 refer to three different time steps (years in our case), while ta refers to the FLUXNET data which are outside the timespan of TERENO data (prior to 2010) and tb refers to the years included in the TERENO data (2010–2014). The figure was recreated and modified after Meyer et al. (2018).

#### 4.2.5 Cross Validation

In order to assess RF performance beyond the scope of training data, NEE predictions have been cross-validated for (a) spatially and (b) temporally independent test sets. The additional FLUXNET data from outside the catchment were only used for training, whereas the TERENO data were used for training

and testing. Figure 4.2 displays the cross-validation strategies in a schematic way. Especially spatially independent test sets may be important for the assessment of the upscaled NEE predictions presented in Section 3.2 because they simulate predictions for pixels without any information used for model training. These cross validation strategies have been performed for all different NEE data sets and feature selection methods.

- a) Data were split into folds by station ID. Stations were only considered for leave-out if they i) were not the only station of their land cover class to ensure that the class was still contained in the training data when excluding the station and ii) had data spanning over at least three years to ensure representative results. Therefore, five stations (SE, RU1, ME, RO, WU1) were regarded, though all other stations were included for training.
- b) Data were split into folds by year. Each fold containing one year of data was left out once and predicted by a model trained with the other years. 2010 has only been regarded for training and not for testing as only data from one TERENO site was available for 2010.

We used the coefficient of determination (R<sup>2</sup>), the mean absolute error (MAE) and the root mean square error (RMSE) as metrics to evaluate model performance.

The relative importance of selected variables for model building was assessed through RF's internal variable importance metric implemented in the randomForest package. For this, data points of each variable are randomly permutated and the relative increase of the mean squared error (MSE) based on an internal cross validation within in the training data is measured. This error is assumed to increase if the variable is important.

#### 4.3 Results

#### 4.3.1 Cross Validation Results

We evaluated NEE predictions with a leave-one-fold-out cross validation by withholding either sites (spatial cross validation) or years (temporal cross validation). Table 4 summarizes the spatial and temporal cross validation results of different NEE data sets and feature selection methods. The results indicate that spatial prediction was generally more difficult than temporal prediction. Models trained with the 48 data set had the lowest RMSE values, though with the 45 data set slightly higher R² could be obtained. Especially for temporal cross validation, RMSE/MAE and R² did not coincide well with each other. The feature selection methods FFS and BFE were either closely in line with each other or BFE gave considerably better results than FFS. In these cases, FFS always selected less variables than BFE. Furthermore, BFE always performed better than no feature selection, indicating that BFE is more suitable than FFS or no feature selection for this analysis. Few patterns can be observed regarding selected variables, most notably that elevation was selected for every model with temporal cross validation, though very seldom for spatial prediction. The variables LAI, fAPAR and Precip, however, were almost always excluded. For the final upscaling we selected the model with the best RMSE by spatial cross-validation in order to optimize it for spatial prediction and avoiding high errors. Hence, we chose the model trained with the 48 data set and tuned with BFE.

The relative importance of selected variables was assessed by the importance function of the randomForest package. As shown in Table 5, the most important variables were EVI and ETpot. Figure 4.3 displays an assessment of the quality of NEE predictions in comparison to observed TERENO validation data. While predictions and observations have almost the same mean values (-2.31 and -2.3 g C m<sup>-2</sup>d<sup>-1</sup>) and rather similar median values (-1.84 and -1.33 g C m<sup>-2</sup>d<sup>-1</sup>), and the regression line a slope close to 1 (y = 0.15 + 1.06x; Fig. 4.3a), the standard deviation of predictions (2.5 g C m<sup>-2</sup>d<sup>-1</sup>) is much

lower compared to observations (3.73 g C  $m^{-2}d^{-1}$ ). The interquartile range of predictions is also narrower than of observations (-3.96 to -0.27 compared to -4.49 to 0.29 g C  $m^{-2}d^{-1}$ ; Fig. 4.3b). As for predictions, values from about -5 to 1 g C  $m^{-2}d^{-1}$  were more frequent, and outside of that range less frequent than in observations, resulting in a narrower distribution of values (Fig. 4.3c). This results in higher absolute errors for high flux magnitudes, especially for positive fluxes (Fig. 4.3d).

Table 4.4 Cross Validation Results for Different NEE Data Sets and Different Feature Selection Methods.

Cross	Data	Feature	RMSE	MAE	R²	n Var	Variables selected
Validation	Set	Selection					
spatial							
	48	FFS	2.96	2.25	0.35	6	9,12,19,22,24
		BFE	2.72	1.9	0.41	15	2,5:7,10:12,14:20,22
		none	3.01	2.19	0.34	24	1:24
	45	FFS	2.88	2.07	0.43	10	2,5,7,8,12,14,19:21,23
		BFE	2.84	2.07	0.42	10	5,7,11,12,14,17,19:22
		none	3.16	2.24	0.34	24	1:24
	42	FFS	3.18	2.23	0.34	9	1,2,5,7,8,12,15,21,22
		BFE	3.2	2.25	0.33	14	1,2,5:8,12,14,:16,19,21,23
		none	3.32	2.37	0.31	24	1:24
	36	FFS	3.4	2.42	0.32	10	1,2,5:9,11,21,22
		BFE	3.4	2.41	0.32	17	1:3,5:9,11,14:18,20:22
		none	3.51	2.54	0.3	24	1:24
temporal							
	48	FFS	2.54	1.89	0.31	8	5,6,8,9,16,19,22,24
		BFE	2.55	1.78	0.32	11	1,5,8,14,16,19,21:24
		none	2.91	2.02	0.24	24	1:24
	45	FFS	2.67	1.84	0.46	8	1,5,10,17,19,21,23:24
		BFE	2.59	1.79	0.5	15	1,5:8,11,12,15,17,19:24
		none	2.66	1.82	0.46	24	1:24
	42	FFS	3.01	2.08	0.44	12	1,2,6:9,14,17:19,23:24
		BFE	2.95	2.05	0.45	14	2,5:9,11,14,15,17,18,21:22,24
		none	3.06	2.1	0.43	24	1:24
	36	FFS	3.34	2.32	0.44	13	1:3,5:8,11,17:19,21,24
		BFE	3.32	2.28	0.44	16	2,3,5:11,14,17,18,21:22,24
		none	3.41	2.39	0.42	24	1:24

**Note.** RMSE, MAE and R<sup>2</sup> values are reported as averages of the respective folds. Performance is displayed as Root Mean Squared Error (RMSE; in g C m<sup>-2</sup>d<sup>-1</sup>), Mean Absolute Error (MAE; in g C m<sup>-2</sup>d<sup>-1</sup>) and coefficient of determination (R<sup>2</sup>). n Var gives the number of selected variables, Variables selected lists which variables were selected by the Nr. stated in Table 2

 Table 4.5 Importance of Each Variable Selected by BFE for the 48 Data Set.

Variable	%IncMSE
EVI	13.85
ETpot	12.29
Season	3.49
rH	3.02
LWB	2.70
Tree	2.55
LWU	2.26
LWI	2.24
Tsoil	2.18
NonTree	2.11
Tair	2.06
Soilm	1.74
V	1.11
NonVeget	1.01
u	0.60

**Note**: %IncMSE describes the percental increase of the mean squared error after permutation as implemented in the randomForest package

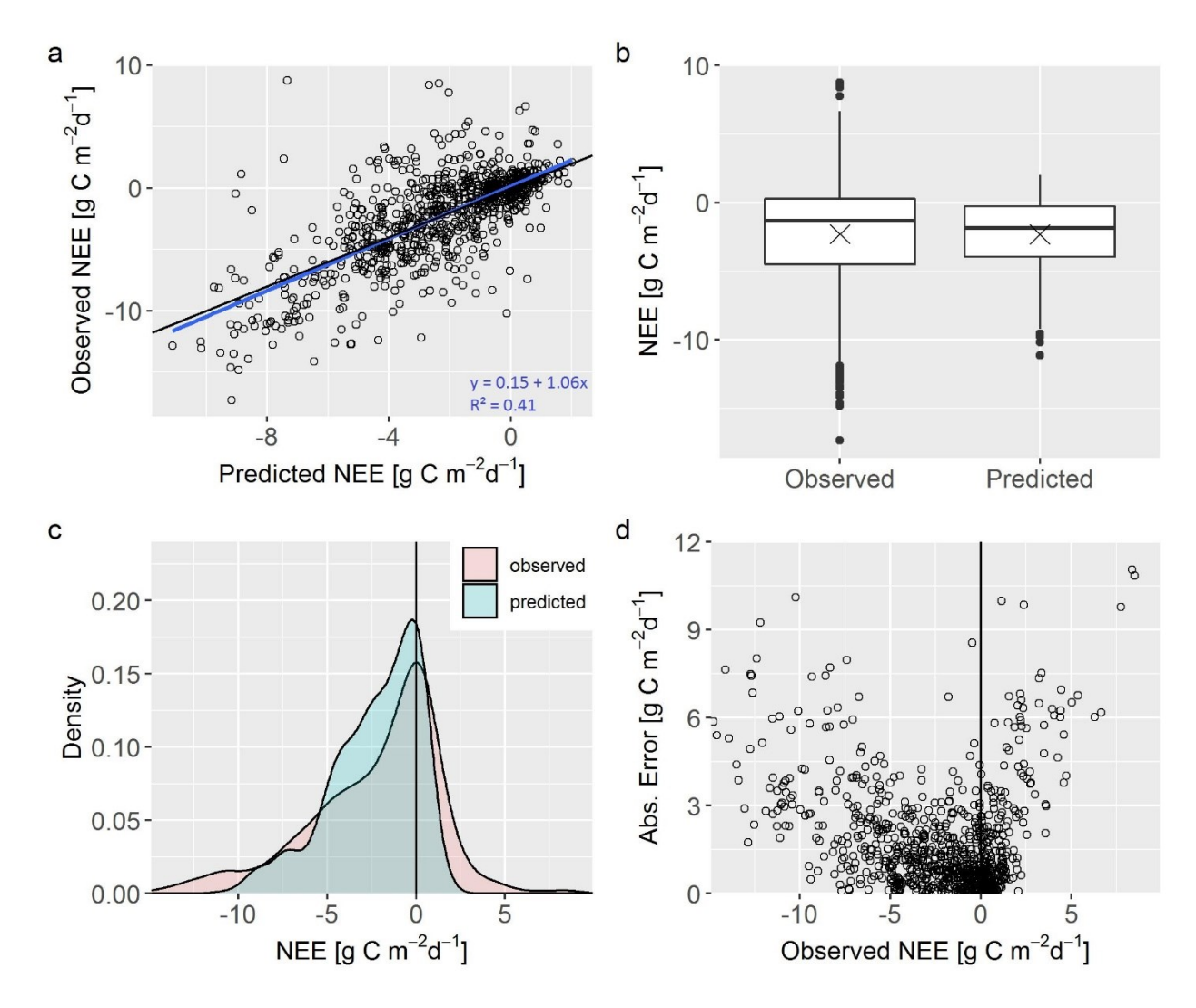


Figure 4.3 Assessment of prediction quality in comparison to observations from TERENO test data. (a) scatter plot with regression line (blue) and identity line (black); (b) boxplots with mean values displayed as crosses; (c) density plot of predicted (blue) and observed (red) NEE values; (d) absolute error by observed NEE. The vertical line at zero marks the border between CO<sub>2</sub> sinks (left) and CO<sub>2</sub> sources (right).

# 4.3.2 Upscaling Results

We predicted daily NEE data at 250 m spatial resolution for the Rur catchment from 2010 to 2018. According to the results of the previous section, the 48 NEE data set and explanatory variables selected with spatial BFE were used for model training. Table 6 shows the upscaled results aggregated by land cover class and season. To put these results into perspective, such aggregations over actual measurements within the catchment are also included in Table 6. Pixels classified as urban or built-up were excluded from the analysis because anthropogenic CO<sub>2</sub> emissions were not represented in the training data. Results show that vegetated areas of the Rur catchment were on average a CO<sub>2</sub> sink between 2010 and 2018 with about -0.65 g C m<sup>-2</sup>d<sup>-1</sup>. Grasslands and deciduous forests were the strongest sink (-0.76 g C m<sup>-2</sup>d<sup>-1</sup> and -0.72 g C m<sup>-2</sup>d<sup>-1</sup>, respectively), while croplands captured the least net amount of CO<sub>2</sub> (-0.56 g C m<sup>-2</sup>d<sup>-1</sup>). During winter (December-February) and fall (September-November), the Rur catchment was a CO<sub>2</sub> source (0.86 g C m<sup>-2</sup>d<sup>-1</sup> and 0.75 g C m<sup>-2</sup>d<sup>-1</sup>, respectively), while in spring (March-May) it was a strong sink (-2.14 g C m<sup>-2</sup>d<sup>-1</sup>), closely followed by summer (June-August; -2.02 g C m<sup>-2</sup>d<sup>-1</sup>). Figure 4.4 shows yearly courses of predicted NEE aggregated by land cover

for the investigation period. Additionally, daily NEE raster were aggregated by season and the whole investigation period (Fig. 4.5). These results show that all land cover classes were a CO<sub>2</sub> source in fall and winter and sink in spring and summer, although the CO<sub>2</sub> uptake started decreasing in summer already. Croplands were the earliest to become a sink in spring and also to turn into a source after day of year 200. This NEE sink capacity decrease of croplands from spring to summer is also observable in Figure 4.5 as croplands prevail in the northern half of the catchment. Forests were a stronger source than croplands and grasslands in fall and winter, though deciduous forests were also the strongest sink with average NEE below -5 g C m<sup>-2</sup>d<sup>-1</sup> around day of year 170. However, coniferous forests and especially deciduous forests were a greater sink in summer in actual measurements, and no CO<sub>2</sub> source in fall. In contrast, grasslands were predicted to be a greater sink in summer compared to actual measurements. Differences between land cover classes were in general less pronounced in upscaled predictions than in measurements.

**Table 4.6** NEE in g C m<sup>-2</sup>d<sup>-1</sup> Aggregated by Land Cover and Season of Upscaled Data Over Vegetated Parts of the Rur Catchment (above) and of eddy covariance (EC) Measurements Within the Catchment Described in Table 1 (below).

Opscar	ling Resul	u

opseaming nesares							
Land Cover	Winter	Spring	Summer	Fall	Year		
Coniferous F.	0.92	-1.75	-2.54	0.9	-0.63		
Deciduous F.	1.07	-1.99	-2.77	0.85	-0.72		
Grassland	0.87	-2.14	-2.35	0.6	-0.76		
Cropland	0.67	-2.41	-1.17	0.74	-0.56		
Study Area	0.86	-2.14	-2.02	0.75	-0.65		

#### **EC Tower Measurements**

Land Cover	Winter	Spring	Summer	Fall	Year	
Coniferous F.	0.46	-2.36	-3.5	-1.1	-1.63	
Deciduous F.*	1.15	-0.95	-6.11	-0.64	-1.64	
Grassland	0.56	-1.71	-0.83	0.55	-0.36	
Cropland	0.38	-3.08	-1.79	0.76	-0.93	

*Note*. \*Values for the class deciduous forest were calculated from the two FLUXNET stations De-Hai and De-Lnf as no measurements of that class were available within the catchment.

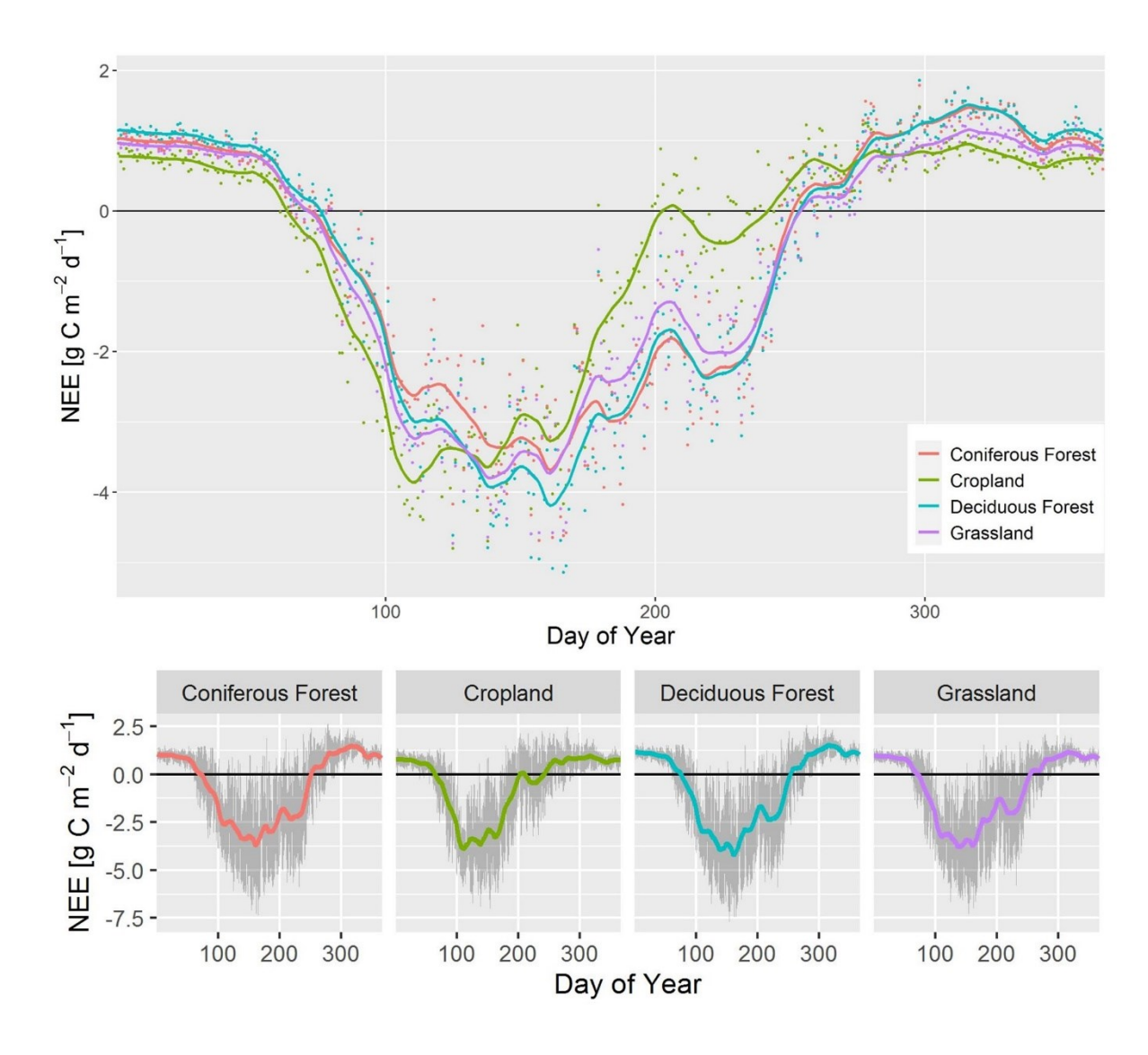


**Figure 4.4** Yearly courses of predicted net ecosystem exchange (NEE) aggregated by each land cover class for the period 2010-2018 (points), and smoothed by a loess function (lines; above). Standard deviation (±) for each of those lines separately (gray bands; below).

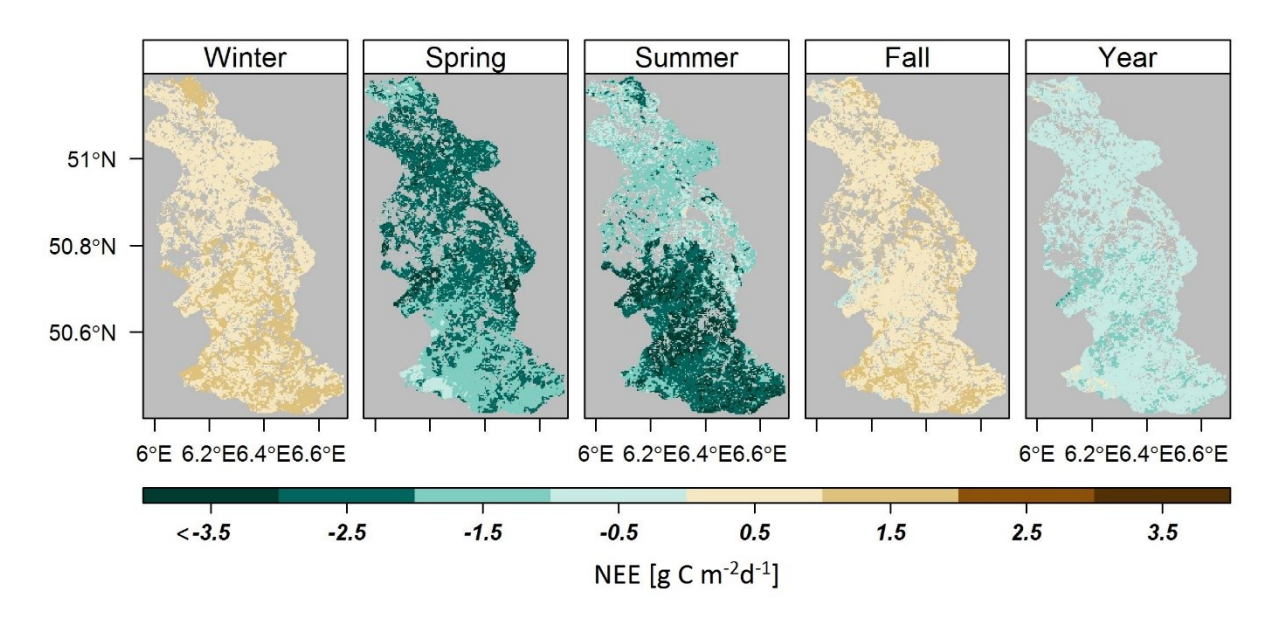


**Figure 4.5** Predicted net ecosystem exchange (NEE) of the Rur catchment aggregated for the whole investigation period 2010-2018 and for each season. Mean values for each map are  $0.86 \text{ g C m}^{-2}\text{d}^{-1}$  (winter), -2.14 (spring), -2.02 (summer), 0.75 (fall) and -0.65 (year).

# 4.4 Discussion

The results of the study showed that a data-driven upscaling of NEE to the regional scale predicted the average NEE well though underestimated the variance (Fig. 4.3b). Feature selection and the right quality-quantity balance of NEE data, however, can improve model performance. Similar to our results, high errors for NEE upscaling have also been observed in other studies (Jung et al., 2011; Tramontana et al., 2016). J. Xiao et al. (2011) showed that an ecosystem model predicted NEE with an  $R^2$  between 0 and 0.66, depending on the site. Richardson et al. (2012) demonstrated increasing random errors with flux magnitude for half-hourly  $CO_2$  flux measurements. The absolute errors displayed in Figure 4.3d show a similar pattern, indicating that high flux magnitudes may be difficult to predict and validate because actual measurements in those ranges are already error-prone.

Meyer et al. (2018) demonstrated that random cross validation lead to an overoptimistic view of the model performance compared to spatial cross validation. In our case, RMSE could be improved to 1.85 g C m<sup>-2</sup>d<sup>-1</sup> and R<sup>2</sup> up to 0.82 with a random cross validation, indicating that mere data reproduction is much easier than actual spatial prediction. Elevation was named as a typical example of a spatially autocorrelated predictor by Meyer et al. (2019). Hence, it is reasonable that it was removed by FFS and BFE for spatial cross validation, but not for temporal cross validation. Besnard et al. (2019) concluded that integrating memory effects of past disturbances in a recurrent neural network outperforms nondynamic statistical models like RF. So not including memory effects in our study might limit the prediction capacities.

One intrinsic feature of RF is to not extrapolate beyond the input data due to the prediction being the average target value of the subgroup within a leaf node. Although we attempted to overcome this limitation by including sites from outside the catchment and hence broadening the environmental envelope, outliers with high flux magnitudes were still underpredicted. A portion of the prediction

error can also be attributed to uncertainties in the raster data sets used for model training and predictions. Some of the most important variables such as ETpot, Tair and rH were also measured insitu at the EC stations SE, RO, WU1 and WU2. Averaged over these four stations, Tair from Cosmo-REA6 coincided very well with in-situ Tair ( $R^2 = 0.99$ ); the same applies to rH ( $R^2 = 0.88$ ) and modeled ETpot ( $R^2 = 0.93$ ). SWI was combined from two different sources without data overlap but both sources also agree well with in-situ measurements (Heliosat: R<sup>2</sup> of 0.96; MODIS: R<sup>2</sup> of 0.92). However, we assume that MODIS-based vegetation indices did not capture smallscale vegetation structures well and hence contributed to prediction errors. A possibility to improve vegetation data to inform the RF model would be to use remote sensing data with a higher spatial resolution such as Sentinel-2 (Drusch et al., 2012), which was not used here because it did not cover the whole investigation period. Another limitation of our study comprises the exclusion of 20.4% of the land area from the analysis because anthropogenic fluxes were not measured. This high proportion results from the high population density in the northern part of the catchment and the relatively large (13 km<sup>2</sup>) Inden open pit mine. However, only small biospheric net fluxes are to be expected from these areas as they are to a large extent non vegetated and thus may not contribute much to the overall biospheric fluxes of the catchment.

The results indicate that smaller data sets incorporating only few (< 6.25%) or no low-quality intervals in the aggregated daily fluxes are more beneficial than larger data sets with more low-quality data. Small data sets can increase overfitting of a predictive model, however the ensemble characteristic of RF of averaging multiple trees also counteracts overfitting. Thus, it seems reasonable for RF to select for small data sets with higher quality. Although a standardized quality-flag scheme was used on the TERENO-data set, it should be noted that quality-flagging is not fully standardized in the flux-community yet. Thus, our thresholds may not be transferable to other schemes.

As uncertainty is correlated with flux magnitude, filtering the FLUXNET data by small relative uncertainties has the side-effect to favor large NEE values and discriminate small ones, whereas quality flags are not correlated with magnitude. However, the distribution of the TERENO NEE magnitudes shows that, naturally, small fluxes occur much more frequent than large fluxes (Fig. 4.3c). Such imbalanced data is a problem for RF, which requires about equally sized domains in the training data to not overpredict the largest domains (Krawczyk, 2016; Torgo et al., 2015). Therefore, favoring large fluxes in the FLUXNET data improves their representation in the training data sets. The test data sets, however, consisting only of quality-flag filtered data, remained unbiased and are thus regarded suitable for model cross validation. Even so, Figure 4.3c shows that the maximum around NEE=0 in the training data was still overpredicted and rare domains underpredicted, indicating that the training data probably was still not balanced enough.

The performance differences between BFE and FFS can partly be explained by local optima of variable subsets, as sequential feature selection algorithms are prone to being trapped in such local optima (Liu & Motoda, 2008). In these cases, the first local optimum trap for BFE is much closer or even identical to the absolute optimum than the first local optimum trap for FFS. Hence, a BFE is regarded superior in such cases. The relatively high variance between RF model runs increased fluctuations and can thus amplify this effect by creating artificial local optima, leading to a suboptimal variable selection. Averaging five model runs reduced the variance within 100 model runs by about 76%, generally leading to more robust results. However, it should be noted that variance between model runs can be lower for other machine learning algorithms and that repeating and averaging is computationally expensive and therefore not suitable for large numbers of variables to select from. For such cases, a genetic algorithm like GHGA (Jung & Zscheischler, 2013) may be more appropriate.

The relatively high elevations of forests and grasslands in the catchment resulted in lower average annual temperatures in years 2010-2018 (coniferous forests: 8.9 °C, deciduous forests: 9.6 °C,

grasslands: 9.5 °C) compared to croplands (10.8 °C), and hence a later start of the growing season might be an explanation for croplands being an earlier  $CO_2$  sink. Deciduous trees, on the other hand, first need to build-up the canopy leaf area to utilize suitable conditions for photosynthesis, though having higher photosynthetic capacities when fully leafed. However, differences between land cover types were less pronounced in upscaled results than in actual measurements (Table 6). One explanation for this might be mixed pixels in MODIS EVI (250 m spatial resolution) containing spectral responses from different land cover types.

The catchment was a slightly stronger CO<sub>2</sub> sink in spring than in summer. Lindroth et al. (2008) stated that net CO<sub>2</sub> uptake in Swedish spruce forests is shifted toward the earlier parts of the growing season because respiration was still low while radiation was already high. Managed grasslands on the other hand, usually are cut several times during summer. For example, Rollesbroich was cut three times in the growing season of 2013 (Borchard et al., 2015) and each defoliation had the potential to turn grassland temporally into a CO<sub>2</sub> source (Wohlfahrt et al., 2008). Croplands showed the largest decrease of CO<sub>2</sub> uptake in late summer. Schmidt et al. (2012) analyzed vegetation parameters of a winter wheat field in the catchment over the course of two years. LAI of living/green leaves reached the maximum in early May, plant senescence (LAI of brown leaves) already started in late April and reached its peak in July. Although these patterns can differ for other crops, the results still indicate that specific croplands uptake the most CO2 in spring. The EC aggregations in Table 6 further confirm a decrease of CO<sub>2</sub> uptake in summer for croplands and grasslands. In comparison, the aggregated EVI of the whole Rur catchment started slowly increasing in late February, peaked in early June, and declined afterward. Graf et al. (2020) showed that the exceptional drought and heat across Central Europe during the 2018 growing season resulted in a reduced net CO<sub>2</sub> uptake for many drought-affected EC stations, including SE, RO and WU1. The whole catchment was predicted to be a significantly weaker CO₂ sink in summer 2018 (-0.89 g C m<sup>-2</sup>d<sup>-1</sup>) compared to 2010-2017 (-2.16  $\pm$  0.45 g C m<sup>-2</sup>d<sup>-1</sup>). Whereas in spring 2018 the sink capacity decrease to 2010-2017 was less distinct (-1.92 g C  $m^{-2}d^{-1}$  in 2018 compared to -2.16  $\pm$  0.51 g C m<sup>-2</sup>d<sup>-1</sup> 2010-2017), indicating that the seasonal averages may be influenced by one exceptional year. In view of these findings, we consider the seasonal variations of upscaled NEE as largely plausible.

# 4.5 Conclusion

In this study, we scaled up daily EC NEE data to the regional scale at 250 m spatial resolution with a RF model integrating remote sensing and reanalysis data. Furthermore, we evaluated the impact of feature selection and NEE data quality-quantity balance on the model performance. We conclude that upscaling results can be improved with a BFE to remove unnecessary predictors and by incorporating no or only small (< 6.25%) amounts of low-quality intervals in the aggregated daily NEE data. Therewith, we provided a data-driven approach for predicting spatial NEE data sets which can be used for assessing the  $CO_2$  uptake of heterogeneous local and regional ecosystems or calibrating and validating process-based models. However, the spread of NEE observations and differences between land cover types were underestimated.

Vegetated parts of the Rur catchment acted as a  $CO_2$  sink between 2010 and 2018 with about -0.65 g C m<sup>-2</sup>d<sup>-1</sup>. The catchment was predicted to be a slightly stronger sink in spring than in summer probably partly due to the onset of plant senescence in summer in cropland and grassland ecosystems, while it was a  $CO_2$  source during fall and winter. In future work, a model incorporating emissions from urban and built-up areas should be implemented to produce spatially continuous NEE data sets. Furthermore, remotely sensed vegetation products with a higher spatial resolution are likely to improve model accuracy as they would allow to distinguish small-scale vegetation structures.

# 4.6 Data Availability Statement

Data used in this study are freely available from the TERENO (https://www.tereno.net/ddp/) and TR32 (https://www.tr32db.uni-koeln.de/) FLUXNET2015 database portals, the (https://fluxnet.org/data/fluxnet2015-dataset/), the LP DAAC Catalog (https://lpdaac.usgs.gov/), the German Weather Service (ftp://opendata.dwd.de), the **EUMETSAT** Navigator (https://navigator.eumetsat.int/start), and CGIAR-CSI (http://srtm.csi.cgiar.org/srtmdata/). Upscaled daily NEE data for the Rur catchment are stored at <a href="http://doi.org/10.5281/zenodo.3776011">http://doi.org/10.5281/zenodo.3776011</a>.

# 4.7 Acknowledgements

The eddy covariance data set used in this study was contributed by within the projects TERENO and the collaborative research centre TR32 funded by the DFG (Deutsche Forschungsgemeinschaft). In particular, we thank the Meteorological (Jan Schween, site RU1), and the Geographical Institute (Karl Schneider, site ME) of the University of Cologne, the Institute of Environmental Meteorology of the University of Trier (Uwe Baltes, Clemens Drüe, Günther Heinemann, site WU1) for hardware and maintenance assistance as well as Daniel Dolfus, Nicole Adels, David Symanzik and Martina Kettler, Agrosphere Institute of the Forschungszentrum Jülich, for maintenance and calibration. We also thank Alexander Knohl (University of Göttingen), Christian Bernhofer (TU Dresden) and Christian Brümmer (Thünen Institute) for providing data to the FLUXNET2015 data set. We thank Ladislav Šigut and one anonymous reviewer for very helpful comments during the review process, which improved the manuscript substantially.

# 5 Effects of Measurement Height and Low-Pass-Filtering Corrections on Eddy-Covariance Flux Measurements Over a Forest Clearing with Complex Vegetation

Oliver Reitz<sup>1</sup>, Alexander Graf<sup>2</sup>, Marius Schmidt<sup>2</sup>, Gunnar Ketzler<sup>1</sup>, Michael Leuchner<sup>1</sup>

This chapter was originally published as the following article: Reitz, O., Graf, A., Schmidt, M., Ketzler, G., & Leuchner, M. (2022), Effects of Measurement Height and Low-Pass-Filtering Corrections on Eddy-Covariance Flux Measurements Over a Forest Clearing with Complex Vegetation. *Boundary-Layer Meteorology*, 184, 277–299. https://doi.org/10.1007/s10546-022-00700-1

As the first and corresponding author, OR together with AG designed the research framework, conducted the field experiments with the lower EC system with the help of all co-authors, and processed and primarily analyzed the flux data. OR further designed the structure and content of the article and wrote the manuscript with input from all co-authors.

#### **Abstract**

Flux measurements over heterogeneous surfaces with growing vegetation and a limited fetch are a difficult task, as measurement heights that are too high or too low above the canopy adversely affect results. The aim of this study is to assess implications from measurement height in regard to low-pass filtering, footprint representativeness, and energy balance closure for a clear-cut site with regrowing vegetation of varying height. For this, measurements from two open-path eddy-covariance systems at different heights are compared over the course of one growing season. Particular attention is paid to low-pass-filtering corrections, for which five different methods are compared. Results indicate significant differences between fluxes from the upper and lower systems, which likely result from footprint differences and an insufficient spectral correction for the lower system. Different low-pass-filtering corrections add an uncertainty of 3.4% (7.0%) to CO<sub>2</sub> fluxes and 1.4% (3.0%) to H<sub>2</sub>O fluxes for the upper (lower) system, also leading to considerable differences in cumulative fluxes. Despite limitations in the analysis, which include the difficulty of applying a footprint model at this study site and the likely influence of advection on the total exchange, the analysis confirms that information about the choice of spectral correction method and measurement height changes are critical for interpreting data at complex sites.

<sup>&</sup>lt;sup>1</sup> Physical Geography and Climatology, RWTH Aachen University

<sup>&</sup>lt;sup>2</sup> Agrosphere Institute, IBG-3, Forschungszentrum Jülich

# 5.1 Introduction

With the establishment of the eddy-covariance technique over wide ranges of ecosystems and applications, more research is focused on sites with non-ideal heterogeneous characteristics (Griebel et al., 2020; Chu et al., 2021). This challenges basic assumptions of the method and can imply unknown modifications on measured fluxes as well as reducing the energy balance closure (Stoy et al., 2013). Furthermore, internal boundary layers form over surfaces with heterogeneous roughness or a limited fetch. It has been shown that they alter wind and friction velocity ( $u_*$ ) profiles depending on the type of roughness transition (Jegede & Foken 1999; Dellwik & Jensen 2005). However, most footprint models, such as the one after Kljun et al. (2015), do not consider these non-ideal conditions inducing horizontally heterogeneous flow.

A particular difficulty is the growth of vegetation, which demands a regular adjustment of the measurement height to ensure flux contributions from the same source area (Munger et al., 2012). Sensors too far above the canopy are susceptible to measured contributions from fluxes originating outside the area of interest when the fetch is limited (Gash 1986; Nicolini et al., 2017). In addition, steep roughness changes, such as forest edges, can induce recirculation areas behind the edge (Detto et al., 2008), further constraining the available fetch for measurements in forest clearings. On the other hand, multiple issues can result from measurements too close to the canopy. Measurements within the roughness layer may not be representative of the average ecosystem, rather sensors detect a nearfield contribution of individual roughness elements leading to flux biases (Katul et al., 1999; Moureaux et al., 2012). Over inhomogeneous surfaces, a small source area resulting from a measurement height below the blending height can also induce a location bias, which is not representative of the average ecosystem flux (Schmid & Lloyd 1999). Lastly, spectral attenuation in the high frequency range, also called low-pass filtering (LPF), is expected to increase with a lower height of eddy-covariance sensors. This increase occurs because smaller eddies, which prevail closer to the ground, are more attenuated than larger eddies by individual LPF causes. For open-path systems, these causes mainly are sensor separation, time response, and path averaging (Burba 2013). A number of correction schemes exist to compensate for LPF, such as fully analytical methods modelling individual sources of attenuation (e.g., Moore 1986; Moncrieff et al., 1997; Massman 2000), in situ methods incorporating scalar spectra (e.g., Ibrom et al., 2007; Fratini et al., 2012), and fully experimental methods using the ratio of cospectral densities (e.g., Su et al., 2004; Polonik et al., 2019). Despite the availability of a variety of approaches and corresponding software packages, which in turn have different options, only a few studies have conducted a comparison of different LPF corrections (Fratini and Mauder 2014; Polonik et al., 2019), and no comparison of multiple corrections exists. Different LPF corrections are deemed suitable for specific set-ups. For example, Ibrom et al. (2007) proved good performance of their method for measurements taken high above a rough forest surface, while Fratini et al. (2012) showed improvements of their method for measurements taken low over a smooth clover field. For measurements taken low over a regrowing clear-cut area, the contribution of high-frequency turbulence likely is important too, but in such a case the surface is comparatively rough. Thus it has to be investigated if the method of Fratini et al. (2012) also performs well compared to other corrections for such conditions.

Besides previous research at the deforested site of this study (Wiekenkamp et al., 2016, 2019; Ney et al., 2019), observations at a single height focusing on carbon budgets have been conducted at wind-thrown sites, either for the growing season following a storm (Lindroth et al., 2009) or long term (Lindauer et al., 2014; Matthews et al., 2017). Vickers and Mahrt (2006) investigated mean vertical

motions above a forest clearing, indicating horizontal divergence. Peltola et al. (2015) analyzed the spatial representativeness of CH<sub>4</sub> fluxes over extensive and homogeneous grassland, while Nicolini et al. (2017) measured fluxes at two heights above a fetch limited crop field. However, the influence of measurement height on fluxes over heterogeneous surfaces with limited fetch, such as forest clearings, is still not sufficiently known.

For this study, we added an eddy-covariance system at a second height of 5.4 m to an already existing one at 2.7 m above a deforested site, which has a relatively inhomogeneous surface created by undisturbed vegetation growth. We hypothesize that (i) flux data from the old and new measurement heights can seamlessly be used together to estimate the cumulative carbon uptake and evapotranspiration from the clear-cut area, and (ii) the choice of LPF correction methods available in EddyPro© significantly affects flux results. In this respect, we also evaluated the performance of each method for data with high expected flux loss.

#### 5.2 Materials and Methods

# 5.2.1 Site Description

Measurements took place at the upper Wüstebach catchment, located in the Eifel National Park near the Belgian border (50.50305 N, 6.33596 E, 618 m elevation; see Fig. 5.1). The site is part of the TERENO (TERrestrial Environmental Observatories) Eifel/Lower Rhine Valley observatory, which is one of four observatories in Germany to analyze long-term impacts of climate and land-use changes (Zacharias et al., 2011). Mean annual precipitation is 1332 mm and mean annual temperature 7 °C during the reference period 1981–2010 (Ney et al., 2019). Cambisols are the dominant soil type in the north-eastern part of the study area, whereas Gleysols and Histosols prevail in a boggy area in the southern part and near the stream (Bogena et al., 2015). Elevation within the target area ranges between 596 m at the outflow of the Wüstebach stream in the north-west, and 628 m at the eastern edge, with an average slope of 4°.

The site mostly consisted of spruce monoculture (Picea abies and Picea sitchensis) until 2013, when an 8.6 ha area of it was cut to allow for natural succession towards a European beech forest. The only major exception to this were isolated alder stocks near the stream, which were not cut. The eddycovariance station is located approximately in the center of the clear-cut with the forest edge closest to the north and north-east, with a minimum distance of 72 m, and farthest to the west, with a maximum distance of about 292 m (see Fig. 5.1a). Only 3% of the original biomass remained on site (Baatz et al., 2015), mostly tree stumps, litter, and a few tree trunks. In 2020, the vegetation of the clear-cut area consisted of various grasses (e.g., Deschampsia spec., Molinia spec.), shrubs and bushes of different size (e.g., Cytisus scoparius, Calluna vulgaris, Epilobium angustifolium), and young trees (Sorbus aucuparia, Betula pubescens, Picea abies), some of which are typical pioneer species. In general, regrown vegetation inside the fence, which had been established against browsing damage, was denser than outside. After the 2020 growing season, young trees within the clear-cut had an average height of 1.60  $\pm$  0.89 m. The spruce trees demarcating the forest edge had a uniform height of about 25 m and measured alder trees near the stream heights between 8.0 m and 18.3 m. These characteristics resulted in a very heterogeneous study site with vegetation of different height and composition and scattered coarse woody debris, which is expected to result in heterogeneous source and sink areas for CO<sub>2</sub> and energy fluxes.

The site heterogeneity can be further characterized by flow tilt angles, calculated as  $\tan^{-1}(W/U)$ , where W is the vertical wind component and U is horizontal wind speed during neutral conditions (z/L

< 0.1, where z is the measurement height and L is the Obukhov length) and U > 1 m s<sup>-1</sup>. For flow tilt angles shown in Fig. 5.2a, we applied a yaw rotation on unrotated u and v wind components to include both horizontal wind components in U. Positive flow tilt angles prevailed from western wind directions and likely originated from the sloping terrain. On the other hand, negative flow tilt angles from the north and northeast possibly originated from the nearby forest edge. Figure 5.2b shows flow tilt angles after the application of a sector-wise planar fit rotation of wind components after Wilczak et al. (2001) for each 45° sector. Here, flow tilt angles were largely diminished, especially for the prevailing western wind directions. A significant influence of the alder trees is not evident, which might be attributed to the fact that the lower elevation next to the creek prevents the tree tops from protruding considerably above the canopy surface around the station and on the far side of the creek. Issues with the northern wind sector between about 325° and 025° are indicated by large  $u_*$  discrepancies between the upper and lower system from the north after planar fit rotation (Fig. 5.2c), indicating distortions from the nearby forest edge on the measurements at the upper height.

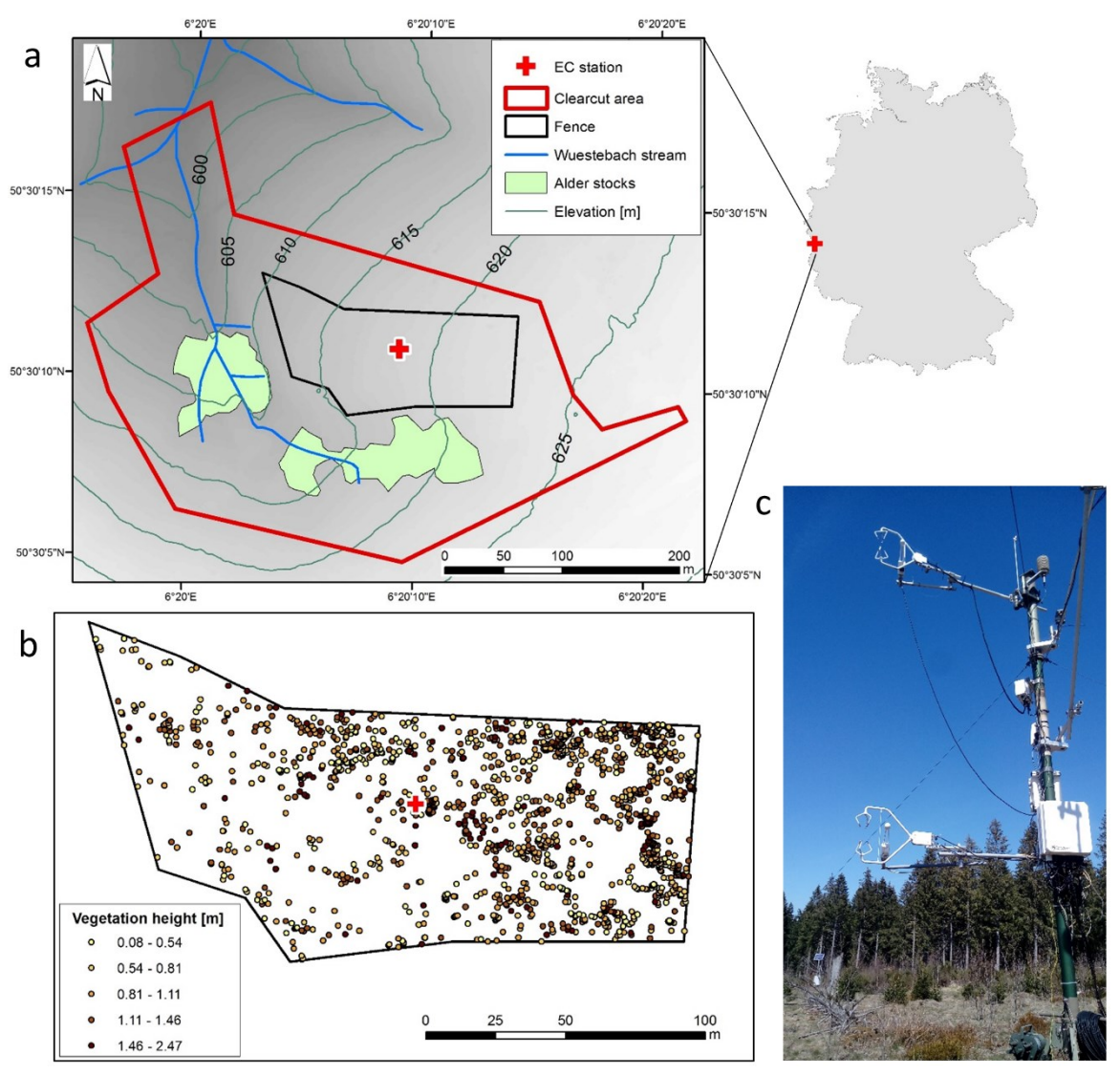


**Figure 5.1** Location of the study area in EPSG:32632 (a), vegetation heights of woody plants from a 2017 vegetation mapping in inside the fence (b), and view of the eddy-covariance (EC) tower looking north (c).

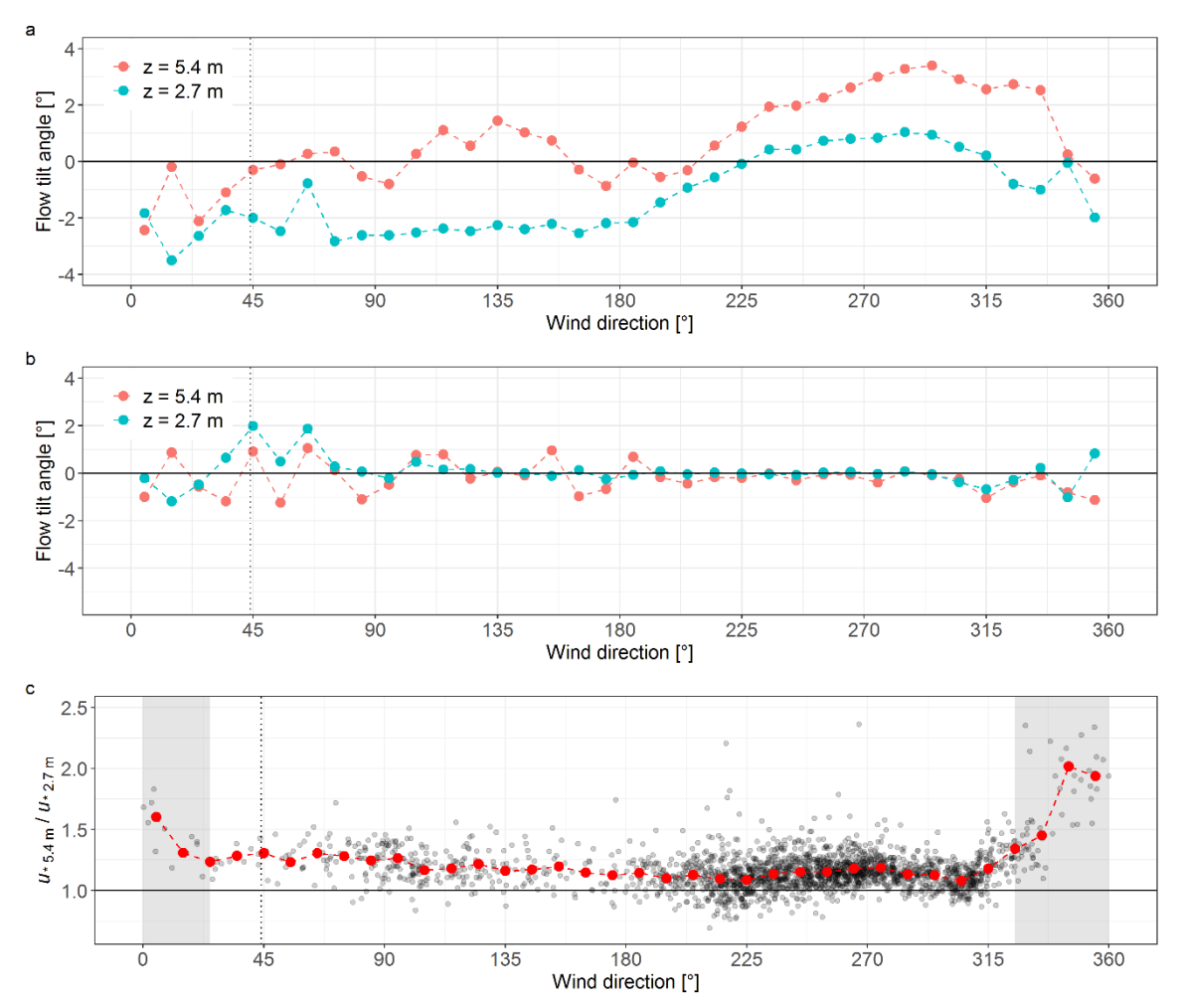


Figure 5.2 Binned means of flow tilt angles by wind direction during near-neutral conditions calculated from yaw-rotated wind components (a) and after application of a sector-wise planar fit rotation (b), as well as the  $u_*$  ratio between the upper and lower system after planar fit rotation, with binned mean values displayed in red and the distorted sector shaded in grey (c). Vertical dotted lines indicate the direction of the tower.

# 5.2.2 Eddy-Covariance Set-Up and Processing

Turbulent fluxes of latent heat  $(\lambda E)$ , sensible heat (H), and  $CO_2$  have been measured at the study site with an eddy-covariance system since 2013. In April 2020, a second eddy-covariance system was established to replace the first one at its current height of 2.7 m, which in turn was moved to a new height of 5.4 m due to vegetation growth. The upper system consisted of a CSAT3 sonic anemometer (Campbell Scientific, Logan, Utah, USA) and a LI-7500 open-path gas analyzer (LI-COR, Lincoln, Nebraska, USA). The lower system also consisted of a CSAT3, and a LI-7500RS open-path gas analyzer, which features optical hardware improvements compared to the LI-7500. Both systems had an orientation of 224°, while the upper system had a sensor separation of 22 cm and the lower system of 19 cm to account for higher LPF. In addition, a net radiometer (NR01, Hukseflux Thermal Sensors, Delft, Netherlands) at 4.54 m and two heat flux plates (HFP01, Hukseflux Thermal Sensors, Delft, Netherlands) at -8 cm were installed to provide 10-min averages of net radiation and soil heat flux. Measurements taken between 17 April and 30 September during the 2020 growing season were analyzed for this work.

Raw data of wind components (u, v, w), sonic temperature  $(T_s)$ , and  $H_2O$  and  $CO_2$  densities logged at 20 Hz were corrected and processed to 30-min fluxes using the software EddyPro© (v7.04, LI-COR, Lincoln, Nebraska, USA). A sectorial planar fit rotation for 45° sectors after Wilczak et al. (2001) was applied for tilt correction of an anemometer misalignment and to account for inclination of the ground (see Fig. 5.2). Time lags between the anemometer and gas analyzer were compensated for with the Covariance maximization with default method, which uses a default value if no covariance maximum can be attained within a time-lag window. A high-pass-filtering correction (Moncrieff et al., 2004) was applied to account for attenuation resulting from block averaging. As LPF is expected to have a stronger impact on the lower system, emphasis was put on LPF correction methods. Hence, all five methods implemented in EddyPro© were selected and compared. These are the corrections after Moncrieff et al. (1997), Massman (2000) and Massman (2001), Horst (1997), Ibrom et al. (2007), and Fratini et al. (2012) (hereafter referred to by the first authors' names). A short description of each method and their implementation in this study is given in the next section. Lastly, the density correction of Webb et al. (1980) was added to the fluxes and the 0-1-2 flagging policy after Mauder and Foken (2004) was applied. The latter includes spike removal, a steady state test, and a test on developed turbulence after Foken and Wichura (1996). Fluxes were further separated for daytime conditions based on sunrise and sunset times to exclude several potential problems at night, such as advection and drainage flows (Aubinet 2008). Besides that,  $u_*$  filtering implemented in the REddyProc library (Wutzler et al., 2018) was applied to remove remaining low-turbulence data. Furthermore, data from the northern wind sector between 325° and 025° were fully excluded because of likely distortions from the nearby forest edge (see Fig. 5.2c). Finally, data were rejected for which the source area originated to less than 70% inside the target area (see Sect. 2.5). For further analysis, only such timestamps were considered, for which the respective flux had the highest quality (flag 0) and all further criteria were also met simultaneously at both systems.

Surface heat correction for the LI-7500 of the upper system after Burba et al. (2008) was not applied because the correction was intended for vertically adjusted sensors while the gas analyzers had an inclination of 45°. Furthermore, errors from self-heating are expected to be significant during very cold conditions (< -10 °C) whereas only data during the growing season were analyzed here. Ney et al. (2019) previously compared annual sums of surface heat corrected and uncorrected net ecosystem exchange values at this site, and also opted for uncorrected fluxes.

# 5.2.3 Low-Pass-Filtering Correction

Out of the five methods applied here, the ones after Moncrieff and Massman are fully analytical, meaning that filtering is described as individual spectral transfer functions, which are deduced from a priori knowledge of the system's properties, such as sensor separation, the instruments' time responses and path lengths, atmospheric conditions, and site characteristics. Flux attenuation is then estimated using a cospectral model, i.e., after Kaimal et al. (1972), as a reference of ideal cospectra. The method after Horst is also based on an analytical formulation but is parametrized using an in situ assessment of the system's cut-off frequency with measured spectra. The methods after Ibrom and Fratini rely on an empirical determination of the cut-off frequency from the ratio of ensemble gas spectra to ensemble normalized temperature spectra as a proxy of ideal gas spectra. For the Ibrom method, the correction factor is then parametrized using the cut-off frequency, average wind speed, and atmospheric stratification. The Fratini method uses this parametrization in a slightly different way only for small fluxes. For large fluxes, the correction factor is calculated using the cut-off frequency

and sensible heat cospectrum instead. The resulting correction factor of each method is then multiplied by the uncorrected flux to correct for spectral attenuation.

For the corrections after Horst, Ibrom and Fratini, binned (co)spectra were calculated for every 30 min using EddyPro©. They were filtered according to the statistical tests after Vickers and Mahrt (1997), the micrometeorological quality tests after Mauder and Foken (2004), and by friction velocity ( $u_* > 0.2 \, {\rm m \ s^{-1}}$ ) and flux magnitude ( $H > 20 \, {\rm W \ m^{-2}}$ ;  $\lambda E > 20 \, {\rm W \ m^{-2}}$ ;  $CO_2$  flux  $> 2 \, {\rm \mu mol \ m^{-2} \ s^{-1}}$ ) before they were ensemble averaged for unstable stratifications (-650 < L < 0; predefined in EddyPro©). For all correction methods and gas spectra, the frequency range for fitting the in situ transfer function was set from 0.005 to 2 Hz. As the methods after Ibrom and Fratini compensate for LPF on the scalar signal only and thus do not account for sensor separation, the correction after Horst and Lenschow (2009) was applied in addition. However, it was only applied for crosswind and vertical wind components, as along-wind sensor separation was already compensated by the time delay correction using covariance maximization. In addition, H cospectra were preliminarily corrected for small losses due to anemometer path averaging and time response before using them for the Fratini method.

# 5.2.4 Energy Balance

The energy balance closure was calculated for each 30-min interval to estimate the performance of different spectral corrections and to compare the flux results of the upper and lower system. Ideally, the sum of sensible and latent heat flux measured by an eddy-covariance system should equal the available energy, that is net radiation minus ground heat flux and energy stored in the air and biomass (Wilson et al., 2002). Hence, the equation is

$$R_n - G - P - S = H + \lambda E, \tag{Eq. 5.1}$$

where  $R_n$  is the net radiation, G is the ground heat flux, P energy used for photosynthesis, and S the change of energy stored in the air below the eddy-covariance measurements. As measurements were taken relatively close to the surface, S was neglected for this study. P was also not measured but can be considered small compared to the other terms (Oncley et al., 2007). The terms H,  $\lambda E$ , and  $R_n$  were measured directly, and G was assessed by correcting the soil heat flux for the estimated change in heat stored between the soil surface and the heat-flux plate according to Graf et al. (2020). Two energy balance parameters were calculated on a 30 min basis: i) the energy balance ratio (EBR) as the sum of turbulent fluxes divided by the available energy and ii) the energy balance closure (EBC) as the regression between the sum of turbulent fluxes and available energy. Here, a reduced major axis regression was used instead of an ordinary regression. In this way it is possible to handle likely random errors of available energy by evaluating the slope as the geometric mean of an ordinary regression and one with switched dependent and independent variables (Wilson et al., 2002). For net radiation, the maximum error was estimated at about 25 W m<sup>-2</sup> (Kohsiek et al., 2007).

# 5.2.5 Footprint Estimation

Prior to footprint determination, roughness length  $z_0$  and displacement height d were first estimated for each wind direction quadrant using wind velocities from the two systems during neutral conditions (z/L < 0.1). This was done by solving the logarithmic law after  $z_0$  and d according to the Integrated Surface Flux System Guide (UCAR/NCAR 1990):

$$d = z_1 - \frac{z_2 - z_1}{\exp(k(U_2 - U_1)/u_*) - 1}$$
 (Eq. 5.2)

$$z_0 = \frac{z_2 - z_1}{\exp(kU_2/u_*) - \exp(kU_1/u_*)}$$
 (Eq. 5.3)

where k is the von Kármán constant (0.41),  $U_1$  and  $U_2$  the wind speeds at measurement height  $z_1$  and  $z_2$ , and  $u_*$  the mean of both heights. Values for d ranged from 1.07 m (north-east), 0.61 m (south-east), 0.53 m (south-west) to 0.51 m (north-west), and for  $z_0$  from 0.29 m (north-east), 0.16 m (south-east), 0.24 m (south-west) to 0.18 m (north-west). The relatively small values for d compared to  $z_0$  generally match the patchy structure of the study area well.

The two-dimensional footprint model of Kljun et al. (2015) was then applied to estimate the footprint for both heights for every 30 min, as well as a footprint climatology over the whole timeframe. The planetary boundary-layer height was hereby derived according to Appendix B in the respective paper. To analyze modelled source area differences between the two systems, footprint rasters for individual 30 min at the lower system were subtracted from the ones at the upper system in order to achieve patterns displaying if a pixel was more important for the upper or for the lower system. Two datasets were then created, for which negative (positive) pixels were set to 0 and remaining values converted to absolute values to show only pixels that were more important for the upper (lower) system. Lastly, the datasets were averaged over all timesteps to two raster images.

#### 5.3 Results

# 5.3.1 Spectral Analysis

Ensemble cospectra for the upper and lower system were calculated after the time delay correction was applied and are displayed in Fig. 5.3 for unstable conditions. Figure 5.3a and 5.3c show a clear attenuation of w'C' and w'q' cospectra at high frequencies (where C and q are the  $CO_2$  and  $H_2O$  mixing ratios) compared to  $w'T_S'$  cospectra at both systems. The  $w'T_S'$  cospectra can be used as reference cospectra because the sonic temperature is considered as an unfiltered scalar although it is also affected to a small extent by LPF due to path averaging and limited time response of the anemometer (e.g., Ibrom et al., 2007). Hence, the ratio of gas cospectra divided by  $w'T_s{}'$  cospectra gives an experimental transfer function describing the spectral loss of  $CO_2$  and  $H_2O$  fluxes. Both cospectra, w'C'and w'q', start diverging from  $w'T_S'$  cospectra already at lower frequencies for the lower system compared to the upper system (Fig. 5.3b, d), resulting in a larger frequency loss and a higher demand for correction. The integral of w'C' cospectra in the inertial subrange (vertical lines in Fig. 5.3a, c) is 67% of the  $w'T_S'$  cospectra integral for the upper system. For the lower system, this share is only 60%. Furthermore, ensemble sonic temperature spectra have a maximum density at 0.014 Hz for the upper system and at 0.02 Hz for the lower system, demonstrating a shift to higher frequencies for turbulent fluxes at the lower measurement height and thus a higher susceptibility to LPF. Likewise, the infinite impulse response filter cut-off frequency after Ibrom et al. (2007) is 1.1 Hz for the upper system and 1.0 Hz for the lower system.

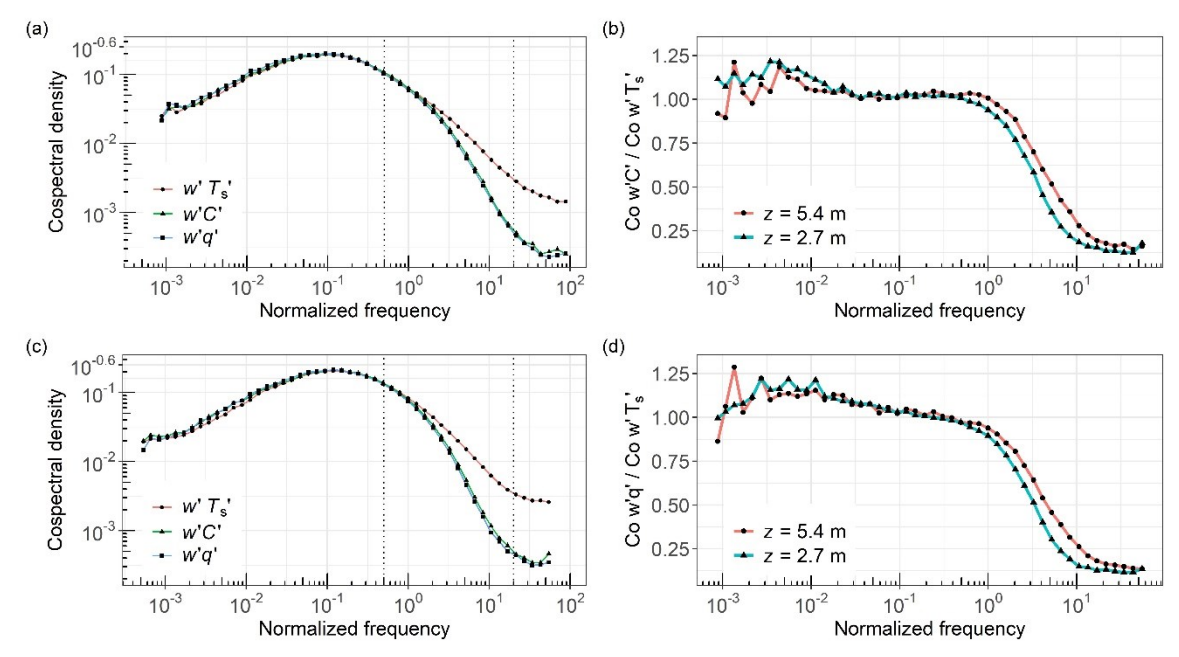


Figure 5.3 Ensemble cospectra (Co) during unstable conditions of fluxes measured at the upper system (a), and at the lower system (c), as well as the ratio between w'C' and w'Ts' cospectra (b), and w'q' flux and w'Ts' cospectra (d). The normalized frequency is the natural frequency in Hz multiplied with z and divided by U. Vertical dotted lines indicate the range used for calculating integrals.

#### 5.3.2 Correction Factors

Correction factors of the five applied spectral correction methods for  $CO_2$  fluxes of the upper and lower system are shown in Fig. 5.4. The correction factors across different spectral correction methods were similar with slightly higher values for the Fratini method. Correction factors for  $CO_2$  fluxes were on average smaller for the upper system than for the lower system, with 1.06 (Moncrieff), 1.05 (Massman), 1.06 (Horst), 1.05 (Ibrom), and 1.08 (Fratini) for the upper system compared to 1.11 (Moncrieff), 1.07 (Massman), 1.10 (Horst), 1.09 (Ibrom), and 1.15 (Fratini) for the lower system. Correction factors for  $H_2O$  were almost identical to those for  $CO_2$  and are thus not displayed separately. The outliers of high correction factors from the Moncrieff and Massman methods are associated with low U, for which the high-pass-filtering correction increased correction factors. For the Fratini method, not constraining correction factors to the bounds of Eq. 9 in Ibrom et al. (2007) but depending on the stochastic nature of turbulence by incorporating H cospectra may have led to the outliers.

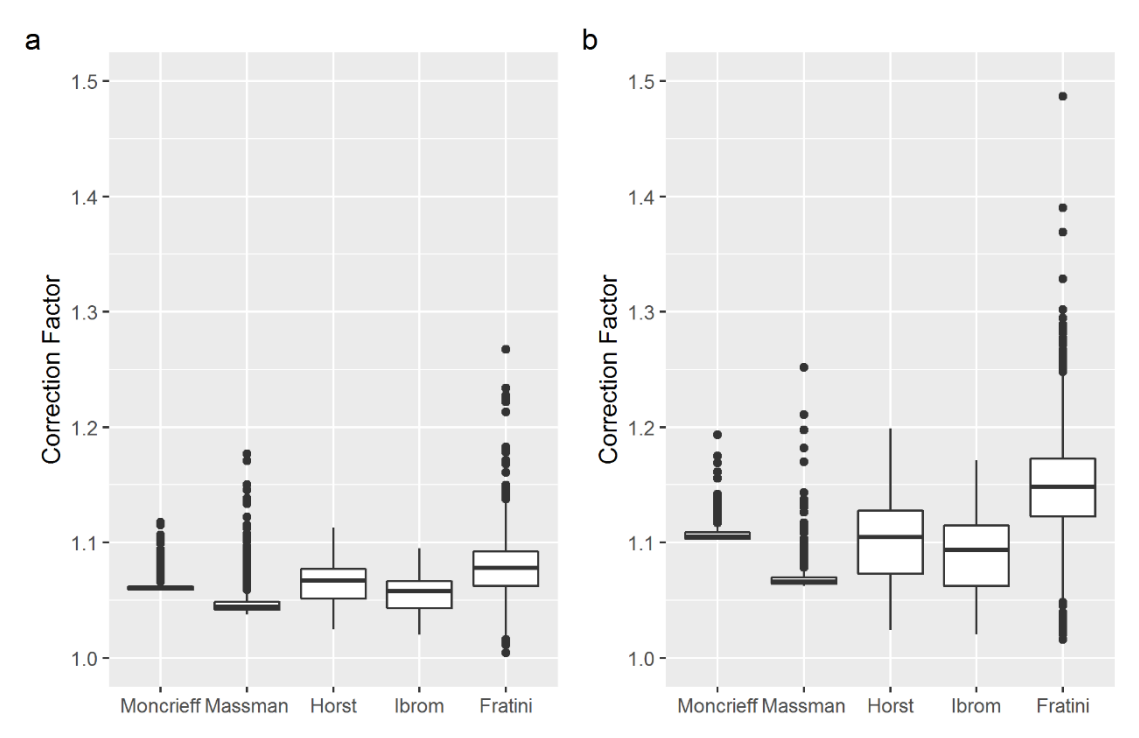


Figure 5.4 Boxplots of  $CO_2$  flux correction factors at the upper system (a) and lower system (b) for each spectral correction method.

Furthermore, U is considered an important factor for spectral attenuation as high wind speeds favour high-frequency eddies and therefore correction factors might be expected to increase with U (Moncrieff et al., 1997). The dependency of the  $CO_2$  correction factors on U is shown in Fig. 5.5 for the different LPF methods and for both systems. The correction factors after Moncrieff, Horst, Ibrom, and Fratini slightly raised with increasing U, more pronounced for the lower system than for the upper one. The correction factors after Massman, however, do not show any dependence on high U at all.

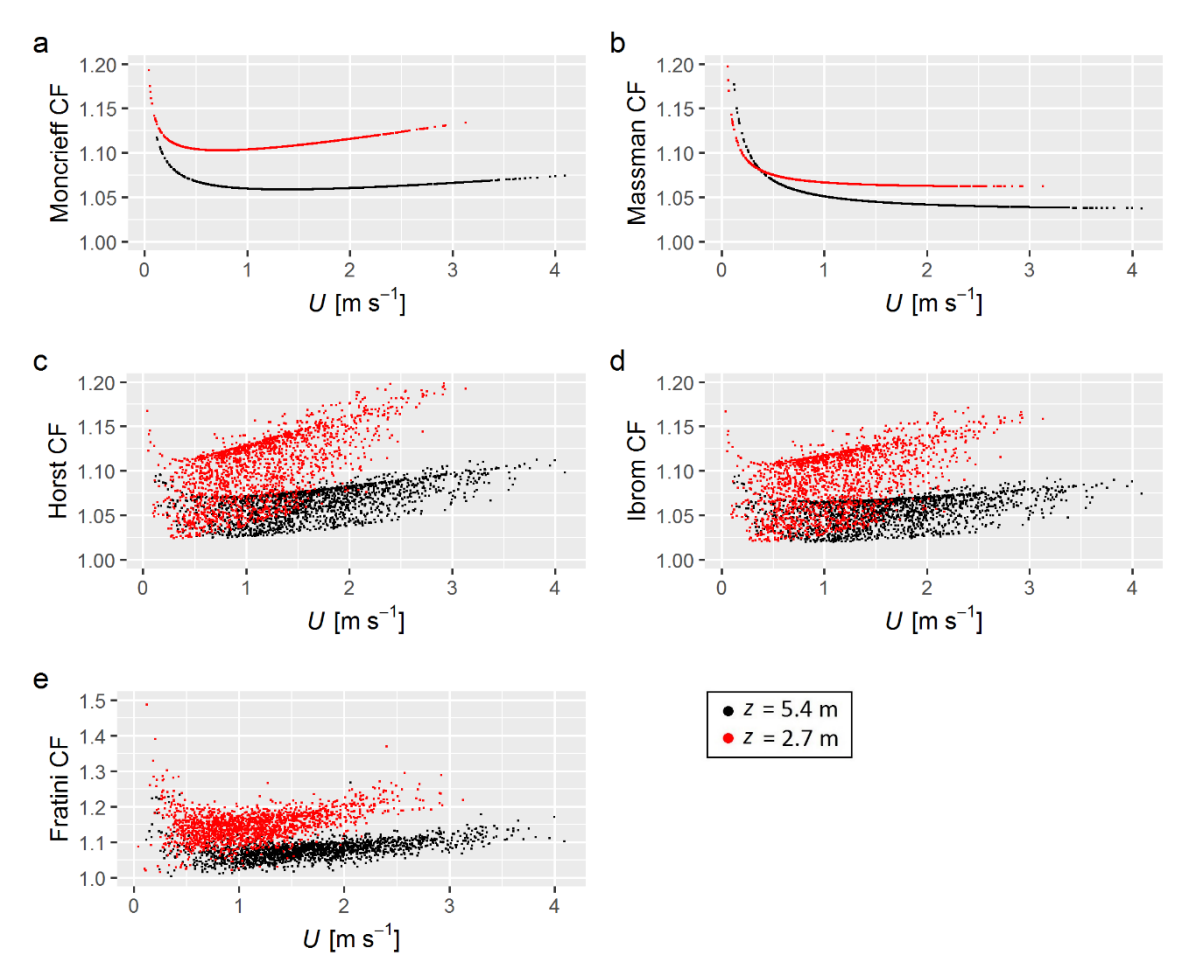


Figure 5.5 CO<sub>2</sub> flux correction factors (CF) of the low-pass filtering correction methods against wind speed (U) for the upper system (black dots) and the lower system (red dots).

# 5.3.3 Flux Results

Out of 4729 possible daytime 30 min intervals, 1992 (42%)  $CO_2$  flux data points passed the quality tests at both heights simultaneously ( $\lambda E$ : 47%; H: 47%). A substantial part of missing data does not result from quality control but is caused by a data acquisition failure of the upper system during 20 days in July. Table 1 lists mean values of LPF-corrected and uncorrected fluxes for those selected 30 min intervals. It can be noted that higher H and especially  $\lambda E$  were measured at the upper system compared to the lower one.  $CO_2$  fluxes, however, were slightly more negative at the lower system, especially after corrections were applied. As expected, uncorrected H values differ only slightly from corrected ones, whereas the  $CO_2$  flux and  $\Delta E$  differ more strongly, especially at the lower system. A reduced major axis regression between 30-min flux values of the upper and lower system corrected after Moncrieff gives slopes of 1.14 ( $R^2$  = 0.71), 1.23 ( $R^2$  = 0.93) and 1.03 ( $R^2$  = 0.97) for  $CO_2$ ,  $\Delta E$ , and H fluxes, respectively. For  $CO_2$  fluxes, the two least correlated LPF corrections were Massman against Fratini at the lower system with a slope of 0.86 and an  $R^2$  of 0.95. The average Bowen ratio is 0.83 for the upper system and 0.98 for the lower system.

**Table 5.1** Mean daytime values of 30 min H,  $\lambda E$ , and  $CO_2$  fluxes that passed the quality tests for both systems and each LPF correction method with cumulative fluxes in parentheses. For  $CO_2$ ,  $u_*$ -filtered night-time values are also given.

	None	Moncrieff	Massman	Horst	Ibrom	Fratini
Upper System						
H [W m <sup>-2</sup> ]	89.9	90.4	91.0	90.5	90.4	90.4
([MJ m <sup>-2</sup> ])	(360.5)	(362.4)	(364.9)	(362.8)	(362.4)	(362.4)
$\lambda E \text{ [W m}^{-2}\text{]}$	106.2	111.6	110.1	110.8	110.9	113.3
([MJ m <sup>-2</sup> ])	(422.5)	(444.1)	(438.1)	(441.1)	(441.3)	(450.8)
$CO_2 [\mu mol \ m^{-2} \ s^{-1}]$	-4.4	-4.8	-4.6	-4.7	-4.7	-5.0
$([g C m^{-2}])$	(-187.4)	(-205.9)	(-199.0)	(-201.8)	(-203.4)	(-213.8)
$CO_2$ night [ $\mu$ mol m <sup>-2</sup> s <sup>-1</sup> ]	4.2	4.7	4.5	4.8	4.6	4.7
$([g C m^{-2}])$	(44.8)	(49.8)	(47.9)	(50.6)	(49.1)	(50.1)
Lower System						
H [W m <sup>-2</sup> ]	88.3	89.5	89.7	89.5	89.5	89.5
([MJ m <sup>-2</sup> ])	(353.9)	(358.1)	(359.5)	(358.8)	(358.8)	(385.8)
$\lambda E \text{ [W m}^{-2}\text{]}$	86.2	94.6	91.4	94.4	93.3	98.8
([MJ m <sup>-2</sup> ])	(343.1)	(376.7)	(363.8)	(375.5)	(371.1)	(393.4)
$CO_2 [\mu mol \ m^{-2} \ s^{-1}]$	-4.8	-5.7	-5.3	-5.6	-5.5	-6.1
$([g C m^{-2}])$	(-205.5)	(-243.6)	(-227.3)	(-240.5)	(-235.8)	(-264.2)
$CO_2$ night [ $\mu$ mol m <sup>-2</sup> s <sup>-1</sup> ]	4.4	5.2	4.8	5.2	5.0	5.2
([g C m <sup>-2</sup> ])	(46.3)	(55.3)	(51.3)	(55.5)	(53.1)	(55.4)

The uncertainty induced from the choice of LPF corrections was calculated as the standard deviation between fluxes of the five LPF corrections averaged over all 30-min intervals. For CO<sub>2</sub> fluxes of the upper system, the average flux with uncertainty of the five LPF corrections was -4.75  $\pm$  0.16  $\mu$ mol m<sup>-2</sup> s<sup>-1</sup> (3.4%), for the lower system it was -5.63  $\pm$  0.35  $\mu$ mol m<sup>-2</sup> s<sup>-1</sup> (7.0%). For  $\lambda E$ , these values were 111.33  $\pm$  1.51 W m<sup>-2</sup> (1.4%) for the upper system and 94.50  $\pm$  2.91 W m<sup>-2</sup> (3.0%) for the lower system (the percentages represent the size of this uncertainty compared to the flux, averaged over all time steps). Likewise, the uncertainty from the two measurement heights was on average 24.8% of CO<sub>2</sub> fluxes and 9.7% of  $\lambda E$ , averaged over all LPF corrections. As a comparison between the two most contrasting LPF corrections, CO<sub>2</sub> ( $\lambda E$ ) fluxes corrected after Fratini were on average 7.4% (2.9%) higher than after Massman at the upper system and 16.2% (8.1%) higher at the lower system. In contrast, CO<sub>2</sub> fluxes averaged over all LPF corrections were 18.3% higher at the lower system, whereas  $\lambda E$  was 17.8% higher at the upper system. For comparison, random errors were estimated according to Finkelstein and Sims (2001) on a 30 min basis and were on average 34.2% (26.3%) of CO<sub>2</sub> fluxes of the upper (lower) system and 16.2% (10.6%) of  $\lambda E$ .

Figure 5.6 shows the frequency of the  $CO_2$  flux and  $\lambda E$  corrected after Moncrieff separated for 10° wind direction sectors. Wind generally prevailed from western directions, whereas wind from southern and especially northern directions was less frequent. For western wind directions, a slight clockwise wind direction shift from the lower to the upper system is also noticeable. At both heights, the highest average  $CO_2$  uptake was detected from wind directions between 225° and 270°, with a  $CO_2$  flux of 5.85 (-6.43) µmol m<sup>-2</sup> s<sup>-1</sup> at the upper (lower) system. The smallest  $CO_2$  uptake was recorded from 090–135° (-3.30 µmol m<sup>-2</sup> s<sup>-1</sup>) at the upper system and from 180–225° (-3.59 µmol m<sup>-2</sup> s<sup>-1</sup>) at the lower system. The highest  $CO_2$  flux differences between the two systems were recorded from 45–90°, both on average (1.14 µmol m<sup>-2</sup> s<sup>-1</sup>) and summed up (8.17 g C m<sup>-2</sup>). For  $\lambda E$ , the highest average flux was recorded from 135–180° (131.0 W m<sup>-2</sup>) at the upper system, and from 180–225° (107.3 W m<sup>-2</sup>) at the

lower system. The highest  $\lambda E$  differences between the two systems occurred on average from 135–180° (131.0 W m<sup>-2</sup>), and summed up from 225–270° (16.36 mm), as it was a more frequent wind direction.

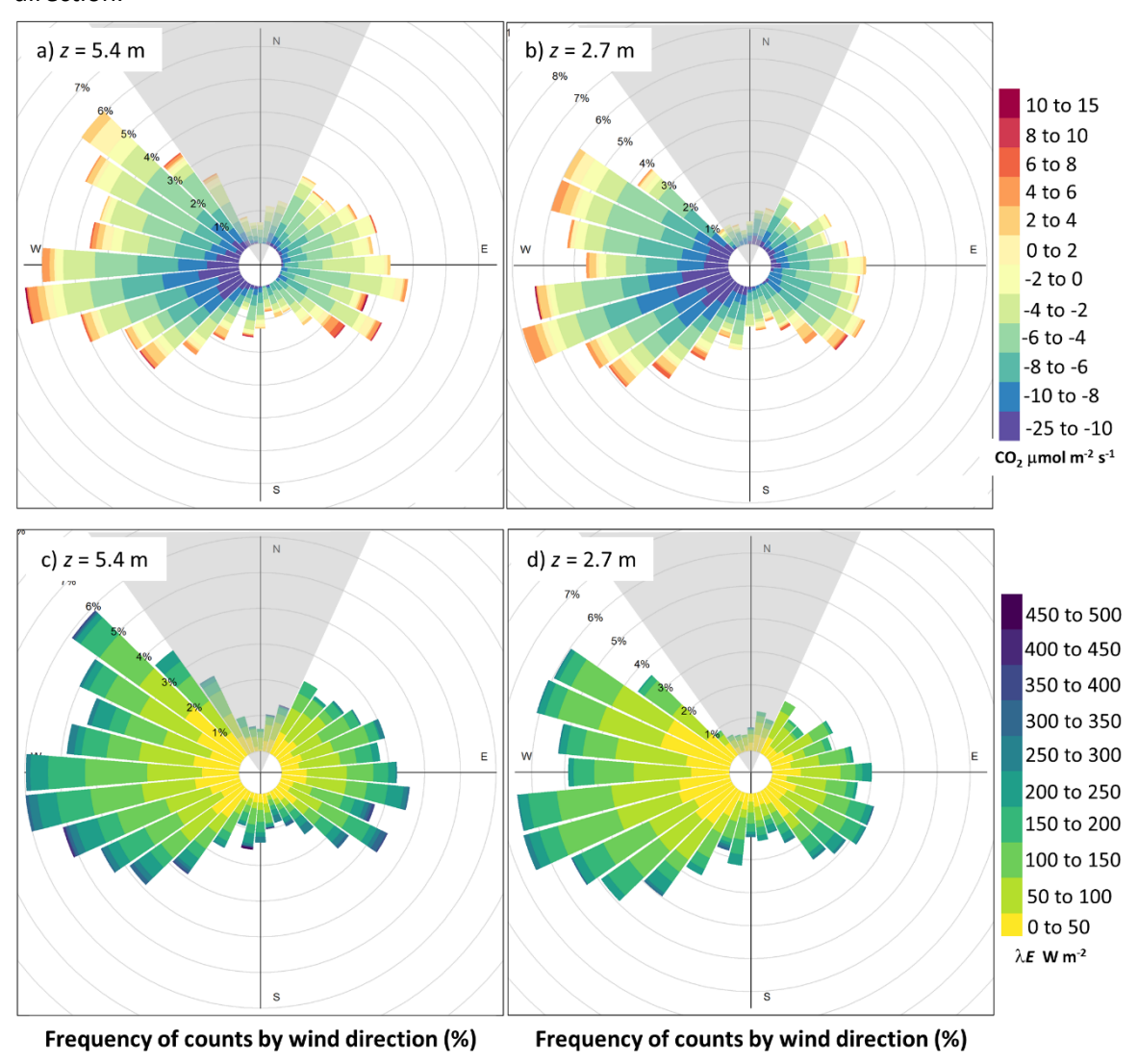
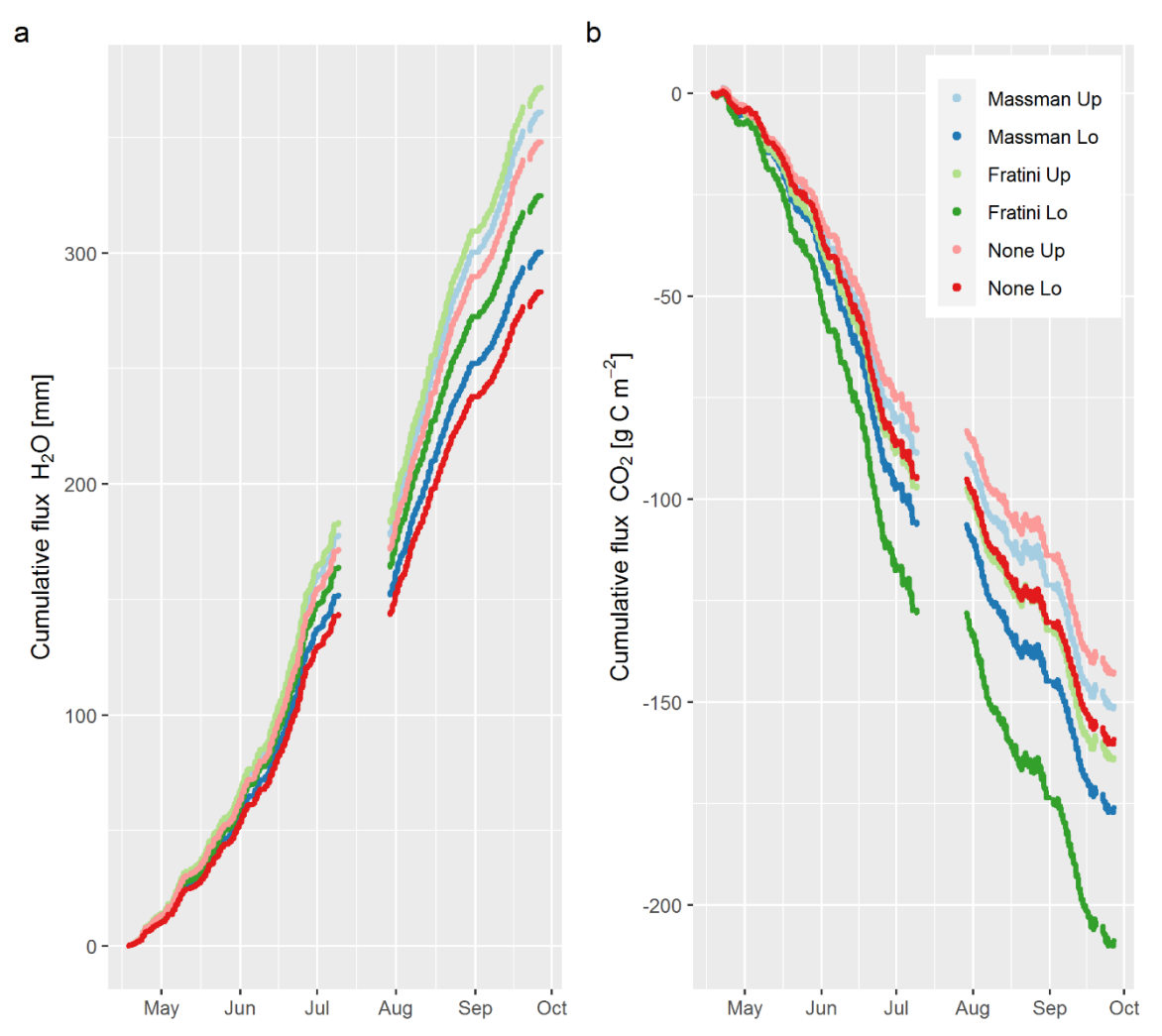


Figure 5.6 CO<sub>2</sub> fluxes and  $\lambda E$  aggregated by wind direction for the upper system (a, c) and the lower system (b, d). The shaded area indicates excluded data from northern wind directions.

Fluxes of both daytime and night-time conditions are visualized as cumulative fluxes in Fig. 5.7 for the corrections after Massman and Fratini, as examples of an analytical and an in situ method, as well as without correction. Cumulated  $H_2O$  fluxes were 23% higher at the upper system than at the lower one without LPF correction, but this discrepancy was smaller after corrections were applied (14% higher after Fratini). For cumulative  $CO_2$  sequestration, in contrast, the lower system yielded larger cumulative fluxes (12% without correction), and corrections even increased this discrepancy (28% after Fratini). The correction after Fratini produced larger fluxes than the correction after Massman of both  $CO_2$  (upper system: 8%, lower system: 19%) and  $H_2O$  (upper system: 3%, lower system: 8%). Relations between the upper and lower system and between correction schemes remained consistent over the vegetation period.



**Figure 5.7** Cumulative non gap-filled evapotranspiration (a) and CO<sub>2</sub> fluxes (b) including both daytime and night-time situations that passed quality control. Up and Lo stand for the upper and lower system, respectively.

# 5.3.4 Energy Balance Closure

An ideal EBC would be represented by a slope of 1 and an intercept of 0 from a linear regression of the sum of turbulent fluxes versus available energy, and an ideal EBR would be 1. Table 2 demonstrates that EBC and EBR were generally better at the upper system than at the lower system with a higher EBR of about 0.09, though at both heights the sum of turbulent energy fluxes was lower than the available energy. All correction methods improved the EBC as well as the EBR and had relatively similar results, with Fratini performing slightly better especially for the lower system (EBR of 0.81). However,  $R^2$  of the reduced major axis regression was slightly higher at the lower system than at the upper one.

**Table 5.2** Energy balance coefficients from reduced major axis regression, as well as its coefficient of determination ( $R^2$ ), and energy balance ratio (EBR).

	Slope	Intercept [W m <sup>-2</sup> ]	R <sup>2</sup>	EBR	
Upper System					
None	0.86	-6.8	0.91	0.84	
Moncrieff	0.88	-5.8	0.91	0.86	
Massman	0.88	-6.4	0.91	0.86	
Horst	0.88	-5.6	0.90	0.86	
Ibrom	0.88	-6.0	0.91	0.86	
Fratini	0.89	-6.4	0.91	0.87	
Lower System					
None	0.77	-6.4	0.94	0.75	
Moncrieff	0.81	-4.7	0.93	0.79	
Massman	0.80	-5.5	0.94	0.77	
Horst	0.80	-4.7	0.93	0.79	
Ibrom	0.80	-5.1	0.93	0.78	
Fratini	0.83	-6.7	0.92	0.81	

# 5.3.5 Footprint

The footprint climatology estimations are displayed in Fig. 5.8 and show footprints for the upper system extending about 2.5 times as far from the tower than for the lower system. The 90% cumulative footprint contour line contains forest outside the target area, whereas the 90% line of the lower system is still within the target area. Only 0.8% of all 30 min intervals of the lower system originated to less than 70% within the target area, whereas for the upper system that value was 4.2%. When considering daytime conditions only, these values dropped to 0.1% for the lower system and 0.2% for the upper system. A 70% threshold was used for flux filtering to be in line with a previous study at the research site (Ney et al., 2019), discarding all affected values from the further analysis. The general shape of the footprints extends in the east–west direction, with long upwind distances resulting from prevailing winds from western directions.

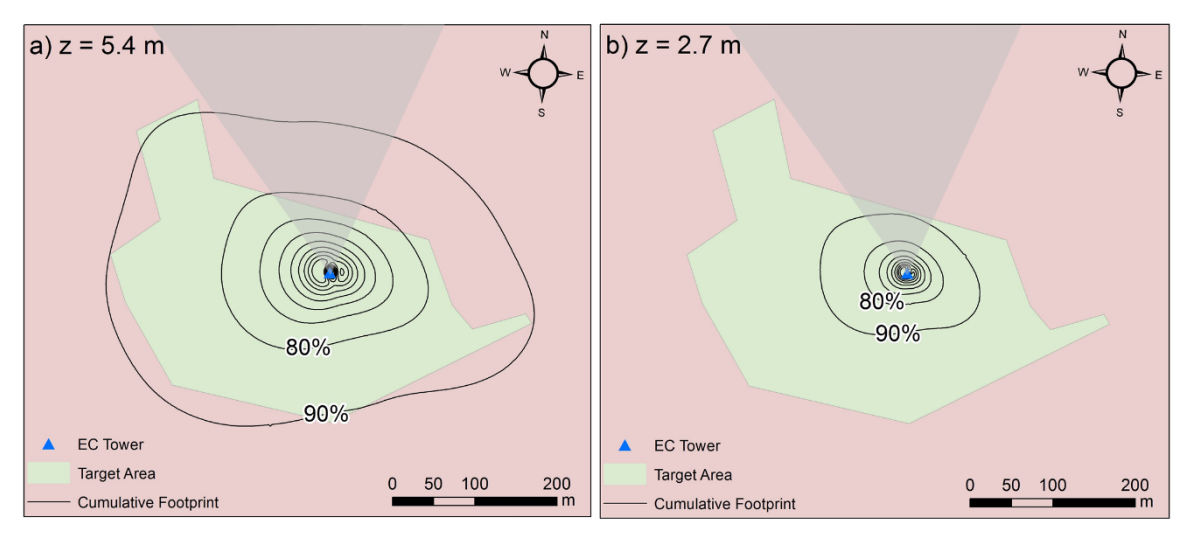


**Figure 5.8** Cumulative flux footprint estimates for daytime situations and all wind directions of the upper system (a) and the lower system (b) in 10% steps from 10 to 90%. The shaded area indicates excluded wind directions for data filtering.

Wind direction changes between the upper and lower system are expressed in the averaged footprint differences between the two systems (Fig. 9). The upper system recorded more wind from northwestern and north-eastern directions, while the lower system recorded more wind from western and south-eastern directions. The relatively large wind frequency differences between the heights from north-western wind directions, however, did not yield to analogous  $\lambda E$  or  $CO_2$  flux differences from these directions. The modelled results further indicate that source area differences between the two systems mostly originated from within the fence not farther than about 130 m from the tower, while the area in the direct vicinity (< 20 m) around the tower was more important for the lower system.

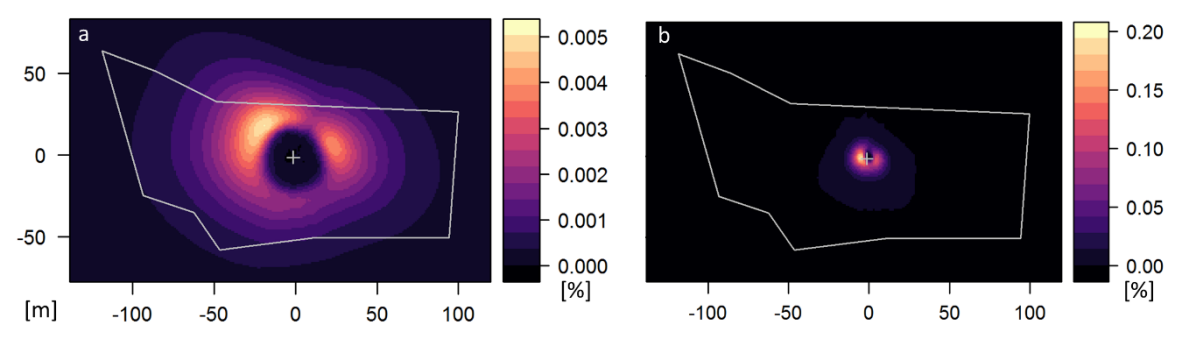


**Figure 5.9** Relative importance of pixels more important for the upper system (a) and pixels more important for the lower system (b), without observations from north. Please note the different colour scales for the subplots, which were expedient to visualize the relatively smaller importance of individual pixels in (a) compared to (b). The coordinate origin is at the eddy-covariance station and the white line delineates the fence for orientation.

# 5.4 Discussion

# 5.4.1 Assessment of Measurement Height

The higher daytime CO<sub>2</sub> uptake observed at the lower system despite lower evapotranspiration is a counterintuitive result that requires clarification. One possible explanation is that within the source area of the upper system more evaporation without accompanied photosynthesis occurs. Such an area could be the wetter and temporarily flooded Gleysols and Histosols in the southern part of the clearcut and near the stream to the west. The soil moisture measurements of Wiekenkamp et al. (2016) show that soil moisture was about 30% higher there compared to the direct vicinity of the tower in summer 2014. Furthermore, Graf et al. (2020) showed that peatlands responded with a disproportionately low ratio of CO2 uptake to evapotranspiration compared to other ecosystems during drought conditions. For the study site, this was the case in the previous two years and may have affected fluxes in 2020. Accordingly, the highest mean  $\lambda E$  and CO<sub>2</sub> flux were recorded from different wind directions, and the highest  $\lambda E$  differences between the two systems were recorded from southsouth-east on average, while cumulative differences were largest from west-south-west due to more observations from there. The ratio between CO<sub>2</sub> uptake and evapotranspiration was also the lowest from 135-180° compared to other wind directions at both systems. However, it remains not fully explained why the south-south-east sector stands out compared to south-western wind directions with similar or even wetter soil properties (Wiekenkamp et al., 2016). Figures 5.8 and 5.9 also indicate that source area differences between the two heights mostly originated from within the fence, thus not clearly demonstrating a strong influence of the boggy area outside of it. The lower system, on the other hand, could have a location bias of young, fast-growing trees located in the direct vicinity of the tower (see Fig. 5.1b), which could have increased CO<sub>2</sub> uptake there.

The energy balance could not be closed with either LPF correction for both systems but was generally better for the upper system. A number of studies demonstrated that even with very carefully applied eddy-covariance set-ups, the sum of turbulent energy fluxes remained below the amount of available energy (Foken et al., 2010; Stoy et al., 2013). It is assumed that this results from low frequency eddies not detectable by eddy-covariance systems because of a limited averaging period (Foken 2008). In addition, closure of the energy balance cannot be expected for a heterogeneous exchange surface inducing advection (Mauder et al., 2020). Hence, the lower sums of  $H + \lambda E$  compared to the available energy are in line with expectations based on previous research. Since advection could be present even in rigorously filtered data, it could have both increased or decreased the EBR at both systems. Vickers and Mahrt (2006) showed that a mass continuity approach indicated long-term sinking motions above a forest clearing. Tilt corrections such as planar fit, however, remove the mean vertical motion, hence partially not taking into account vertical advection in the flux averaging period. Such long-term sinking motions above the study area may be induced by the rough-to-smooth surface change or by drainage flows following the sloped terrain (Lee 1998). On the other hand, Vickers and Mahrt (2006) also pointed out that vertical advection of CO<sub>2</sub> based on mass continuity was a large term of net ecosystem exchange mainly on weak mixing nights, which were excluded for this analysis altogether. Besides that, the EBR discrepancies between the upper and lower system can have multiple causes. G can differ within the footprint of each system from the measurements beneath the tower as soil properties are not uniform throughout the deforested area (Bogena et al., 2015). However, it is expected that average G of the lower system's smaller footprint is more similar to measured G than that of the upper system. The same applies to possible differences in net radiation, in particular due to different surface albedos. The energy stored in the air and biomass was investigated to be negligible for similar vegetation heights (Oncley et al., 2007). If anything, the error induced by disregarding the energy storage in the air should be higher for the upper system, where the air column beneath is larger compared to the radiometer. Hence, EBC might be poorer at the lower system partially because high frequency attenuation is not fully compensated by spectral corrections, as indicated by considerably lower  $\lambda E$  at the lower system in Table 1. This raises the question of whether the CO2 flux at the lower system is likewise underestimated, given the spectral similarity between CO2 and H2O fluxes. Thus, insufficient LPF corrections at the lower system may also have contributed to the counterintuitive flux results described above.

Spectral corrections might be insufficient for the lower system because sensors are not placed high enough in the inertial sublayer. Moore (1986) stated that for his analytical correction the measurement height above d should be at least 10 times the sensor separation. For the lower system this means 2.58 m above ground, which was barely met in our case. Measurements in the roughness layer can yield the  $CO_2$  flux and  $\lambda E$  representing only local disturbances and thus being spatially variable within the same ecosystem (Katul et al., 1999). However, a precise definition of the roughness layer height and thus an appropriate measurement height is still lacking. For structurally complex ecosystems, Munger et al. (2012) recommended  $z \approx d + 4(h_c - d)$ , where  $h_c$  is the average canopy height. Since rough estimates of the average  $h_c$  are generally accepted (Rebmann et al., 2018), we calculated it as d/0.67 according to the EddyPro© manual, which results in  $z \approx 2.48$  m above ground. For shrublands, however, Munger et al. (2012) recommended a fixed height of about 6 m, which in our case was barely satisfied by the upper system. Nicolini et al. (2017) accomplished feasible measurements as low as 0.9 m above d, though over a homogeneous surface. Although these recommended heights can only be seen as very rough estimates, they indicate that the lower system might be at best at the lower end of the suitable range of z and will be in the roughness layer with further expected vegetation growth.

The footprint estimates revealed that the source area of the upper system was to a large extent within the target area and therefore only few observations were removed. However, during 2014–2017 the 90% cumulative footprint of the lower system had a maximum distance of about 200 m from the tower (Ney et al., 2019). In 2020, this distance decreased to 123 m, while the 90% footprint of the upper system had a maximum distance of about 311 m. This result indicates that the source area of both systems differed from previous observations, but with further vegetation growth it is expected that the upper system's source area will approximate that of previous measurements by the lower system. The footprint model of Kljun et al. (2015) assumes horizontal homogeneity of the flow and thus has limited applicability to the study area. The complex flow over the forest edge particularly cannot be resolved, for which large-eddy simulations or, as a less computationally intensive solution, turbulence closure models such as SCADIS would be more suited (Sogachev & Lloyd 2004). This model was also able to indicate source hotspots in contrast to analytical footprint models in heterogeneous areas (Sogachev & Dellwik 2017). A recirculation area behind the edge inducing downward flows can be expected for a distance of 2-5 times the forest canopy height (Detto et al., 2008), corresponding to a distance between 50 and 125 m at the study site. This is a problem for northern wind directions where the forest edge is within this distance, and distortion of the mean flow is indicated by much higher  $u_st$ at the upper system (see Fig. 5.2c). On the other hand, for the prevailing western wind directions, such edge turbulence effects were not detected. Roughness changes were also roughly taken into account for footprint modelling by including  $z_0$  for each wind direction quadrant. Hence, the footprint results might be useful for a first approximation of the source area and for testing spatial representativeness of the fluxes.

Despite these general considerations, the presented results strongly speak against the first hypothesis. The large differences between fluxes of the two heights (see Table 1 and Fig. 5.7) prevent a seamless use of data from both time series and likely result from a different source area within the heterogeneous clear-cut area and insufficient LPF corrections for the lower system. Instead, in any future analysis of CO<sub>2</sub> fluxes at the clear-cut, the period with two simultaneous measurements heights can be used to estimate the uncertainty from measurement height choice, which can then be compared to long-term trends or differences between sites.

# 5.4.2 Spectral Corrections

The higher average correction factors for the lower system throughout all methods are in line with the higher spectral attenuation observed there compared to the upper system (see Fig. 5.3c, d). This observed shift to higher frequencies with a lower sensor height coincides well with other experiments and well-known theoretical considerations (e.g., Moncrieff et al., 1997; Foken et al., 2012; Zhao et al., 2019). The correction factors after Moncrieff and Massman show a clear dependence on U because specific quantities of transfer functions are defined as functions of U there. However, correction factors actually decrease initially with increasing U, since attenuation dominates in the low frequency range due to block averaging at  $U < 0.5 \text{ m s}^{-1}$  but becomes less important with increasing U in unstable conditions. An insensitivity of correction factors to U can be observed for the Massman method because for open-path systems, time constant equivalents from path averaging and sensor separation decrease with increasing U, and thus were assumed to compensate the shift to high frequency eddies (Massman 2000). These comparatively small correction factors at higher wind speeds resulted in slightly smaller  $\lambda E$  and  $CO_2$  fluxes at both systems for the Massman method.

Polonik et al. (2019) concluded that the Fratini correction is not well-suited for open-path analysers because it accounts only for scalar attenuation, as it does not consider sensor separation, and therefore produced smaller fluxes than Massman. However, with the additional correction after Horst and Lenschow (2009), this limitation was not an issue for our analysis. The fluxes of the lower system corrected after Fratini had a higher magnitude and better energy balance closure compared to Massman or other methods, confirming its applicability to low measurement heights, even for a comparatively rough surface. Polonik et al. (2019) did not apply the correction after Horst and Lenschow (2009) because it produced unrealistically high correction factors in stable conditions, but in our case this correction increased the correction factor only by 0.07 for the upper system and 0.13 for the lower system during stable conditions. Nonetheless, in a few cases it added large values up to 0.7 to the correction factor. In unstable conditions, the maximum value added was 0.07 for the upper system and 0.24 for the lower system.

Fratini and Mauder (2014) found a difference of about 3% in  $\lambda E$  and CO<sub>2</sub> fluxes caused by the use of spectral corrections either after Moore (1986) or Horst (1997), which contributed most to discrepancies between flux processing in EddyPro© and TK3. In our analysis, the highest differences (16.2%) were found between CO<sub>2</sub> fluxes at the lower system corrected after Fratini and Massman. In contrast, Rannik et al. (2020) assessed that differences in fluxes from the choice of coordinate rotation were less than 10%. Nevertheless, it should be kept in mind when comparing different spectral correction schemes that spectral corrections are not the last step in the processing chain of EddyPro©, but density correction terms (Webb et al., 1980) are further added, which in addition can be implemented differently in other software (Fratini & Mauder 2014). It is also important to assess the importance of sources of uncertainty, such as measurement height and LPF correction, against the magnitude of real fluxes between sites or years that are the target of past and future studies on carbon budgets of forests and clear-cuts. For example, for annual net ecosystem exchange over the first four years after deforestation, Ney et al. (2019) found a source-towards-neutral change of 439 g C m<sup>-2</sup>, and differences of more than 600 g C m<sup>-2</sup> compared to the surrounding spruce forest. The largest differences of daytime cumulative growing season C uptake resulting from combinations of LPF correction and measurement height in our study, 65 g C m<sup>-2</sup> between Massman of the upper system and Fratini of the lower system, would not change these results fundamentally but account for a nonnegligible additional relative uncertainty.

The uncertainty resulting from the choice of LPF correction can be subsumed under systematic errors associated with data processing in the classification scheme of Mauder et al. (2013). Other sources of uncertainty include systematic errors from instrumental calibration and random errors due to changes in footprint, instrumental noise, or the stochastic nature of turbulence. Stochastic errors estimated according to Finkelstein and Sims (2001) were considerably larger than the differences induced by the choice of a LPF correction method on a 30 min basis. Over longer time periods, however, random errors are cancelled out, whereas systematic differences from LPF corrections add up, as is illustrated in Fig. 5.7. These discrepancies of different LPF corrections were stronger at the lower system, where LPF and concurrent correction factors were higher than at the upper system. Therefore, the results support the hypothesized importance of the choice of LPF correction, although flux differences between the two measurement heights were larger than even between the two most contrasting LPF corrections.

#### 5.5 Conclusion

We compared turbulent flux measurements at two heights above a clear-cut site, demonstrating the trade-offs that have to be considered when choosing the measurement height above a fetch-limited heterogeneous surface. Major limitations of these results include potential advection biasing the EBR at both heights and the limited applicability of the Kljun et al. (2015) footprint model to a study site with heterogeneous flow. However, the footprint model has shown a limited utility for estimating the influence of source and sink heterogeneities within the clearing. The upper system, with its larger footprint, is more influenced by the forest and edge turbulence effects from the northern sector, while the lower system likely lacks representativeness of the clearing and is susceptible to higher LPF. These effects resulted in significant flux discrepancies between the two heights, which oppose the first hypothesis that a seamless use of the data from both time series is acceptable. We also evaluated different LPF correction schemes. The differences between the methods after Moncrieff, Massman, Horst, Ibrom, and Fratini induced a systematic uncertainty to the fluxes, which was stronger for the lower system (CO<sub>2</sub>: 7.0%, H<sub>2</sub>O: 3.0%) than for the upper system (CO<sub>2</sub>: 3.4%, H<sub>2</sub>O: 1.4%). The flux discrepancies of the different correction methods added up over time and hence support the second hypothesis. Compared to other methods, the Fratini approach yielded higher fluxes and a better energy balance closure for the lower system. Hence, our analysis confirms that for long-term singlepoint flux observations above forest clearings, information about changes of measurement height are critical for interpreting the data, and that it is also important to consider the spectral correction method when comparing fluxes between sites.

# 5.6 Acknowledgements

The basic equipment of the Wüstebach site with measurements was funded by the TERENO project (<a href="www.tereno.net">www.tereno.net</a>). In particular, we thank Daniel Dolfus and Judith Mattes from the Agrosphere Institute of the Forschungszentrum Jülich for maintenance and calibration. We also thank Andreas Ibrom for his helpful support with data processing and three anonymous reviewers for very helpful comments, which improved the manuscript substantially. Associated data is available at <a href="http://doi.org/10.5281/zenodo.5648270">http://doi.org/10.5281/zenodo.5648270</a>.

# 6 Environmental Drivers of Gross Primary Productivity and Light Use Efficiency of a Temperate Spruce Forest

O. Reitz<sup>1</sup>, H. Bogena<sup>2</sup>, B. Neuwirth<sup>3</sup>, A. Sanchez-Azofeifa<sup>4</sup>, A. Graf<sup>2</sup>, J. Bates<sup>2</sup>, M. Leuchner<sup>1</sup>

This chapter was originally published as the following article: Reitz, O., Bogena, H., Neuwirth, B., Sanchez-Azofeifa, A., Graf, A., Bates, J., & Leuchner, M. (2023), Environmental Drivers of Gross Primary Productivity and Light Use Efficiency of a Temperate Spruce Forest. *Journal of Geophysical Research: Biogeosciences*, 128(2), e2022JG007197. https://doi.org/10.1029/2022JG007197

As the first and corresponding author, OR together with ML designed the research framework, conducted the PAR and R/FR measurements with the help of all co-authors, and processed and analyzed the data. OR further designed the structure and content of the article and wrote the manuscript with input from all co-authors.

#### **Abstract**

Various environmental variables drive gross primary productivity (GPP) and light use efficiency (LUE) of forest ecosystems. However, due to their intertwined nature and the complexity of measuring absorbed photosynthetically active radiation (APAR) of forest canopies, the assessment of LUE and the importance of its environmental drivers are difficult. Here, we present a unique combination of measurements during the 2021 growing season including eddy covariance derived GPP, sap flow, Sentinel-2 derived canopy chlorophyll content and in situ measured APAR. The importance of environmental variables for GPP models is quantified with state-of-the-art machine learning techniques. A special focus is put on photosynthesis-limiting conditions, which are identified by a comparison of GPP and sap flow hysteretic responses to vapor pressure deficit and APAR. Results demonstrate that a) LUE of the canopy's green part was on average  $4.0\% \pm 2.3\%$ , b) canopy chlorophyll content as a seasonal variable for photosynthetic capacity was important for GPP predictions, and c) on days with high vapor pressure deficit, tree-scale sap flow and ecosystem-scale GPP both shift to a clockwise hysteretic response to APAR. We demonstrate that the onset of such a clockwise hysteretic pattern of sap flow to APAR is a good indicator of stomatal closure related to water-limiting conditions at the ecosystem-scale.

#### **Plain Language Summary**

The efficiency by which a forest uses sunlight to perform photosynthesis is an important feature for climate and ecosystem modeling. However, the light that is actually captured by forests and is useable for photosynthesis is difficult to assess. Here, we show a sophisticated approach to estimate the light use efficiency of a spruce forest in Germany and analyze environmental influences on it and on photosynthesis. Our results indicate that about 4% of the light useable for photosynthesis was actually used by the forest during the 2021 growing season and that seasonal variations of chlorophyll in the canopy are a good indicator for carbon capture.

<sup>&</sup>lt;sup>1</sup>Physical Geography and Climatology, RWTH Aachen University, Aachen, Germany

<sup>&</sup>lt;sup>2</sup>Agrosphere Institute, IBG-3, Forschungszentrum Jülich GmbH, Jülich, Germany

<sup>&</sup>lt;sup>3</sup>DeLaWi Tree-Ring Analyses, 51570 Windeck, Germany

<sup>&</sup>lt;sup>4</sup>Earth and Atmospheric Sciences Department, Centre for Earth Observation Sciences (CEOS), Edmonton, Alberta, Canada

#### 6.1 Introduction

The gross primary productivity (GPP) of terrestrial ecosystems, of which forests are the dominant factor (Pan et al., 2011), is a key element of the global carbon cycle (Canadell et al., 2021). The resulting biomass further is important for human demands of food, energy, and construction materials (Taye et al., 2021). The assimilation of atmospheric CO<sub>2</sub> via photosynthesis is primarily driven by photosynthetically active radiation (PAR), though it is also sensitive to intertwined environmental and physiological variables, such as temperature, water and nutrient availability, or chlorophyll content of the canopy (Anav et al., 2015; Bao et al., 2022; Keenan et al., 2012).

The light use efficiency (LUE) concept was established by Monteith (1972) and describes how efficiently solar energy is converted to chemical energy. It can be expressed as the ratio of GPP to the absorbed PAR (APAR). Under optimal conditions, a linear relation between GPP and APAR is assumed (Monteith, 1972), and LUE models utilize this logic for estimating GPP based on APAR and sensitivity functions for environmental conditions limiting LUE (e.g., Horn & Schulz, 2011; Stocker et al., 2020; Wang et al., 2018). The shape of these functions representing the response of LUE to meteorological variables, however, varies widely between approaches (Bao et al., 2022). Although LUE models are widely used to predict GPP, such as for the MODIS GPP product (Running & Zhao, 2015), they rely on accurate APAR measurements. For most sites with GPP data, these are only available from remote sensing derived fraction of APAR (fAPAR) products (Garbulsky et al., 2010). For forest ecosystems, however, fAPAR differed among satellite products (Tao et al., 2015) and deviated from in situ fAPAR measurements, especially for temperate coniferous forests (Putzenlechner et al., 2019a). On the other hand, in situ measurements of fAPAR are laborious, especially for forest canopies, because of the high spatiotemporal variability of their light transmissivity (Leuchner et al., 2011; Vesala et al., 2000), which requires a sophisticated network of PAR sensors to capture the variability of different flux terms (Putzenlechner et al., 2019b; Widlowski, 2010). Hence, few studies investigated environmental controls of LUE for forest ecosystems based on in-situ APAR measurements (Goulden et al., 1997; Urban et al., 2012).

With climate change, a shift from energy-limited to water-limited conditions is expected for many terrestrial ecosystems (Denissen et al., 2022), making it important to accurately identify and distinguish those conditions. Vapor pressure deficit (VPD) was found to be a dominant control for stomatal conductance and, thus, for limiting photosynthesis (Katul et al., 2003; Castro et al., 2018). Sap flow sensors measure the transport of water through the xylem and in this way provide a continuous proxy of stomatal conductance (Ewers et al., 2007; Köstner et al., 1998; Steppe et al., 2015). Brinkmann et al. (2016) compared the sap flow response to drying conditions of different European tree species and showed that the sap flow of *Picea abies* was especially sensitive to limited water availability. Hence, despite being promising for analyzing limiting conditions of photosynthesis, as shown by the usefulness of sap flow to estimate GPP (Klein et al., 2016), a combination of sap flow and GPP measurements has rarely been performed to show that the tree-scale sap flow response is analogous to that of the ecosystem-scale GPP.

Furthermore, the ratio of available light in the red to light in the far-red domain (R/FR) is a measure of light quality (Ammer, 2003; Turnbull, 1991) and can adapt chlorophyll content, though a direct relation to  $CO_2$  assimilation could not be found (Heraut-Bron et al., 1999). Besides meteorological drivers, canopy nitrogen and leaf mass per area were shown to be important to explain the variation in LUE across species and environments (Green et al., 2003), though both are rarely considered in LUE models. The canopy chlorophyll content (CCC) incorporates both of these measures and showed a stronger relationship to GPP than leaf area index (LAI) or leaf chlorophyll content ( $C_{ab}$ ) alone (Croft et al., 2015).

GPP seasonality of a soybean field was further dominated by CCC, while APAR and sun induced chlorophyll fluorescence peaked about two weeks earlier (Wu et al., 2022). In view of such a plethora of environmental controls on GPP, variable importance measures of machine-learning models are a valuable tool to quantify the model importance of individual highly non-linear sensitivities that are otherwise difficult to quantify (Archer & Kimes, 2008; Grömping, 2009; Williamson et al., 2021).

For this study, a multitude of environmental data were collected for a European spruce forest, including eddy covariance derived GPP, APAR from a network of PAR sensors, sap flow of three trees, and various environmental variables including satellite derived CCC. Based on these data, our goals were threefold, to (i) assess the LUE of a spruce forest and analyze the impact of various environmental drivers on it, (ii) quantify the importance of single environmental variables for machine-learning GPP models, and (iii) identify limiting conditions of photosynthesis by linking tree-scale sap flow measurements to ecosystem-scale GPP and meteorological data.

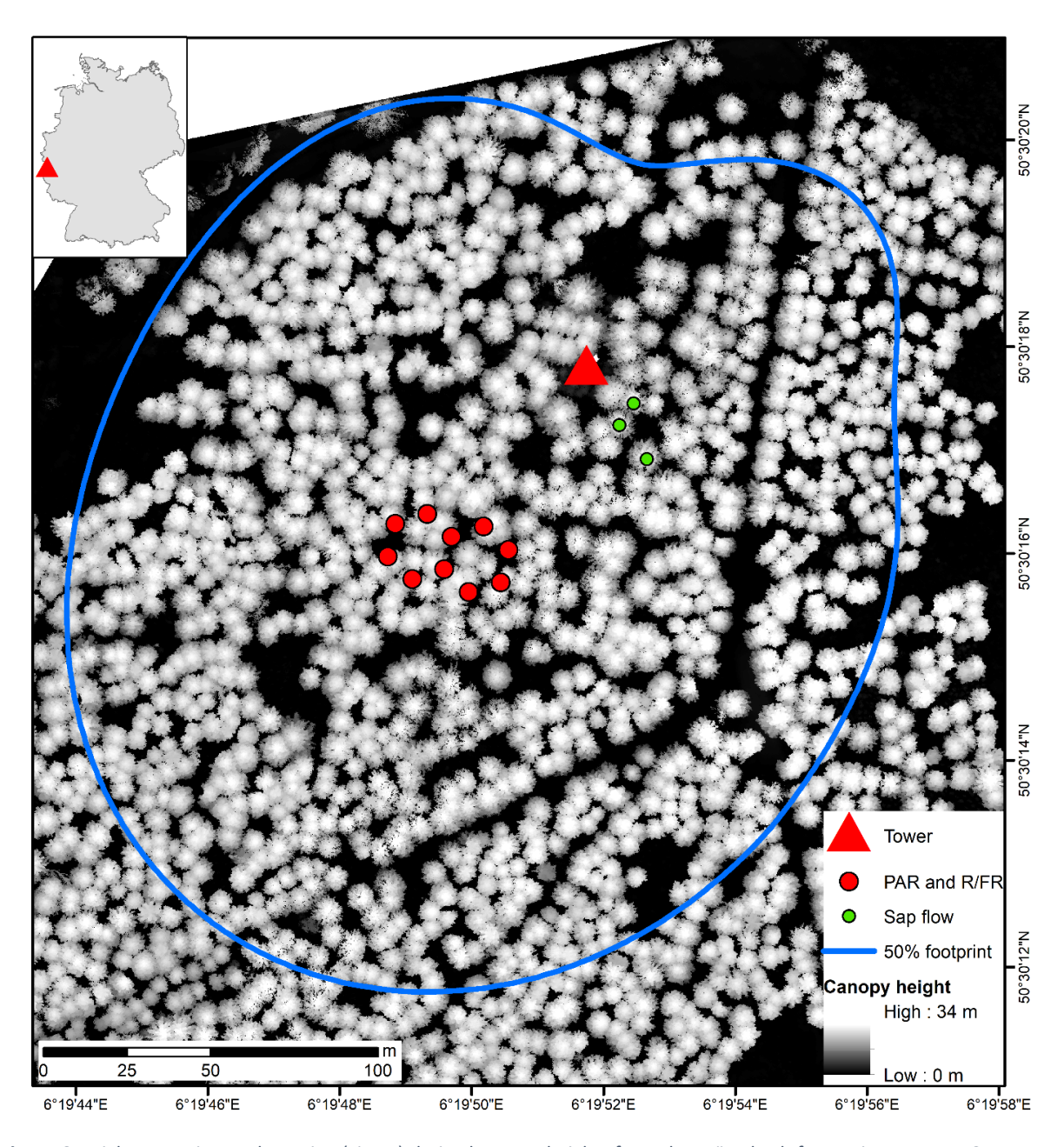


**Figure 6.1** Light Detection And Ranging (LiDAR) derived canopy heights from the Wüstebach forest site, western Germany. LiDAR data collected on a March 2022 measurement campaign and were used for visualization only.

# 6.2 Materials and Methods

# 6.2.1 Study Area Description

Measurements took place between April 28 and September 30, 2021 at the Wüstebach forest site (50°30'16"N, 6°19'50"E), Germany, which is part of the TERENO network (TERrestrial ENvironmental Observatories; Bogena et al., 2018). The forest lies at 600-620 m asl within the Eifel National Park near the Belgian border and is a spruce monoculture (*Picea abies* (L.) H. Karst.) planted in 1946 with an overall tree density of 370 trees/ha (Etmann, 2009) and an average canopy height of 25 m. The understory mostly consisted of young beech plantings (*Fagus sylvatica* L.), *Vaccinium myrtillus* L., ferns (e.g., *Struthiopteris spicant* (L.) Roth) and various mosses. The dominant soil types are Cambisols and Planosols (Graf et al., 2014) and the dominant soil textures are silt loam and silty clay loam (Borchardt, 2012). During April – September 2021 the site had a mean temperature of 12.2 °C, and received 629 mm of precipitation. At the nearest long-term official weather station Kall-Sistig of the German Weather Service, about 13 km to the east, this period was 0.6 °C colder and had 158% of the precipitation compared to the 1991-2020 averages. April and May were especially cold (-3.2 and -2.4 °C deviation, respectively) and July was especially wet (347% of average), while June was significantly warmer than average (+2.4 °C).

# 6.2.2 Eddy Covariance, Meteorological, and Sap Flow Measurements

Turbulent fluxes of CO<sub>2</sub>, water vapor and sensible heat were measured with an eddy covariance system consisting of a sonic anemometer (CSAT-3, Campbell Scientific, Logan, Utah, USA) and an open-path infrared gas analyzer (LI-7500, LI-COR, Lincoln, Nebraska) with 15 cm sensor separation. The instruments were mounted at 38 m above ground on a tower above the forest canopy (Fig 1). Raw data recorded at 20 Hz were processed to 30-min fluxes with the software TK3 (Mauder & Foken, 2011), applying the strategy for quality control after Mauder et al. (2013), which includes tests for stationarity, well-developed turbulence, and source area representativeness. Following this, only data of the highest quality (flag 0) were retained and a storage flux estimated from single point CO<sub>2</sub> measurements was added. Post-processing was carried out using the *REddyProc* software package (Wutzler et al., 2018), which includes friction velocity filtering, gap filling and partitioning of net ecosystem exchange of CO<sub>2</sub> into ecosystem respiration (R<sub>eco</sub>) and GPP. For partitioning, the method after Reichstein et al. (2005) was applied, which determines the temperature sensitivity of R<sub>eco</sub> from nighttime data and extrapolates this to daytime.

Further environmental variables used for the analysis include measurements of global radiation (I) and diffuse radiation (d) measured at 34 m (NR01, Hukseflux Thermal Sensors, Delft, Netherlands), from which the diffuse fraction (d/I) was calculated. In addition, air temperature ( $T_{air}$ ) and relative humidity (rH) were measured at 38 m (HMP45, Vaisala Inc., Helsinki, Finland), from which VPD was derived. From measurements of soil water content (SWC) in 2 cm, 5 cm, 10 cm, 20 cm, 50 cm and 80 cm depth (CS616, Campbell Scientific, Logan, Utah, USA) a root zone SWC weighted by thickness of layer was calculated as  $SWC_{AVG} = (SWC_{02}*3 + SWC_{05}*4 + SWC_{10}*7 + SWC_{20}*20 + SWC_{50}*30 + SWC_{80}*36)$  /100, where each subscript denotes the depth in cm to account for dynamic root growth (Wang et al., 2021).

As an indicator of stomatal responses, sap flow density ( $J_S$ ) was derived from three spruce trees about 20 m to the southeast of the tower (Fig. 6.1). Each tree was instrumented with a Granier sensor comprising four needles (Ecomatik SF-L, Ecomatik, Dachau, Germany), mounted at 1.5 m height, from which the average  $J_S$  of the trees was derived from the temperature difference between two probes

(Bogena et al., 2015, Neuwirth et al., 2021). The respective equation follows empirical relations (Granier, 1987):

$$J_S = 119 * \left(\frac{\Delta T_{max} - \Delta T}{\Delta T}\right)^{1.231},\tag{Eq. 6.1}$$

where  $J_S$  is the sap flow density (g m<sup>-2</sup> s<sup>-1</sup>),  $\Delta T$  is the actual temperature gradient between the two probes and  $\Delta T_{max}$  the maximum temperature gradient measured between the probes in a given time period. The length of this time period depends on the prevailing environmental conditions, because  $\Delta T_{max}$  represents a state of zero sap flow. According to the manufacturer's recommendations (Ecomatik, 2005) we identified  $\Delta T_{max}$  as the maximum  $\Delta T$  of the vegetation period representing no radial tree-trunk increment and an rH of 100% with transpiration tending to zero. With these measurements, the relationships between  $J_S$ , VPD, and APAR were then analyzed to identify energy-limited and water-limited conditions for photosynthesis.

# 6.2.3 Sentinel-2 Derived Vegetation Indices

The normalized difference vegetation index (NDVI) was used for the estimation of APAR by green vegetation and CCC was used as an indicator of photosynthetic capacity to incorporate nutrient availability and past environmental conditions, especially the delayed response of chlorophyll content to suitable meteorological conditions in the early growing season (Gitelson et al., 2014). In order to estimate NDVI and CCC, Sentinel Level-2A bottom of atmosphere images between April and October 2021 were downloaded from Google Cloud via sen2r (Ranghetti et al., 2020). A mask was applied to filter out clouds and shadows, and the images were further visually inspected to exclude scenes with undetected clouds or cloud shadows over the study area, after which 13 scenes well distributed over the growing season remained. NDVI was calculated as

$$NDVI = (B_{842} - B_{665}) / (B_{842} + B_{665}),$$
 (6.2)

where the subscript denotes the wavelength in nm of the respective Sentinel-2 band (B), i.e. band 8 (near infra-red) for  $B_{842}$  and band 4 (red) for  $B_{665}$ . For CCC, the 13 scenes were resampled to 20 m spatial resolution and processed with the Biophysical Processor in SNAP (https://step.esa.int/main/toolboxes/snap/) to yield LAI and  $C_{ab}$  products. The algorithm for biophysical variables included in SNAP consists of an artificial neural network trained with PROSAIL radiative transfer model input variables (Weiss et al., 2020). CCC was then derived by multiplying LAI with  $C_{ab}$  and for both NDVI and CCC pixel values of the woodlot were averaged. Finally, values from the 13 scenes were linearly interpolated to a daily scale.

# 6.2.4 PAR and R/FR Measurements

PAR was recorded instantaneously every 10 min with full-spectrum quantum sensors (SQ-521-SS, Apogee Instruments, Logan, Utah, USA) measuring the photon flux in the spectral range from 389 to 692  $\pm$  5 nm. The sensors' error due to temperature response is below 2% for prevalent temperatures of the 2021 growing season (5 °C–30 °C). The R/FR ratio was recorded likewise with S2-431-SS sensors (Apogee Instruments, Logan, Utah, USA) measuring red light from 645 to 665 nm  $\pm$  5 and far-red light from 720 to 740 nm  $\pm$  5 nm. All PAR and R/FR sensors were connected to the wireless sensor network SoilNet (Bogena et al., 2010). Incident PAR (PAR<sub>in</sub>) and outgoing PAR (PAR<sub>out</sub>) and incident R/FR (R/FR<sub>in</sub>) were measured with two opposite PAR sensors and one R/FR sensor above the forest canopy on a

tower at 38 m above ground (Fig. 6.1). In order to find a suitable field for measurements of transmitted PAR (PAR<sub>trans</sub>) and R/FR (R/FR<sub>trans</sub>) below the canopy, several criteria were set. According to these, the field had to be: (i) within the 50% cumulative source area of the eddy covariance station as calculated after Kormann and Meixner (2001), (ii) at least 80 m away from the forest edge to minimize the influence of lateral radiation fluxes, and (iii) representative of the general woodlot comprising the 50% footprint area in terms of canopy density. For the latter, a LiDAR (Light Detection And Ranging) point cloud from Geobasis NRW (2019) was used and the ratio of above ground to total LiDAR points for each 30-m cell of the woodlot was calculated. A representative cell was identified as being within one standard deviation from the mean ratio of the whole woodlot. Based on these criteria, a measurement field 70 m to the southwest of the tower was chosen (Fig. 6.1). There, 10 PAR sensors were mounted on tripods in 1.3 m height and arranged with 10 m distance in two hexagons to maximize the sensing area (Putzenlechner et al., 2019b) and one of these hexagons was also equipped with six R/FR sensors.

For calculating APAR, cases with PAR $_{trans}$  > PAR $_{in}$  were excluded as a sign of cloud cover only above the tower. High wind speeds can induce an increase of the sampling error of PAR $_{trans}$  measurements from a limited number of sensors during direct light conditions (Putzenlechner et al., 2019b). This sampling error is caused by the high spatial variability of forest canopies (Leuchner et al., 2011; Widlowski, 2010). Therefore, the fAPAR was calculated first and filtered for low wind speeds (< 5 m s $^{-1}$ ), and data gaps were linearly interpolated. We also considered reducing the sampling error further by filtering for diffuse light conditions (d/I > 0.9). However, important conditions such as the highest VPD typically occur during direct light conditions, and only considering diffuse light would also ignore the bowl-shaped diurnal cycle of fAPAR during direct light (Widlowski, 2010). The domain-level fAPAR was calculated as a two-flux product instead of a three-flux product because in this way the bias to fAPAR from all four flux terms is expected to be smaller (Putzenlechner et al., 2020; Widlowski, 2010):

$$fAPAR = \frac{1}{n}\sum_{i}^{n} 1 - PAR_{trans_i}/PAR_{in},$$
 (Eq. 6.3)

where i is the sensor location of each PAR<sub>trans</sub> sensor, however, without measurements from one sensor due to malfunctioning (n=9). APAR of green parts of the tree canopy was then calculated as

$$APAR_q = PAR_{in} * fAPAR * NDVI, (Eq. 6.4)$$

for which each 10-min values of PAR<sub>in</sub> and fAPAR were linked to the NDVI values of the corresponding day. NDVI was used for the proportion of green vegetation because of its normalized nature and utility in previous research to estimate APAR<sub>g</sub> (Nestola et al., 2016).

Data from the six R/FR sensors were averaged for the calculation of R/FR<sub>trans</sub>. As R/FR is strongly dependent on solar elevation and the precipitable water vapor in the atmosphere, which attenuates light in the far-red but not in the red domain (Doroszewski et al., 2015; Kotilainen et al., 2020), we also calculated the difference between the R/FR ratios above and below the canopy as  $R/FR_{diff} = R_{in}/FR_{in} - R_{trans}/FR_{trans}$  to represent the change of the spectral ratio caused by the canopy alone. All radiation data were filtered for daytime conditions (PAR<sub>in</sub> > 10  $\mu$ mol m<sup>-2</sup> s<sup>-1</sup>) and linked to GPP estimates by aggregating them to 30-min values. Finally, green LUE was calculated as

$$LUE_{q} = GPP/APAR_{q}. (Eq. 6.5)$$

#### 6.2.5 Evaluation of Environmental Drivers

LUE $_{\rm g}$  was calculated at the half-hourly scale and at the daily scale from daytime integrals of GPP and APAR $_{\rm g}$ . Half-hourly LUE $_{\rm g}$ , however, has the problem of being skewed because a ratio is more affected by changes of the denominator (APAR $_{\rm g}$ ), especially if it is low (Hedges et al., 1999). At the daily scale, the range of APAR $_{\rm g}$  was much smaller, and hence the dependence on APAR $_{\rm g}$  was not as dominant (see Fig. 6.8). For this reason it is necessary to present half-hourly LUE $_{\rm g}$  with a log10-transformed y-axis so that LUE $_{\rm g}$  is affected equally by changes of the numerator and denominator. However, Feng et al. (2014) stated to use log-transformations with caution as statistical modeling on those data may not be relevant for the original data. Therefore, we also provide an alternative approach in the supporting information, that uses deviations of GPP from a year- and site-specific optimal GPP (GPP $_{\rm opt}$ ) in relation to APAR $_{\rm g}$  instead (see Text S1 and Fig. 6.9 and 6.10).

In order to robustly quantify the importance of environmental variables for predicting half-hourly daytime GPP, two different feature importance measures based on different machine-learning algorithms were applied. First, permutation importance based on random forest (RF; Breiman, 2001), and second, SHAP values (SHapley Additive exPlanations; Lundberg & Lee, 2017) based on gradient boosting (GB; Friedman, 2002). Both RF and GB have the advantage of capturing even highly non-linear relations between target and predictors and are based on an ensemble of decision trees. For RF, all trees are grown independently with a random subsample of data, while the trees for GB are built based on the errors of the previous tree in order to minimize a loss function. The permutation importance is assessed by randomly shuffling the values of each variable and measuring the decrease in prediction accuracy. To avoid a bias from correlated predictors, we used the conditional permutation scheme of Strobl et al. (2008), where values are permuted within a grid of correlated variables. For this, we applied the latest version of this algorithm in the permimp package in R, which also considers nonlinear dependence between variables (Debeer & Strobl, 2020), based on the conditional inference trees implementation of RF in cforest (Hothorn et al., 2006). SHAP is a local method to explain the importance for individual predictions by unifying various Shapley value methods, which use equations from game theory to fairly allocate rewards. For this study, we applied SHAP via SHAPforxgboost (Liu & Just, 2021) based on the XGBoost implementation of GB (Chen & Guestrin, 2016). For both models, only non-gap-filled values were considered and hyperparameter tuning and a random 5-fold crossvalidation was conducted with caret (Kuhn, 2008). As RF and GB are subject to random variation, the procedures were repeated 10 times and results were averaged to produce more robust estimations.

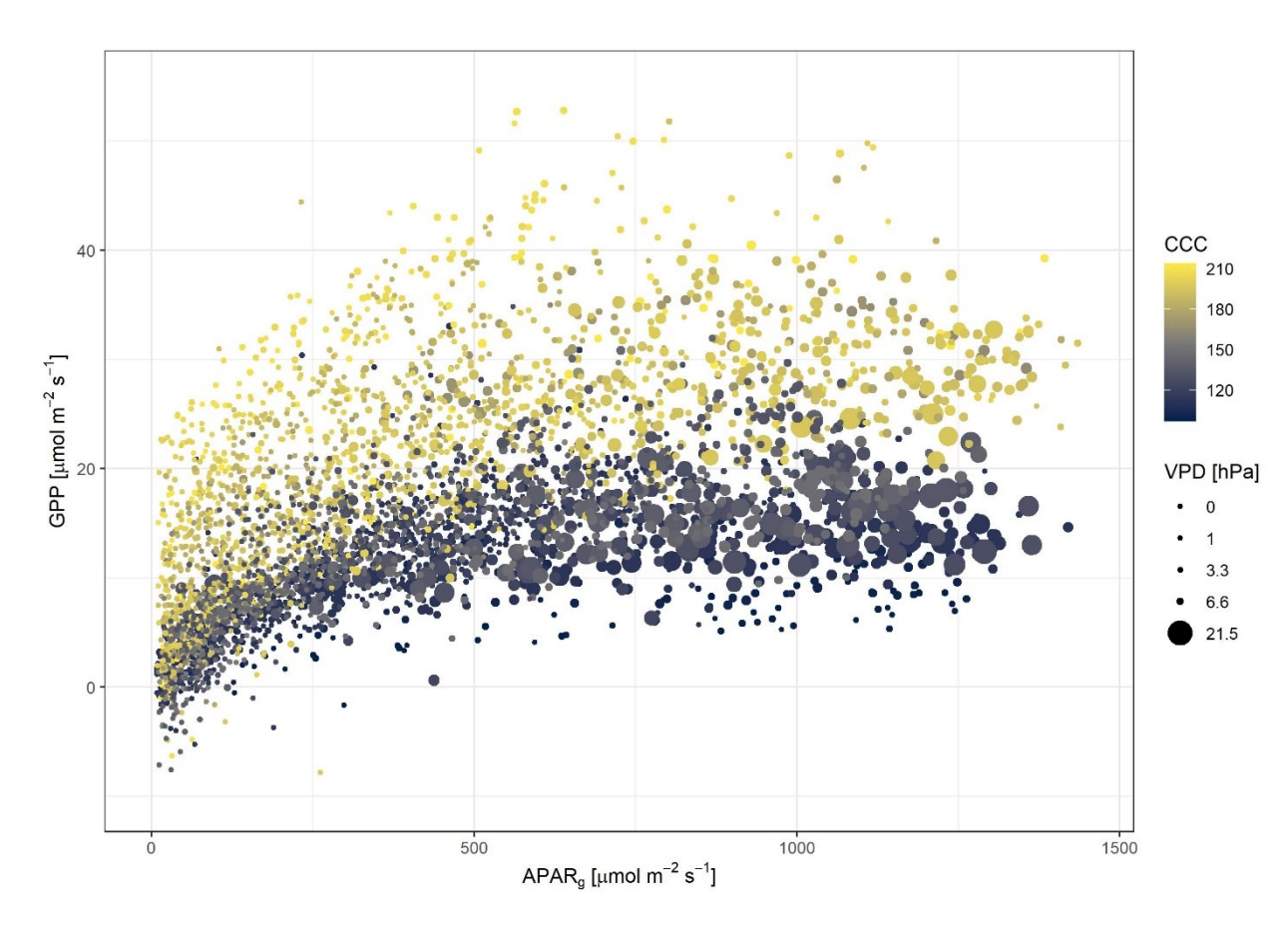


**Figure 6.2** Gross primary productivity (GPP) against green canopy absorbed photosynthetically active radiation (APAR<sub>g</sub>) during the 2021 growing season, colored by canopy chlorophyll content (CCC) and dot sizes by vapor pressure deficit (VPD).

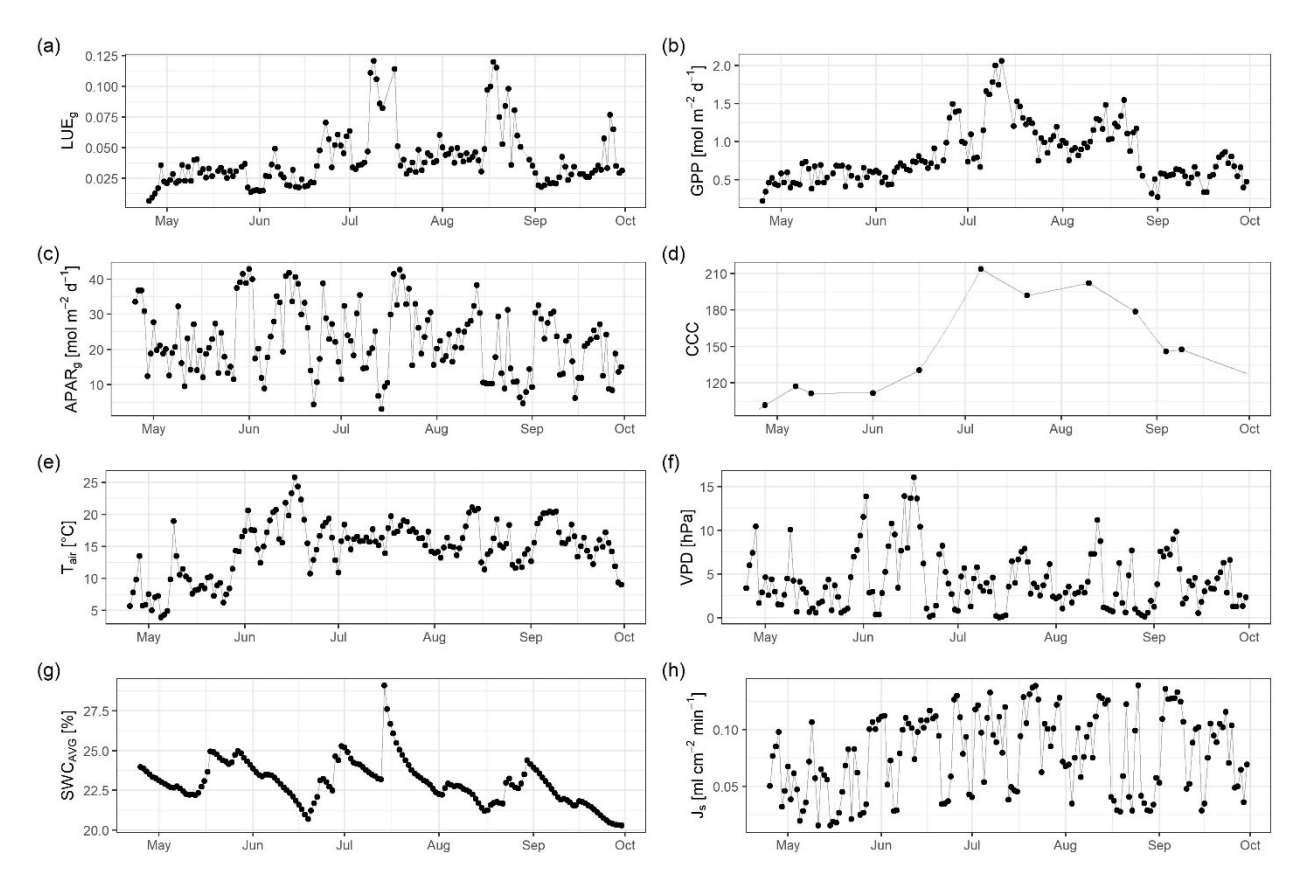


**Figure 6.3** Time series of daily averaged daytime values of (a) green canopy light use efficiency (LUE<sub>g</sub>), (b) gross primary productivity (GPP), (c) green canopy absorbed photosynthetically active radiation (APAR<sub>g</sub>), (d) canopy chlorophyll content (CCC), (e) air temperate (T<sub>air</sub>), (f) vapor pressure deficit (VPD), (g) soil water content (SWC<sub>AVG</sub>), and (h) sap flow density (J<sub>S</sub>) from April 20 to September 30. For LUE<sub>g</sub> and GPP, only those days with at least 25% non-gap-filled GPP data were considered.

### 6.3 Results

## 6.3.1 Interpretation of Environmental Drivers

The efficiency by which APAR<sub>g</sub> is used for photosynthesis is observed by a light response curve of GPP (Fig. 6.2). For each APAR<sub>g</sub> domain, a wide range of GPP values was recorded. Low GPP values at a particular APAR<sub>g</sub> corresponded well with a low CCC, indicating a limiting effect on photosynthetic capacity. In general, GPP displays an increasing trend with increasing APAR<sub>g</sub> until about 600  $\mu$ mol m<sup>-2</sup> s<sup>-1</sup>, after which a saturation of APAR occurred. The larger circles further show that many of the lowest GPP values at high APAR coincided with high VPD, most of them during a warm and dry spell in June.

The good agreement between CCC and GPP can also be seen in time series (Fig. 6.3b,c) and a scatterplot (Fig. 6.11a). In Fig. 6.3, no significant increase of GPP, LUE $_g$  or CCC can be noticed until midJune. In mid-July and mid-August, however, LUE $_g$  exhibited two marked peaks with a minimum in between. APAR $_g$  and J $_s$  had a high day-to-day variation while T $_{air}$  and VPD peaked in mid June. Over the whole research period, daily LUE $_g$  was 4.0%  $\pm$  2.3%, with daily values ranging from 0.7% to 12.1%. Out of total APAR, the LUE was 3.1% on average, and of PAR $_{in}$  just 2.8%.

In general, the response to environmental drivers was similar for half-hourly and daily LUE $_{\rm g}$ . T $_{\rm air}$  had a relatively clear optimum around 15 °C for both 30 min and daytime averages, though even around 15 °C low LUE $_{\rm g}$  values were observed (Fig. 6.4a, b). Half-hourly LUE $_{\rm g}$  was rather insensitive to VPD until it reached values above about 7.5 hPa, after which a decrease was noticeable. For daily LUE $_{\rm g}$  a similar

pattern was evident, although the decrease started at daytime averaged VPD > 3 hPa (Fig. 6.4c, d). Half-hourly and especially daily LUE $_{\rm g}$  were higher during diffuse compared to direct light conditions. Similarly, they tended to be higher when R/FR $_{\rm diff}$  was lower (Fig. 6.4e-h), meaning that the ratio was shifted comparatively less to the far-red spectrum after passing the canopy. However, neither showed a clear response to SWC $_{\rm AVG}$  (Fig. 6.4i, j).

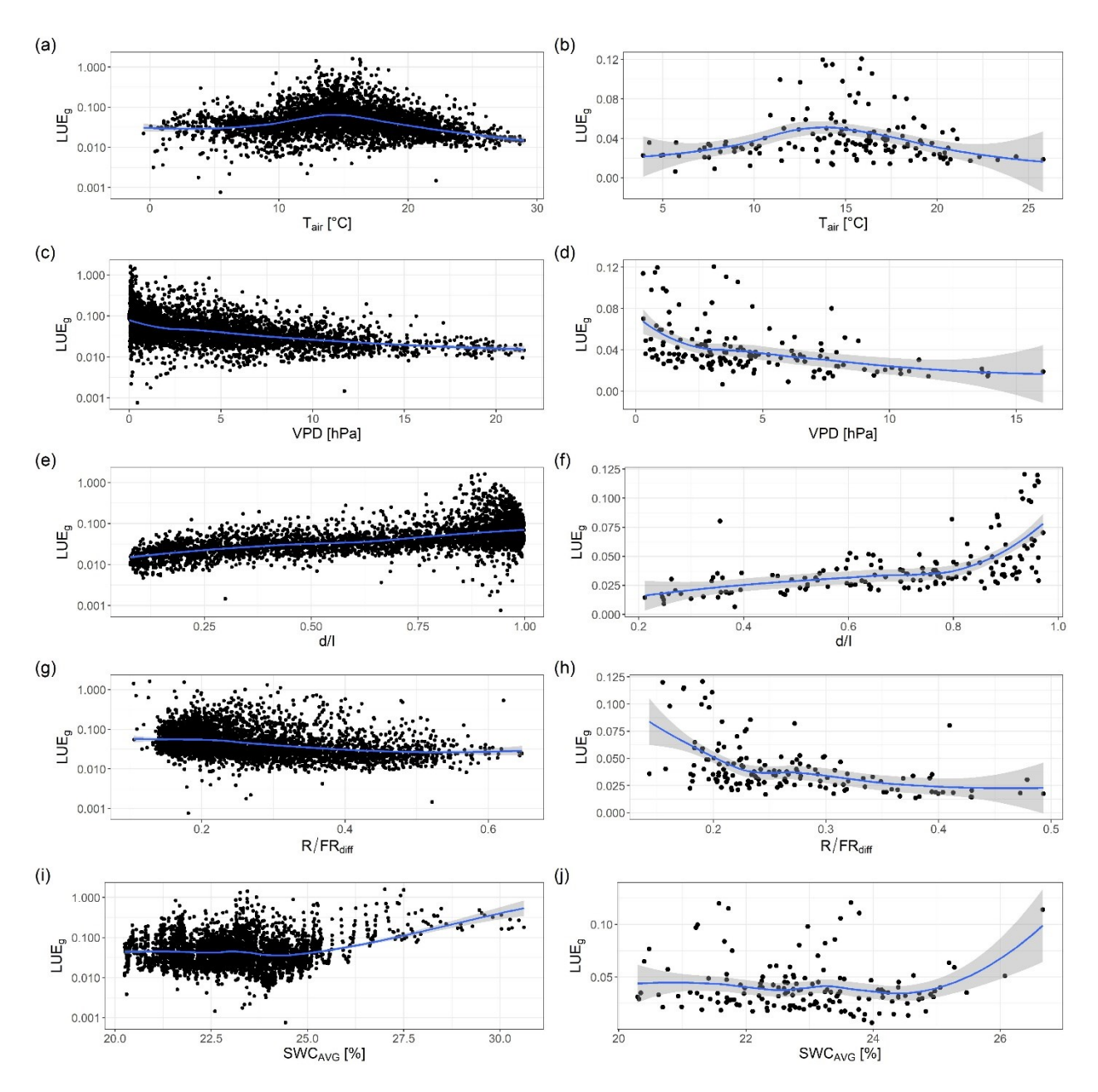


**Figure 6.4** Green canopy light use efficiency (LUE<sub>g</sub>) at a half-hourly scale with log10-transformed y-axes (left) and at a daytime scale (right) against air temperature (a,b), vapor pressure deficit (c,d), diffuse fraction (e,f), red to far-red ratio difference between above and below canopy (g,h), and soil water content (i, j), each with a LOESS (locally estimated scatterplot smoothing) function in blue and a 0.95 confidence interval in grey. For daily LUE<sub>g</sub>, only those days with at least 25% non-gap-filled GPP data were considered.

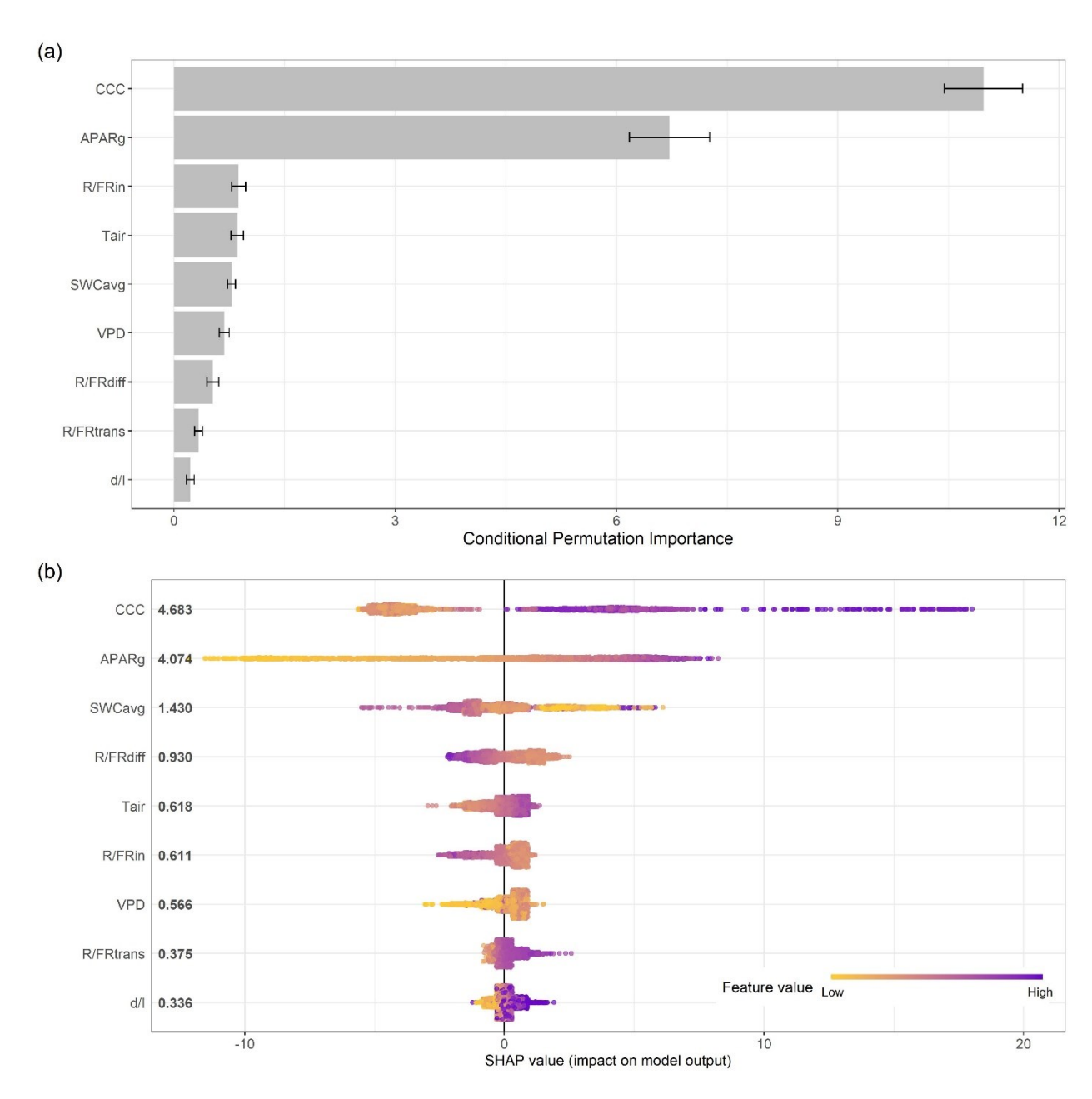


**Figure 6.5** Average conditional permutation importance (unitless) of environmental variables for a random forest gross primary productivity (GPP) model with error bars displaying one standard deviation between 10 iterations (a), and SHAP values of those variables for a gradient boosting GPP-model (b). The more values deviate from 0, the more important was the respective variable for the prediction, with negative values related to low GPP outcomes. Numbers on the left show the average absolute SHAP value (unitless) of each variable. R<sup>2</sup> of a random 5-fold cross-validation of the models was 0.83 for random forest and 0.84 for gradient boosting.

### 6.3.2 Importance of Environmental Drivers for Machine Learning Models

The results from permutation importance and SHAP agree well, indicating that the importance estimations can be considered robust. For both approaches, CCC was the most valuable feature for predicting GPP closely followed by  $APAR_g$  (see Fig. 6.5). Though only according to SHAP,  $SWC_{AVG}$  had a higher importance than the remainder variables. RF and GB both could reproduce GPP well within a 5-fold random cross-validation, resulting in an  $R^2$  of 0.83 for RF and 0.84 for GB (Fig. 6.12), though this does not tell how good the models are for spatiotemporal extrapolation. However, when replacing  $APAR_g$  and CCC by the rough proxies of solar zenith angle (SZA) and day of year (DOY), the RF model

performance drops only to an  $R^2$  of 0.81 with SZA and DOY as the most important variables (see Fig. 6.13). A RF model with neither of them, on the other hand, has only an  $R^2$  of 0.56. This leads to the impression that the diurnal and seasonal information contained in APAR<sub>g</sub> and CCC are more important than their specific quantities.

The analysis of individual SHAP values further revealed that high CCC values yielded higher GPP predictions and the limiting effect of low APAR was also evident. Dependence plots of SHAP values of each variable give a more detailed view, especially for variables with a rather small range of SHAP values (see Fig. 6.14). Here, it is notable that both very low and high VPD yielded a low GPP outcome, while high and low SWC<sub>AVG</sub> values are related to high GPP outcomes.

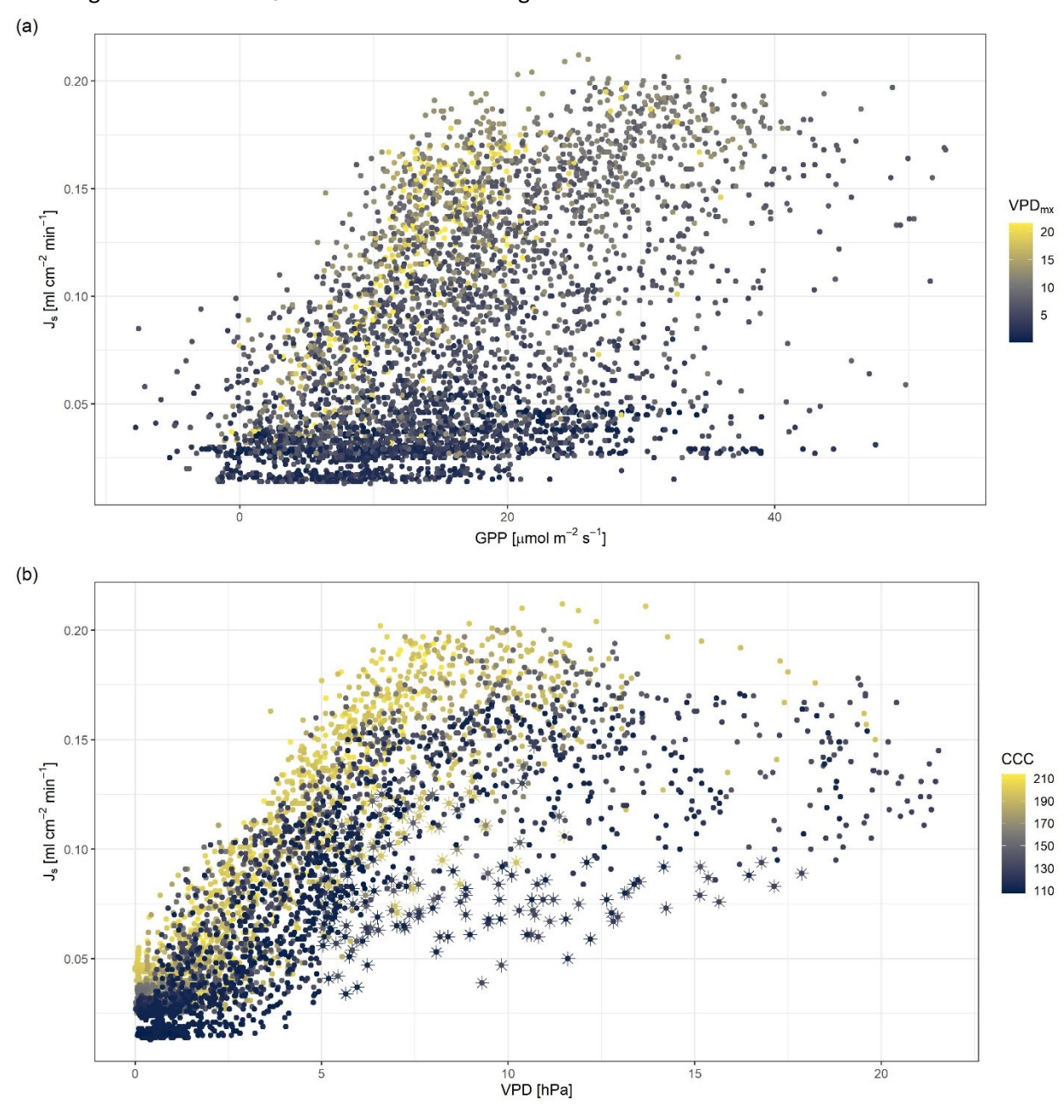
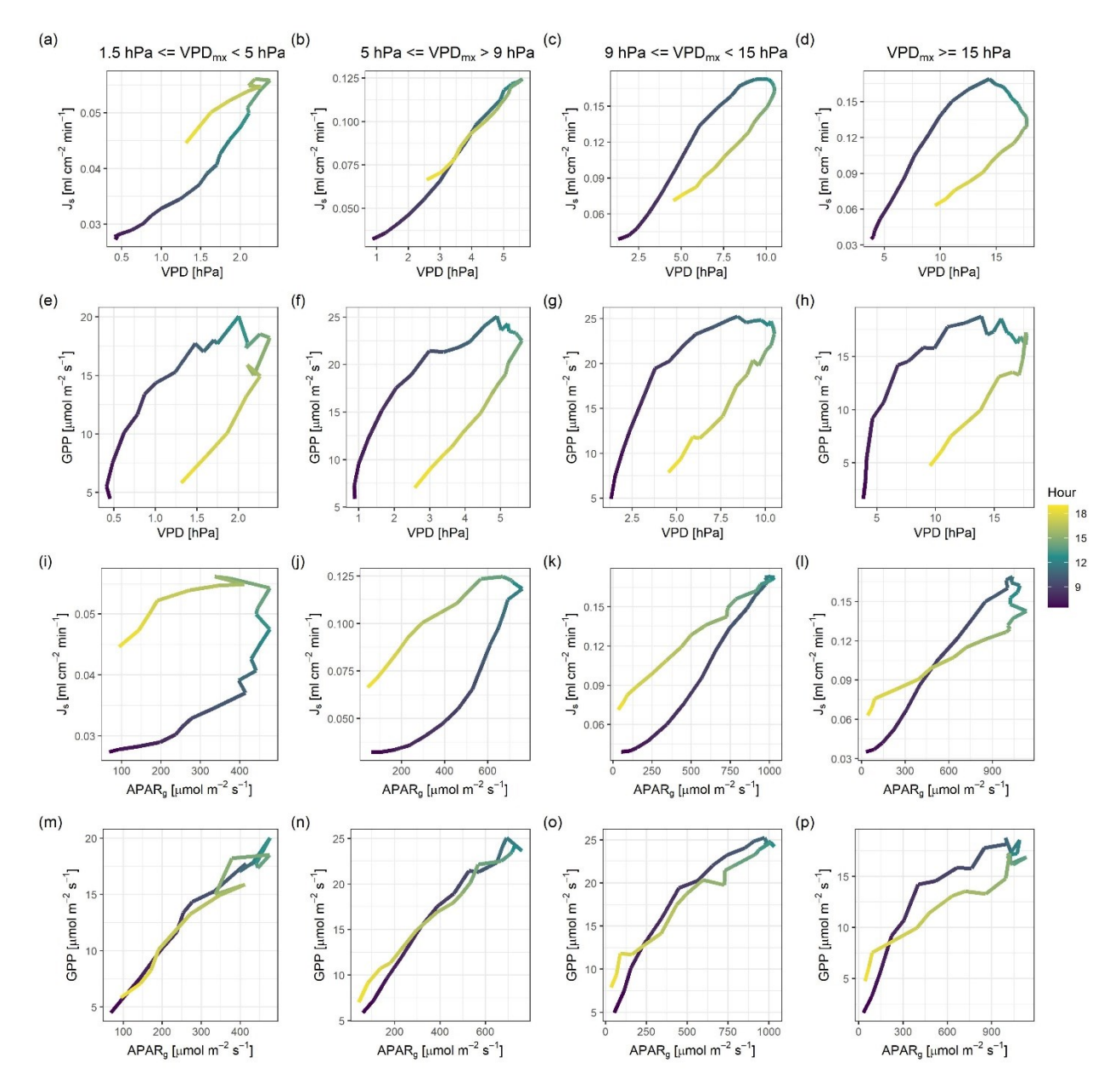


Figure 6.6 Sap flow density ( $J_S$ ) against gross primary productivity (GPP) colored by daily maximum vapor pressure deficit (VPD<sub>mx</sub>) (a) and  $J_S$  against VPD colored by canopy chlorophyll content (CCC) (b). The star symbols in panel (b) represent observations with solar zenith angle > 70° and VPD > 5 hPa.



**Figure 6.7** Hysteresis plots between sap flow density ( $J_S$ ) and vapor pressure deficit (VPD) (a-d), gross primary productivity (GPP) and VPD (e-h),  $J_S$  and green canopy absorbed photosynthetically active radiation (APAR<sub>g</sub>) (i-l), and GPP and APAR<sub>g</sub> (m-p), averaged for four different daily maximum VPD classes (columns). A clockwise (anti-clockwise) pattern occurs if afternoon and evening values of  $J_S$  or GPP are higher (lower) than in the morning at the same VPD or APAR<sub>g</sub>.

## 6.3.3 Sap Flow – GPP Relationship and their Response to Environmental Drivers

The correlation of  $J_S$  to GPP in relation of VPD and CCC is shown in Fig. 6.6. Half-hourly periods with high GPP despite very low  $J_S$  (< 0.025 ml cm<sup>-2</sup> min<sup>-1</sup>) occurred on very low maximum daily VPD (VPD<sub>mx</sub>) days (Fig. 6.6a), indicating that  $J_S$  and GPP were not correlated when photosynthesis required little transpiration. For a given value of  $J_S$  above 0.05 ml cm<sup>-2</sup> min<sup>-1</sup>, GPP was generally lower on high VPD<sub>mx</sub> days and likewise for the same GPP, a higher  $J_S$  occurred on high VPD<sub>mx</sub> days. In the relation to VPD,  $J_S$  showed a strong increase with increasing VPD until about 7.5 hPa were reached, after which  $J_S$  seems to be capped and even showed a slightly decreasing trend for VPD > 12.5 hPa (Fig. 6.6b). However, even at low VPDs,  $J_S$  was within a broad range of about 0.1 ml cm<sup>-2</sup> min<sup>-1</sup>. Lower  $J_S$  values corresponded well to low CCC, indicating a limiting influence on sap flow potential. Extraordinarily low  $J_S$  values stand

out at moderate VPD values of about 10 hPa. These values correspond to low sun angles (SZA >  $70^{\circ}$ ; star symbol in Fig. 6.6b) and occurred in the early morning after nights during which VPD remained relatively high but APAR and thus  $J_S$  were still low.

The hysteretic responses of  $J_S$  and GPP to VPD and APAR<sub>g</sub> are shown in Fig. 6.7 for different VPD<sub>mx</sub> classes. The averaged hysteresis of  $J_S$  to VPD showed markedly different patterns for different VPD<sub>mx</sub> domains. For VPD<sub>mx</sub> < 1.5 hPa (not shown), a chaotic pattern generally dominated, though for days with VPD<sub>mx</sub> between 1.5 and 5 hPa, an anti-clockwise pattern with higher  $J_S$  later in the day at same VPD could be observed (Fig. 6.7a). A transitional pattern occurred for days with VPD<sub>mx</sub> between 5 and 9 hPa without a clear hysteresis or just a clockwise loop around midday (Fig. 6.7b). On VPD<sub>mx</sub> days between 9 and 15 hPa, instead, a clear clockwise pattern with lower  $J_S$  later in the day at the same VPD levels was visible (Fig. 6.7c). For days with VPD<sub>mx</sub> above 15 hPa, the clockwise hysteresis was even more pronounced, and a decreasing  $J_S$  despite further rising VPD in the early afternoon occurred (Fig. 6.7d). GPP, on the other hand, always showed a clockwise response to VPD independent of the VPD<sub>mx</sub> scale (Fig. 6.7e-h). In the response to APAR<sub>g</sub>, however,  $J_S$  and GPP both showed a clockwise pattern on high VPD<sub>mx</sub> days. Though on lower VPD<sub>mx</sub> days, GPP did not have a time lag towards APAR<sub>g</sub>, while  $J_S$  had an anti-clockwise pattern that shifted towards a clockwise pattern with increasing VPD<sub>mx</sub> (Fig. 6.7i-p).

### 6.4 Discussion

## 6.4.1 Identification of Photosynthesis Limiting Conditions

Besides this study, an anti-clockwise hysteretic response of  $J_S$  to VPD was reported only for *P. sylvestris* growing in a wet and cool climate (Wang et al., 2019b). This hysteretic response has not been found for plants in tropical (Motzer et al., 2005; Roddy, 2013) or semi-arid climates (Li et al., 2016; Zha et al., 2017). A delayed response of  $J_S$  to VPD can be explained by the use of water stored in the upper stem during the morning hours (Goldstein et al., 1998; Perämäki et al., 2005). Stored water is only sufficient on low VPD and APAR<sub>g</sub> days, and is not detected by sap flow measurements usually carried out at 1–1.5 m height (Wang et al., 2019b). We hence interpret the shift of the  $J_S$  response to VPD from anticlockwise to clockwise as a sign of non-sufficient water storage in the upper plant. Main possible reasons for afternoon stomatal closure causing a clockwise response of  $J_S$  to VPD given by previous studies (O'Brien et al., 2004; Zeppel et al., 2004; Q. Zhang et al., 2014) can be summarized to: (i) a declined soil—root conductance due to decreased SWC, (ii) a higher stomatal sensitivity to VPD due to changed water potential gradients or xylem sap chemical composition, and (iii) decreased APAR<sub>g</sub>, caused by the delay of VPD to radiation resulting in higher APAR<sub>g</sub> values earlier in the day at a given VPD (see Fig. 6.15).

Given that GPP showed a clockwise response to VPD even on very low VPD $_{mx}$  days, we conclude that a decrease of APAR $_g$  and hence stomatal closure induced by energy limitations is the main cause for such cases at this particular site. This means that for higher VPD $_{mx}$  days a clockwise  $J_S$ -VPD pattern by itself is not a sufficient indicator for water stress or atmospheric demand induced stomatal closure. The decrease of  $J_S$  despite increasing VPD only on the highest VPD $_{mx}$  days can be considered a clearer sign of such conditions. As photosynthesis is primarily driven by APAR $_g$ , the non-hysteretic response of GPP to APAR $_g$  on low VPD $_{mx}$  days seems reasonable. Since  $J_S$  is likewise driven by APAR $_g$ , but also scaled by VPD, which is typically highest in the afternoon, a slight anti-clockwise response to APAR $_g$  can be expected (Zeppel et al., 2004) that is also enhanced by the use of stem water in the morning. Hence, the shift to a clockwise pattern of both GPP and  $J_S$  to APAR $_g$  only on the highest VPD $_{mx}$  days can be regarded as a good indicator of stomatal closure related to high atmospheric water demand at this site and year. Water-limited conditions, however, also depend on soil water potential, which can only be

roughly estimated for this site. According to the soil water retention curve for the dominant silt loam texture after Tuller and Or (2004), even the minimum SWC<sub>AVG</sub> of 20.3% during the 2021 growing season would have resulted in a pressure head of no less than about -10 m.

Limiting conditions for photosynthesis can also be identified by a time series of the relevant variables (see Fig. 6.3 and Fig. 6.16). For example, June 12 saw a marked minimum of APAR $_g$  around noon, which was likewise evident for VPD, J $_S$  and GPP, demonstrating an energy-limited response. During a high APAR $_g$  period from June 14-19 with the highest VPD values (21.5 hPa) recorded during the whole growing season, both J $_S$  and GPP were lower than during June 25-28 with distinctively lower VPD (< 12.5 hPa). This could be interpreted as a water-limited response. However, the photosynthetic capacity also increased markedly from mid to late June (Fig. 6.3d), complicating the analysis. For the hysteretic response differing CCC is not an issue as GPP and J $_S$  are compared within the same day. In summary, the analysis of the J $_S$  response especially to APAR $_g$  can reveal useful information to identify photosynthesis limiting conditions, although GPP and J $_S$  are not always related as shown by discrepancies during very low VPD conditions.

#### 6.4.2 Environmental Drivers

Both machine learning analyses show the consistency of CCC as the most important environmental variable for GPP. This high ranking also reveals that even for evergreen trees, meteorological drivers alone may not be sufficient to explain the variability in GPP. Moreover, a variable containing seasonal information about photosynthetic capacity will be also required. Our results are in agreement with previous research for mixed forests and maize crops (Croft et al., 2015; Gitelson et al., 2014; Peng et al., 2011). The higher importance of CCC even over APARg agrees with the results from Wu et al. (2022). However, other variables influencing photosynthetic capacity, such as atmospheric CO<sub>2</sub> concentrations, were not included in the analysis (Dusenge et al., 2019; Farquhar et al., 1980). Furthermore, Cabon et al. (2022) showed that wood growth in contrast to GPP is more limited by water stress than temperature-related leaf phenology.

As for environmental drivers of LUE $_g$ , we found a unimodal response to  $T_{air}$  with decreasing LUE $_g$  at high temperatures. With this analysis, however, it is not possible to single out the effect of a specific variable on LUE $_g$  because co-dependencies between variables occur. High values of  $T_{air}$  were strongly correlated to high VPD values (89% of  $T_{air} > 25$  °C had VPD > 15 hPa). Nevertheless, the observed decrease of LUE $_g$  can also be caused by high  $T_{air}$  alone due to higher photorespiration in relation to photosynthesis with increasing leaf temperatures (Long, 1991), a process which also relates to high APAR $_g$ . Likewise, as summarized by Bao et al. (2022), the temperature sensitivity has been represented by bell-shaped functions many times in LUE-models though with differing optimum ranges (e.g., Horn & Schulz, 2011; Stocker et al., 2020; X. Xiao et al., 2004). Otherwise, it was also modeled by a linearly increasing function that reaches a plateau at ca. 16 °C (Mäkelä et al., 2008).

VPD was overall not a very important variable for machine learning models despite its impact on stomatal conductance as shown by the sap flow analysis. This discrepancy can be attributed to the fact that the site is typically energy- rather than water-limited (Graf et al., 2014) with a particular cool and wet 2021 growing season. This resulted in many low VPD observations that were rather indifferent to LUE<sub>g</sub>, though nonetheless some high VPD days occurred that restricted stomatal conductance. The wet growing season probably also explains the relatively low importance of SWC, which reacts slower to dry periods with increasing depth (Xu et al., 2021). In comparison, for a drought-affected tropical dry forest, a high importance of VPD and latent heat flux to explain GPP was detected by Castro et al.

(2018). A similar response to VPD as ours, i.e., a decrease of LUE only at VPD above ca. 5 hPa, was found by Horn and Schulz (2011), while others found an immediate decrease of LUE with increasing VPD (Kalliokoski et al., 2018; Wang et al., 2018). Likewise, Fu et al. (2021) showed that during soil moisture dry downs, the covariance between GPP and VPD was positive at first, and changed to negative only after a certain soil moisture threshold was surpassed. The low LUEg values even within the optimum range of environmental variables such as Tair shows those are necessary but not sufficient conditions. During the occurrence of highest GPP and LUEg values in mid-July and mid-August all or most environmental drivers likely were within their optimal range.

While half-hourly LUE<sub>g</sub> showed only a modest increase with d/I, which is also reflected in a low importance for machine learning models, daily LUE<sub>g</sub> was significantly higher during diffuse light conditions (Fig. 6.4f). A similar response was observed to low R/FR<sub>diff</sub> and both were highly correlated (correlation coefficient of -0.92; see also Fig. 6.11b). This is probably linked to lower APAR<sub>g</sub> values during diffuse light and therefore less excessive light. Besides that, an enhancement of LUE<sub>g</sub> under diffuse conditions has been linked to a smaller fraction of the canopy in deep shade (Williams et al., 2014) and previous research showed that coniferous forests can also be larger CO<sub>2</sub> sinks under diffuse conditions (Law et al., 2002; Urban et al., 2007, 2012). A linear increase between cloudiness and LUE was hence included in LUE-models (Wang et al., 2018), though Bao et al. (2022) found an exponential increase more suitable that also fits better with our results. As the R/FR ratio was always shifted to FR after passing the canopy but less so during diffuse conditions, obscured parts of the canopy received not only a higher light quantity, but also a higher light quality than under clear skies. Such a vertical R/FR profile was shown for spruce trees by previous research (Dengel et al., 2015; Hertel et al., 2011), and in this way the higher LUE<sub>g</sub> at small R/FR<sub>diff</sub> might not be attributed to higher d/I and less excessive light alone.

## 6.4.3 Variability and Uncertainties of LUEg Estimates

Variation of LUE<sub>g</sub> shown in Fig. 6.3a can primarily be attributed to variations of APAR<sub>g</sub> and GPP. APAR<sub>g</sub> was predominantly dependent on fluctuating cloud cover patterns, while GPP likely was influenced by various current and past environmental drivers (see sect. 3.2). LUE remained within a rather low range between late April and late June. This can be attributed to below average temperatures in April and May with a subsequent low CCC well into June, as well as a warm and dry period with comparatively high VPD values in mid-June probably causing water-related stomatal closure (see sect. 3.3). As the first peak of GPP corresponds to an increase of CCC as well as low VPD, we attribute this peak to the probably first suitable growing conditions after cold temperatures in May and dryness in June. The first LUE<sub>g</sub> drop in late July saw decreasing APAR<sub>g</sub>, GPP, T<sub>air</sub> and CCC (although from few observations) and thus may be related to energy-limited conditions. The second GPP and LUE<sub>g</sub> peak did not occur during the same days. A peak of GPP occurred from Aug 12–15 but was associated with relatively high APARg values and thus did not result in a high LUEg. The LUEg peak instead occurred from Aug 16–19 with only moderate GPP (1.03–1.24 mol m<sup>-2</sup> d<sup>-1</sup>) during the rapid onset of very low and consistent APAR<sub>g</sub> in consequence of the passage of the low pressure system Luciano. Explaining why GPP did not likewise decrease to lower values is beyond this analysis. However, the low amounts of PAR<sub>in</sub> were perhaps still enough to sustain a moderate GPP. The last drop of GPP in late August then is accompanied by a continuous decrease of CCC, which can be interpreted as the onset to the end of the growing season.

GPP derived from eddy covariance measurements is subject to well-known limitations including the difficulty of estimating a storage term without a vertical CO<sub>2</sub> profile (Montagnani et al., 2018), the identification of vertically decoupled flows (Peltola et al., 2021a), and the uncertainty from partitioning

net ecosystem exchange into GPP and Reco (Raj et al., 2016). PARtrans measurements from a limited number of sensors were subject to a sampling error during direct light conditions, as indicated by a non-flattening curve of the coefficient of variation as a function of the number of sensors (see Fig. 6.17). Additionally, a bias to an ideal APAR calculated from all PAR flux terms can be expected (Widlowski, 2010). In our case, we did not measure horizontal and ground-reflected PAR fluxes. Green APAR has the advantage over total APAR that only light actually usable for photosynthesis is considered. In this way, the effect of short-term drivers such as VPD and Tair on the partitioning of energy in photosynthesis and, e.g., transpiration, non-photochemical quenching and fluorescence can be investigated. However, environmental conditions causing a reduction of NDVI such as drought, insect infestation or wind storms will not properly be reflected in a decreased LUEg. With total APAR, these conditions would decrease LUE as long as the canopy surface area is not reduced. Chlorophyll content, on the other hand, can be low despite an apparently 'green' leaf (Gitelson & Gamon, 2015). Hence it is important for GPP models that PAR absorbable by chlorophyll might still be overestimated by NDVI-based APAR<sub>g</sub> and thus LUE<sub>g</sub> underestimated. The Sentinel-2 derived NDVI estimates induce a further uncertainty to APAR<sub>g</sub>, although a validation with in-situ measurements showed the reliability of Sentinel-2 NDVI (Lange et al., 2017). By measuring PAR<sub>trans</sub> in 1.3 m, the light used for photosynthesis by the ground vegetation was not included in fAPAR, though their productivity was included in GPP. The contribution of ground vegetation to GPP, however, can be expected minor in an old growth forest stand (Kulmala et al., 2011). Excluding photosynthesis of ground vegetation would hence slightly decrease LUEg, which is a counterweight to the former limitation. Although calculating LUE as in Eqn 5 is most straightforward and commonly used (e.g., Gitelson & Gamon, 2015; Martini et al., 2022; Wieneke et al., 2018), LUE can also be assessed by metrics of the light response curve, such as the initial slope or the half saturation point (Williams et al., 2014). In addition, the SQ-521-SS sensors measured PAR from 389 to 692 nm, though Zhen and Bugbee (2020) argued to include FR light (701-750 nm) in the definition of PAR, as FR causes a balanced excitation of the two photosystems, and hence improves photochemical efficiency.

## 6.5 Conclusions

Our study found that i) a seasonal variable such as CCC is consistently necessary for accurate GPP estimations by machine learning models and hence should be considered as a possible improvement for LUE-based approaches and ii) tree-scale  $J_s$  and ecosystem-scale GPP showed a congruent clockwise hysteretic response to APAR $_g$  on high VPD days, thus likely being a good indicator of water stress induced stomatal closure. In this way, this novel dual-scale comparison of hysteretic cycles has the potential to be of general value for identifying photosynthesis-limiting conditions. We anticipate these findings will be valuable for the development of GPP-modeling approaches, and can serve as a basis to be confirmed by multi-site and multi-year studies across different environments and climate zones.

### 6.6 Data Availability Statement

Associated data are available at <a href="http://doi.org/10.5281/zenodo.7014604">http://doi.org/10.5281/zenodo.7014604</a>. LiDAR data used in this study can be freely accessed at

https://www.opengeodata.nrw.de/produkte/geobasis/hm/3dm\_l\_las/3dm\_l\_las/ and Sentinel-2 data can be freely accessed at https://scihub.copernicus.eu/.

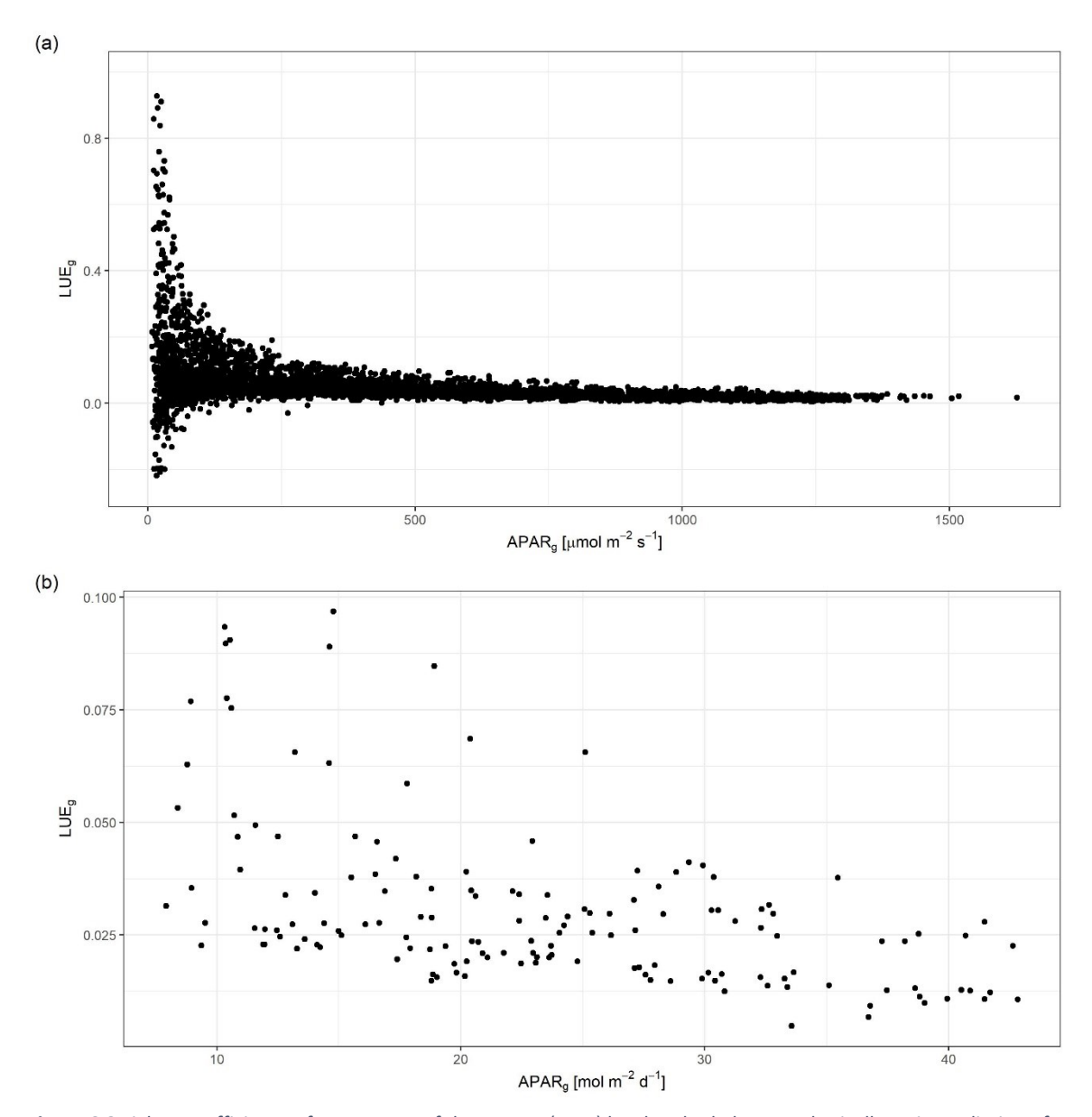
## 6.7 Acknowledgments

The project was co-funded under the Excellence Strategy of the Federal Government and the Länder (Project ComRadE, SFUoA002) and the University of Alberta, Canada / RWTH Aachen University, Germany. The research was also funded by the Waldklimafonds (project MW3; grant agreements 2220WK86A4 and 2220WK86B4). The Waldklimafonds itself is funded by the German Federal Ministry of Food and Agriculture (BMEL) and Federal Ministry for the Environment, Nature Conservation, Nuclear Safety and Consumer Protection (BMUV) administrated by the Agency for Renewable Resources (FNR). The basic equipment of the Wüstebach site with measurements was funded by the TERENO project (www.tereno.net). We acknowledge support from the Helmholtz research infrastructure Modular Observation Solutions for Earth Systems (MOSES). In particular, we thank Marius Schmidt, Ansgar Weuthen, Bernd Schilling, Daniel Dolfus, and Martina Kettler for installation and maintenance of the radiation sensors and the eddy covariance system, Carsten Montzka for gathering and processing LiDAR data, and Lutz Weihermüller for providing soil properties. We thank two anonymous reviewers, who helped to improve the manuscript substantially.

- 6.8 Supporting Information
- 6.8.1 Text S1. Calculation of GPP<sub>dev</sub>

Deviations of GPP from a year- and site-specific optimal GPP (GPP<sub>opt</sub>) in relation to APAR<sub>g</sub> are presented here as an alternative approach to a half-hourly LUE ratio. For GPP<sub>opt</sub>, a generalized additive model (Hastie & Tibshirani, 1990) was fitted to the maximum non-gap-filled GPP values of each 20  $\mu$ mol m<sup>-2</sup> s<sup>-1</sup> APAR<sub>g</sub> interval until the overall maximum GPP value was reached (Fig. 6.9). After that, maximum GPP was kept constant, assuming that this maximum value (52.8  $\mu$ mol m<sup>-2</sup> s<sup>-1</sup>) can theoretically also be reached at higher APAR<sub>g</sub> values. The deviation of observed GPP (GPP<sub>dev</sub>) from GPP<sub>opt</sub> was then related to different environmental variables. This approach thus has the advantage of factoring out the limiting influence of non-saturated APAR<sub>g</sub> without additional log-transformations. A disadvantage, however, is that the results depend on a specific model fit. Fig. 6.10 thus compares GPP<sub>dev</sub> to the log10-transformed LUE ratio, and shows no fundamental differences in regard to the influence of environmental drivers.

# 6.8.2 Figures



 $\textbf{Figure 6.8} \ \, \text{Light use efficiency of green parts of the canopy (LUE_g) by absorbed photosynthetically active radiation of green parts of the canopy (APAR_g) for half-hourly values (a) and daytime averaged values (b).$ 

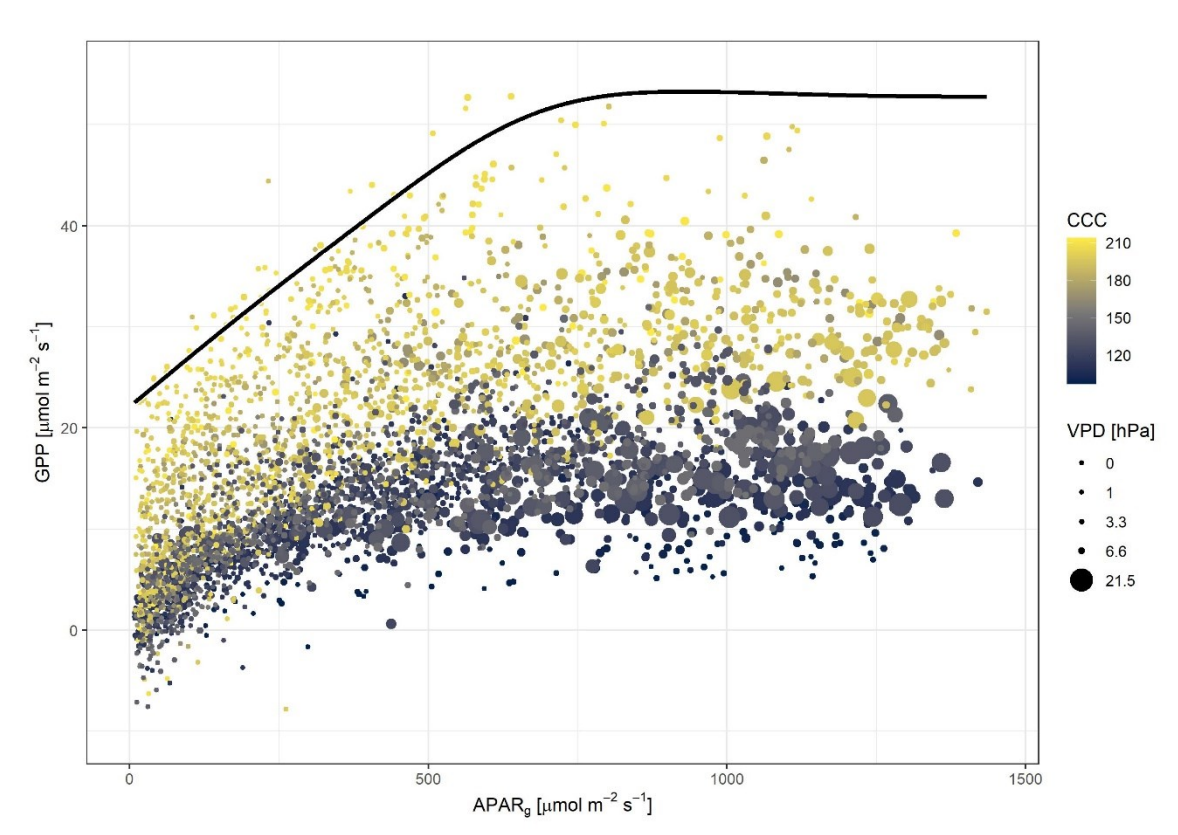


**Figure 6.9** Gross primary productivity (GPP) plotted against green canopy absorbed photosynthetically active radiation by green parts of the canopy (APAR<sub>g</sub>), colored by canopy chlorophyll content (CCC) and dot sizes by vapor pressure deficit (VPD). The black line denotes an upper limit of GPP in relation to APAR<sub>g</sub> bins (GPP<sub>opt</sub>) as modelled by a generalized additive model.

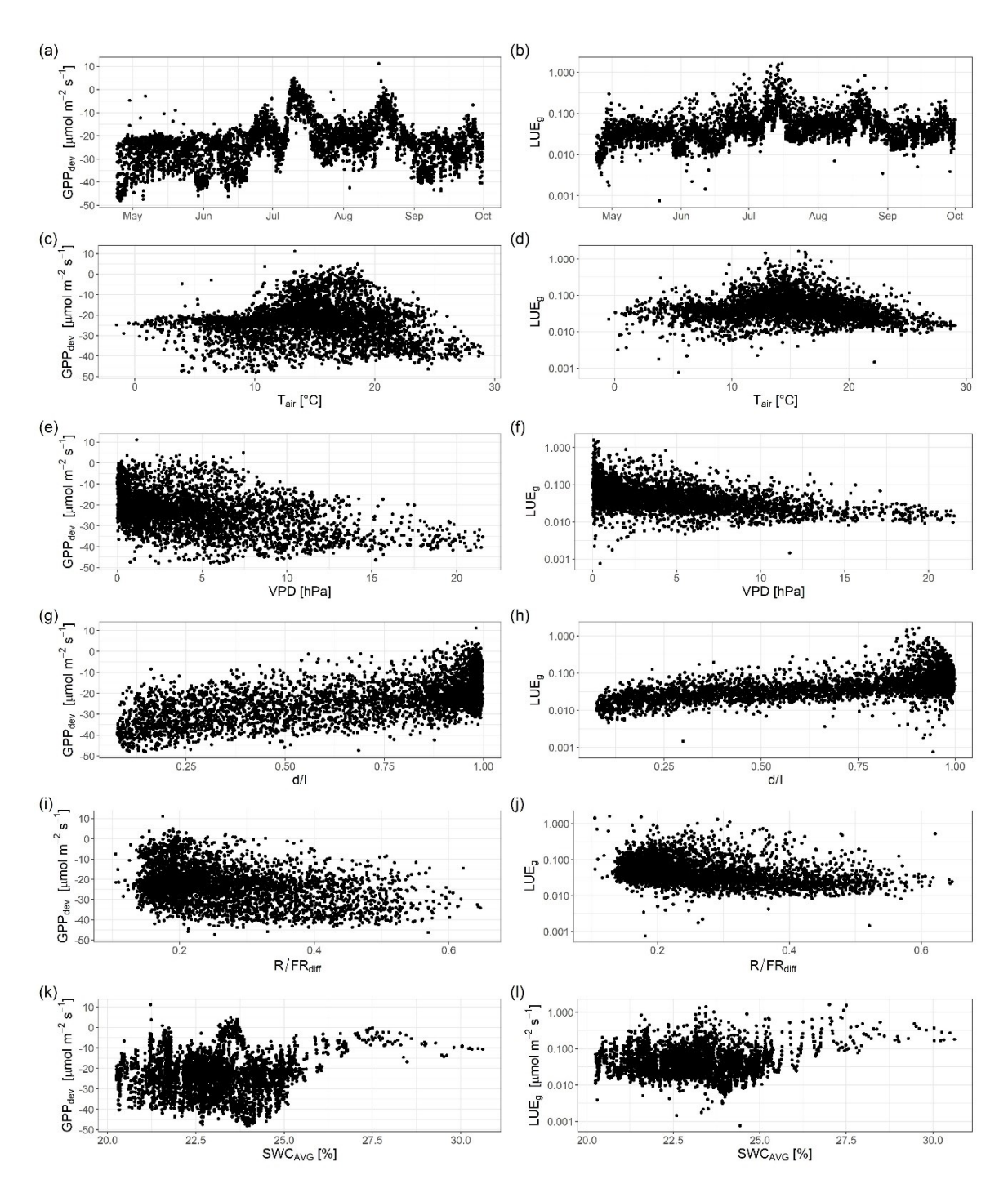
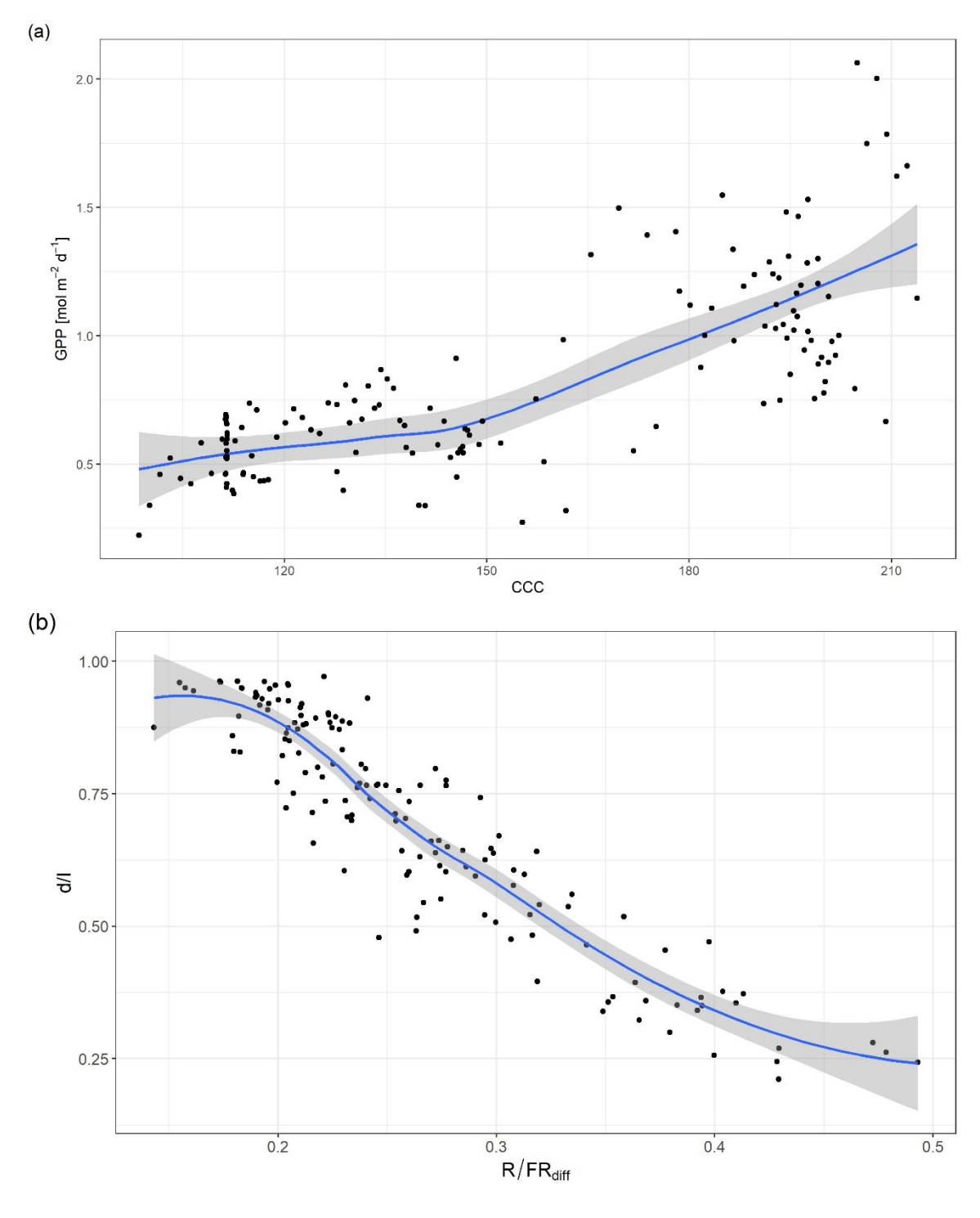


Figure 6.10 Deviations from optimal gross primary productivity ( $GPP_{dev}$ ) (left columns) and green canopy light use efficiency ( $LUE_g$ ) with a log10-transformed y-axis (right column) at a half-hourly scale against time (a, b), air temperature ( $T_{air}$ ) (c, d), vapor pressure deficit (VPD) (e, f), diffuse fraction (d/I) (g, h), the difference of the red to far-red ratios between above and below canopy ( $R/FR_{diff}$ ) (i, j) and soil water content ( $SWC_{AVG}$ ) (k, I).



**Figure 6.11** Scatterplots of daily gross primary productivity (GPP) and Canopy Chlorophyll Content (CCC) (a) and diffuse fraction (d/l) against the difference of the R/FR ratio above and below the canopy (R/FR<sub>diff</sub>) (b), with a LOESS (locally estimated scatterplot smoothing) function in blue and a 0.95 confidence interval in grey.

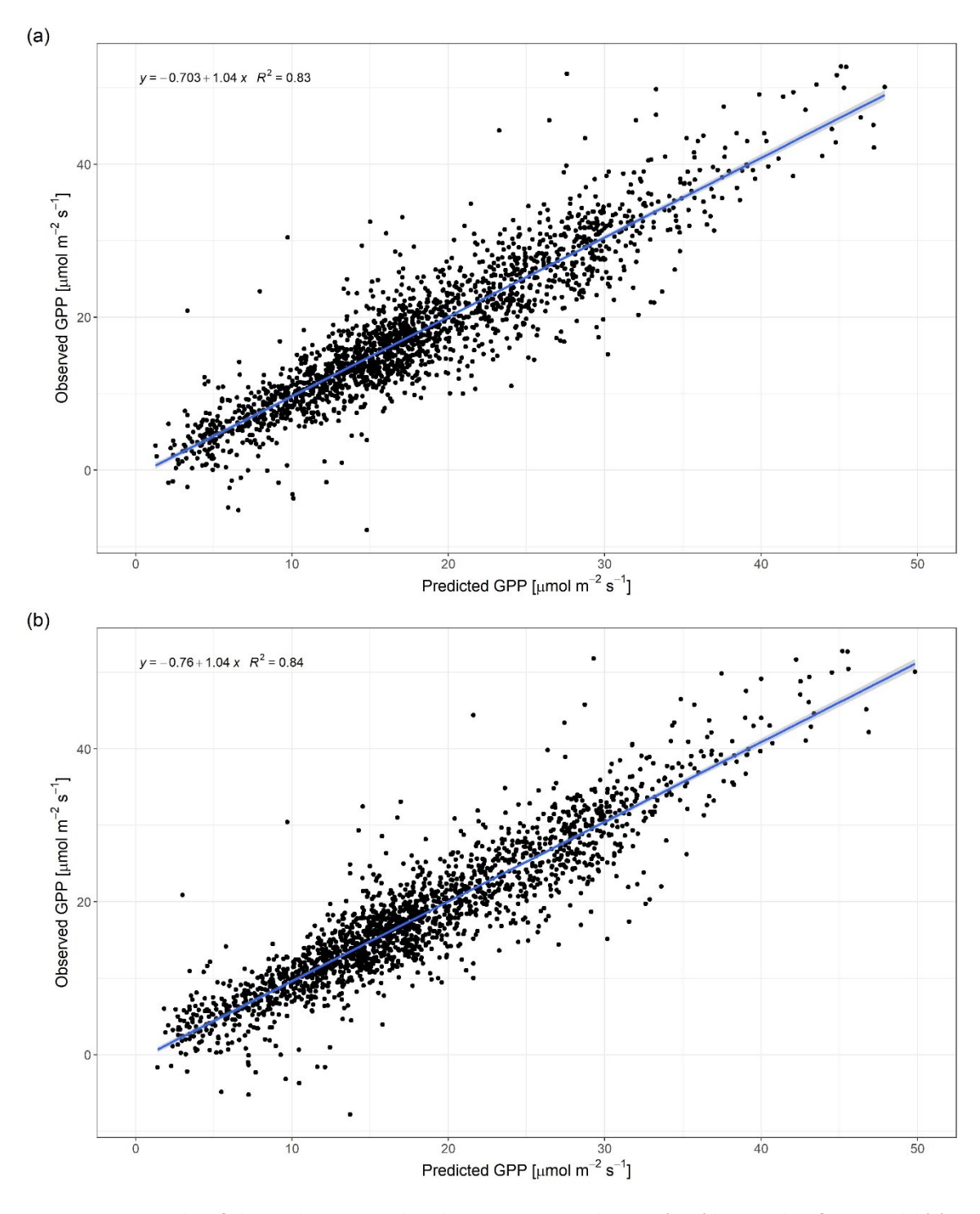
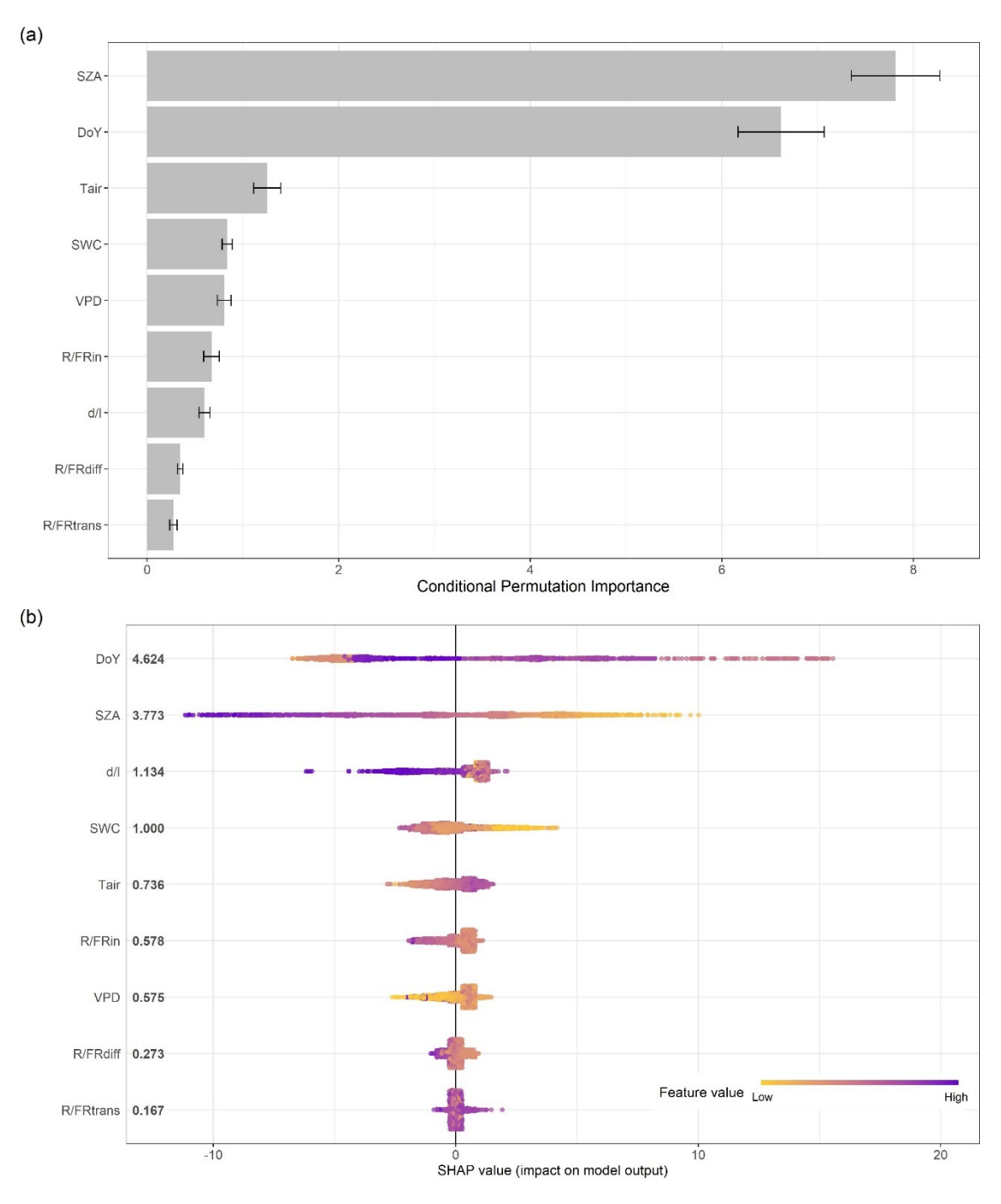
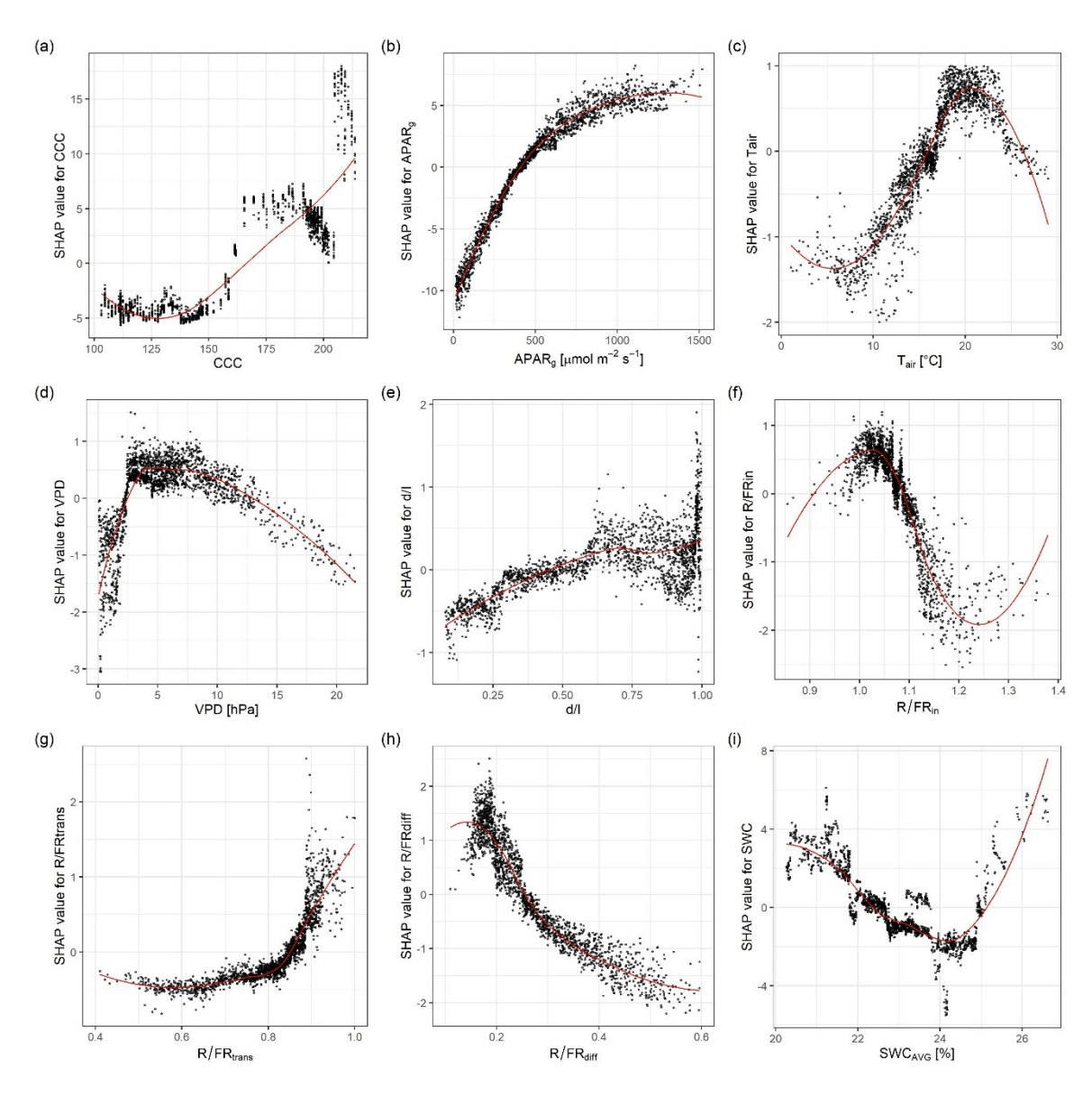


Figure 6.12 Scatterplot of observed against predicted gross primary productivity (GPP) by a random forest model (a) and a gradient boosting model (b) with a linear fit displayed in blue.



**Figure 6.13** Variable importance results for predictors but in contrast to Fig. 6.4 with solar zenith angle (SZA) and day pf year (DOY) instead of absorbed photosynthetically active radiation and canopy chlorophyll content. Average conditional permutation importance (unitless) for a random forest gross primary productivity model with error bars displaying one standard deviation between 10 iterations (a), and SHAP values of those variables for a gradient boosting GPP model (b). Numbers on the left show the average absolute SHAP value (unitless) of each variable.



**Figure 6.14** SHAP values of each predictor of Fig. 6.4b against the predictor values, with a locally estimated scatterplot smoothing (LOESS) function in red.

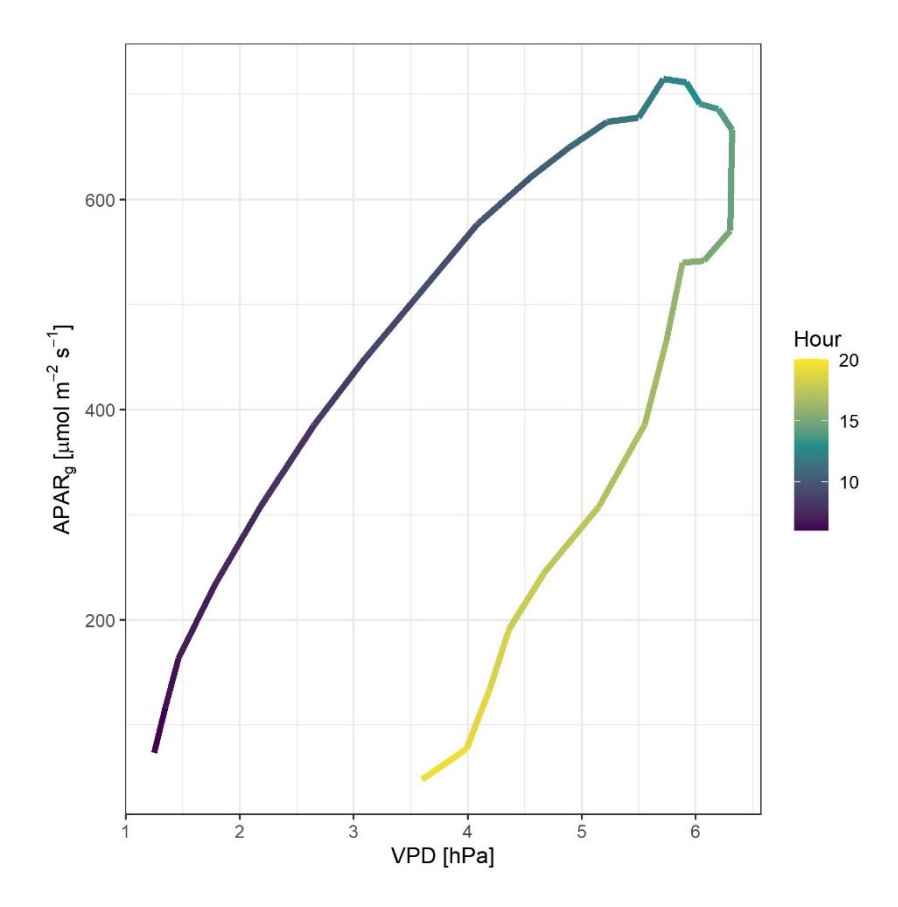


Figure 6.15 Hysteresis plot for vapor pressure deficit (VPD) in relation to green canopy absorbed photosynthetically active radiation (APA $R_g$ ), averaged over all days of the 2021 growing season.

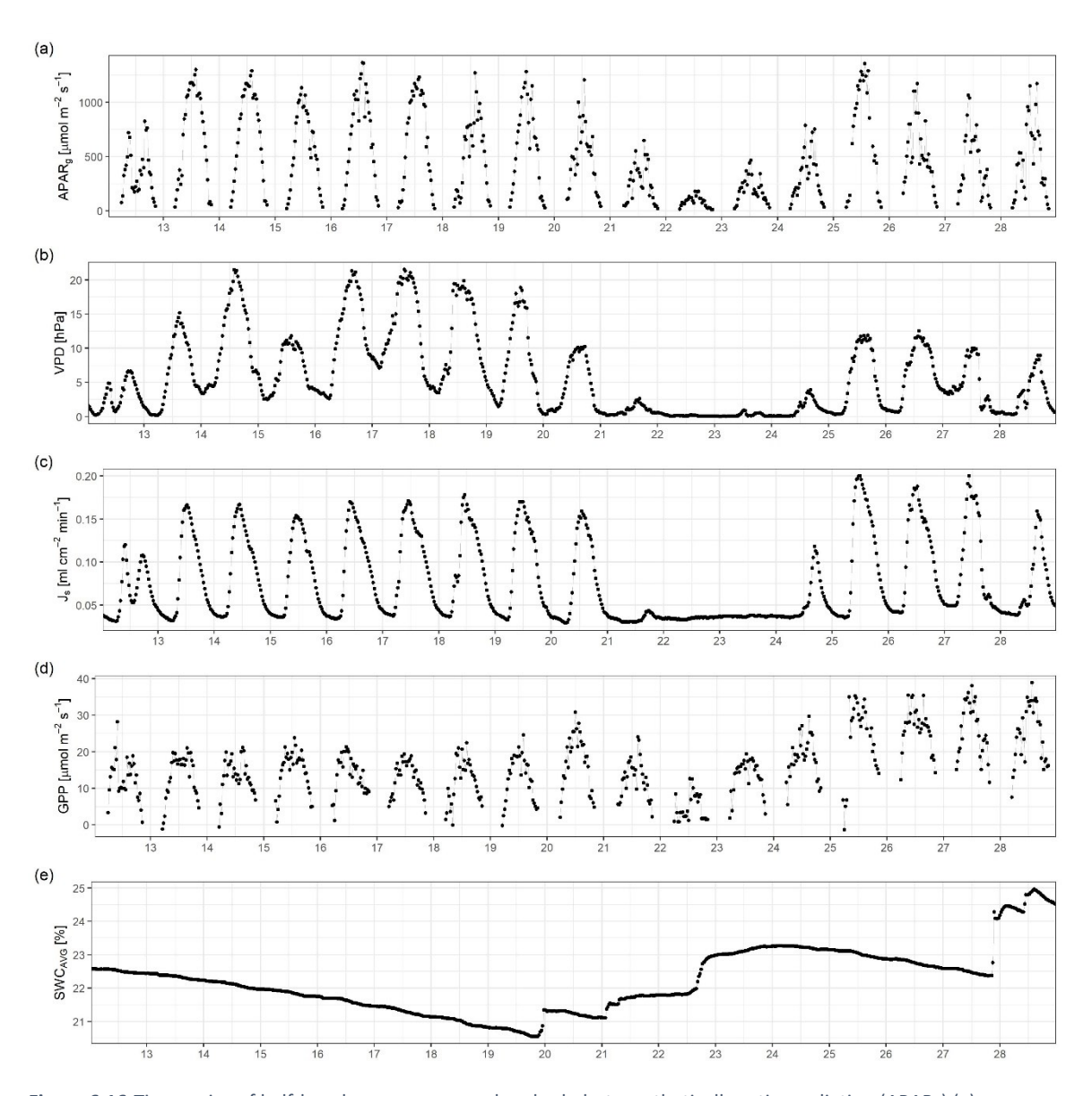
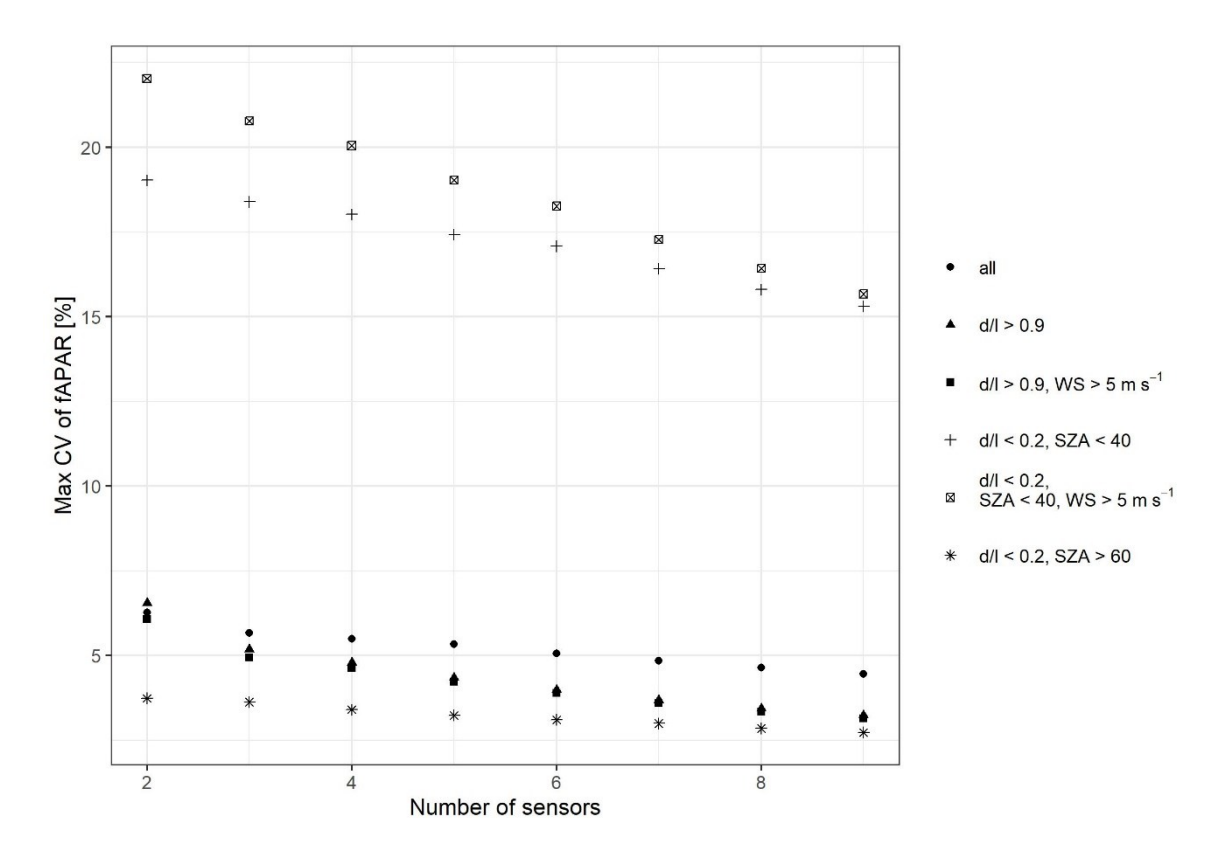


Figure 6.16 Time series of half-hourly green canopy absorbed photosynthetically active radiation (APAR<sub>g</sub>) (a), vapor pressure deficit (VPD) (b), sap flow density ( $J_S$ ) (c), gross primary productivity (GPP) (d) and soil water content (SWC<sub>AVG</sub>) (e) between June 12 and June 29, 2021.



**Figure 6.17** Maximum coefficient of variation (CV) of fraction of absorbed photosynthetically active radiation (fAPAR) by the number of canopy-transmitted PAR sensors and for different dataset filtered by diffuse fraction (d/I), solar zenith angle (SZA) and wind speed (WS). Calculation of CV was conducted analogous to Putzenlechner et al. 2019b.

# 7 Synthesis and Outlook

In this chapter, the general research questions outlined in Chapter 1 are addressed and the main conclusions from the research presented in Chapters 4, 5 and 6 are summarized. Moreover, suggestions for possible and planned future research are outlined accompanied by a critical evaluation of the results in this work. In summary, the research presented in this doctoral dissertation concerned (i) the expansion of eddy covariance flux data with machine learning models to generate spatiotemporal flux information for a whole river catchment (Chapter 4), (ii) methodological aspects for a better interpretability of obtained flux data at a deforested site (Chapter 5), and (iii) the use of eddy covariance based products, among other measurements, and machine learning to improve the understanding of plant physiology and plant-atmosphere interactions (Chapter 6).

Research question 1 was how accurate CO<sub>2</sub> fluxes from eddy covariance stations can be upscaled to the Rur catchment across different land covers using machine learning with state-of-the-art feature selection methods. In general, the random forest approach with spatiotemporal feature selection methods and a combination of eddy covariance CO2 flux data, MODIS vegetation indices and meteorological reanalysis data provided promising upscaling results at the regional scale. One main conclusion is that, despite being computationally more expensive, averaging five model runs in the feature selection process could significantly decrease the risk of being trapped in a local maximum. Furthermore, spatial cross validation results could be improved by using smaller flux training data sets with strict quality control rather than larger ones incorporating also days with more gap-filled data. Although an R<sup>2</sup> of just 0.41 is in the range of other approaches with a spatial cross validation scheme (Shi et al., 2022), there is still room for improvement that should be addressed in future research. Results showed that differences between land cover classes were narrower in the upscaled product than between eddy covariance stations (Table 4.6). Separate models for each land cover class might improve this limitation but would require more flux stations per class to perform a spatial cross validation. With separate models by land cover class, training data of managed land covers could further be adjusted for lateral fluxes. In the current implementation, the model was fitted to eddy covariance data only. Hence, inherent limitations of the eddy covariance method, such as the omission of lateral fluxes, are automatically reproduced by the machine learning models.

MODIS remote sensing products have the advantage of a high temporal resolution. Though with a spatial resolution of 250 m at best, they are also prone to contain mixed pixels, i.e., spectral responses from various land covers in the same pixel, which probably contributed to the above-mentioned limitation. Within the spatial cross validation, predicted NEE displayed also a narrower range than observed NEE (Fig. 4.3). This underestimation of rare cases can be attributed to the natural imbalance in the training data between rare and most frequent cases, which can be tackled by further enriching the environmental envelope of the training data or by using, e.g., synthetic minority over-sampling techniques (Torgo et al., 2015). For random forest specifically, this problem is enhanced by the averaging of many trees, which might be less pronounced in algorithms without averaging such as neural networks or gradient boosting. However, the study presented in Chapter 4 was also part of a meta-analysis comparing different NEE upscaling approaches (Shi et al., 2022). The authors showed that random forest and support vector machines performed better than other algorithms and that half-hourly models were more accurate (average R<sup>2</sup> of 0.73) than daily models (average R<sup>2</sup> of 0.50). Further impact of the paper is evident in Zhang et al. (2021), which used the research framework of the study as a role model to estimate actual evapotranspiration at northern Chinese weather stations. The aforementioned issue regarding the environmental envelope of training data was addressed in detail by Meyer and Pebesma (2021). They introduced a method to assess an area of applicability where a machine learning model can be reliably applied for spatial predictions. In Chapter 4, urban areas were manually excluded from the analysis because different CO<sub>2</sub> exchange processes (i.e., fuel combustion) were assumed to dominate the total CO<sub>2</sub> flux, and which would require other predictor variables. With an area of applicability analysis, such areas and maybe others that are non-intuitive might be excluded with a more quantitative justification. The importance of predictor variables for the final model are presented in Table 4.5. However, further insight into the use of variable importance measures presented in Chapter 6 showed that possible correlations between predictors should be taken into account for future variable importance analyses (Debeer & Strobl, 2020), which was realized only at a later stage of the doctoral work and after the publication of Chapter 4. Moreover, future upscaling approaches should make use of the FluxnetEO data set, which is a standardized procedure to extract, quality control and gap-fill MODIS and Landsat spectral information for 338 FLUXNET and ICOS sites (Walther et al., 2022). Besides MODIS, reanalysis data were an important source of predictor variables for the upscaling in Chapter 4. In order to account for spatiotemporal uncertainties in such reanalysis products, spatiotemporal lagging of meteorological predictors was indicated advantageous in machine learning NEE modelling approaches (Kämäräinen et al., 2023).

Another task for future research is the comparison of regional upscaling products to regional processbased model simulations such as from the Community Land Model (Lawrence et al., 2019). A high agreement between those would imply a higher-order validation of the gridded NEE product than just a cross validation with eddy covariance measurements, which themselves are prone to uncertainties, especially at high flux magnitudes (Richardson et al., 2012). On the global scale, an eddy covariancebased upscaling product obtained a significantly larger terrestrial CO<sub>2</sub> sink (by about 10 Pg C yr<sup>-1</sup>) than a process-based global budget (Zscheischler et al., 2017). This mismatch was partly attributed to an underrepresentation of recently disturbed ecosystems in global flux datasets (Ciais et al., 2022). Those ecosystems are, however, in particular prone to high flux uncertainties due to their oftentimes nonideal characteristics for eddy covariance measurements. Consequently, research question 2 was how eddy covariance measurements over a deforested, fetch-limited site with unmanaged regrowth are affected by choices of measurement height and spectral corrections. The results demonstrate the trade-offs that have to be considered in the eddy covariance measurement design for a site with nonideal characteristics. By comparing two measurement heights, it was shown that at the lower height LPF corrections were higher and differed more among methods (Fig. 5.4). On the other hand, the estimated footprints of both heights did not match the average footprint of the previous years at the lower height. Hence, the study supports the difficulty of achieving a stable flux source area over longer time periods for fast growing vegetation with infrequent stepwise height changes. Results further showed that flux differences resulting from the choice of LPF correction and measurement height induced a non-negligible uncertainty to daytime fluxes, although those differences had a relatively small magnitude of NEE differences between the deforested and forested flux site at Wüstebach (11% at most). Hence, the choice of LPF correction likely would not invert the general CO2 sink comparison between these land covers, but still is one important factor in the accurate quantification of NEE, that should always be explicitly stated, especially for sites with high spectral corrections. Furthermore, FLUXNET only unifies the post processing such as u\*-filtering, gap-filling and partitioning of flux data, but the actual processing of high frequency measurements to half-hourly fluxes is not unified yet within the FLUXNET data set (Pastorello et al., 2020). Hence, the uncertainty from different processing choices is of importance not only for disturbed ecosystems but for all sites in general. Such choices concern, for example, the detrending method and the quality control policy, for which different methods exist (e.g., Göckede et al., 2006; Mauder et al., 2013). Rannik et al. (2020) already evaluated the impact of different coordinate rotations on fluxes, but an overarching analysis for a site with almost ideal conditions for eddy covariance measurements could reveal whether such choices add up to a large systematic uncertainty. Within the comparison of different LPF corrections, five different analytical and empirical approaches were applied. The comparison could be further enriched by the inclusion of direct approaches relying on measured cospectra only, which are not yet implemented in EddyPro© (e.g., Polonik et al., 2019). If the comparison of different LPF corrections is transferred to closed-path gas analyzer designs, existing LPF corrections should also be revised in order to account for overestimated travel times in the sampling tube due to interrelated time delay and frequency response corrections (Peltola et al., 2021b).

Flux differences, however, were even larger between the two measurement heights than between LPF corrections at the same height, with standard deviations between fluxes of the two heights of 24.8% for  $CO_2$  and 9.7% for  $H_2O$ . This probably resulted at least partly from different flux source areas within the heterogeneous site. These results imply that the measurement height and the footprint should be carefully evaluated for small, disturbed ecosystems with a limited fetch and heterogeneous, fast-growing vegetation. For these sites, however, conventional footprint models (e.g., Kormann & Meixner, 2001; Kljun et al., 2015) cannot account for the high surface heterogeneity and especially cannot resolve the complex flow over forest edges. Because of this, future research on such sites should consider applying large-eddy simulations (e.g., Auvinen et al., 2017), turbulence closure models (e.g., Sogachev et al., 2002) or artificial tracer experiments (e.g., Arriga et al., 2017). Moreover, vertical and horizontal  $CO_2$  concentration profile measurements, as well as the application of cold air drainage models such as  $KLAM_21$  (Sievers & Kossmann, 2016), could help to identify advective processes influencing the  $CO_2$  budget at the deforested site.

In this way, flux data from the deforested site can be more accurately interpreted and used for comparisons to flux data from other land covers such as the Wüstebach forest site, as well as for other applications such as upscaling. Although the measurement height at the deforested site was regularly adjusted by rule of thumb even before the 2020 experiment, the possibility that data used for the upscaling in Chapter 4 may partly not be representative of the deforested site cannot be fully ruled out. For the NEE data from the forested site at Wüstebach used to derive GPP in Chapter 6, a regular adjustment of measurement height is a minor (albeit non-negligible) issue due to the slower growing rate of the mature trees. Regarding this spruce forest, research question 3 was how different environmental conditions are related to its light use efficiency and gross primary productivity. To address this question, the difficulty of assessing the LUE of forest canopies first had to be approached. In general, the research highlighted the utility of ecosystem-scale flux information and machine learning for the analysis of environmental influences on plant physiological processes and thus on the terrestrial carbon sink. In this way, eddy covariance derived GPP was used in combination with in-situ measured APAR to assess the LUE of the Wüstebach spruce forest. Over the whole growing season, LUE of green parts of the canopy was  $4.0 \pm 2.3\%$  and showed a unimodal response to air temperature with a maximum LUE at about 15 °C and a higher LUE during diffuse than during direct light conditions, indicating excessive light in such cases. However, for comparing LUE and its environmental drivers among different studies, the definition of LUE should be carefully taken into account (Gitelson & Gamon, 2015). Photosynthesis defined either as GPP or NPP can be related to global radiation, incoming PAR, absorbed PAR, or absorbed PAR by green parts of the canopy. Each definition of LUE will have different responses to certain environmental controls, such as those that change the canopy chlorophyll content but not likewise the canopy surface. Hence, for the analysis of instantaneous meteorological conditions on LUE, future research should focus on an LUE definition that is scaled by the photosynthetic capacity to achieve accurate comparisons between different phenological stages. Though for investigating long-term environmental drivers, it should be focused on an LUE definition which excludes the photosynthetic capacity. In this way it is ensured that a change of photosynthetic capacity due to, for example, insect infestation results in a change of LUE. In Chapter 6, the NDVI was used to calculate green-canopy APAR and LUE due to its simplicity to reckon up the product as it is normalized from 0 to 1 for non-water surfaces. However, the high importance of CCC indicates that it is worthwhile to develop an APAR product that incorporates CCC for the analysis of instantaneous meteorological conditions. This LUE study could be further enhanced by the investigation of other pathways besides utilization in the Calvin cycle that energy from absorbed PAR can take. Out of these other biochemical processes, dissipation as heat from non-photochemical quenching can be monitored via remote sensing with the photochemical reflectance index (Gamon et al., 1997; Garbulsky et al., 2011). In this way, a downregulation of LUE due to high light intensity, water stress or extreme temperatures can be observed. Another possibility is the observation of solar-induced chlorophyll fluorescence (SIF) from remote sensing or in-situ measurements (Verma et al., 2017; Mohammed et al., 2019; Morozumi et al., 2023). As SIF basically is a leakage of photons from photosynthetic membranes, which depends on the flux of photons absorbed by chlorophyll, it can be used as a proxy measure of the actual PAR absorbed by photosynthetic pigments (Gonsamo & Chen, 2018). In order to achieve a complete assessment of influencing factors on GPP and LUE, further variables should be investigated, which include atmospheric CO<sub>2</sub> content, availability of nutrients such as nitrates and phosphates, and memory effects of past conditions such as drought, frost or pest infestation (Desai, 2014; Aubinet et al., 2018; Besnard et al., 2019).

Besides atmospheric water deficit and soil water content, considering the actual vegetation water content, such as derived from microwave satellite missions, is also promising for future studies on photosynthetic performance (Cosh et al., 2019; Pei et al., 2022). Water-limiting conditions for photosynthesis were also identified in Chapter 6 by the analysis of mutual hysteretic responses of ecosystem-scale GPP and tree-scale sap flow density to VPD and APARg. Here, it was demonstrated that a standardly anticlockwise hysteretic pattern of sap flow to APARg under non water stress conditions shifted to a clockwise pattern on high VPD days, which happened likewise for GPP. Hence, a clockwise hysteretic pattern of sap flow to radiation was indicated as a potential indicator for afternoon stomatal closure. In this way, eddy covariance based data could help to confirm insights to plant physiological responses to environmental conditions. Possible constraints of the applied Granier type sap flow measurements include flow obstructions through wound effects around the sensor needles, which possibly result in an underestimation of sap flow, especially if the two needles are close to each other (Steppe et al., 2015; Wiedemann et al., 2016). The hysteretic results should also be validated by investigations of plants with different water stress responses, i.e. anisohydric and isohydric strategies or C<sub>3</sub> and C<sub>4</sub> plants (Sade et al., 2012).

In contrast to Chapter 4, where machine learning was applied with a focus on prediction, it was applied in Chapter 6 with a focus on inference. Here, the importance of various potential environmental drivers as predictor variables to model GPP was assessed by the application of two different variable importance measures. Both agreed that CCC followed by APAR<sub>g</sub> were the most important variables for the prediction of GPP by tree-based machine learning models, which thus can be considered a relatively robust result. However, it should be noted that the variable importance results do not prove any causal relations, although they were in line with processual knowledge. Accordingly, results also showed that the model performance was insignificantly worse if CCC and APAR<sub>g</sub> were replaced by the more general variables DOY and SZA. This indicates that CCC and APAR<sub>g</sub> rather are important as general representatives of seasonal variables for photosynthetic capacity and diurnal variables for energy supply. Nevertheless, it should be noted that results of this work are based on a single growing season, and it should be verified whether DOY still is a viable replacement of CCC if the respective days correspond to different phenological stages in different growing seasons. In addition, the results of this chapter in general are only based on a single research site dominated by a single tree species, Picea abies. Consequently, they have to be confirmed for other tree species growing in different climates, and more years encompassing different environmental conditions. This will be accomplished by an ongoing project, which expands the general research framework of Chapter 6 to other tree species along climatic gradients in Germany.

Overall, this work i) applied and refined state-of-the-art spatiotemporal feature selection schemes for the regional upscaling of eddy covariance flux measurements, ii) assessed the uncertainty of flux measurements over a deforested site in regard to measurement height and the choice of LPF correction, and iii) used a unique set of elaborate measurements and methods to assess and analyze the LUE and limiting conditions for photosynthesis of a temperate spruce forest. Thus, the dissertation contributed to the general goal of accurately quantifying the effect of land cover changes and of environmental influences on the  $CO_2$  source and sink strengths of terrestrial ecosystems, as well as to generate experimentally based spatiotemporal flux information.

## 8 Danksagung/Acknowledgments

When I started working on this dissertation almost four years ago, the doctorate lay before me like an unclimbable mountain. Without the support of numerous people, this work would have never been possible. During this special time, I was able to learn a lot, both professionally and personally, and despite the Corona pandemic I was able to get to know many new places and to experience unforgettable moments with other people.

Als ich vor knapp vier Jahren angefangen habe auf diese Dissertation hinzuarbeiten, lag die Promotion wie ein unerklimmbarer Berg vor mir. Ohne die Unterstützung zahlreicher Personen wäre mir diese Arbeit niemals möglich gewesen. In dieser besonderen Zeit durfte ich fachlich, aber auch persönlich viel hinzulernen, und konnte trotz Corona Pandemie viele neue Orte kennenlernen und unvergesslich schöne Momente mit anderen Personen erleben.

An erster Stelle möchte ich mich bei meinen Doktorvater **Prof. Dr. Michael Leuchner** dafür bedanken, dass er mir vom ersten Tag an sowie auch nach Rückschlägen und damit verbundenen Zweifeln an der Promotion immer vollstes Vertrauen geschenkt hat. Als Mitglied seiner Arbeitsgruppe konnte ich meine wissenschaftlichen Interessen frei entfalten und hatte immer ein offenes Ohr für fachliche und administrative Fragen. Ich bin ihm für seine freundliche Art dankbar, durch die stets eine sehr kollegiale Atmosphäre in der Arbeitsgruppe geherrscht hat. Durch ihn habe ich kennengelernt, was es heißt für die Wissenschaft zu brennen und bin auch dankbar für die vielen fruchtbaren wissenschaftlichen Diskussionen und Denkanstöße sowie die interessanten Projekte, die ich bearbeiten durfte.

Einen ganz besonderen Dank möchte ich auch meinem Kollegen **Dr. Gunnar Ketzler** für die vielfältige Unterstützung in fachlicher und auch persönlicher Hinsicht aussprechen. Unvergessen bleiben unsere oft vergeblichen und am Ende doch geglückten Versuche die Eddy Kovarianz Station am Wüstebach in Eiseskälte ans Laufen zu kriegen. Durch sein enzyklopädisches Wissen hat er mich zudem die Aachener Region auf spannenden Privatexkursionen näher kennenlernen lassen und meine Promotionszeit durch viele interessante, nicht nur klimatologische Gespräche bereichert.

**Dr. Alexander Graf** vom Forschungszentrum Jülich danke ich für seine große Hilfsbereitschaft mir mit großer Geduld komplexe mikrometeorologische Zusammenhänge zu erklären sowie für seine kritischen Denkanstöße, welche diese Dissertation substantiell verbessert haben. Insbesondere danke ich ihm und dem gesamten **Forschungszentrum Jülich**, dass ich Daten ihrer wissenschaftlichen Arbeit vielfältig für meine Dissertation verwenden durfte, ohne welche diese Arbeit nicht möglich gewesen wäre. Hervorzuheben sind hierbei **Dr. Marius Schmidt** und **Dr. Heye Bogena** für ihre stets hilfsbereite wissenschaftliche Zusammenarbeit und **Daniel Dolfus, Ansgar Weuthen** und **Bernd Schilling** für ihre technische Unterstützung und Wartung der Messgeräte. Dieser Dank gilt ebenso **Dr. Burkhard Neuwirth** von DeLaWi Jahrringanalytik für die freundliche Bereitstellung seiner Saftflussmessungen.

Ich danke ebenfalls **Prof. Dr. Jörg Bendix** von der Philipps Universität Marburg. Durch ihn habe ich während des Studiums das nötige klimatologische und methodische Rüstzeug erhalten. Vor allem aber wurde ich während meiner Zeit als HiWi in seiner Arbeitsgruppe von der Wissenschaft begeistert.

Meinen lieben (ehemaligen) Kolleg\*innen aus der Arbeitsgruppe Physische Geographie und Klimatologie, meinem Bürogenossen Niels Döscher sowie Dr. Eliza Płaczkowska, Larissa Böhrkircher, Dr. Mariam Tsitsagi und Quinghua Yu danke ich neben den vielen Hilfen zwischendurch vor allem für die schönen gemeinsamen Mittagessen und Aktivitäten, sodass der Spaß bei der Arbeit nicht zu kurz gekommen ist. Es hat mir immens geholfen regelmäßig meine Forschungsprobleme in eurer Runde ansprechen zu können. Einen besonderen Dank möchte ich zudem Mona Ziemes und Gernot Frommelt für ihre Hilfe mit allerhand administrativen und technischen Problemen aussprechen. Allen

**Mitarbeiter\*innen des Geographischen Instituts** danke ich, dass Mittwoch Mittag zum Höhepunkt der Woche wurde!

I thank **Prof. Dr. Arturo Sanchez-Azofeifa** and **Prof. Dr. Chakravarthy Balaji** as well as all my **Indian friends at IIT Madras** for hosting me in Canada and India. These two research trips truly enriched my time as a PhD student.

Ich danke auch allen meinen Freunden, darunter besonders Thomas Hauer, Gil Nolde-Zilhao und Andreas Krauskopf. Ihr seid meine zweite Familie. Eure bedingungslose Unterstützung, auch in den schwierigsten Phasen, ist durch nichts aufzuwiegen. Ich danke auch meinen lieben Mitbewohnern Misch Wolter und Dany Teixeira für die vielen schönen Filmabende und Kneipenbesuche und dafür ein angenehmes Zuhause zu haben.

Ich danke meinem Bruder **Daniel Lauer**, meiner **Oma Illa** sowie meiner **gesamten Familie** Teil meines Lebens zu sein. Durch euer Interesse an meiner Arbeit hatte ich die Möglichkeit diese fachfremden Menschen zu erläutern und dabei selbst auf wunde Punkte zu stoßen.

Abschließend danke ich von ganzem Herzen meinen Eltern **Stefani Lauer-Reitz** und **Walter Lauer** dafür, dass ihr eine unverzichtbare Stütze in meinem Leben seid. Ihr habt mich immer bestärkt meinen Interessen nachzugehen und das Geographiestudium durchzuziehen. Ohne eure aufopferungsvolle Unterstützung wäre mir diese Promotion nicht möglich gewesen. Vor allem danke ich euch dafür, dass ich mich immer auf euch verlassen kann.

## 9 References

### 9.1 Publication List

- Reitz, O., Bogena, H., Neuwirth, B., Sanchez-Azofeifa, A., Graf, A., Bates, J., & Leuchner, M. (2023), Environmental Drivers of Gross Primary Productivity and Light Use Efficiency of a Temperate Spruce Forest. *Journal of Geophysical Research: Biogeosciences*, 128(2), e2022JG007197. https://doi.org/10.1029/2022JG007197
- Reitz, O., Graf, A., Schmidt, M., Ketzler, G., & Leuchner, M. (2022), Effects of Measurement Height and Low-Pass-Filtering Corrections on Eddy-Covariance Flux Measurements Over a Forest Clearing with Complex Vegetation. *Boundary-Layer Meteorology*, 184, 277–299. https://doi.org/10.1007/s10546-022-00700-1
- Reitz, O., Graf, A., Schmidt, M., Ketzler, G., & Leuchner, M. (2021a), Upscaling Net Ecosystem Exchange Over Heterogeneous Landscapes With Machine Learning. *Journal of Geophysical Research: Biogeosciences*, 126, e2020JG005814. https://doi.org/10.1029/2020JG005814
- Reitz, O., Yaroslavtsev, A., Meshalkina, J.L., Vasenev, I.I., Vasenev, V., Valentini, R., & Leuchner, M. (2021b), Carbon Dioxide Fluxes of an Urban Forest in Moscow. In: Vasenev, V., et al.:

  Advanced Technologies for Sustainable Development of Urban Green Infrastructure.

  Proceedings of Smart and Sustainable Cities 2020. Springer Geography. Springer, Cham, Switzerland. https://doi.org/10.1007/978-3-030-75285-9\_5

### 9.2 External References

- Abdalla, M., Saunders, M., Hastings, A., Williams, M., Smith, P., Osborne, B., et al. (2013), Simulating the impacts of land use in Northwest Europe on Net Ecosystem Exchange (NEE), The role of arable ecosystems, grasslands and forest plantations in climate change mitigation. *Science of the Total Environment*, 465, 325–336. https://doi.org/10.1016/j.scitotenv.2012.12.030
- Acosta, M., Darenova, E., Krupkova, L., & Pavelka, M. (2018), Seasonal and inter-annual variability of soil CO2 efflux in a Norway spruce forest over an eight-year study. *Agricultural and Forest Meteorology*, 256-257, 93-103. <a href="https://doi.org/10.1016/j.agrformet.2018.03.005">https://doi.org/10.1016/j.agrformet.2018.03.005</a>
- Aide, T. M., Clark, M. L., Grau, H. R., Lopez-Carr, D., Levy, M. A., Redo, D., et al. (2012), Deforestation and Reforestation of Latin America and the Caribbean (2001–2010), *Biotropica*, 45, 262-271. https://doi.org/10.1111/j.1744-7429.2012.00908.x
- Alexandrov, G.A., Brovkin, V.A., Kleinen, T., & Yu, Z. (2020), The capacity of northern peatlands for long-term carbon sequestration. *Biogeosciences*, 17, 47–54. <a href="https://doi.org/10.5194/bg-17-47-2020">https://doi.org/10.5194/bg-17-47-2020</a>
- Ammer, C. (2003), Growth and biomass partitioning of Fagus sylvatica L. and Quercus robur L. seedlings in response to shading and small changes in the R/FR-ratio of radiation. *Annals of Forest Science*, 60, 163–171. <a href="https://doi.org/10.1051/forest:2003009">https://doi.org/10.1051/forest:2003009</a>
- Anav, A., Friedlingstein, P., Beer, C., Ciais, P., Harper, A., Jones, C., et al. (2015), Spatiotemporal patterns of terrestrial gross primary production, A review. *Reviews of Geophysics*, *53*, 785–818. <a href="https://doi.org/10.1002/2015RG000483">https://doi.org/10.1002/2015RG000483</a>
- Andreasen, M., Jensen, K.H., Desiletis, D., Franz, T.E., Zreda, M., Bogena, H.R., & Looms, M.C. (2017), Status and Perspectives on the Cosmic-Ray Neutron Method for Soil Moisture Estimation and

- Other Environmental Science Applications. *Vadose Zone Journal*, 16(8). https://doi.org/10.2136/vzj2017.04.0086
- Appelhans, T., Mwangomo, E., Hardy, D.R., Hemp, A., Nauss, T. (2015), Evaluating machine learning approaches for the interpolation of monthly air temperature at Mt. Kilimanjaro, Tanzania. Spatial Statistics, 14, 91–113. http://dx.doi.org/10.1016/j.spasta.2015.05.008
- Archer, K.J., & Kimes, R.V. (2008), Empirical characterization of random forest variable importance measures. *Computational Statistics & Data Analysis*, 52, 2249–2260. https://doi.org/10.1016/j.csda.2007.08.015
- Arriga, N., Rannik, Ü., Aubinet, M., Carrara, A., Vesala, T., & Papale, D. (2017), Experimental validation of footprint models for eddy covariance CO2 flux measurements above grassland by means of natural and artificial tracers. *Agricultural and Forest Meteorology*, 242, 75–84. <a href="https://doi.org/10.1016/j.agrformet.2017.04.006">https://doi.org/10.1016/j.agrformet.2017.04.006</a>
- Atzberger, C., & Eilers, P.H.C. (2011), A time series for monitoring vegetation activity and phenology at 10-daily time steps covering large parts of South America. *International Journal of Digital Earth*, 4(5), 365–386. https://doi.org/10.1080/17538947.2010.505664
- Aubinet, M. (2008), Eddy covariance CO<sub>2</sub> flux measurements in nocturnal conditions: An analysis of the problem. *Ecological Applications*, 18, 1368–1378. <a href="https://doi.org/10.1890/06-1336.1">https://doi.org/10.1890/06-1336.1</a>
- Aubinet, M., Hurdebise, Q., Chopin, H., Debacq, A., De Ligne, A., Heinesch, B. et al. (2018), Interannual variability of Net Ecosystem Productivity for a temperate mixed forest: A predominance of carry-over effects? *Agricultural and Forest Meteorology*, 262, 340–353. https://doi.org/10.1016/j.agrformet.2018.07.024
- Auvinen, M., Järvi, L., Hellsten, A., Rannik, Ü., & Vesala, T. (2017), Numerical framework for the computation of urban flux footprints employing large-eddy simulation and Lagrangian stochastic modeling. *Geoscientific Model Development*, 10, 4187–4205. https://doi.org/10.5194/gmd-10-4187-2017
- Baatz, R., Bogena, H. R., Hendicks Franssen, H. J., Huisman, J. A., Qu, W., Montzka, C., & Vereecken, H. (2014), Calibration of a catchment scale cosmic-ray probe network: A comparison of three parameterization methods. *Journal of Hydrology*, 516, 231–244. https://doi.org/10.1016/j.jhydrol.2014.02.026
- Baatz R., Bogena, H.R., Hendricks Franssen, H.J., Huisman, J.A., Montzka, C., & Vereecken, H. (2015), An empirical vegetation correction for soil water content quantification using cosmic ray probes. *Water Resources Research*, 51, 2030–2046. https://doi.org/10.1002/2014WR016443
- Baatz, R., Hendricks Franssen, H.J., Han, X., Hoar, T., Bogena, H.R., & Vereecken, H. (2017), Evaluation of a cosmic-ray neutron sensor network for improved land surface model prediction.

  Hydrology and Earth System Science, 21, 2509–2530. <a href="https://doi.org/10.5194/hess-21-2509-2017">https://doi.org/10.5194/hess-21-2509-2017</a>
- Baccini, A., Walker, W., Carvalho, L., Farina, M., Sulla-Menashe, D., & Houghton, R.A. (2017). Tropical forests are a net carbon source based on aboveground measurements of gain and loss. *Nature*, 358(6360), 230–234. <a href="https://doi.org/10.1126/science.aam5962">https://doi.org/10.1126/science.aam5962</a>
- Baldocchi, D.D. (2014), Measuring fluxes of trace gases and energy between ecosystems and the atmosphere the state and future of the eddy covariance method. *Global Change Biology*, 20, 3600-3609. <a href="https://doi.org/10.1111/gcb.12649">https://doi.org/10.1111/gcb.12649</a>
- Baldocchi, D.D. (2019), How eddy covariance flux measurements have contributed to our understanding of Global Change Biology. *Global Change Biology*, 26, 242–260. https://doi.org/10.1111/gcb.14807
- Bao, S., Wutzler, T., Koirala, S., Cuntz, M., Ibrom, A., Besnard, S., et al. (2022), Environment-sensitivity functions for gross primary productivity in light use efficiency models. *Agricultural and Forest Meteorology*, 312, 108708. <a href="https://doi.org/10.1016/j.agrformet.2021.108708">https://doi.org/10.1016/j.agrformet.2021.108708</a>

- Bates, J., Jonard, F., Bajracharya, R., Vereecken, H., & Montzka, C. (2022). Machine Learning with UAS LiDAR for Winter Wheat Biomass Estimations. *AGILE: GIScience Series*, 3, 23. https://doi.org/10.5194/agile-giss-3-23-2022
- Bergen, K.J., Johnson, P.A., de Hoop, M.V., & Beroza, G.C. (2019), Machine learning for data-driven discovery in solid Earth geoscience. *Science*, 63, eaau0323. https://doi.org/10.1126/science.aau0323
- Besnard, S., Carvalhais, N., Arain, M. A., Black. A., Brede, B., Buchmann, N., et al. (2019) Memory effects of climate and vegetation affecting net ecosystem CO<sub>2</sub> fluxes in global forests. *PLoS ONE*, 14(2), e0211510. https://doi.org/10.1371/journal.pone.0211510
- Bodesheim, P., Jung, M., Gans, F., Mahecha, M. D., & Reichstein, M. (2018), Upscaled diurnal cycles of land—atmosphere fluxes: a new global half-hourly data product, *Earth System Science Data*, 10, 1327–1365. https://doi.org/10.5194/essd-10-1327-2018
- Bogena, H.R., Bol, R., Borchard, N., Brüggemann, N., Diekkrüger, B., Drüe, C., et al. (2015), A terrestrial observatory approach to the integrated investigation of the effects of deforestation on water, energy, and matter fluxes. *Science China, Earth Sciences*, 57, 1-6. <a href="https://doi.org/10.1007/s11430-014-4911-7">https://doi.org/10.1007/s11430-014-4911-7</a>
- Bogena, H., Borg, E., Brauer, A., Dietrich, P., Hajnsek, I., Heinrich, I., et al. (2016), TERENO: German network of terrestrial environmental observatories. *Journal of large-scale research facilities*, 2, A52. http://dx.doi.org/10.17815/jlsrf-2-98
- Bogena, H., Herbst, M., Hake, J.F., Kunkel, R., Montzka, C., Pütz, T., et al. (2005), MOSYRUR. Water balance analysis in the Rur basin. Schriften des Forschungszentrums Jülich Reihe Umwelt/Environment, Band/Volume 52. Jülich, Germany.
- Bogena, H.R., Herbst, M., Huisman, J.A., Rodenbaum, U., Weuthen, A., & Vereecken, H. (2010), Potential of Wireless Sensor Networks for Measuring Soil Water Content Variability. *Vadose Zone Journal*, 9, 1002–1013. <a href="https://doi.org/10.2136/vzj2009.0173">https://doi.org/10.2136/vzj2009.0173</a>
- Bogena, H.R., Montzka, C., Huisman, J.A., Graf, A., Schmidt, M., Stockinger, M., et al. (2018), The TERENO-Rur Hydrological Observatory, A Multiscale Multi-compartment Research Platform for the Advancement of Hydrological Science. *Vadose Zone Journal*, 17, 1–22. <a href="https://doi.org/10.2136/vzj2018.03.0055">https://doi.org/10.2136/vzj2018.03.0055</a>
- Bollmeyer, C., Keller, J. D., Ohlwein, C., Wahl, S., Crewell, S., Friederichs, P., et al. (2015), Towards a high-resolution regional re-analysis for the European CORDEX domain. *Quarterly Journal of the Royal Meteorological Society*, 141, 1–15. https://doi.org/10.1002/qj.2486
- Bond-Lamberty, B., Wang, C., & Gower, S.T. (2004), A global relationship between the heterotrophic and autotrophic components of soil respiration? *Global Change Biology*, 10, 1756–1766. https://doi.org/10.1111/j.1365-2486.2004.00816.x
- Borchard, N., Schirrmann, M., von Hebel, C., Schmidt, M., Baatz, R., Firbank, L., et al. (2015), Spatiotemporal drivers of soil and ecosystem carbon fluxes at field scale in an upland grassland in Germany. *Agriculture, Ecosystems and Environment,* 211, 84-93. <a href="https://doi.org/10.1016/j.agee.2015.05.008">https://doi.org/10.1016/j.agee.2015.05.008</a>
- Borchardt, H. (2012), Einfluss periglazialer Deckschichten auf Abflusssteuerung am Beispiel des anthropogen überprägten Wüstebaches (Nationalpark Eifel), (Doctoral dissertation). Retrieved from RWTH publications. (urn:nbn:de:hbz:82-opus-45676). Aachen, Germany: RWTH Aachen University.
- Breiman, L. (2001), Random Forests. *Machine Learning*, *45*, 5-32. https://doi.org/10.1023/A:1010933404324
- Brinkmann, N., Eugster, W., Zweifel, R., Buchmann, N., & Kahmen, A. (2016), Temperate tree species show identical response in tree water deficit but different sensitivities in sap flow to summer soil drying. *Tree Physiology*, *36*, 1508–1519. <a href="https://doi.org/10.1093/treephys/tpw062">https://doi.org/10.1093/treephys/tpw062</a>

- Burba, G.G. (2013), Eddy covariance method for scientific, industrial, agricultural and regulatory applications. LI-COR Biosciences, Lincoln, USA.
- Burba, G.G. (2022), Eddy covariance method for scientific, industrial, agricultural and regulatory applications. LI-COR Biosciences, Lincoln, USA.
- Burba G.G., & McDermitt, D.K., Grelle, A., Anderson, D.J., Xu, L. (2008), Addressing the influence of instrument surface heat exchange on the measurements of CO2 flux from open-path gas analyzers. *Global Change Biology*, *14*, 1854–1876. <a href="https://doi.org/10.1111/j.1365-2486.2008.01606.x">https://doi.org/10.1111/j.1365-2486.2008.01606.x</a>
- Cabon, A., Kannenberg, A., Arain, A., Babst, F., Baldocchi, D., Belmecheri, S., et al. (2022), Cross-biome synthesis of source versus sink limits to tree growth. *Science*, 376, 758–761. https://doi.org/10.1126/science.abm4875
- Canadell, J.G., Monteiro, P.M.S., Costa, M.H., Cotrim da Cunha, L., Cox, P.M., Eliseev, A.V., et al. (2021), Global Carbon and other Biogeochemical Cycles and Feedbacks. In *Climate Change 2021, The Physical Science Basis. Contribution of Working Group I to the Sixth Assessment Report of the Intergovernmental Panel on Climate Change* (pp. 673–816). Cambridge, United Kingdom and New York, NY, USA: Cambridge University Press. <a href="https://doi.org/10.1017/9781009157896.007">https://doi.org/10.1017/9781009157896.007</a>
- Castro, S.M., Sanchez-Azofeifa, G.A., & Sato, H. (2018), Effect of drought on productivity in a Costa Rican tropical dry forest. *Environmental Research Letters*, 13, 045001. https://doi.org/10.1088/1748-9326/aaacbc
- Chapin, F.S., McFarland, J., McGuire, A.D., Euskirchen, E.S., Ruess, R.W., & Kielland, K. (2009), The changing global carbon cycle: linking plant—soil carbon dynamics to global consequences. *Journal of Ecology*, 97, 840–850. https://doi.org/10.1111/j.1365-2745.2009.01529.x
- Chen, B., Black, T. A., Coops, N. C., Hilker, T., Trofymow, J. A., & Morgenstern, K. (2009), Assessing Tower Flux Footprint Climatology and Scaling Between Remotely Sensed and Eddy Covariance Measurements. *Boundary Layer Meteorology*, 130, 137–167. https://doi.org/10.1007/s10546-008-9339-1
- Chen, C., He, W., Zhou, H., Xue, Y., & Zhu, M. (2020), A comparative study among machine learning and numerical models for simulating groundwater dynamics in the Heihe River Basin, northwestern China. *Scientific Reports*, 10, 3904. <a href="https://doi.org/10.1038/s41598-020-60698-9">https://doi.org/10.1038/s41598-020-60698-9</a>
- Chen, T., & Guestrin, C. (2016), XGBoost, A Scalable Tree Boosting System. *Proceedings of the 22nd ACM SIGKDD International Conference on Knowledge Discovery and Data Mining*, 785–794. https://doi.org/10.48550/arXiv.1603.02754
- Chu, H., Luo, X., Ouyang, Z., Chan, W.S., Dengel, S., et al. (2021), Representativeness of eddy-covariance flux footprints for areas surrounding AmeriFlux sites. Agricultural and Forest Meteorology 301–302, 108350. https://doi.org/10.1016/j.agrformet.2021.108350
- Ciais, P., Bastos, A., Chevallier, F., Lauerwald, R., Poulter, B., Canadell, J.G., et al. (2022), Definitions and methods to estimate regional land carbon fluxes for the second phase of the REgional Carbon Cycle Assessment and Processes Project (RECCAP-2). *Geoscientific Model Development*, 15, 1289–1316. <a href="https://doi.org/10.5194/gmd-15-1289-2022">https://doi.org/10.5194/gmd-15-1289-2022</a>
- Clark, K.L., Skowronski, N., Hom, J., & Heilman, W.E. (2009), Fireflux Experiments in the New Jersey Pine Barrens. *Eighth Symposium on Fire and Forest Meteorology*, P1.8.
- Cosh, M.H., White, W.A., Colliander, A., Jackson, T.J., Prueger, J.H., Hornbuckle, B.K., et al. (2019), Estimating vegetation water content during the Soil Moisture Active Passive Validation Experiment 2016. *Journal of Applied Remote Sensing*, 13(1), 014516. <a href="https://doi.org/10.1117/1.JRS.13.014516">https://doi.org/10.1117/1.JRS.13.014516</a>

- Croft, H., Chen, J.M., Froelich, N.J., Chen, B., & Staebler, R.M. (2015), Seasonal controls of canopy chlorophyll content on forest carbon uptake, Implications for GPP modeling. *Journal of Geophysical Research, Biogeosciences*, 120, 1576–1586. <a href="https://doi.org/10.1002/2015JG002980">https://doi.org/10.1002/2015JG002980</a>
- Cutler, D.R., Edwards, T.C., Beard, K.H., Cutler, A., Hess, K. T., Gibson, J., & Lawler, J. J. (2007), Random forests for classification in ecology. *Ecology*, 88, 2783–2792.
- Debeer, D., & Strobl, C. (2020), Conditional permutation importance revisited. *BMC Bioinformatics*, 21, 307. <a href="https://doi.org/10.1186/s12859-020-03622-2">https://doi.org/10.1186/s12859-020-03622-2</a>
- Dellwik, E., & Jensen, N.O. (2005), Flux-profile relationships over a fetch limited beech forest.

  Boundary-Layer Meteorology 115, 179–204. https://doi.org/10.1007/s10546-004-3808-y
- Delwiche, K.B., Knox, S.H., Malhotra, A., Fluet-Chouinard, E., McNicol, G., Feron, S., et al. (2021), FLUXNET-CH4: a global, multi-ecosystem dataset and analysis of methane seasonality from freshwater wetlands. *Earth System Science Data*, 13, 3607–3689. https://doi.org/10.5194/essd-13-3607-2021
- Dengel, S., Grace, J., & MacArthur, A. (2015), Transmissivity of solar radiation within a Picea sitchensis stand under various sky conditions. *Biogeosciences*, 12, 4195–4207. https://doi.org/10.5194/bg-12-4195-2015
- Denissen, J.M.C., Teuling, A.J., Pitman, A.J., Koirala, S., Migliavacca, M., Li, W., et al. (2022), Widespread shift from ecosystem energy to water limitation with climate change. *Nature Climate Change*, 12, 677–684. https://doi.org/10.1038/s41558-022-01403-8
- Denman, K. L., Brasseur, G., Chidthaisong, A., Ciais, P., Cox, P. M., Dickinson, R. E., et al. (2007), Couplings Between Changes in the Climate System and Biogeochemistry. In Solomon, S., D. Qin, M. Manning, Z. Chen, M. Marquis, K.B. Averyt, et al. (Eds.) *Climate Change 2007: The Physical Science Basis. Contribution of Working Group I to the Fourth Assessment Report of the Intergovernmental Panel on Climate Change* (pp. 499-588), Cambridge University Press, Cambridge, United Kingdom and New York, NY, USA.
- Desai, A.R. (2014), Influence and predictive capacity of climate anomalies on daily to decadal extremes in canopy photosynthesis. *Photosynthesis Research*, 119, 31–47. https://doi.org/10.1007/s11120-013-9925-z
- Detto, M., Katul, G.G., Siqueira, M., Juang, J.Y., & Stoy, P. (2008), The structure of turbulence near a tall forest edge: The backward-facing step flow analogy revisited. *Ecological Applications*, 18(6), 1420–1435. <a href="https://doi.org/10.1890/06-0920.1">https://doi.org/10.1890/06-0920.1</a>
- Didan, K. (2015), MOD13Q1 MODIS/Terra Vegetation Indices 16-Day L3 Global 250m SIN Grid V006 [Data set]. NASA EOSDIS Land Processes DAAC. Accessed 2020-02-06 from <a href="https://doi.org/10.5067/MODIS/MOD13Q1.006">https://doi.org/10.5067/MODIS/MOD13Q1.006</a>
- Dimiceli, C., Carroll, M., Sohlberg, R., Kim, D.H., Kelly, M., & Townshend, J.R.G. (2015), MOD44B MODIS/Terra Vegetation Continuous Fields Yearly L3 Global 250m SIN Grid V006 [Data set]. NASA EOSDIS Land Processes DAAC. Accessed 2020-02-06 from <a href="https://doi.org/10.5067/MODIS/MOD44B.006">https://doi.org/10.5067/MODIS/MOD44B.006</a>
- Doelman, J.C., Stehfest, E., van Vuuren, D.P., Tabeau, A., Hof, A.F., Braakhekke, M.C., et al. (2019), Afforestation for climate change mitigation: Potentials, risks and trade-offs. *Global Change Biology*, 26, 1576–1591. https://doi.org/10.1111/gcb.14887
- Doroszewski, A., Gorski, T., & Kozyra, J. (2015), Atmospheric moisture controls far-red irradiation, a probable impact on the phytochrome. *International Agrophysics*, 29, 283–289. https://doi.org/10.1515/intag-2015-0033
- Dou, X., Yang, Y., & Luo, J. (2018), Estimating Forest Carbon Fluxes Using Machine Learning Techniques Based on Eddy Covariance Measurements. *Sustainability*, 10(1), 203. https://doi.org/10.3390/su10010203

- Dramsch, J.S. (2020), 70 years of machine learning in geoscience in review. Advances in Geophysics, 61, 1–55. <a href="https://doi.org/10.1016/bs.agph.2020.08.002">https://doi.org/10.1016/bs.agph.2020.08.002</a>
- Drusch, M., Del Bello, U., Carlier, S., Colin, O., Fernandez, V., Gascon, F., et al. (2012), Sentinel-2: ESA's Optical High-Resolution Mission for GMES Operational Services. *Remote Sensing of Environment*, 120, 25–36. https://doi.org/10.1016/j.rse.2011.11.026
- Dusenge, M.E., Duarte, A.G., & Way, D.A. (2019), Plant carbon metabolism and climate change, elevated CO<sub>2</sub> and temperature impacts on photosynthesis, photorespiration and respiration. *New Phytologist*, 221, 32–49. https://doi.org/10.1111/nph.15283
- DWD Climate Data Center (2019), Daily grids of potential evapotranspiration over grass and soil moisture under grass and sandy loam, version 0.x
- DWD Deutscher Wetterdienst (2022), Vieljährige Mittelwerte. Retrieved on 14.03.2023. https://www.dwd.de/DE/leistungen/klimadatendeutschland/vielj\_mittelwerte.html
- Ecomatik. (2005), User manual for SF-L Sensor-Patent pending. Version 1.3. Dachau, Germany: Ecomatik Umweltmess-und Datentechnik. 9
- Eder, F., Schmidt, M., Damian, T., Träumner, K., & Mauder, M. (2015), Mesoscale Eddies Affect Near-Surface Turbulent Exchange: Evidence from Lidar and Tower Measurements. *Journal of Applied Meteorology and Climatology, 54,* 189–206. <a href="https://doi.org/10.1175/JAMC-D-14-0140.1">https://doi.org/10.1175/JAMC-D-14-0140.1</a>
- Efron, B. (1979), Bootstrap Methods: Another Look at the Jackknife. *The Annals of Statistics*, 7, 1-26. Estoque, R.C., Dasgupta, R., Winkler, K., Avitable, V., Johnson, B.A., Myint, S.W, et al. (2022), Spatiotemporal pattern of global forest change over the past 60 years and the forest transition theory. *Environmental Research Letters*, 17, 084022. <a href="https://doi.org/10.1088/1748-9326/ac7df5">https://doi.org/10.1088/1748-9326/ac7df5</a>
- Etmann M. (2009), Dendrologische Aufnahmen im Wassereinzugsgebiet Oberer Wüstebach anhand verschiedener Mess- und Schätzverfahren, (Master thesis). Retrieved from JUSER. (https://juser.fz-juelich.de/record/10505). Münster, Germany: University of Münster.
- Eugster, W., & Merbold, L. (2015), Eddy covariance for quantifying trace gas fluxes from soils. *SOIL*, 1, 187–205. https://doi.org/10.5194/soil-1-187-2015
- Ewers, B.E., Mackay, D.S., & Samanta, S. (2007), Interannual consistency in canopy stomatal conductance control of leaf water potential across seven tree species. *Tree Physiology*, 27, 11–24. https://doi.org/10.1093/treephys/27.1.11
- Farquhar, G.D., von Caemmerer, S., & Berry, J.A. (1980). A Biochemical Model of Photosynthetic CO<sub>2</sub>
  Assimilation in Leaves of C<sub>3</sub> Species. *Planta*, 149, 78-90. <a href="https://doi.org/10.1007/BF00386231">https://doi.org/10.1007/BF00386231</a>
- Feng, C., Wang, H., Lu, N., Chen, T., He, H., Lu, Y., & Tu, X.M. (2014), Log-transformation and its implications for data analysis. *Shanghai Archives of Psychiatry*, 26, 105–109. https://doi.org/10.3969/j.issn.1002-0829.2014.02.009
- Finkelstein, P.L., & Sims, P.F. (2001), Sampling error in eddy correlation flux measurements. *Journal of Geophysical Research*, 106, 3503–3509. <a href="https://doi.org/10.1029/2000JD900731">https://doi.org/10.1029/2000JD900731</a>
- Finnigan, J. (2008), An Introduction to Flux Measurements in Difficult Conditions. *Ecological Applications*, 18(6), 1340–1350. <a href="https://doi.org/10.1890/07-2105.1">https://doi.org/10.1890/07-2105.1</a>
- Fischer, L., Breitenlechner, M., Canaval, E., Scholz, W., Striednig, M., Graus, M., et al. (2021), First eddy covariance flux measurements of semi-volatile organic compounds with the PTR3-TOF-MS. *Atmospheric Measurement Techniques*, 14, 8019–8039. <a href="https://doi.org/10.5194/amt-14-8019-2021">https://doi.org/10.5194/amt-14-8019-2021</a>
- Foken, T. (2008), The energy balance closure problem: an overview. *Ecological Applications*, 18(6), 1351–1367. https://doi.org/10.1890/06-0922.1

- Foken, T., Aubinet, M., & Leuning, R. (2012), The Eddy Covariance Method. In: Aubinet, M., Vesala, T., & Papale, D. (eds), Eddy covariance. A practical guide to measurement and data analysis. Springer, Dordrecht Heidelberg London New York, pp 1–19.
- Foken, T., Mauder, M., Liebethal, C., Wimmer, F., Beyrich, F., Leps, J.P., et al. (2010), Energy balance closure for the LITFASS-2003 experiment. *Theoretical and Applied Climatology*, 101, 149–160. https://doi.org/10.1007/s00704-009-0216-8
- Foken, T., & Wichura, B. (1996), Tools for quality assessment of surface-based flux measurements. Agricultural and Forest Meteorology, 78, 83-105. <a href="https://doi.org/10.1016/0168-1923(95)02248-1">https://doi.org/10.1016/0168-1923(95)02248-1</a>
- Foyer, C.H., Bloom, A.J., Queval, G. & Noctor, G. (2009), Photorespiratory Metabolism: Genes, Mutants, Energetics, and Redox Signaling. *Annual Reviews of Plant Biology*, 60, 455–84. https://doi.org/10.1146/annurev.arplant.043008.091948
- Fratini, G., Ibrom, A., Arriga, N., Burba, G., & Papale, D. (2012), Relative humidity effects on water vapour fluxes measured with closed-path eddy-covariance systems with short sampling lines. *Agricultural and Forest Meteorology*, 165, 53–63.

  <a href="https://doi.org/10.1016/j.agrformet.2012.05.018">https://doi.org/10.1016/j.agrformet.2012.05.018</a>
- Fratini, G., & Mauder, M. (2014), Towards a consistent eddy-covariance processing: an intercomparison of EddyPro and TK3. *Atmospheric Measurement Techniques*, 7, 2273–2281. https://doi.org/10.5194/amt-7-2273-2014
- Friedlingstein, P., Bopp, L., Ciais, P., Dufresne, J.L., Fairhead, L., Letreut, H., et al. (2001), Positive feedback between future climate change and the carbon cycle. *Geophysical Research Letters*, 28(8), 1543–1546. <a href="https://doi.org/10.1029/2000GL012015">https://doi.org/10.1029/2000GL012015</a>
- Friedlingstein, P., Jones, M.W., O'Sullivan, M.O., Andrew, R.M., Bakker, D.C.E., Hauck, J., et al. (2022), Global Carbon Budget 2021. Earth System Scientific Data, 14, 1917–2005. https://doi.org/10.5194/essd-14-1917-2022
- Friedman, J.H. (2002), Stochastic gradient boosting. *Computational Statistics & Data Analysis*, 38, 367–378. https://doi.org/10.1016/S0167-9473(01)00065-2
- Fu, Z., Ciais, P., Makowski, D., Bastos, A., Stoy, P.C., Ibrom, A., et al. (2021), Uncovering the critical soil moisture thresholds of plant water stress for European ecosystems. *Global Change Biology*, 28, 2111–2123. https://doi.org/10.1111/gcb.16050
- Gamon, J.A., Serrano, L., & Surfus, J.S. (1997), The photochemical reflectance index: an optical indicator of photosynthetic radiation use efficiency across species, functional types, and nutrient levels. *Oecologia*, 112, 492–501. https://doi.org/10.1007/s004420050337
- Garbulsky, M.F., Penuelas, J., Gamon, J., Inoue, Y., & Filella I. (2011), The photochemical reflectance index (PRI) and the remote sensing of leaf, canopy and ecosystem radiation use efficiencies. A review and meta-analysis. *Remote Sensing of Environment*, 115, 281–297. https://doi.org/10.1016/j.rse.2010.08.023
- Garbulsky, M.F., Penuelas, J., Papale, D., Ardö, J., Goulden, M.L., Kiely, G., et al. (2010), Patterns and controls of the variability of radiation use efficiency and primary productivity across terrestrial ecosystems. *Global Ecology and Biogeography*, 19, 253–267. https://doi.org/10.1111/j.1466-8238.2009.00504.x
- Gash, J.H.C. (1986), A note on estimating the effect of a limited fetch on micrometeorological evaporation measurements. *Boundary-Layer Meteorology*, 35, 409–413. https://doi.org/10.1007/BF00118567
- Gasser, T., Crepin, L., Quilcaille, Y., Houghton, R.A., Ciais, P., & Obersteiner, M. (2020), Historical CO2 emissions from land use and land cover change and their uncertainty. *Biogeosciences*, 17, 4075–4101. https://doi.org/10.5194/bg-17-4075-2020

- Gatti, L.V., Basso, L.S., Miller, J.B., Gloor, M., Domingues, L.G., Cassol, H.L.G., et al. (2021), Amazonia as a carbon source linked to deforestation and climate change. *Nature*, 595, 388–393. https://doi.org/10.1038/s41586-021-03629-6
- Gebler, S., Hendricks Franssen, H.-J., Pütz, T., Post, H., Schmidt, M., & Vereecken, H. (2015), Actual evapotranspiration and precipitation measured by lysimeters: a comparison with eddy covariance and tipping bucket. *Hydrology and Earth System Sciences, 19,* 2145–2161. https://doi.org/10.5194/hess-19-2145-2015
- Genesio, L., Bassi, R., & Miglietta, F. (2021), Plants with less chlorophyll: A global change perspective. Global Change Biology, 27(5), 959–967. https://doi.org/10.1111/gcb.15470
- Gitelson, A.A., & Gamon, J.A. (2015), The need for a common basis for defining light-use efficiency, Implications for productivity estimation. *Remote Sensing of Environment*, 156, 196–201. https://doi.org/10.1016/j.rse.2014.09.017
- Gitelson, A.A., Peng, Y., Arkebauer, T.J., & Schepers, J. (2014), Relationships between gross primary production, green LAI, and canopy chlorophyll content in maize, Implications for remote sensing of primary production. *Remote Sensing of Environment*, 144, 65–72. <a href="https://doi.org/10.1016/j.rse.2014.01.004">https://doi.org/10.1016/j.rse.2014.01.004</a>
- Göckede, M., Markkanen, T., Hasager, C.B., & Foken, T. (2006), Update of a Footprint-Based Approach for the Characterisation of Complex Measurement Sites. *Boundary-Layer Meteorology*, 118, 635–655. https://doi.org/10.1007/s10546-005-6435-3
- Goldstein, G., Andrade, J.L., Meinzer, F.C., Holbrook, N.M., Cavelier, J., Jackson, P., & Celis, A. (1998). Stem water storage and diurnal patterns of water use in tropical forest canopy trees. *Plant, Cell and Environment*, 21, 397–406. <a href="https://doi.org/10.1046/j.1365-3040.1998.00273.x">https://doi.org/10.1046/j.1365-3040.1998.00273.x</a>
- Gonsamo, A., & Chen, J.M. (2018), Vegetation Primary Productivity. In: Liang, S., Comprehensive Remote Sensing, 3, 163-189. Elsevier. <a href="https://doi.org/10.1016/B978-0-12-409548-9.10535-4">https://doi.org/10.1016/B978-0-12-409548-9.10535-4</a>
- Gorham, E., Lehman, C., Dyke, A., Clymo, D., & Janssens, J. (2012), Long-term carbon sequestration in North American peatlands. *Quaternary Science Reviews*, 28, 77–82. https://doi.org/10.1016/j.quascirev.2012.09.018
- Goulden, M.L., Daube, B.C., Fan, S.M., Sutton, D.J., Bazzaz, A., Munger, J.W., & Wofsy, S.C. (1997), Physiological responses of a black spruce forest to weather. *Journal of Geophysical Research*, 102, 28987–28996. https://doi.org/10.1029/97JD01111
- Goulden, M.L., Munger, W., Fan, S.M., Daube, B.C., Wofsy, S.C. (1996), Measurements of carbon sequestration by long-term eddy covariance: methods and a critical evaluation of accuracy. *Global Change Biology*, 2(3), 169–182. https://doi.org/10.1111/j.1365-2486.1996.tb00070.x
- Graf, A., Bogena, H. R., Drüe, Hardelauf, H., Pütz, T., Heinemann, G., & Vereecken, H. (2014), Spatiotemporal relations between water budget components and soil water content in a forested tributary catchment, *Water Resource Research*, *50*, 4837–4857. <a href="https://doi.org/10.1002/2013WR014516">https://doi.org/10.1002/2013WR014516</a>
- Graf, A., Klosterhalfen, A., Arriga, N., Bernhofer, C., Bogena, H., & Bornet, F. et al. (2020), Altered energy partitioning across terrestrial ecosystems in the European drought year 2018. *Philosophical transactions of the Royal Society of London. Series B, Biological sciences*, 375, 20190524. <a href="https://doi.org/10.1098/rstb.2019.0524">https://doi.org/10.1098/rstb.2019.0524</a>
- Graf, A., Werner, J., Langensiepen, M., van de Boer, A., Schmidt, M., Kupisch, M., & Vereecken, H. (2013), Validation of a minimum microclimate disturbance chamber for net ecosystem flux measurements. *Agricultural and Forest Meteorology*, 174–175, 1–14. <a href="http://dx.doi.org/10.1016/j.agrformet.2013.02.001">http://dx.doi.org/10.1016/j.agrformet.2013.02.001</a>
- Granier, A. (1987), Evaluation of transpiration in a Douglas-fir stand by means of sap flow measurements. *Tree Physiology* 3, 309–320. <a href="https://doi.org/10.1093/treephys/3.4.309">https://doi.org/10.1093/treephys/3.4.309</a>

- Green, D.S., Erickson, J.E., & Kruger, E.L. (2003), Foliar morphology and canopy nitrogen as predictors of light-use efficiency in terrestrial vegetation. *Agricultural and Forest Meteorology*, 115, 163–171. https://doi.org/10.1016/S0168-1923(02)00210-1
- Griebel, A., Metzen, D., Pendall, E., Burba, G., & Metzger, S. (2020), Generating spatially robust carbon budgets from flux tower observations. *Geophysical Research Letters*, 47, e2019GL085942. https://doi.org/10.1029/2019GL085942
- Grömping, U. (2009), Variable Importance Assessment in Regression, Linear Regression versus Random Forest. *The American Statistician* 63, 308–319. https://doi.org/10.1198/tast.2009.08199
- Hall, M. A., & Smith, L. A. (1999), Feature Selection for Machine Learning: Comparing a Correlation-based Filter Approach to the Wrapper. *Proceedings of the Twelfth International FLAIRS Conference*, 235–239.
- Hansis, E., Davis, S.J., & Pongratz, J. (2015), Relevance ofmethodological choices for accounting of land use change carbon fluxes. *Global Biogeochemical Cycles*, 29, 1230–1246. https://doi.org/10.1002/2014GB004997
- Hastie, T.J., & Tibshirani, R.J. (1990), Generalized Additive Models. London, UK: Chapman and Hall.
- Hedges, L.V., Gurevitch, J., & Curtis, P.S. (1999), The Meta-Analysis of Response Ratios in Experimental Ecology. *Ecology*, 80, 1150–1156. <a href="https://doi.org/10.1890/0012-9658(1999)080[1150:TMAORR]2.0.CO;2">https://doi.org/10.1890/0012-9658(1999)080[1150:TMAORR]2.0.CO;2</a>
- Heiskanen, J., Brümmer, C., Buchmann, N., Calfapietra, C., Chen, H., Gielen, B., et al. (2022), The Integrated Carbon Observation System in Europe. *Bulletin of the American Meteorological Society*, 103(3), 855–872. <a href="https://doi.org/10.1175/BAMS-D-19-0364.1">https://doi.org/10.1175/BAMS-D-19-0364.1</a>
- Heldt, H.W., & Piechulla, B. (2015), Pflanzenbiochemie. 5. Auflage. Springer Spektrum Berlin, Heidelberg, Germany. <a href="https://doi.org/10.1007/978-3-662-44398-9">https://doi.org/10.1007/978-3-662-44398-9</a>
- Heraut-Bron, V., Robin, C., Varlet-Grancher, C., Afif, D., & Guckert, A. (2000), Light quality (red,far-red ratio), does it affect photosynthetic activity, net CO2 assimilation, and morphology of young white clover leaves? *Canadian Journal of Botany*, 77, 1425 –1431. https://doi.org/10.1139/b99-099
- Hertel, C., Leuchner, M., & Menzel, A. (2011), Vertical variability of spectral ratios in a mature mixed forest stand. *Agricultural and Forest Meteorology*, 151, 1096–1105. https://doi.org/10.1016/j.agrformet.2011.03.013
- Hijmans, G. (2020), raster: Geographic Data Analysis and Modeling. R package version 3.0-12. https://CRAN.R-project.org/package=raster
- Hong, C., Burney, J.A., Pongratz, J., Nabel, J.E.M.S., Mueller, N.D., Jackson, R.B., & Davis, S.J. (2021), Global and regional drivers of land-use emissions in 1961–2017. *Nature*, 589, 554–561. https://doi.org/10.1038/s41586-020-03138-y
- Horn, J.E., & Schulz, K. (2011), Identification of a general light use efficiency model for gross primary production. *Biogeosciences*, 8, 999–1021. <a href="https://doi.org/10.5194/bg-8-999-2011">https://doi.org/10.5194/bg-8-999-2011</a>
- Horst, T.W. (1997), A simple formula for attenuation of eddy fluxes measured with first-order-response scalar sensors. *Boundary-Layer Meteorology*, 82, 219–233. https://doi.org/10.1023/A:1000229130034
- Horst, T.W., & Lenschow, D.H. (2009), Attenuation of scalar fluxes measured with spatially-displaced sensors. *Boundary-Layer Meteorology*, 130, 275–300. <a href="https://doi.org/10.1007/s10546-008-9348-0">https://doi.org/10.1007/s10546-008-9348-0</a>
- Hothorn, T., Hornik, K., & Zeileis, A. (2006), Unbiased Recursive Partitioning: A Conditional Inference Framework. *Journal of Computational and Graphical Statistics*, 15:3, 651–674, <a href="https://doi.org/10.1198/106186006X133933">https://doi.org/10.1198/106186006X133933</a>

- Houghton, R.A, & Nassikas, A.A. (2017), Global and regional fluxes of carbon from land use and land cover change 1850–2015. *Global Biogeochemical Cycles*, 31, 456–472, <a href="https://doi.org/10.1002/2016GB005546">https://doi.org/10.1002/2016GB005546</a>
- Ibrom, A., Dellwik, E., Klyvberg, H., Jensen, N.O., & Pilegaard, K. (2007), Strong low-pass filtering effects on water vapour flux measurements with closed-path eddy correlation systems. *Agricultural and Forest Meteorology*, 147, 140–156. https://doi.org/10.1016/j.agrformet.2007.07.007
- Ichii, K., Ueyama, M., Kondo, M., Saigusa, N., Lim, J., Alberto, M.C., et al. (2017). New data-driven estimation of terrestrial CO2 fluxes in Asia using a standardized database of eddy covariance measurements, remote sensing data, and support vector regression. *Journal of Geophysical Research: Biogeosciences*, 122, 767–795, https://doi.org/10.1002/2016JG003640
- Ishtiaq, K.S., & Abdul-Aziz, O.I. (2015), Relative Linkages of Canopy-Level CO2 Fluxes with the Climatic and Environmental Variables for US Deciduous Forests. *Environmental Management*, 55, 943–960. https://doi.org/10.1007/s00267-014-0437-1
- Jahns, P., & Holzwarth, A.R. (2012), The role of the xanthophyll cycle and of lutein in photoprotection of photosystem II. *Biochimica et Biophysica Acta*, 1817, 182–193. https://doi.org/10.1016/j.bbabio.2011.04.012
- Jakobi, J., Huisman, J.A., Schrön, M., Fiedler, J., Brogi, C., Vereecken, H., & Bogena, H.R. (2020), Error Estimation for Soil Moisture Measurements With Cosmic Ray Neutron Sensing and Implications for Rover Surveys. *Frontiers in Water*, 2(10). https://doi.org/10.3389/frwa.2020.00010
- James, G., Witten, D., Hastie, T., Tibshirani, R. (2021), An Introduction to Statistical Learning. Springer New York, NY, USA. <a href="https://doi.org/10.1007/978-1-4614-7138-7">https://doi.org/10.1007/978-1-4614-7138-7</a>
- Jarvis, A., Reuter, H. I., Nelson, A., & Guevara, E. (2008), Hole-filled seamless SRTM data V4.

  International Centre for Tropical Agriculture (CIAT), available from <a href="http://srtm.csi.cgiar.org">http://srtm.csi.cgiar.org</a>
- Jegede, O.O., & Foken, T. (1999), A study of the internal boundary layer due to a roughness change in neutral conditions observed during the LINEX field campaigns. *Theoretical and Applied Climatology*, 62, 31–41. <a href="https://doi.org/10.1007/s007040050072">https://doi.org/10.1007/s007040050072</a>
- Jung, M., Koirala, S., Weber, U., Ichii, K., Gans, F., Camps-Valls, G., et al. (2019), The FLUXCOM ensemble of global land-atmosphere energy fluxes. Scientific Data, 6, 74. https://doi.org/10.1038/s41597-019-0076-8
- Jung, M., Reichstein, M., Margolis, H. A., Cescatti, A., Richardson, A. D., Arain, M. A., et al. (2011), Global patterns of land-atmosphere fluxes of carbon dioxide, latent heat, and sensible heat derived from eddy covariance, satellite, and meteorological observations. *Journal of Geophysical Research*, 116, G00J07. https://doi.org/10.1029/2010JG001566
- Jung, M., Schwalm, C., Migliavacca, M., Walther, S., Camps-Valls, G., Koirala, S., et al. (2020), Scaling carbon fluxes from eddy covariance sites to globe: synthesis and evaluation of the FLUXCOM approach, *Biogeosciences*, 17, 1343–1365. <a href="https://doi.org/10.5194/bg-17-1343-2020">https://doi.org/10.5194/bg-17-1343-2020</a>
- Jung, M., & Zscheischler, J. (2013), A guided hybrid genetic algorithm for feature selection with expensive cost functions. *Procedia Computer Science*, 18, 2337 2346. https://doi.org/10.1016/j.procs.2013.05.405
- Kämäräinen, M., Tuovinen, J.P., Kulmala, M., Mammarella, I., Aalto, J., Vekuri, H., et al. (2023), Spatiotemporal lagging of predictors improves machine learning estimates of atmosphere–forest CO<sub>2</sub> exchange. *Biogeosciences*, 20, 897–909. https://doi.org/10.5194/bg-20-897-2023
- Kaimal, J.C., & Businger, J.A. (1963), A Continuous Wave Sonic Anemometer-Thermometer. *Journal of Applied Meteorology and Climatology*, 2(1), 156–164. <a href="https://doi.org/10.1175/1520-0450(1963)002<0156:ACWSAT>2.0.CO;2">https://doi.org/10.1175/1520-0450(1963)002<0156:ACWSAT>2.0.CO;2</a>

- Kaimal, J.C., Wyngaard, J.C., Izumi, Y., & Cote, O.R. (1972), Spectral characteristics of surface-layer turbulence. *Quarterly Journal of the Royal Meteorological Society*, 98, 563–589. https://doi.org/10.1002/qj.49709841707
- Kalliokoski, T., Mäkelä, A., Fronzek, S., & Minunno, F. (2018), Decomposing sources of uncertainty in climate change projections of boreal forest primary production. *Agricultural and Forest Meteorology*, 262, 192–205. https://doi.org/10.1016/j.agrformet.2018.06.030
- Katul, G., Cava, D., Poggi, D., Albertson, J., & Mahrt, L. (2004), Stationarity, homogeneity, and ergodicity in canopy turbulence. In: X. Lee et al. (eds.), Handbook of Micrometeorology, 161–180. Springer, Dordrecht, Netherlands. https://doi.org/10.1007/1-4020-2265-48
- Katul, G., Hsieh, C., Bowling, D., Clark, K., Shurpali, N., Turnispeed, A., et al. (1999), Spatial variability of turbulent fluxes in the roughness sublayer of an even-aged pine forest. *Boundary-Layer Meteorology*, 93, 1–28. <a href="https://doi.org/10.1023/A:1002079602069">https://doi.org/10.1023/A:1002079602069</a>
- Katul, G., Leuning, R., & Oren, R. (2003), Relationship between plant hydraulic and biochemical properties derived from a steady-state coupled water and carbon transport model. *Plant, Cell, Environment*, 26, 339–350. https://doi.org/10.1046/j.1365-3040.2003.00965.x
- Keenan, T.F., Baker, I., Barr, A., Ciais, P., Davis, K., Dietze, M., et al. (2012), Terrestrial biosphere model performance for inter-annual variability of land-atmosphere CO₂ exchange. *Global Change Biology*, 18, 1971–1987. https://doi.org/10.1111/j.1365-2486.2012.02678.x
- Kim. Y., Johnson, M.S., Knox, S.H., Black, T.A., Dalmagro, H.J., Kang, M., et al. (2019). Gap-filling approaches for eddy covariance methane fluxes: A comparison of three machine learning algorithms and a traditional method with principal component analysis. *Global Change Biology*, 26, 1499–1518. <a href="https://doi.org/10.1111/gcb.14845">https://doi.org/10.1111/gcb.14845</a>
- Kirschbaum, M.U.F., Eamus, D., Gifford, R.M., Roxburgh, S.H., & Sands, P.J. (2001), Definitions Of Some Ecological Terms Commonly Used In Carbon Accounting. NEE Workshop Proceedings 2001, 2–5.
- Kirschbaum, M.U.F., Whitehead, D., Dean, S.M., Beets, P.N., Shepherd, J.D., & Ausseil, A.G.E. (2011), Implications of albedo changes following afforestation on the benefits of forests as carbon sinks. *Biogeosciences*, 8, 3687–3696. https://doi.org/10.5194/bg-8-3687-2011
- Klein, T., Rotenberg, E., Tatarinov, F., & Yakir, D. (2016), Association between sap flow-derived and eddy covariance-derived measurements of forest canopy CO<sub>2</sub> uptake. *New Phytologist*, 209, 436–446. https://doi.org/10.1111/nph.13597
- Kljun, N., Calanca, P., Rotach, M.W., & Schmid, H.P. (2015), A simple two-dimensional parameterisation for Flux Footprint Prediction (FFP). *Geoscientific Model Development*, 8, 3695–3713. <a href="https://doi.org/10.5194/gmd-8-3695-2015">https://doi.org/10.5194/gmd-8-3695-2015</a>
- Köstner, B., Granier, A., & Cermak, J. (1998), Sapflow measurements in forest stands, methods and uncertainties. *Annals of Forest Science*, 55, 13–27. <a href="https://doi.org/10.1051/forest:19980102">https://doi.org/10.1051/forest:19980102</a>
- Kohsiek, W., Liebethal, C., Foken, T., Vogt, R., Oncley, S.P., Bernhofer, C., & Debruin, H.A.R. (2007), The Energy Balance Experiment EBEX-2000. Part III: Behaviour and quality of the radiation measurements. *Boundary-Layer Meteorology*, 123, 55–75. <a href="https://doi.org/10.1007/s10546-006-9135-8">https://doi.org/10.1007/s10546-006-9135-8</a>
- Kondo, M., Ichii, K., Takagi, H., & Sasakawa, M. (2015), Comparison of the data-driven top-down and bottom-up global terrestrial CO₂ exchanges: GOSAT CO₂ inversion and empirical eddy flux upscaling. *Journal of Geophysical Research: Biogeosciences,* 120, 1226–1245. https://doi.org/10.1002/2014JG002866
- Kondo, M., Saitoh, T. M., Sato, H., & Ichii, K. (2017), Comprehensive synthesis of spatial variability in carbon flux across monsoon Asian forests. *Agricultural and Forest Meteorology, 232*, 623–634. http://dx.doi.org/10.1016/j.agrformet.2016.10.020

- Kormann, R., & Meixner, F.X. (2001). An Analytical Footprint Model For Non-Neutral Stratification. *Boundary-Layer Meteorology*, 99, 207–224. <a href="https://doi.org/10.1023/A:1018991015119">https://doi.org/10.1023/A:1018991015119</a>
- Korres, W., Koyama, C. N., Fiener, P., & Schneider, K. (2010), Analysis of surface soil moisture patterns in agricultural landscapes using Empirical Orthogonal Functions. *Hydrology and Earth System Science*, 14, 751–764. <a href="https://doi.org/10.5194/hess-14-751-2010">https://doi.org/10.5194/hess-14-751-2010</a>
- Korres, W., Reichenau, T.G., Fiener, P., Koyama, C.N., Bogena, H.R., Cornelissen, T., et al. (2015), Spatio-temporal soil moisture patterns A meta-analysis using plot to catchment scale data. *Journal of Hydrology*, 520, 326–341. http://dx.doi.org/10.1016/j.jhydrol.2014.11.042
- Kotilainen, T., Aphalo, P.J., Brelsford, C.C., Böök, H., Devraj, S., Heikkilä, A., et al. (2020), Patterns in the spectral composition of sunlight and biologically meaningful spectral photon ratios as affected by atmospheric factors. *Agricultural and Forest Meteorology*, 291, 108041. https://doi.org/10.1016/j.agrformet.2020.108041
- Krawczyk, B. (2016), Learning from imbalanced data: open challenges and future directions. *Progress in Artificial Intelligence, 5,* 221-232. https://doi.org/10.1007/s13748-016-0094-0
- Kubat, M. (2017), An Introduction to Machine Learning. Second Edition. Springer, Cham, Switzerland. https://doi.org/10.1007/978-3-319-63913-0
- Kuhn, M. (2008), Building Predictive Models in R Using the caret Package. *Journal of Statistical Software*, 28, 1–26. <a href="https://doi.org/10.18637/jss.v028.i05">https://doi.org/10.18637/jss.v028.i05</a>
- Kuhn, M. (2020), caret: Classification and Regression Training. R package version 6.0-86. https://CRAN.R-project.org/package=caret
- Kulmala, L., Pumpanen, J., Kolari, P., Muukkonen, Hari, P., & Vesala, T. (2011), Photosynthetic production of ground vegetation in different-aged Scots pine (Pinus sylvestris) forests. Canadian Journal of Forest Research, 41, 2020–2030. https://doi.org/10.1139/x11-121
- Kunkel, R., Sorg, J., Eckardt, R., Kolditz, O., Rink, K., & Vereecken, H. (2013), TEODOOR: a distributed geodata infrastructure for terrestrial observation data. *Environmental Earth Sciences*, 69, 507–521. https://doi.org/10.1007/s12665-013-2370-7
- Lange, M., Dechant, B., Rebmann, C., Vohland, M., Cuntz, M., & Doktor, D. (2017), Validating MODIS and Sentinel-2 NDVI Products at a Temperate Deciduous Forest Site Using Two Independent Ground-Based Sensors. Sensors, 17, 1855. <a href="https://doi.org/10.3390/s17081855">https://doi.org/10.3390/s17081855</a>
- Law, B.E., Falge, E., Gu, L., Baldocchi, D.D., Bakwin, P., Berbigier, P., et al. (2002), Environmental controls over carbon dioxide and water vapor exchange of terrestrial vegetation. *Agricultural and Forest Meteorology*, 113, 97–120. https://doi.org/10.1016/S0168-1923(02)00104-1
- Lawrence, D.M., Fisher, R.A., Koven, C.D., Oleson, K.W., Swenson, S.C., Bonan, G., et al. (2019), The Community Land Model Version 5: Description of New Features, Benchmarking, and Impact of Forcing Uncertainty. Journal of Advances in Modeling Earth Systems, 11, 4245–4287. https://doi.org/10.1029/2018MS001583
- Lee, X. (1998), On micrometeorological observations of surface-air exchange over tall vegetation. Agricultural and Forest Meteorology, 91, 39–49. <a href="https://doi.org/10.1016/S0168-1923(98)00071-9">https://doi.org/10.1016/S0168-1923(98)00071-9</a>
- Lehmkuhl, F., Loibl, D., & Borchardt, H. (2010), Geomorphological map of the Wüstebach (Nationalpark Eifel, Germany)—an example of human impact on mid-European mountain areas. Journal of Maps, 6:1, 520-530. <a href="https://doi.org/10.4113/jom.2010.1118">https://doi.org/10.4113/jom.2010.1118</a>
- Leuchner, M., Hertel, C., & Menzel, A. (2011), Spatial variability of photosynthetically active radiation in European beech and Norway spruce. *Agricultural and Forest Meteorology*, 151, 1226–1232. <a href="https://doi.org/10.1016/j.agrformet.2011.04.014">https://doi.org/10.1016/j.agrformet.2011.04.014</a>
- Li, W., Yu, T.F., Li, X.Y., & Zhao, C.Y. (2016), Sap flow characteristics and their response to environmental variables in a desert riparian forest along lower Heihe River Basin, Northwest

- China. *Environmental Monitoring and Assessment*, 188, 561. https://doi.org/10.1007/s10661-016-5570-2
- Liaw, A., & Wiener, M. (2002), Classification and Regression by randomForest. *R News 2*(3), 18--22. https://www.stat.berkeley.edu/~breiman/RandomForests/
- LI-COR Biosciences (2019), EddyPro software instruction manual. LI-COR Biosciences, Lincoln, USA Ließ, M, Glaser, B., & Huwe, B. (2012), Uncertainty in the spatial prediction of soil texture Comparison of regression tree and Random Forest models. *Geoderma*, 170, 70-79. https://doi.org/10.1016/j.geoderma.2011.10.010
- Lindauer, M., Schmid, H.P., Grote, R., Mauder, M., Steinbrecher, R., & Wolpert, B. (2014), Net ecosystem exchange over a non-cleared wind-throw-disturbed upland spruce forest—Measurements and simulations. *Agricultural and Forest Meteorology*, 197, 219–234. <a href="https://doi.org/10.1016/j.agrformet.2014.07.005">https://doi.org/10.1016/j.agrformet.2014.07.005</a>
- Lindroth, A., Klemedtsson, L., Grelle, A., Weslien, P., & Langvall, O. (2008), Measurement of net ecosystem exchange, productivity and respiration in three spruce forests in Sweden shows unexpectedly large soil carbon losses. *Biogeochemistry*, 89, 43–60. https://doi.org/10.1007/s10533-007-9137-8
- Lindroth, A., Lagergren, F., Grelle, A., Klemedtsson, L., Langvall, O., Weslien, P., & Tuulik, J. (2009), Storms can cause Europe-wide reduction in forest carbon sink. *Global Change Biology*, 15, 346–355. https://doi.org/10.1111/j.1365-2486.2008.01719.x
- Liu, Y., & Just, A. (2021). SHAPforxgboost, SHAP Plots for 'XGBoost'. R package version 0.1.1.
- Liu, H., & Motoda, H. (2008), Computational Methods of Feature Selection. *Data Mining and Knowledge Discovery Series*. Boca Raton, FL: Chapman & Hall/CRC.
- Löpmeier, F.-J. (1994), Berechnung der Bodenfeuchte und Verdunstung mittels agrarmeteorologischer Modelle. *Zeitschrift für Bewässerungswirtschaft*, 29, 157–167.
- Long, SP. (1991), Modification of the response of photosynthetic productivity to rising temperature by atmospheric CO₂ concentrations: Has its importance been underestimated? *Plant, Cell and Environment*, 14, 729-739. https://doi.org/10.1111/j.1365-3040.1991.tb01439.x
- Lundberg, S.M., & Lee, S.I. (2017), A Unified Approach to Interpreting Model Predictions. *Advances in Neural Information Processing Systems*, 30, 4768–4777. https://doi.org/10.48550/arXiv.1705.07874
- Lussem, U., & Herbrecht, M. (2019), Land use classification of 2018 for the Rur catchment. *TR32DB*. https://doi.org/10.5880/TR32DB.38
- Luyssaert, S., Guillaume, M.Valade, A., Chen, Y.Y., Njakou Djomo, S., Ryder, J., et al. (2018), Trade-offs in using European forests to meet climate objectives. *Nature*, 562, 259–262. https://doi.org/10.1038/s41586-018-0577-1
- Luyssaert, S., Inglima, I., Jung, M., Richardson, A.D., Reichstein, M., Papale, D., et al. (2007), CO<sub>2</sub> balance of boreal, temperate, and tropical forests derived from a global database. *Global Change Biology*, 13(12), 2509-2537. https://doi.org/10.1111/j.1365-2486.2007.01439.x
- Luyssaert, S., Schulze, E.D., Börner, A., Knohl, A., Hessenmöller, D., & Law, B.E. (2008), Old-growth forests as global carbon sinks. *Nature*, 455, 213–215. https://doi.org/10.1038/nature07276
- Mahrt, L. (2014), Stably Stratified Atmospheric Boundary Layers. *Annual Review of Fluid Mechanics*, 46, 23-45. <a href="https://doi.org/10.1146/annurev-fluid-010313-141354">https://doi.org/10.1146/annurev-fluid-010313-141354</a>
- Mailund, T. (2017), Beginning Data Science in R. Apress. Berkely, CA, USA. https://doi.org/10.1007/978-1-4842-8155-0
- Mäkelä, A., Pulkkinen, M., Kolari, P., Lagergren, F., Berbigier, P., Lindroth, A., et al. (2008), Developing an empirical model of stand GPP with the LUE approach, analysis of eddy covariance data at five contrasting conifer sites in Europe. *Global Change Biology*, 14, 92–108. https://doi.org/10.1111/j.1365-2486.2007.01463.x

- Malhotra, A., Roulet N.T., Wilson, P., Giroux-Bougard, X. & Harris, L.I. (2016), Ecohydrological feedbacks in peatlands: an empirical test of the relationship among vegetation, microtopography and water table. *Ecohydrology*, 9, 1346–1357. <a href="https://doi.org/10.1002/eco.1731">https://doi.org/10.1002/eco.1731</a>
- Martini, D., Sakowska, K., Wohlfahrt, G., Pacheco-Labrador, J., van der Tol, C., Porcar-Castell, A., et al. (2022), Heatwave breaks down the linearity between sun-induced fluorescence and gross primary production. *New Phytologist*, 233, 2415–2428. https://doi.org/10.1111/nph.17920
- Massman, W.J. (2000), A simple method for estimating frequency response corrections for eddy covariance systems. *Agricultural and Forest Meteorology*, 104, 185–198. https://doi.org/10.1016/S0168-1923(00)00164-7
- Massman, W.J. (2001), Reply to comment by Rannik on "A simple method for estimating frequency response corrections for eddy covariance systems". *Agricultural and for Meteorology*, 107, 247–251. https://doi.org/10.1016/S0168-1923(00)00237-9
- Massman, W.J., & Lee, X. (2002), Eddy covariance flux corrections and uncertainties in long-term studies of carbon and energy exchanges. *Agricultural and Forest Meteorology*, 113, 121–144. https://doi.org/10.1016/S0168-1923(02)00105-3
- Matricardi, E.A.T., Skole, D.L., Costa, O.B., Pedlowski, M.A., Samek, J.H., & Miguel, E.P. (2020), Long-term forest degradation surpasses deforestation in the Brazilian Amazon. *Science*, 369(6509), 1378–1382. https://doi.org/10.1126/science.abb3021
- Matthews, B., Mayer, M., Katzensteiner, K., Gobold, D.L., & Schume, H. (2017), Turbulent energy and carbon dioxide exchange along an early-successional windthrow chronosequence in the European Alps. *Agricultural and Forest Meteorology*, 232, 576–594. https://doi.org/10.1016/j.agrformet.2016.10.011
- Mauder, M., Cuntz, M., Drüe, C., Graf, A., Rebmann, C., Schmid, H. P., et al. (2013), A strategy for quality and uncertainty assessment of long-term eddy-covariance measurements.

  \*\*Agricultural and Forest Meteorology, 169, 122–135.\*\*

  https://doi.org/10.1016/j.agrformet.2012.09.006
- Mauder, M., & Foken, T. (2004), Documentation and instruction manual of the eddy-covariance software package TK2. *Universität Bayreuth, Abteilung Mikrometeorologie*, Arbeitsergebnisse 26, ISSN 1614–8924, 44.
- Mauder, M., & Foken, T. (2011), Documentation and Instruction Manual of the Eddy-Covariance Software Package TK3. Documentation and Instruction Manual of the Eddy-Covariance Software Package TK3. *Universität Bayreuth, Abteilung Mikrometeorologie: Arbeitsergebnisse* 46, ISSN 1614-8924 60 pp.
- Mauder, M., Foken, T., & Cuxart, J. (2020), Surface-energy-balance closure over land: A review. Boundary-Layer Meteorology, 177, 395–426. https://doi.org/10.1007/s10546-020-00529-6
- Maxwell, K., & Johnson, G.N. (2000), Chlorophyll fluorescence a practical guide. *Journal of Experimental Botany*, 51(345), 659–668. <a href="https://doi.org/10.1093/jexbot/51.345.659">https://doi.org/10.1093/jexbot/51.345.659</a>
- McGrath, M.J., Lyssaert, S., Meyfroidt, P., Kaplan, J.O., Bürgi, M., Chen, Y., et al. (2015):

  Reconstructing European forest management from 1600 to 2010. *Biogeosciences*, 12, 4291–4316. https://doi.org/10.5194/bg-12-4291-2015
- Meyer, H. (2018), CAST: 'caret' Applications for Spatial-Temporal Models. R package version 0.3.1. https://CRAN.R-project.org/package=CAST
- Meyer, H., & Pebesma, E. (2021), Predicting into unknown space? Estimating the area of applicability of spatial prediction models. *Methods in Ecology and Evolution*, 2, 1620–1633. https://doi.org/10.1111/2041-210X.13650
- Meyer, H., Reudenbach, C., Hengl, T., Katurji, M., & Nauss, T. (2018), Improving performance of spatio-temporal machine learning models using forward feature selection and target-

- oriented validation. *Environmental Modelling & Software,* 101, 1-9. https://doi.org/10.1016/j.envsoft.2017.12.001
- Meyer, H., Reudenbach, C., Wöllauer, S., & Nauss, T. (2019), Importance of spatial predictor variable selection in machine learning applications Moving from data reproduction to spatial prediction. *Ecological Modelling*, 411, 108815. https://doi.org/10.1016/j.ecolmodel.2019.108815
- Mohammed, G.H., Colombo, R., Middleton, E.M., Rascher, U., van der Tol, C., Nedbal, L., et al. (2019), Remote sensing of solar-induced chlorophyll fluorescence (SIF) in vegetation: 50 years of progress. *Remote Sensing of Environment*, 231, 111177. https://doi.org/10.1016/j.rse.2019.04.030
- Moncrieff, J.B., Clement, R., Finnigan, J., & Meyers, T. (2004), Averaging, detrending and filtering of eddy covariance time series. In: Lee X, Massman WJ, Law BE (eds), Handbook of micrometeorology: a guide for surface flux measurements. Kluwer Academic, Dordrecht, Netherlands, pp 7–31.
- Moncrieff, J.B., Masshelder, J.M., de Bruin, H., Elbers, J., Friborg, T., Heusinkveld, B., et al. (1997), A system to measure surface fluxes of momentum, sensible heat, water vapour and carbon dioxide. *Journal of Hydrology*, 188-189, 589–611. <a href="https://doi.org/10.1016/S0022-1694(96)03194-0">https://doi.org/10.1016/S0022-1694(96)03194-0</a>
- Montagnani, L., Grünwald, T., Kowalski, A., Mammarella, I., Merbold, L., Metzger, S., et al. (2018), Estimating the storage term in eddy covariance measurements, the ICOS methodology. *International Agrophysics*, 32, 551–567. https://doi.org/10.1515/intag-2017-0037
- Monteith, J.L. (1972), Solar Radiation and Productivity in Tropical Ecosystems. *Journal of Applied Ecology*, 9, 747–766.
- Montzka, C., Bayat, B., Tewes, A., Mengen, D., & Vereecken, H. (2021), Sentinel-2 Analysis of Spruce Crown Transparency Levels and Their Environmental Drivers After Summer Drought in the Northern Eifel (Germany). Frontiers in Forest and Global Change. 4, 667151. https://doi.org/10.3389/ffgc.2021.667151
- Moore, C.J. (1986), Frequency response corrections for eddy correlation systems. *Boundary-Layer Meteorology*, 37, 17–35. <a href="https://doi.org/10.1007/BF00122754">https://doi.org/10.1007/BF00122754</a>
- Morozumi, T., Kato, T., Kobayashi, H., Sakai, Y., Nakashima, N., Buareal, K., et al. (2023), Contributions of the understory and midstory to total canopy solar-induced chlorophyll fluorescence in a ground-based study in conjunction with seasonal gross primary productivity in a cool-temperate deciduous broadleaf forest. *Remote Sensing of Environment*, 284, 113340. https://doi.org/10.1016/j.rse.2022.113340
- Motzer, T., Munz, N., Küppers, M., Schmitt, D., & Anhuf, D. (2005), Stomatal conductance, transpiration and sap flow of tropical montane rain forest trees in the southern Ecuadorian Andes. *Tree Physiology*, 25, 1283–1293. <a href="https://doi.org/10.1093/treephys/25.10.1283">https://doi.org/10.1093/treephys/25.10.1283</a>
- Moureaux, C., Ceschia, E., Arriga, N., Beziat, P., Eugster, W., Kutsch, W.L., & Pattey, E. (2012), Eddy covariance measurements over crops. In: Aubinet, M., Vesala, T., & Papale, D. (eds), *Eddy covariance*. *A practical guide to measurement and data analysis*. Springer, Dordrecht Heidelberg London New York, pp 319–332.
- Munger, J.W., Loescher, H.W., & Luo, H. (2012), Measurement, tower, and site design considerations. In: Aubinet M., Vesala T., & Papale, D. (eds), *Eddy covariance. A practical guide to measurement and data analysis*. Springer, Dordrecht Heidelberg London New York, pp 21–58.
- Mykleby, P.M., Snyder, P.K., & Twine, T.E. (2017), Quantifying the trade-off between carbon sequestration and albedo in midlatitude and high-latitude North American forests. *Geophysical Research Letters*, 44(5), 2493–2501. https://doi.org/10.1002/2016GL071459

- Myneni, R., Knyazikhin, Y., & Park, T. (2015), MCD15A2H MODIS/Terra+Aqua Leaf Area Index/FPAR 8-day L4 Global 500m SIN Grid V006 [Data set]. NASA EOSDIS Land Processes DAAC. Accessed 2020-02-06 from <a href="https://doi.org/10.5067/MODIS/MCD15A2H.006">https://doi.org/10.5067/MODIS/MCD15A2H.006</a>
- Nationalparkverwaltung Eifel (2014), Informationen zu flächigen Talentfichtungen in der westlichen Rureifel / NRW unter besonderer Berücksichtigung der Maßnahme am Oberen Wüstebach im Nationalpark (NLP) Eifel von 08-09/2013. <a href="https://www.nationalpark-eifel.de/cache/dl-Informationen-zu-flaechigen-Talentfichtungen-b1961f39466133dd230884fdd79e0ffc.pdf">https://www.nationalpark-eifel.de/cache/dl-Informationen-zu-flaechigen-Talentfichtungen-b1961f39466133dd230884fdd79e0ffc.pdf</a>
- Nestola, E., Calfapietra, C., Emmerton, C.A., Wong, C.Y.S., Thayer, D.R., & Gamon, J.A. (2016), Monitoring Grassland Seasonal Carbon Dynamics, by Integrating MODIS NDVI, Proximal Optical Sampling, and Eddy Covariance Measurements. *Remote Sensing*, 8(3), 260. https://doi.org/10.3390/rs8030260
- Neuwirth, B., Rabbel, I., Bendix, J., Bogena, H.R., & Thies, B. (2021), The European heat wave 2018, The dendroecological response of oak and spruce in Western Germany. *Forests*, 12, 283. https://doi.org/10.3390/f12030283
- Ney, P. & Graf, A. (2018), High-Resolution Vertical Profile Measurements for Carbon Dioxide and Water Vapour Concentrations Within and Above Crop Canopies. *Boundary-Layer Meteorology*, 166, 449–473. https://doi.org/10.1007/s10546-017-0316-4
- Ney, P., Graf, A., Bogena, H., Diekkruger, B., Drüe, C., Esser, et al. (2019), CO<sub>2</sub> fluxes before and after partial deforestation of a Central European spruce forest. *Agricultural and Forest Meteorology*, 274, 61-74. https://doi.org/10.1016/j.agrformet.2019.04.009
- Nicolini, G., Fratini, G., Avilov, V., Kurbatova, J.A., Vasenev, I., & Valentini, R. (2017), Performance of eddy-covariance measurements in fetch-limited applications. *Theoretical and Applied Climatology*, 127, 829–840. https://doi.org/10.1007/s00704-015-1673-x
- O'Brien, J.J., Oberbauer, S.F., & Clark, D.B. (2004), Whole tree xylem sap flow responses to multiple environmental variables in a wet tropical forest. *Plant, Cell and Environment*, 27, 551–567. https://doi.org/10.1111/j.1365-3040.2003.01160.x
- Oncley, S.P., Foken, T., Vogt, R., Kohsiek, W., DeBruin, H.A.R., Bernhofer, C., et al. (2007), The Energy Balance Experiment EBEX-2000. Part I: overview and energy balance. *Boundary-Layer Meteorology*, 123, 1–28. <a href="https://doi.org/10.1007/s10546-007-9161-1">https://doi.org/10.1007/s10546-007-9161-1</a>
- Pan, Y., Birdsey, R.A., Fang, Y., Houghton, R., Kauppi, P.E., Kurz, W.A., et al. (2011), A Large and Persistent Carbon Sink in the World's Forests. *Science*, 333, 988–993. https://doi.org/10.1126/science.1201609
- Papale, D., Black, T. A., Carvalhais, N., Cescatti, A., Chen, J., Jung, M., et al. (2015), Effect of spatial sampling from European flux towers for estimating carbon and water fluxes with artificial neural networks. *Journal of Geophysical Research: Biogeosciences*, 120, 1941–1957. https://doi.org/10.1002/2015JG002997
- Pastorello, G., Trotta, C., Canfora, E., Chu, H., Christianson, D., Cheah, Y.-W., et al. (2020), The FLUXNET2015 dataset and the ONEFlux processing pipeline for eddy covariance data. Scientific Data, 7, 225. https://doi.org/10.1038/s41597-020-0534-3
- Pei, Y., Dong, J., Zhang, Y., Yuan, W., Doughty, R., Yang, J., et al. (2022), Evolution of light use efficiency models: Improvement, uncertainties, and implications. Agricultural and Forest Meteorology, 317, 108905. <a href="https://doi.org/10.1016/j.agrformet.2022.108905">https://doi.org/10.1016/j.agrformet.2022.108905</a>
- Peltola, O., Aslan, T., Ibrom, A., Nemitz, E., Rannik, Ü., & Mammarella, I. (2021b), The high-frequency response correction of eddy covariance fluxes –Part 1: An experimental approach and its interdependence with the time-lag estimation. *Atmospheric Measurement Techniques*, 14, 5071–5088. <a href="https://doi.org/10.5194/amt-14-5071-2021">https://doi.org/10.5194/amt-14-5071-2021</a>
- Peltola, O., Hensen, A., Marchesini, L.B., Helfter, C., Bosveld, F.C., van den Bulk, W.C.M., et al. (2015), Studying the spatial variability of methane flux with five eddy covariance towers of varying

- height. *Agricultural and Forest Meteorology*, 214–215, 456–472. https://doi.org/10.1016/j.agrformet.2015.09.007
- Peltola, O., Lapo, K., & Thomas, C.K. (2021a), A Physics-Based Universal Indicator for Vertical Decoupling and Mixing Across Canopies Architectures and Dynamic Stabilities. *Geophysical Research Letters*, 48, e2020GL091615. https://doi.org/10.1029/2020GL091615
- Peltola, O., Vesala, T., Gao, Y., Räty, O., Alekseychik, P., Aurela, M., et al. (2019), Monthly gridded data product of northern wetland methane emissions based on upscaling eddy covariance observations. Earth System Science Data, 11, 1263–1289. <a href="https://doi.org/10.5194/essd-11-1263-2019">https://doi.org/10.5194/essd-11-1263-2019</a>
- Peng, Y., Gitelson, A.A., Keydan, G., Rundquist, D.C., & Moses, W. (2011), Remote estimation of gross primary production in maize and support for a new paradigm based on total crop chlorophyll content. *Remote Sensing of Environment*, 115, 978–989. https://doi.org/10.1016/j.rse.2010.12.001
- Perämäki, M., Vesala, T., & Nikinmaa, E. (2005), Modeling the dynamics of pressure propagation and diameter variation in tree sapwood. *Tree Physiology*, 25, 1091–1099. https://doi.org/10.1093/treephys/25.9.1091
- Pfeifroth, U., Kothe, S., Trentmann, J., Hollmann, R., Fuchs, P., Kaiser, J., & Werscheck, M. (2019), Surface Radiation Data Set Heliosat (SARAH) Edition 2.1. Satellite Application Facility on Climate Monitoring. https://doi.org/10.5676/EUM\_SAF\_CM/SARAH/V002\_01
- Płaczkowska, E., Mostowik, K., Bogena, H.R., & Leuchner, M. (2022), The Impact of Partial Deforestation on Solute Fluxes and Stream Water Ionic Composition in a Headwater Catchment. Water, 15, 107. <a href="https://doi.org/10.3390/w15010107">https://doi.org/10.3390/w15010107</a>
- Polonik, P., Chan, W.S., Billesbach, D.P., Burba, G., Li, J., Nottrott, A., et al. (2019), Comparison of gas analyzers for eddy covariance: Effects of analyzer type and spectral corrections on fluxes.

  \*\*Agricultural and Forest Meteorology, 272–273, 128–142.

  https://doi.org/10.1016/j.agrformet.2019.02.010
- Pongratz, J., Schwingshackl, C., Bultan, S., Obermeier, W., Havermann, F., & Guo, S. (2021), Land Use Effects on Climate: Current State, Recent Progress, and Emerging Topics. *Current Climate Change Reports*, 7, 99–120. https://doi.org/10.1007/s40641-021-00178-y
- Post, H., Hendricks Franssen, H. J., Graf, A., Schmidt, M., & Vereecken, H. (2015), Uncertainty analysis of eddy covariance CO<sub>2</sub> flux measurements for different EC tower distances using an extended two-tower approach. *Biogeosciences*, 12, 1205–1221. <a href="https://doi.org/10.5194/bg-12-1205-2015">https://doi.org/10.5194/bg-12-1205-2015</a>
- Post, H., Hendricks Franssen, H.-J., Han, X., Baatz, R., Montzka, C., Schmidt, M., & Vereecken, H. (2018), Evaluation and uncertainty analysis of regional-scale CLM4.5 net carbon flux estimates, *Biogeosciences*, 15, 187–208. https://doi.org/10.5194/bg-15-187-2018
- Prasad, A. M., Iverson, L. R. & Liaw, A. (2006), Newer Classification and Regression Tree Techniques: Bagging and Random Forests for Ecological Prediction. *Ecosystems*, *9*, 191-199. https://doi.org/10.1007/s10021-005-0054-1
- Pütz, T., Kiese, R., Wollschläger, U., Groh, J., Rupp, H., Zacharias, S., et al. (2016), TERENO-SOILCan: a lysimeter-network in Germany observing soil processes and plant diversity influenced by climate change. *Environmental Earth Science*, 75:1242. <a href="https://doi.org/10.1007/s12665-016-6031-5">https://doi.org/10.1007/s12665-016-6031-5</a>
- Pugh, T.A.M., Lindeskog, M., Smith, B., Poulter, B., Arneth, A., Haverd, V., & Calle, L. (2019), Role of forest regrowth in global carbon sink dynamics. *PNAS*, 116 (10), 4382-4387. https://doi.org/10.1073/pnas.1810512116
- Putzenlechner, B., Castro, S., Kiese, R., Ludwig, R., Marzahn, P., Sharp, I., & Sanchez-Azofeifa, A. (2019a), Validation of Sentinel-2 fAPAR products using ground observations across three

- forest ecosystems. *Remote Sensing of Environment*, 232, 111310. https://doi.org/10.1016/j.rse.2019.111310
- Putzenlechner, B., Marzahn, P., Kiese, R., Ludwig, R., & Sanchez-Azofeifa, A. (2019b), Assessing the variability and uncertainty of two-flux FAPAR measurements in a conifer-dominated forest. *Agricultural and Forest Meteorology*, 264, 149–163.

  <a href="https://doi.org/10.1016/j.agrformet.2018.10.007">https://doi.org/10.1016/j.agrformet.2018.10.007</a>
- Putzenlechner, B., Marzahn, P., & Sanchez-Azofeifa, A. (2020), Accuracy assessment on the number of flux terms needed to estimate in situ fAPAR. *International Journal of Applied Earth Observation and Geoinformation*, 88, 102061. https://doi.org/10.1016/j.jag.2020.102061
- Qin, Y., Xiao, X., Wigneron, J.P., Ciais, P., Brandt, M., Fan, L., et al. (2021). Carbon loss from forest degradation exceeds that from deforestation in the Brazilian Amazon. *Nature Climate Change*, 11, 442–448. https://doi.org/10.1038/s41558-021-01026-5
- Raj, R., Hamm, N.A.S., van der Tol, C., & Stein, A. (2016), Uncertainty analysis of gross primary production partitioned from net ecosystem exchange measurements. *Biogeosciences*, 13, 1409–1422. https://doi.org/10.5194/bg-13-1409-2016
- Ranghetti, L., Boschetti, M., Nutini, F., & Busetto, L. (2020), "sen2r", An R toolbox for automatically downloading and preprocessing Sentinel-2 satellite data. *Computers & Geosciences*, 139, 104473. https://doi.org/10.1016/j.cageo.2020.104473
- Rannik, Ü., Sogachev, A., Foken, T., Göckede, M., Kljun, N., Leclerc, M.Y., & Vesala, T. (2012), Footprint Analysis. In: Aubinet, M., Vesala, T., & Papale, D. (eds), Eddy covariance. A practical guide to measurement and data analysis. Springer, Dordrecht Heidelberg London New York, pp 211–261.
- Rannik, Ü., Vesala, T., Peltola, O., Novick, K.A., Aurela, M., Järvi, L., et al. (2020), Impact of coordinate rotation on eddy covariance fluxes at complex sites. *Agricultural and Forest Meteorology*, 287, 107940. https://doi.org/10.1016/j.agrformet.2020.107940
- Richardson, A. D., Aubinet, M., Barr, A. G., Hollinger, D. Y., Ibrom, A., & Lasslop, G. (2012),
  Uncertainty Quantification. In Aubinet, M., Vesala, T., & Papale, D. (eds), *Eddy Covariance. A Practical Guide to Measurement and Data Analysis, Springer Atmospheric Sciences*, Springer Dordrecht Heidelberg London New York, (pp 173-209).
- Rebmann, C., Aubinet, M., Schmid, H.P., Arriga, N., Aurela, M., Burba, G., et al. (2018), ICOS eddy covariance flux-station site setup: a review. *International Agrophysics*, 32, 471–494. https://doi.org/10.1515/intag-2017-0044
- Reichenau, T.G., korres, W., Montzka, C., Fiener, P., Wilken, F., Stadler, A., et al. (2016), Spatial Heterogeneity of Leaf Area Index (LAI) and Its Temporal Course on Arable Land: Combining Field Measurements, Remote Sensing and Simulation in a Comprehensive Data Analysis Approach (CDAA). *PLoS ONE*, 11(7): e0158451. https://doi.org/10.1371/journal.pone.0158451
- Reichstein, M., Falge, E., Baldocchi, D., Papale, D., Aubinet, M., Berbigier, P., et al. (2005), On the separation of net ecosystem exchange into assimilation and ecosystem respiration: review and improved algorithm. *Global Change Biology*, 11, 1424–1439, https://doi.org/10.1111/j.1365-2486.2005.001002.x
- Reynolds, O. (1895), IV. On the Dynamical Theory of Incompressible Viscous Fluids and the Determination of the Criterion. *Philosophical Transactions of the Royal Society A*, 186. https://doi.org/10.1098/rsta.1895.0004
- Roberts, D. R., Bahn, V., Ciuti, S., Boyce, M. S., Elith, J., Guillera-Arroita, G., et al. (2017), Cross-validation strategies for data with temporal, spatial, hierarchical, or phylogenetic structure. *Ecography*, 40, 913–929. https://doi.org/10.1111/ecog.02881

- Roddy, A.B. (2013), Novel Patterns of Hysteresis in the Response of Leaf-Level Sap Flow to Vapor Pressure Deficit. *Acta Horticulturae*, 991, 261–267. https://doi.org/10.17660/ActaHortic.2013.991.32
- Running, S.W., & Zhao, M. (2015), Daily GPP and annual NPP (MOD17A2/A3) products NASA Earth Observing System MODIS land algorithm. MOD17 User's Guide. Washington, DC., USA, MODIS Land Team.
- Sade, N., Gebremedhin, A., & Moshelion, M. (2012). Risk-taking plants. Anisohydric behavior as a stress-resistance trait. Plant Signaling & Behavior, 7(7), 767–770. https://doi.org/10.4161/psb.20505
- Safa, B., Arkebauer, T. J., Zhu, Q., Suyker, A., & Irmak, S. (2019), Net Ecosystem Exchange (NEE) simulation in maize using artificial neural networks. *IFAC Journal of Systems and Control*, 7, 100036. https://doi.org/10.1016/j.ifacsc.2019.100036
- Schimel, D. S., House, J. I., Hibbard, K. A., Bousquet, P., Ciais, P., Peylin, P. H., et al. (2001), Recent patterns and mechanisms of carbon exchange by terrestrial ecosystems. *Nature*, 414, 169–172.
- Schmid, H.P., & Lloyd, C.R. (1999), Spatial representativeness and the location bias of flux footprints over inhomogeneous areas. *Agricultural and Forest Meteorology*, 93, 195–209. https://doi.org/10.1016/S0168-1923(98)00119-1
- Schmidt, M. (2014), Post processed fluxes of the roving EC station RUEC004 in Niederzier. *CRC/TR32 Database (TR32DB), TEODOOR Portal.* <a href="http://teodoor.icg.kfa-juelich.de/ibg3searchportal/dispatch?stations=http%3A%2F%2Fibg3wradar.ibg.kfa-juelich.de%3A8080%2Feifelrur public%2Fsos,RU EC 004">http://teodoor.icg.kfa-juelich.de%3A8080%2Feifelrur public%2Fsos,RU EC 004</a>
- Schmidt M. (2019), TERENO data from station(s) RU\_EC\_002 with parameter(s) AirFlux for time period 2012-08-17 to 2012-10-25. https://hdl.handle.net/20.500.11952/TERENO.RU EC 002.1573739908305
- Schmidt, M., Schween, J., (2018), Post processed fluxes of the permanent EC station RUEC001 near Selhausen. *CRC/TR32 Database (TR32DB), TEODOOR Portal*. <a href="http://teodoor.icg.kfa-juelich.de/ibg3searchportal/dispatch?stations=http%3A%2F%2Fibg3wradar.ibg.kfa-juelich.de%3A8080%2Feifelrur\_public%2Fsos,RU\_EC\_001">http://teodoor.icg.kfa-juelich.de%3A8080%2Feifelrur\_public%2Fsos,RU\_EC\_001</a>
- Schmidt, M., Reichenau, T. G., Fiener, P., & Schneider, K. (2012), The carbon budget of a winter wheat field: An eddy covariance analysis of seasonal and inter-annual variability. *Agricultural and Forest Meteorology*, 165, 114–126. https://doi.org/10.1016/j.agrformet.2012.05.012
- Schmitt, M., Bahn, M., Wohlfahrt, G., Tappeiner, U., & Cernusca, A. (2010), Land use affects the net ecosystem CO<sub>2</sub> exchange and its components in mountain grasslands, *Biogeosciences*, 7, 2297–2309. https://doi.org/10.5194/bg-7-2297-2010
- Schopfer, P., & Brennicke, G. (2010), Pflanzenphysiologie. 7. Auflage. Spektrum Akademischer Verlag, Heidelberg, Germany. https://doi.org/10.1007/978-3-8274-2352-8
- Schotanus, P., Nieuwstadt, F.T.M., & De Bruin, H.A.R. (1983). Temperature Measurements with a Sonic Anemometer and its Application to Heat and Moisture Fluxes. *Boundary-Layer Meteorology*, 26, 81-93. <a href="https://doi.org/10.1007/BF00164332">https://doi.org/10.1007/BF00164332</a>
- Schulzweida, U. (2019), CDO User Guide (Version 1.9.8), http://doi.org/10.5281/zenodo.3539275
- Senf, C., & Seidl, R. (2021), Persistent impacts of the 2018 drought on forest disturbance regimes in Europe. *Biogeosciences*, 18, 5223–5230. <a href="https://doi.org/10.5194/bg-18-5223-2021">https://doi.org/10.5194/bg-18-5223-2021</a>
- Serk, H., Nilsson, M.B., Bohlin, E., Ehlers, I., Wieloch, T., Olid, C., et al. (2021), Global CO<sub>2</sub> fertilization of *Sphagnum* peat mosses via suppression of photorespiration during the twentieth century. *Scientific Reports*, 11, 24517. <a href="https://doi.org/10.1038/s41598-021-02953-1">https://doi.org/10.1038/s41598-021-02953-1</a>
- Shi, H., Luo, G., Hellwich, O., Xie, M., Zhang, C., Zhang, Y., et al. (2022), Variability and uncertainty in flux-site-scale net ecosystem exchange simulations based on machine learning and remote

- sensing: a systematic evaluation. *Biogeosciences*, 19, 3739–3756. https://doi.org/10.5194/bg-19-3739-2022
- Sievers, U., & Kossmann, M. (2016), The cold air drainage model KLAM\_21 Model formulation and comparison with observations. *Weather and Climate*, 36, 2–24. https://doi.org/10.2307/26779385
- Sitch, S., Friedlingstein, P., Gruber, N., Jones, S.D., Murray-Tortarolo, G., Ahlström, A., et al. (2015), Recent trends and drivers of regional sources and sinks of carbon dioxide. *Biogeosciences*, 12, 653–679. https://doi.org/10.5194/bg-12-653-2015
- Smith, N.E., Kooijmans, L.M.J., Koren, G., van Schaik, E., van der Woude, A., Wanders, N., et al. (2020), Spring enhancement and summer reduction in carbon uptake during the 2018 drought in northwestern Europe. *Philosophical transactions of the Royal Society of London. Series B, Biological sciences*, 375, 20190509. http://dx.doi.org/10.1098/rstb.2019.0509
- Sogachev, A., & Dellwik, E. (2017), Flux footprints for a tall tower in a land—water mosaic area: A case study of the area around the Risø tower. *Agricultural and Forest Meteorology*, 237, 326–339. https://doi.org/10.1016/j.agrformet.2017.02.037
- Sogachev, A., & Lloyd, J. (2004), Using a one-and-a-half order closure model of the atmospheric boundary layer for surface flux footprint estimation. *Boundary-Layer Meteorology*, 112, 467–502. https://doi.org/10.1023/B:BOUN.0000030664.52282.ee
- Sogachev, A., Menzhulin, G.V., Heimann, M., & Lloyd, J., (2002), A simple three-dimensional canopy planetary boundary layer simulation model for scalar concentrations and fluxes. *Tellus B*, 54, 784–819. http://dx.doi.org/10.1034/j.1600-0889.2002.201353.x
- Steppe, K., Vandegehuchte, M.W., Tognetti, R., & Mencuccini, M. (2015), Sap flow as a key trait in the understanding of plant hydraulic functioning. *Tree Physiology*, 35, 341–345. https://doi.org/10.1093/treephys/tpv033
- Stocker, B.D., Wang, H., Smith, N.G., Harrison, S.P., Keenan, T.F., Sandroval, D., et al. (2020), P-model v1.0, an optimality-based light use efficiency model for simulating ecosystem gross primary production. *Geoscientific Model Development*, 13, 545–1581. <a href="https://doi.org/10.5194/gmd-13-1545-2020">https://doi.org/10.5194/gmd-13-1545-2020</a>
- Stocker, B.D., Zscheischler, J., Keenan, T.F., Prentice, I.C., Penuelas, J., & Senevirantne, S.I. (2018), Quantifying soil moisture impacts on light use efficiency across biomes. *New Phytologist*, 218, 1430–1449. <a href="https://doi.org/10.1111/nph.15123">https://doi.org/10.1111/nph.15123</a>
- Stoy, P.C., Mauder, M., Foken, T., Marcolla, B., Boegh, E., Ibrom, A., et al. (2013), A data-driven analysis of energy balance closure across FLUXNET research sites: The role of landscape scale heterogeneity. *Agricultural and Forest Meteorology*, 171–172, 137–152. https://doi.org/10.1016/j.agrformet.2012.11.004
- Strobl, C., Boulesteix, A.L., Kneib, T., Augustin, T., & Zeileis, A. (2008), Conditional variable importance for random forests. *BMC Bioinformatics*, 9, 307. https://doi.org/10.1186/1471-2105-9-307
- Su, H.B., Schmid, H.P., Grimmond, C.S.B., Vogel, C.S., & Oliphant, A.J. (2004), Spectral characteristics and correction of long-term eddy-covariance measurements over two mixed hardwood forests in non-flat terrain. *Boundary-Layer Meteorology*, 110, 213–253. https://doi.org/10.1023/A:1026099523505
- Suck, R. (1999), Die natürlichen Waldgesellschaften des Schneifel-Hauptkammes (Westliche Hocheifel) und ihre Ersatzgesellschaften. *Tuexenia*, 19, 13–53.
- Suck, R., Bushart, M., Hofmann, G., & Schröder, L. (2014), Karte der Potentiellen Natürlichen Vegetation Deutschlands. Band I Grundeinheiten. BfN-Skripten 348. Bundesamt für Naturschutz, Bonn, Germany.
- Sun, G., Caldwell, P., Noormets, A., McNulty, S. G., Cohen, E., Moore Myers, J., Domec, J. C., et al. (2011), Upscaling key ecosystem functions across the conterminous United States by a

- water-centric ecosystem model, *Journal of Geophysical Research*, 116, G00J05. https://doi.org/10.1029/2010JG001573
- Tammi, I., Mustajärvi, K., & Rasinmäki, J. (2017), Integrating spatial valuation of ecosystem services into regional planning and development, Ecosystem Services, 26(B), 329-344. https://doi.org/10.1016/j.ecoser.2016.11.008
- Tao, X., Liang, S., & Wang, D. (2015), Assessment of five global satellite products of fraction of absorbed photosynthetically active radiation, Intercomparison and direct validation against ground-based data. *Remote Sensing of Environment*, 163, 270–285. https://doi.org/10.1016/j.rse.2015.03.025
- Taye, F.A., Folkersen, M.V., Fleming, C.M., Buckwell, A., Mackay, B., Diwakar, K.C., et al. (2021), The economic values of global forest ecosystem services, A meta-analysis. *Ecological Economics*, 189, 107145. https://doi.org/10.1016/j.ecolecon.2021.107145
- Thompson, R.L., Broquet, G., Gerbig, C., Koch, T., Lang, M., Monteil, G., et al. (2020), Changes in net ecosystem exchange over Europe during the 2018 drought based on atmospheric observations. *Philosophical transactions of the Royal Society of London. Series B, Biological sciences*, 375, 20190512. <a href="http://dx.doi.org/10.1098/rstb.2019.0512">http://dx.doi.org/10.1098/rstb.2019.0512</a>
- Torgo, L., Branco, P., Ribeiro, R.P., & Pfahringer B. (2013), Resampling strategies for regression. *Expert Systems*, 32, 465-476. <a href="https://doi.org/10.1111/exsy.12081">https://doi.org/10.1111/exsy.12081</a>
- Tramontana, G., Jung, M., Schwalm, C. R., Ichii, K., Camps-Valls, G., Ráduly, B., et al. (2016), Predicting carbon dioxide and energy fluxes across global FLUXNET sites with regression algorithms.

  \*Biogeosciences\*, 13, 4291–4313. https://doi.org/10.5194/bg-13-4291-2016
- Tramontana, G., Migliavacca, M., Jung, M., Reichstein, M., Keenan, T., Camps-Valls, G., et al. (2020), Partitioning net carbon dioxide fluxes into photosynthesis and respiration using neural networks. *Global Change Biology*, 26, 5235–5253. https://doi.org/10.1111/gcb.15203
- Tuller, M., & Or, D. (2004), Water Retention and Characteristic Curve. In: D. Hillel (Ed.), *Encyclopedia of Soils in the Environment*. Oxford, United Kingdom: Elsevier Ltd.
- Turnbull, M.H. (1991), The effect of light quantity and quality during development on the photosynthetic characteristics of six Australian rainforest tree species. *Oecologia*, 87, 110-117. <a href="https://doi.org/10.1007/BF00323788">https://doi.org/10.1007/BF00323788</a>
- UCAR/NCAR Earth Observing Laboratory (1990), NCAR Integrated Surface Flux System (ISFS), UCAR/NCAR - Earth Observing Laboratory. https://doi.org/10.5065/D6ZC80XJ
- Urban, O., Janous, D., Acosta, M., Czerny, R., Markova, I., Navratil, M., et al. (2007), Ecophysiological controls over the net ecosystem exchange of mountain spruce stand. Comparison of the response in direct vs. diffuse solar radiation. *Global Change Biology*, 13, 157–168. https://doi.org/10.1111/j.1365-2486.2006.01265.x
- Urban, O., Klem, K., Ac, A., Havrankova, K., Holisova, P., Navratil, M., et al. (2012), Impact of clear and cloudy sky conditions on the vertical distribution of photosynthetic CO<sub>2</sub> uptake within a spruce canopy. *Functional Ecology*, 26, 46–55. <a href="https://doi.org/10.1111/j.1365-2435.2011.01934.x">https://doi.org/10.1111/j.1365-2435.2011.01934.x</a>
- Ustin, S.L., & Jacquemoud, S. (2020), How the Optical Properties of Leaves Modify the Absorption and Scattering of Energy and Enhance Leaf Functionality. In: J. Cavender-Bares et al. (eds.), *Remote Sensing of Plant Biodiversity*, 349–384. <a href="https://doi.org/10.1007/978-3-030-33157-3">https://doi.org/10.1007/978-3-030-33157-3</a> 14
- Verma, M., Schimel, D., Evans, B., Frankenberg, C., Beringer, J., Drewry, D.T., et al. (2017), Effect of environmental conditions on the relationship between solar-induced fluorescence and gross primary productivity at an OzFlux grassland site. *Journal of Geophysical Research:*Biogeosciences, 122, 716–733. <a href="https://doi.org/10.1002/2016JG003580">https://doi.org/10.1002/2016JG003580</a>

- Vesala, T., Markkanen, T., Palva, L., Siivola, E., Palmroth, S., & Hari, P. (2000), Effect of variations of PAR on CO2 exchange estimation for Scots pine. *Agricultural and Forest Meteorology*, 100, 337–347. https://doi.org/10.1016/S0168-1923(99)00146-X
- Vickers, D., & Mahrt, L. (1997), Quality control and flux sampling problems for tower and aircraft data. *Journal of Atmospheric and Ocean Technology*, 14, 512–526. https://doi.org/10.1175/1520-0426(1997)014<0512:QCAFSP>2.0.CO;2
- Vickers, D., & Mahrt, L. (2006), Contrasting mean vertical motion from tilt correction methods and mass continuity. *Agricultural and Forest Meteorology*, 138, 93–103. https://doi.org/10.1016/j.agrformet.2006.04.001
- Vitale, L., Di Tommasi, P., D'Urso, & Magliulo V. (2016), The response of ecosystem carbon fluxes to LAI and environmental drivers in a maize crop grown in two contrasting seasons.

  \*International Journal of Biometeorology, 60, 411–420. <a href="https://doi.org/10.1007/s00484-015-1038-2">https://doi.org/10.1007/s00484-015-1038-2</a>
- Von Buttlar, J., Zscheischler, J., Ramming, A., Sippel, S., Reichstein, M., Knohl, A., et al. (2018). Impacts of droughts and extreme-temperature events on gross primary production and ecosystem respiration: a systematic assessment across ecosystems and climate zones. *Biogeosciences*, 15, 1293–1318. <a href="https://doi.org/10.5194/bg-15-1293-2018">https://doi.org/10.5194/bg-15-1293-2018</a>
- Walther, S., Besnard, S., Nelson, J.A., El-Madany, T.S., Migliavacca, M., Weber, U., et al. (2022). Technical note: A view from space on global flux towers by MODIS and Landsat: the FluxnetEO data set. *Biogeosciences*, 19, 2805–2840. <a href="https://doi.org/10.5194/bg-19-2805-2022">https://doi.org/10.5194/bg-19-2805-2022</a>
- Wang, D. (2017), MODIS/Terra+Aqua Surface Radiation Daily/3-Hour L3 Global 5km SIN Grid V006 [Data set]. NASA EOSDIS Land Processes DAAC. Accessed 2020-02-06 from https://doi.org/10.5067/MODIS/MCD18A1.006
- Wang, H., Jiang, F., Wang, J., Ju, W., & Chen, J. M. (2019a), Terrestrial ecosystem carbon flux estimated using GOSAT and OCO-2 XCO₂ retrievals, *Atmospheric Chemistry and Physics*, 19, 12067–12082, https://doi.org/10.5194/acp-19-12067-2019
- Wang, H., Tetzlaff, D., & Soulsby, C. (2019b), Hysteretic response of sap flow in Scots pine (Pinus sylvestris) to meteorological forcing in a humid low-energy headwater catchment. *Ecohydrology*, 12, e2125. <a href="https://doi.org/10.1002/eco.2125">https://doi.org/10.1002/eco.2125</a>
- Wang, S., Ibrom, A., Bauer-Gottwein, P., & Garcia, M. (2018), Incorporating diffuse radiation into a light use efficiency and evapotranspiration model, An 11-year study in a high latitude deciduous forest. *Agricultural and Forest Meteorology*, 248, 479–493. <a href="https://doi.org/10.1016/j.agrformet.2017.10.023">https://doi.org/10.1016/j.agrformet.2017.10.023</a>
- Wang, Y., Zeng, Y., Yu, L., Yang, P., Van der Tol, C., Yu, Q., et al. (2021), Integrated modeling of canopy photosynthesis, fluorescence, and the transfer of energy, mass, and momentum in the soil–plant–atmosphere continuum (STEMMUS–SCOPE v1.0.0). *Geoscientific Model Development*, 14, 379–1407. https://doi.org/10.5194/gmd-14-1379-2021
- Webb, E.K., Pearman, G.I., & Leuning, R. (1980), Correction of flux measurements for density effects due to heat and water vapour transfer. *Quarterly Journal of the Royal Meteorological Society*, 106, 85–100. <a href="https://doi.org/10.1002/qj.49710644707">https://doi.org/10.1002/qj.49710644707</a>
- Weiss, M., Baret, F., & Jay, S. (2020), S2ToolBox Level 2 products, LAI, FAPAR, FCOVER. V2.0.
- Widlowski, J.L. (2010), On the bias of instantaneous FAPAR estimates in open-canopy forests. Agricultural and Forest Meteorology, 150, 1501–1522. https://doi.org/10.1016/j.agrformet.2010.07.011
- Wiedemann, A., Maranon-Jimenz, S., Rebmann, C., Herbst, M., & Cuntz, M. (2016), An empirical study of the wound effect on sap flux density measured with thermal dissipation probes. *Tree Physiology*, 36(12), 1471–1484. <a href="https://doi.org/10.1093/treephys/tpw071">https://doi.org/10.1093/treephys/tpw071</a>

- Wiekenkamp, I., Huisman, J. A., Bogena, H. R., Graf, A., Lin, H. S., Drüe, C. & Vereecken, H. (2016), Changes in measured spatiotemporal patterns of hydrological response after partial deforestation in a headwater catchment. *Journal of Hydrology*, 542, 648–661. https://doi.org/10.1016/j.jhydrol.2016.09.037
- Wiekenkamp, I., Huisman, J.A., Bogena, H.R., Vereecken, H. (2019), Effects of deforestation on water flow in the vadose zone. *Water*, 12(1), 35. https://doi.org/10.3390/w12010035
- Wieneke, S., Burkart, A., Cendrero-Mateo, M.P., Julitta, T., Rossini, M., Schickling, A., et al. (2018), Linking photosynthesis and sun-induced fluorescence at sub-daily to seasonal scales. *Remote Sensing of Environment*, 219, 247–258. https://doi.org/10.1016/j.rse.2018.10.019
- Wilczak, J.M., Oncley, S.P., Stage, S.A. (2001), Sonic anemometer tilt correction algorithms.

  \*Boundary-Layer Meteorology\*, 99, 127–150. <a href="https://doi.org/10.1023/A:1018966204465">https://doi.org/10.1023/A:1018966204465</a>
- Williams, M., Rastetter, E.B., Van der Pol, L., & Shaver, G.R. (2014), Arctic canopy photosynthetic efficiency enhanced under diffuse light, linked to a reduction in the fraction of the canopy in deep shade. *New Phytologist*, 202, 1266–1276. https://doi.org/10.1111/nph.12750
- Williamson, B.D., Gilbert, P.B., Carone, M., & Simon, N. (2021), Nonparametric variable importance assessment using machine learning techniques. *Biometrics*, 77, 9–22. https://doi.org/10.1111/biom.13392
- Wilson, K., Goldstein, A., Falge, E., Aubinet, M., Baldocchi, D., Berbigier, P., et al. (2002), Energy balance closure at FLUXNET sites. *Agricultural and Forest Meteorology*, 113, 223–343. https://doi.org/10.1016/S0168-1923(02)00109-0
- Wohlfahrt, G., Hammerle, A., Haslwanter, A., Bahn, M., Tappeiner, U., & Cernusca, A. (2008), Seasonal and inter-annual variability of the net ecosystem CO<sub>2</sub> exchange of a temperate mountain grassland: Effects of weather and management. *Journal of Geophysical Research*, 113, D08110. https://doi.org/10.1029/2007JD009286
- Wu, G., Jiang, C., Kimm, H., Wang, S., Bernacchi, C., Moore, C.E., et al. (2022), Difference in seasonal peak timing of soybean far-red SIF and GPP explained by canopy structure and chlorophyll content. *Remote Sensing of Environment*, 279, 113104. https://doi.org/10.1016/j.rse.2022.113104
- Wutzler, T., Lucas-Moffat, A., Migliavacca, M., Knauer, J., Sickel, K., Sigut, L., et al. (2018), Basic and extensible post-processing of eddy covariance flux data with REddyProc. *Biogeosciences*, 15, 5015-5030. https://doi.org/10.5194/bg-15-5015-2018
- Xiao, J., Zhuang, Q., Baldocchi, D. D., Law, B. E., Richardson, A. D., Chen, J., et al. (2008), Estimation of net ecosystem carbon exchange for the conterminous United States by combining MODIS and AmeriFlux data. *Agricultural and Forest Meteorology*, 148, 1827-1847. https://doi.org/10.1016/j.agrformet.2008.06.015
- Xiao, J., Davis, K. J., Urban, N. M., Keller, K., & Saliendra, N. Z. (2011), Upscaling carbon fluxes from towers to the regional scale: Influence of parameter variability and land cover representation on regional flux estimates, *Journal of Geophysical Research*, 116, G00J06. https://doi.org/10.1029/2010JG001568
- Xiao, J., Chen, J., Davis, K. J., & Reichstein, M. (2012), Advances in upscaling of eddy covariance measurements of carbon and water fluxes, *Journal of Geophysical Research*, 117, G00J01. https://doi.org/10.1029/2011JG001889
- Xiao, X., Hollinger, D., Aber, J., Goltz, M., Davidson, E.A., Zhang, Q., & Moore III, B. (2004), Satellite-based modeling of gross primary production in an evergreen needleleaf forest. *Remote Sensing of Environment*, 89, 519–534. https://doi.org/10.1016/j.rse.2003.11.008
- Xu, X., Yang, G., Tan, Y., Tang, X., Jiang, H., Sun, X., et al. (2017), Impacts of land use changes on net ecosystem production in the Taihu Lake Basin of China from 1985 to 2010. *Journal of*

- Geophysical Research: Biogeosciences, 122, 690–707. https://doi.org/10.1002/2016JG003444
- Xu, Z., Wu, Z., He, H., Guo, X., & Zhang, Y. (2021), Comparison of soil moisture at different depths for drought monitoring based on improved soil moisture anomaly percentage index. *Water Science and Engineering*, 14(3), 171–183. <a href="https://doi.org/10.1016/j.wse.2021.08.008">https://doi.org/10.1016/j.wse.2021.08.008</a>
- Yu, Z., Beilman, D.W., Frokling, S., MacDonald, G.M., Roulet, N.T., Camill, P., & D.J. Charman (2011), Peatlands and Their Role in the Global Carbon Cycle. *Eos*, 92(12), 97–108. https://doi.org/10.1029/2011EO120001
- Yuan, W., Liu, S., Yu, G., Bonnefond, J. M., Chen, J., Davis, K., et al. (2010), Global estimates of evapotranspiration and gross primary production based on MODIS and global meteorology data. *Remote Sensing of Environment*, 114, 1416–1431. https://doi.org/10.1016/j.rse.2010.01.022
- Zacharias, S., Bogena, H., Samaniego, L., Mauder, M., Fuß, R., Pütz, T., et al. (2011), A Network of Terrestrial Environmental Observatories in Germany. *Vadose Zone Journal*, 10, 955–973. https://doi.org/10.2136/vzj2010.0139
- Zeppel, M.J.B., Murray, B.R., Barton, C., & Eamus, D. (2004), Seasonal responses of xylem sap velocity to VPD and solar radiation during drought in a stand of native trees in temperate Australia. Functional Plant Biology, 31, 461–470. https://doi.org/10.1071/FP03220
- Zha, T., Qian, D., Jia, X., Bai, Y., Tian, Y., Bourque, C.P.A., et al. (2017), Soil moisture control of sapflow response to biophysical factors in a desert-shrub species, Artemisia ordosica. *Biogeosciences*, 14, 4533–4544. https://doi.org/10.5194/bg-14-4533-2017
- Zhang, C., Luo, G., Hellwich, O., Chen, C., Zhang, W., Xie, M., et al. (2021), A framework for estimating actual evapotranspiration at weather stations without flux observations by combining data from MODIS and flux towers through a machine learning approach. Journal of Hydrology, 603, 127047. https://doi.org/10.1016/j.jhydrol.2021.127047
- Zhang, L., Wylie, B. K., Ji, L., Gilmanov, T. G., Tieszen, L. L., & Howard, D.M. (2011), Upscaling carbon fluxes over the Great Plains grasslands: Sinks and sources. *Journal of Geophysical Research*, 116, G00J03. https://doi.org/10.1029/2010JG001504
- Zhang, Q., Manzoni, S., Katul, G., Porporato, A., & Yang, D. (2014), The hysteretic evapotranspiration—Vapor pressure deficit relation. Journal of Geophysical Research, *Biogeosciences*, 119, 125–140. https://doi.org/10.1002/2013JG002484
- Zhang, T., Xu, M., Xi, Y., Zhu, J., Tian, Li, Zhang, X., et al. (2015). Lagged climatic effects on carbon fluxes over three grassland ecosystems in China. *Journal of Plant Ecology*, 8(3), 291–302. <a href="https://doi.org/10.1093/jpe/rtu026">https://doi.org/10.1093/jpe/rtu026</a>
- Zhao, H., Yan, J., Yuan, S., Liu, J., & Zheng, J. (2019), Effects of submerged vegetation density on turbulent flow characteristics in an open channel. *Water*, 11, 2154. https://doi.org/10.3390/w11102154
- Zhen, S., & Bugbee, B. (2020), Far-red photons have equivalent efficiency to traditional photosynthetic photons, Implications for redefining photosynthetically active radiation. *Plant Cell Environment*, 43, 1259–1272. https://doi.org/10.1111/pce.13730
- Zhong, S., Zhang, K., Bagheri, M., Burken, J.G., Gu, A., Baikun, L., et al. (2021). Machine Learning: New Ideas and Tools in Environmental Science and Engineering. *Environmental Science and Technology*, 55, 12741–12754. https://doi.org/10.1021/acs.est.1c01339
- Zhou, Q., Fellows, A., Flerchinger, G.N., & Flores, A.N. (2019), Examining Interactions Between and Among Predictors of Net Ecosystem Exchange: A Machine Learning Approach in a Semi-arid Landscape. *Scientific Reports*, 9, 2222. <a href="https://doi.org/10.1038/s41598-019-38639-y">https://doi.org/10.1038/s41598-019-38639-y</a>
- Zscheischler, J., Mahecha, M.D., Avitabile, V., Calle, L., Carvalhais, Ciais, P., et al. (2017), Reviews and syntheses: An empirical spatiotemporal description of the global surface—atmosphere carbon

fluxes: opportunities and data limitations. *Biogeosciences*, 14, 3685–3703.

https://doi.org/10.5194/bg-14-3685-2017